THE UNIVERSITY OF CHICAGO

SEARCHING FOR DARK MATTER WITH IONIZATION SIGNALS IN XENONnT

A DISSERTATION SUBMITTED TO
THE FACULTY OF THE DIVISION OF THE PHYSICAL SCIENCES
IN CANDIDACY FOR THE DEGREE OF
DOCTOR OF PHILOSOPHY

DEPARTMENT OF PHYSICS

BY
JIANYU LONG

CHICAGO, ILLINOIS
JUNE 2024

To my family and friends

TABLE OF CONTENTS

LIST OF FIGURES

LIST OF TABLES

ACKNOWLEDGEMENTS

I am deeply grateful to my advisor, Dr. Luca Grandi, for his immense support, guidance, and patience. I also extend my thanks to Dr. Jacques Pienaar for being a supportive and helpful mentor and friend throughout my entire graduate career. Besides, I have enjoyed the time of discussions and chats with the UChicago crew, Lanqing Yuan and David Anton Martin, and benefitted a lot.

Special appreciation goes to the members of the S2-only analysis team, particularly Dr. Pueh Leng Tan and, again, Dr. Jacques Pienaar, for their excellent teamwork, which led to splendid analysis results.

I would like to thank the Physics Department at The University of Chicago and the Kavli Institute for Cosmological Physics for their generous support. Their financial and academic contributions have been crucial in enabling me to pursue my research.

Finally, I owe a profound thank you to my family – my parents, Yingbin Long and Silin Liu, and my fiancée, Siqi Zou. Their limitless support and companionship have been my greatest source of strength and motivation. Their unwavering belief in me has always inspired me to advance forward.

ABSTRACT

A substantial body of astrophysical and astronomical evidence suggests that a significant portion of the mass/energy content of the Universe exists in the form of an exotic type of matter, the nature of which remains a mystery. This additional component, known as Dark Matter (DM), is estimated to make up about 24% of the cosmic mass/energy content, outnumbering baryonic matter by a factor of five. Dark Matter is believed to consist of a new type of elementary particle that has eluded direct detection so far due to its extremely weak interaction with ordinary matter.

The XENON Collaboration, dedicated to Dark Matter searches, has constructed an ultra-low background detector, the XENONnT detector, situated in the Laboratori Nazionali del Gran Sasso. This detector is designed to be sensitive to potential rare and low-energy interactions of DM particles with xenon atoms within its target. In this work, I concentrated on analyzing low-energy ionization signals related to interactions within the detector's active volume, seeking evidence of Dark Matter and, more broadly, Physics Beyond the Standard Model. In particular, to further lower the detector's threshold and enhance its sensitivity, I established a new model to accurately characterize the shape of ionization signals in the lowest possible energy regime, ranging from one to a few ionization electrons. To veto a substantial instrumental background that was caused by large ionization signals, I developed a framework to comprehensively capture the correlations among signals. This new analysis was initially tested on a small subset of the XENONnT Science Run 0 data during calibration, enabling us to establish competitive constraints on various physics beyond the Standard Model. In particular, we focused on three theoretical models: 1) the light Dark Matter, interacting with ordinary matter via electron scattering; 2) the dark photon, kinetically mixed with the Standard Model photons; and 3) the axion-like particles, coupling to the electrons. In the imminent future, we aim to apply it to the Science Run 0 official dataset, which is blinded at the moment, to enhance these constraints further and explore territories

previously untouched.

Finally, beyond the scope of the analysis of the ionization signal in XENONnT, I proposed a new mathematical method for revealing the time correlation between two populations in a dataset under the existence of both correlated and uncorrelated populations. This method provides a novel approach to modeling the time-correlated instrumental backgrounds and can potentially improve the detector sensitivity.

CHAPTER 1

THE DARK MATTER PUZZLE

Precise measurements allowed the development of our current standard model of cosmology (ΛCDM), in which a cosmological constant (Λ), more often referred to as the dark energy, and a Cold Dark Matter (CDM) component (i.e., with typical speed much less than the speed of light, or non-relativistic) are proposed as part of our universe besides the baryonic matters that we are familiar to (i.e., atoms). The existence of dark energy is required to explain the observed accelerating expansion of the universe and is responsible for $\sim$70% of the energy/mass content of the universe [1] with its nature yet to be discovered. The CDM, or simply DM, is responsible for $\sim$26% [2] of the universe and is approximately five times more than the baryonic matter. Despite its evident gravitational effects on galactic and cosmological scales, this type of matter has not yet been directly detected in laboratory setups. The overwhelming gravitational effect and yet inert nature of DM hint at a new species of elementary particle beyond the Standard Model (BSM).

In this chapter, I will briefly review several evidences of the existence of DM (in Sec. 1.1) and introduce the *WIMP Miracle* following a mechanism that can straightforwardly explain the observed DM energy density today, for which the definition will become clearer later (in Sec. 1.2). Finally, I will discuss in more detail three specific types of elementary particles, predicted by some BSM models (Sec. 1.3): light dark matter, dark photon, and axion-like particle, which are the models tested in Ch. 4.

1.1 Evidence of Dark Matter

Since the first observation that led to the formation of the modern concept[1] of DM by the Swiss-American astronomer Fritz Zwicky in 1937 [4], all evidence for DM's existence has been inferred from its gravitational effects at various scales. These effects are observed throughout the universe.

1.1.1 Rotation Curve

The velocities of stars as a function of their distances from the center of the galaxy, or the rotational curve, can be easily derived from Newtonian Mechanics. The tangential (linear) velocity v_t of a rigid body with mass m under the influence of centripetal force F can be expressed as

$$v_t = \sqrt{\frac{FR}{m}}, \tag{1.1}$$

where R is the distance between the moving body and the axis of rotation. In the scope of stars moving in a galaxy, the centripetal force is provided by the gravitational force of the total masses inside its orbit. If we denote the mass density of the galaxy (ρ) as a function of the distance from the center, or core, of the galaxy (R, which is the same as the distance between the considered star and the center of the galaxy, i.e., the axis of rotation), the total mass (M) providing the gravitational potential for a star at a distance R from the core of the galaxy can be expressed as

$$M(R) = 4\pi \int_0^R r^2 \; dr \; \rho(r). \tag{1.2}$$

---

[1] There have been discussions about the term *Dark Matter* since the early 19th century. For example, Öpik mentioned the idea of DM in an attempt to explain the unobserved light-absorbing medium near the Sun [3]. However, early references to the existence of DM were either wrong or hinted at a less concrete concept of DM.

Here, for simplicity, a spherically symmetric galaxy is assumed. The linear velocity (v_t) of the star we are considering can then be expressed as

$$v_t(R) = \sqrt{\frac{GM(R)}{R}}, \tag{1.3}$$

where $G = 6.67 \times 10^{-11}$ $(N \cdot m^2/kg^2)$ is the gravitational constant. Eqn. 1.3 provides a method of establishing the relation between the mass content of the galaxy and the velocities of stars.

As carefully measured in Ref. [5], the observable part of the galaxy M33 (stellar disk[2] and interstellar gases[3]) amounts to an insufficient total mass to support the linear velocities of the stars at the outskirts of the galaxy. In a typical spiral galaxy, the increment of masses from stars and interstellar gases at large radius is negligible, and the linear speed of the stars on the outskirts of the galaxy should roughly follow $\sqrt{1/r}$, which is depicted in Fig. 1.1 as the dashed lines by calculating the expected linear velocities given the observed total masses of the baryonic matters in the galaxy. However, the actually observed linear velocities of stars increase at roughly a constant rate, suggesting the presence of an additional, dominant mass component, dark matter (DM), with a constant mass density (so the increment of mass with radius would be $\sim r^3$), which prevents these stars from escaping the galaxy. This is a direct proof of the existence of DM inside galaxies.

1.1.2 Gravitational Lensing

Predicted by the General Relativity proposed by Albert Einstein, the gravitational field on the galactic scale can function as a lens and bend the light from background galaxies [9]. Such an effect will render a point-like light source to appear as a slightly distorted line, a

---

[2] The masses of stars in a distant galaxy are often obtained by the luminosity-to-mass ratio [6, 7], expressed by an empirical power law $L \sim m^v$ where L is the surface luminosity and m the mass of the star. This provides us with a second way of measuring the mass of the galaxy.

[3] The measurement of the masses of gases was mostly through the infrared emission [8].

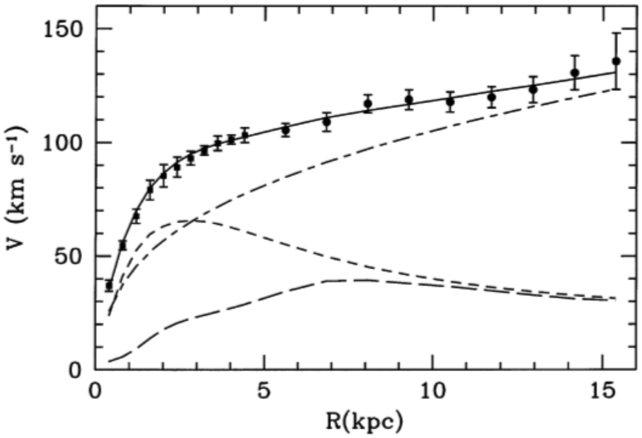

Figure 1.1: The linear velocity of stars (rotation curve) in M33 (dots) compared with the contribution of the stellar disk (short dashed line) and the gases (long dashed line). The dash-dotted line is the contribution of the DM halo needed to explain the observed rotation curve. Plot taken from Ref. [5].

ring, or multiple arcs depending on the exact locations of the object, the observer, and the mass that provides the strong gravitational field in between.

If light passes close to a mass deep within a gravitational field, strong gravitational lensing can occur, complicating the resultant image. As shown in Fig. 1.2, the image of a distant galaxy is distorted by the gravitational field of galaxy ESO325G004 [10]. This effect can help estimate the lens' mass [11] and reveal non-luminous massive components, like the DM components [12].

When light travels far from the center of the lens, only minor image distortion of background objects occurs, a phenomenon known as weak gravitational lensing. A significant indication of dark matter (DM) from weak gravitational lensing is the Bullet Cluster merger event ((1E065756)) [13]. The left plot of Fig. 1.3 shows the X-ray image of the two galaxies, by which we can see the centers of the baryonic matter (with an X-ray image mostly, we are looking at interstellar dust). On the contrary, the gravitational centers, indicated by weak lensing effects on background galaxies, appear significantly shifted and further apart, as shown on the right [14]. This discrepancy between the visible centers and the gravitational

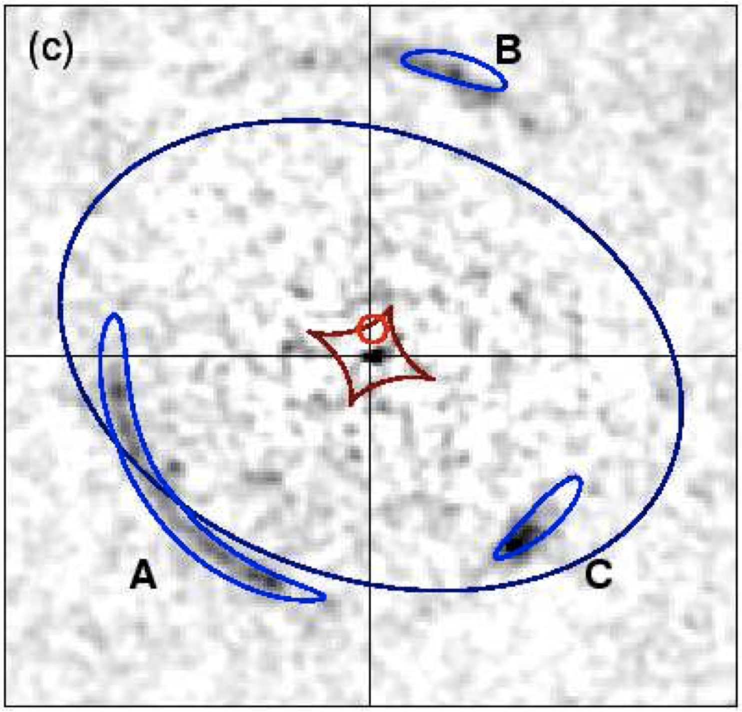

Figure 1.2: The image of a galaxy in the background is distorted into three arcs due to the strong gravitational field of galaxy ESO325G004. Plot taken from Ref. [10]

centers strongly suggests the existence of DM, which differs from the baryonic matters by their inert nature: when the gases pass each other, frictions slow them down, and part of the potential energy is turned into heat, while the DM in the two galaxies pass each other with minimal interactions, resulting in less mechanical energy loss and thus can be more separated after the passing each other. This is evidence of the existence of DM on the scale of galaxies.

1.1.3 Cosmic Microwave Background

One of the evidence of DM on the cosmological scale exists in the Cosmic Microwave Background (CMB), predicted by Ralph A. Alpher and Robert Herman in 1948 [16] and first detected by Arno Penzias and Robert Wilson in 1964 at Bell Telephone Laboratories [17]. CMB is microwave radiation that permeates the whole universe with incredible uniformity.

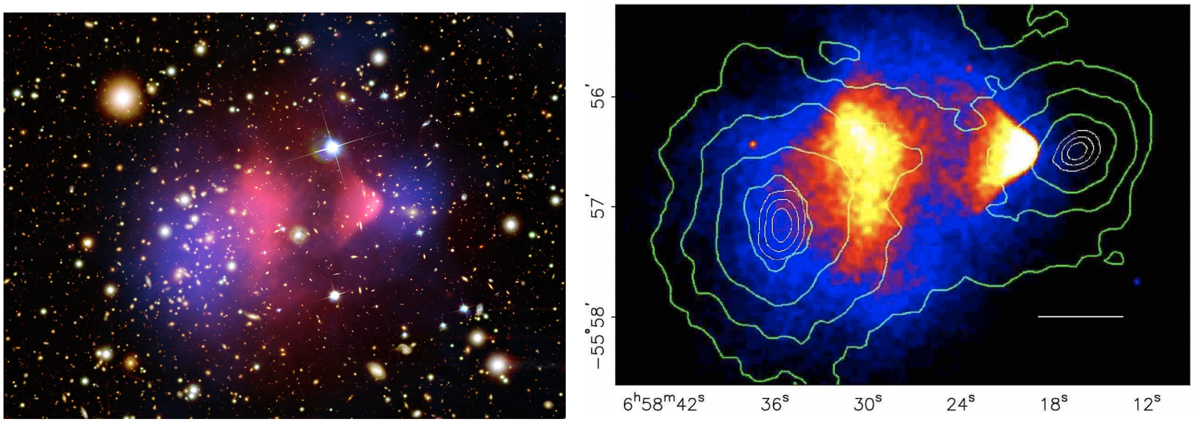

Figure 1.3: The Bullet Cluster 1E0657-558. Left: a blender of X-ray and optical images. Right: the colored image of the Bullet Cluster and the weak gravitational lensing contour (green). The left plot was downloaded from Ref. [15]. The right plot was taken from Ref. [14].

Such uniformity tells that the CMB is not associated with any stars or interstellar dust, which only occupy a negligible portion of the whole universe and are localized within galaxies. According to the Standard Cosmological Model (ΛCMD), in the early stage of the universe, right after the Big Bang, fundamental particles existed in plasma states and interacted with each other vigorously. Within the first 10^{-6} s, quarks and gluons condensed and formed protons and neutrons. While protons are the nuclei of hydrogen atoms, within a few minutes, the neutrons combined with protons and formed heavier nuclei. After around 380000 years from the Big Bang, the universe cooled down to $\sim$3000 $^{\circ}K$, which allowed nuclei to combine with the electrons and form atoms. At this point, the universe became transparent to photons. These photons, after being decoupled from the fermions, travel in space with almost no interaction with other particles, and their wavelengths are dilated by the expansion of the universe. Today, the whole universe glows (radiates) as a blackbody with temperature 2.73 $^{\circ}K$ [18]. Such radiation is the CMB, as shown in Fig. 1.4. More thorough discussions about the early history of the universe can be found in Ref. [19, 20].

Precise measurements [2, 21] showed that there is fluctuation in the CMB. The analysis of such a fluctuation was carried out in the temperature power spectrum, i.e., the parameter space of the coefficients of spherical harmonic decomposition of the CMB distribution [21] as

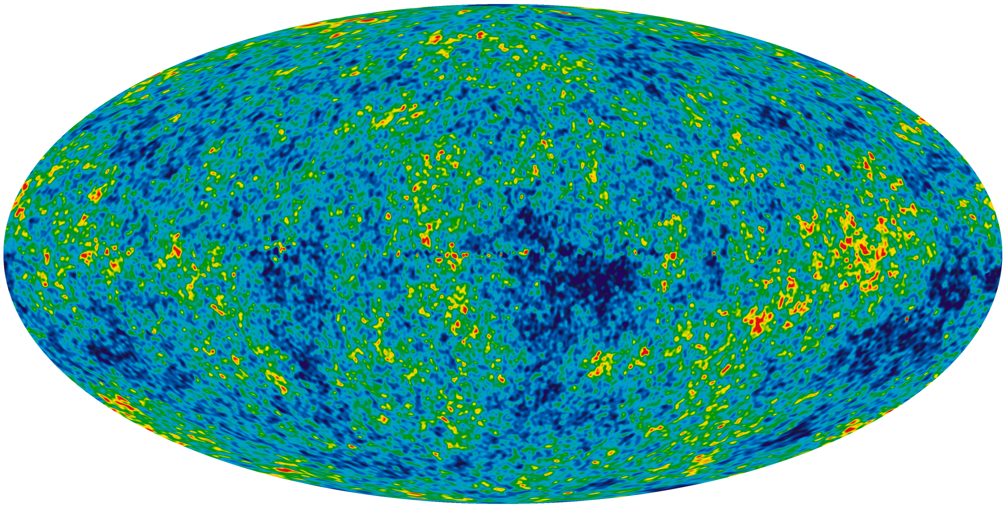

Figure 1.4: CMB map. Plot from NASA Website [25]

shown in Fig. 1.5. The fluctuation arises as a result of the acoustic oscillations (compression and dilation of matters – baryonic and dark), driven by the gravitational pulling of baryons with the tendency to form clusters and the pressure of photons that tends to separate the baryons and makes the universe more homogeneous. The pattern of this acoustic oscillation at the time when the universe became transparent to the photons (i.e., around 380000 years after the Big Bang) is then recorded by the photons that scattered with the baryons for a last time. The first peak at around $l = 250$ (corresponding to an angular range of 1°) indicates that the curvature of the universe is consistent with 0 (the universe is flat) [22], and the second peak indicates that the baryonic matter constitutes 5% of the universe. The third peak can be used to infer the content of DM [23] and indicates a $\sim$26% DM contribution to the whole universe. Also, the fitting of the temperature power spectrum tells that the DM has to be cold (non-relativistic), or at least the major contribution should be cold instead of hot (relativistic). A more detailed introduction to the interpretation of CMB and its temperature power spectrum can be found in Ref. [24].

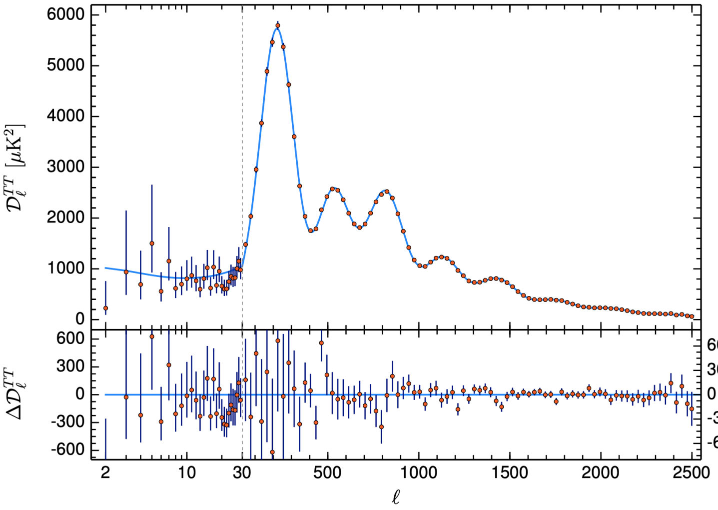

Figure 1.5: The temperature power spectrum of CMB. This spectrum represents the CMB fluctuations on different angular scales. Top: the dots are the spherical harmonic decomposition of CMB data, and the blue line is the fitting with the ΛCDM model. Bottom: the dots with error bars are the residuals with respect to the model. Different algorithms were used for the fittings of $l > 30$ and $l < 30$. Plot is taken from Planck [21].

1.1.4 Structure Formation

Another evidence of DM on the cosmological scale is the Structure Formation, which means the formation process of galaxies, galaxy clusters, and larger structures in the universe. At the early stage of the universe, the acoustic oscillations created small ripples that finally evolved into the structure of the universe today. Complicated models were adopted to explain the process [26, 27, 28], and the current best theory (again, ΛCDM) explains the structure on large scales satisfactorily. Fig. 1.6 [29] shows comparisons between the observed galactic structures (blue) and simulations (red).

In simple words, the existence of DM (more specifically, the dominance of DM) is needed in the early stage of structure formation before the decoupling of photons and baryons. During this stage, DM condensed into clusters under the influence of the gravitational effect, while the baryonic matter was still not combined into atoms due to the pressure of photons because DM does not interact (or at least extremely weakly) with photons. These DM clusters function as gravitational potential wells and promote the baryonic structure formation

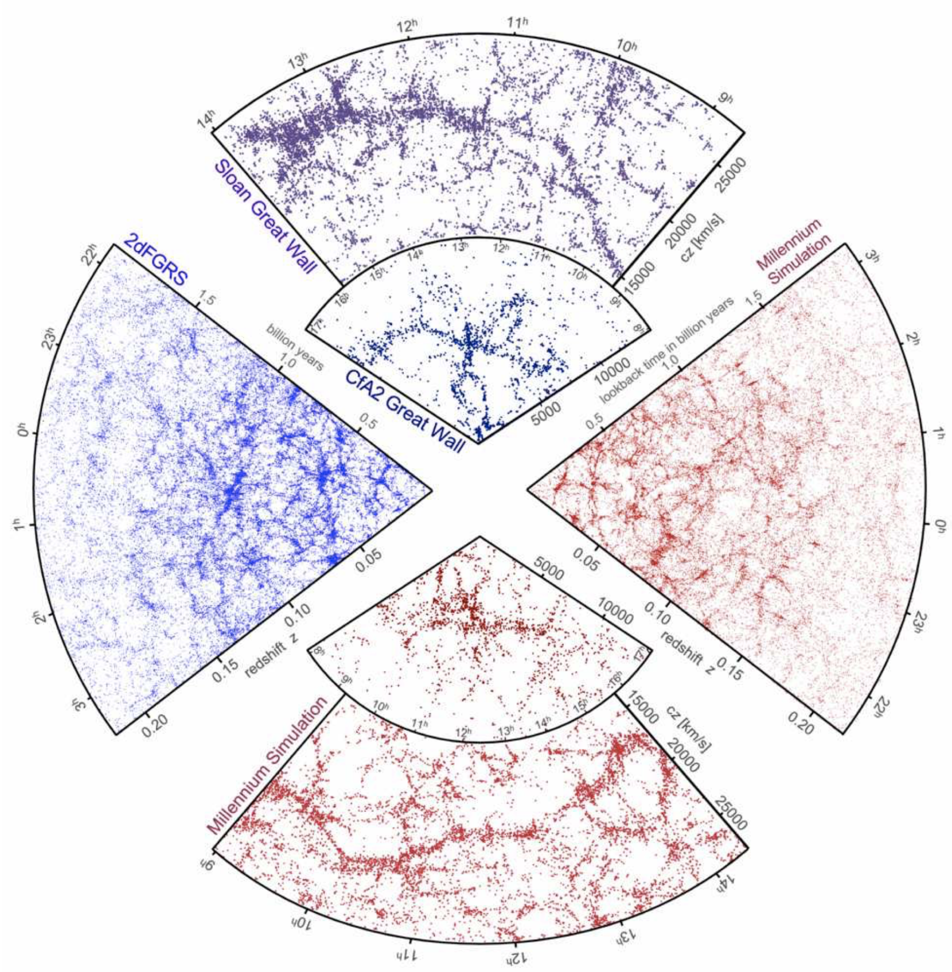

Figure 1.6: The galaxy distribution in space from simulation vs data. The blue plots are the structures observed in four different galaxies, and the red ones are the corresponding simulations. The simulation successfully recreated the web-like structures and the "Great Wall" structure. Plot were taken from Ref. [29].

process. Without the participation of DM, the condensation of baryonic matters would occur much later than what was observed.

1.2 The WIMP Miracle

Despite the compelling evidence, the nature of dark matter (DM) remains elusive. Efforts to reveal its nature have varied, from modifying Newtonian Dynamics [30] and extending these modifications to General Relativity [31] to hypothesizing non-luminous objects like brown dwarfs and neutron stars in galaxies. However, while these efforts explain some phenomena, they fail to fully account for the observed missing mass across all scales. Although we have little knowledge of the nature of the DM, if it exists in the form of matter, it has to meet the following criteria:

1. Having a relatively long lifetime. Due to a lack of observed reduction of baryonic matters in the universe, the conversion from baryonic matter to the DM – if such a conversion channel exists – is extremely rare, i.e., the production rate of DM is negligible compared to the existing amount. Therefore, short-lived DM candidates would have decayed away;

2. Interacting weakly with the baryonic matters. Otherwise, we should've observed phenomena from their interactions with atoms besides the gravitational effects;

3. Travelling at a speed much less than the speed of light (cold). Such a feature is required by the ΛCDM model to describe the current hierarchical structure of the universe [21]. This feature excludes hot (relativistic) DM, like neutrinos, from being a major component of the DM population, as they can easily escape from potential wells and do not contribute to the early stage of galaxy formations, during which the DM component was assumed to have played a crucial role;

4. Interacting gravitationally;

Therefore, it is natural to hypothesize that DM is composed of one or multiple new species of fundamental particles beyond the SM. Such a type of particle is referred to as *the Weakly Interacting Massive Particles*. Most of the time, the word "weakly" specifically points toward the DM candidates that interact with ordinary matters through the weak force. There are also DM candidates that do not interact through this channel, like the milli-charged particles and Axion-like particles, which can couple with the SM photons. These candidates are conventionally not referred to as WIMPs, although they interact weakly and are assumed non-relativistic.

Although the focus of this work is not on the search for WIMPs with masses on a TeV scale, it is important to mention this well-motivated DM candidate. Broader and more detailed discussions can be found in Ref. [32, 33, 34, 35]. Here, I will briefly describe a simple mechanism of WIMP that can intuitively explain the DM energy density we observe today.

In a wide range of theoretical models, dark matter particles are thought to have been in thermal equilibrium with all other species in the early Universe, when the average temperature was much higher than the mass of the particles, and interactions among them were vigorous. For such a thermal DM, the creation and annihilation from and to ordinary species were at equilibrium. Specifically, the conversion of the DM particles (χ) and their antiparticles into the SM fermions (f) and the reverse process can be expressed as

$$\chi\overline{\chi} \Leftrightarrow f\overline{f}. \tag{1.4}$$

The rate of the annihilation process (Γ) can be expressed as [33]

$$\Gamma = \langle\sigma v\rangle n_{\chi}, \tag{1.5}$$

where $\langle\sigma v\rangle$ is called the thermally averaged annihilation cross-section, and n_{χ} is the number density of DM particles. As the universe cools down, the average kinetic energy of the SM fermions becomes much lower than double the mass of DM particles (m_{χ}), and the creation process stops. In this phase, the annihilation process dominates, and the amount of DM decreases. As the universe expands and n_{χ} decreases, the annihilation also stops, leaving a constant (relic) DM mass in the universe, or equivalently, a constant DM number

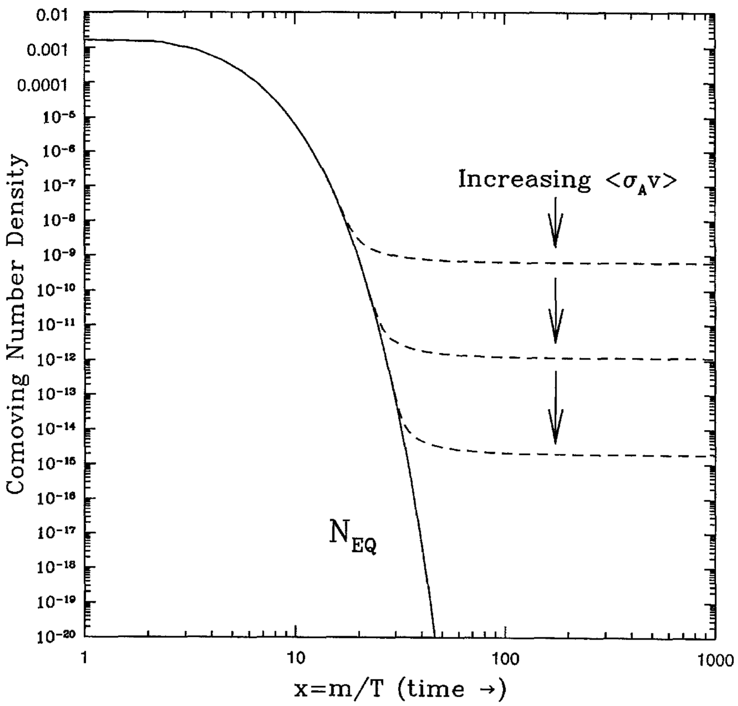

Figure 1.7: Comoving number density evolution in the history of the universe. Time is represented as $x = m/T$ on the x-axis: as a simple explanation, the temperature of the universe monotonically decreases, and thus, we can use $1/T$ to represent time. The solid line shows the equilibrium number density curve. The dashed lines represent the different relic number densities with different annihilation cross-sections. The larger the cross-section, the lower the relic number density. Plot taken from Ref. [32]

density (n^{eq}) in a comoving volume[4]. Such a process is called *freeze-out.* Fig. 1.7 shows the evolution of the comoving number density of DM particles. The solid line shows the equilibrium number density curve. The dashed lines represent the different relic number densities with different annihilation cross-sections. The larger the cross-section, the lower the relic number density, as the DM particles can more easily annihilate away.

Following the calculation in Ref. [32] and Ref. [35], and using the measured DM critical density ($\Omega_\chi h^2 = 0.12$, where $h^2 = H_0/(100\ km{\cdot}s^{-1}{\cdot}Mpc^{-1})$ and H_0 is the Hubble Constant)

---

[4] The comoving volume is defined as the proper volume factoring out the cosmological expansion factor, $a(t)$, and the two quantities are set equal at the present time, i.e. $a(t = \text{now}) = 1$. Due to this definition, the comoving volume is constant and independent from the expansion of the universe.

from Ref. [2], we can establish the equation

$$\Omega_\chi h^2 = 0.12 \approx \frac{3 \times 10^{-27}\ cm^3 \cdot s^{-1}}{\langle \sigma v \rangle} \Rightarrow \langle \sigma v \rangle \approx 2.5 \times 10^{-26}\ cm^3 \cdot s^{-1}. \tag{1.6}$$

From the particle physics perspective, we can also probe the annihilation cross-section of $\chi\overline{\chi} \to f\overline{f}$. Assuming the annihilation process happens through an s-channel vector mediator V with mass m_V

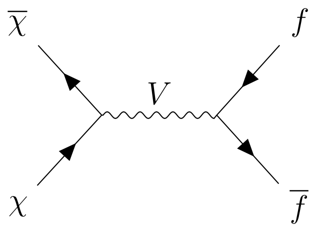

and following the derivations in Ref. [33], the thermally averaged annihilation cross-section can be expressed as

$$\langle \sigma v \rangle \approx \frac{|\mathcal{M}|^2}{32\pi m_\chi^2}. \tag{1.7}$$

If the DM particle is fermionic, the square of the matrix $|\mathcal{M}|^2$ can be expressed as

$$|\mathcal{M}|^2 \approx g_\chi^2 g_f^2 \frac{32 m_\chi^4}{\left(s - m_V^2\right)^2}. \tag{1.8}$$

g_χ and g_f are the coupling strength of the mediator V to the DM particle and the final state fermion, respectively. In the limit that the mass of the mediator is much less than the DM particle mass, and the coupling between V and the SM fermions (g_f) is small, the creation of the SM fermions would be suppressed while a new process is allowed and expressed as

$$\langle \sigma v \rangle_{\chi\overline{\chi} \to VV} \simeq \frac{\pi \alpha_\chi^2}{m_\chi^2}, \tag{1.9}$$

where $\alpha_\chi = g_\chi^2/(4\pi)$. The DM particle χ and the mediator V form a dark sector, and if long-lived, they can be a generic explanation for the DM population. Relating Eqn.1.9 and

Eqn.1.6, a DM candidate of masses in the order of TeV and a coupling strength $\alpha_\chi \sim 0.03$, which is of the scale of the weak interaction, can reproduce the observed DM energy density observed today.

The coincidence of an unknown DM candidate interacting on the weak scale and producing the observed relic DM abundance while following a straightforward mechanism is called *the WIMP miracle*. A lot of theoretical frameworks predict candidates for WIMPs, like Supersymmetry, which proposes a bosonic counterpart for each fermion in the SM and vice versa.

1.3 Searches for the Candidates of Dark Matter

In addition to the WIMPs discussed previously, other BSM particle candidates could serve as DM. Because we focused on the interactions that deposit sub-keV energy in our detector, while the WIMPs of TeV masses feature 1-100 keV energy transfer to nuclei [36], they are excluded from our analysis.

Broadly speaking, there are two channels in which a DM particle can interact with an SM fermion (in this work, we will only talk about electrons): scattering, which will produce a continuous spectrum, and absorption, which will produce a mono-energetic absorption peak with energy characteristic equal to the DM particle. The characteristics of an unknown DM particle (χ) scattering off an orbital electron can be captured by the interaction cross-section, the kinematic process, and the ionization process of the orbital electron, and thus can be derived in a model-independent way [37, 38, 39]. Therefore, we use the term *Light Dark Matter (LDM)* to capture the DM candidates that transfer their energy to the SM matters in this channel. The absorption, however, requires a concrete physical model to describe the exact process. Therefore, we chose the Dark Photon (DP) and Axion-like Particles (ALPs) as our physics model for the discussion.

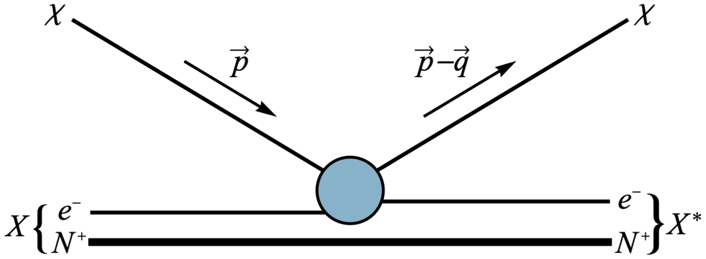

Figure 1.8: Illustration of an LDM particle scattering off an orbital electron, deposition $\vec{q}$ momentum, exciting the atom X into X^*, in which the electron can be either unbound or bound at a higher-energy state. N^+ is the ensemble of the nucleus and the electron cloud, except for the orbital electron participating in the scattering process. Plot taken from Ref. [37].

1.3.1 Light Dark Matter

There are lots of hypotheses on the nature of LDM, similar to that of the WIMPs. The way in which they interact with ordinary matters depends on the exact model proposed [40, 41, 33]. However, in the most generic way, we can assume that the LDM particle of mass m_χ on the scale of MeV can scatter off electrons on the orbitals of atoms, like xenon, as depicted in Fig. 1.8. In the rest of this subsection, I will introduce the derivation of the differential rate of LDM-electron scattering following the discussions in Ref. [37] and Ref. [38].

For a scattering process depicted in Fig. 1.8, we can parametrize the process by defining the scattering cross-section ($\overline{\sigma}_{\chi e}$) at a reference momentum transfer ($q = \alpha m_e$, where α is the fine-structure constant and m_e is the mass of an electron) as

$$\overline{\sigma}_{\chi e} = \frac{\mu_{\chi e} |\mathcal{M}(q = \alpha m_e)|^2}{16\pi m_\chi^2 m_e^2}, \tag{1.10}$$

where $\mu_{\chi e}$ is the reduced mass of an electron and an LDM particle of mass m_χ. $|\mathcal{M}|^2$ averages over all initial states and summing over all final states, for which the specific value is not of concern here and can only be obtained with a concrete physics model. $|\mathcal{M}(q)|^2$ at an arbitrary momentum transfer $\vec{q}$ can be captured by accounting for the variations from the reference value with a DM form factor, $F_{DM}(q)$, defined as

$$F_{DM}(q) = \begin{cases} 1 & \text{For a heavy vector mediator or magnetic dipole moment coupling} \\ \frac{\alpha m_e}{q} & \text{For electric dipole moment coupling} \\ \left(\frac{\alpha m_e}{q}\right)^2 & \text{For a massless or extremely light vector mediator} \end{cases} . \tag{1.11}$$

With the DM form factor, $|\mathcal{M}(q)|^2$ can then be expressed as

$$|\mathcal{M}(q)|^2 = |\mathcal{M}(q = \alpha m_e)|^2 |F_{DM}(q)|^2. \tag{1.12}$$

The scattering process excites the orbital electron from one state to another. In the scope of this analysis, we are only interested in the full ionization process, i.e., the electron transit from the ground state to an unbound state with momentum $\vec{p'}$. The amplitude of such a process for an electron with quantum numbers (n, l), where n is the principle quantum number and l the orbital angular momentum quantum number, is described by the so-called *ionization form factor* ($f^{nl}_{ion}(p', q)$):

$$\left| f^{nl}_{ion}(p', q) \right|^2 = \frac{2p'^3}{(2\pi)^3} \sum_{deg.states} \sum_{l', m'} \left| \int d^3r \, \phi^*_{p', l', m'}(\mathbf{r}) \psi_{n,l}(\mathbf{r}) \exp(i\mathbf{qr}) \right|^2 , \tag{1.13}$$

where $\phi^*_{p',l',m'}$ and $\psi_{n,l}$ are the wavefunctions of an unbound electron and the orbital electron, respectively. The formula averages over the whole phase space and sums over all degeneracies of the initial and final electron states, yielding the amplitude of getting a final state electron with momentum p' from an initial momentum transfer q. The final unbound electron will carry an energy of $(p')^2/(2m_e)$. Such energy will be exhausted in the *electronic recoil* (ER) and produce further γ or e^- signals. The details of this ER process will be discussed in Sec. 2.2.1. Exact calculations of the ionization form factor and discussions on corrections to heavy atoms like xenon can be found in Ref. [39, 42, 43].

Collecting the various components above, the thermally averaged cross-section for an LDM to scatter off and free an orbital electron with the quantum numbers (n, l) evaluated in an infinitesimal segment of the energy of the unbound electron (E_{er}) can be expressed as:

$$\frac{d\langle\sigma_{ion}^{nl}u\rangle}{d\ln E_{er}} = \frac{\overline{\sigma}_{\chi e}}{8\mu_{\chi e}^2}\int q\left|f_{ion}^{nl}(p', q)\right|^2 |F_{DM}(q)|^2\eta(u_{min})dq. \tag{1.14}$$

This quantity is called the *differential averaged cross-section.* $\eta(u_{min})$ is the mean inverse speed function that embeds the kinetic energy distribution of the halo DM, defined as

$$\eta(q) = \int_{u_{min}}^{u_{max}} \frac{1}{x}\sqrt{\frac{2}{\pi}}\frac{x^2}{a^3}e^{-\frac{x^2}{2a^2}}dx, \tag{1.15}$$

where $a = \frac{220km/s}{c}$, and u_{min} is defined by the minimum velocity required for a DM particle with mass m_χ, given a momentum transfer of q and a binding energy of $E_{binding}^{nl}$, that can result in a final electron kinetic energy E_{er}:

$$u_{min} = \frac{\left|E_{binding}^{nl}\right| + E_{er}}{q} + \frac{q}{2m_\chi}. \tag{1.16}$$

u_{max} is defined as a hard cutoff for the allowed DM velocity at 544 km/s (the escaping velocity from the galaxy) + 232 km/s (the linear velocity of the earth).

Eventually, we can express the expected interaction rate (R) as a function of the final electron kinetic energy (or the ER energy):

$$\frac{dR}{d\ln E_{er}} = N_T\frac{\rho_\chi}{m_\chi}\sum_{n,l}\frac{d\langle\sigma_{ion}^{nl}u\rangle}{d\ln E_R}. \tag{1.17}$$

ρ_χ is the local DM energy density and is independently measured to be $\sim 0.3\ GeV/cm^3$ [44]. The DM particle mass m_χ is treated as a free parameter. N_T is the number density per mass of the target with unit [targets/kg^{-1}]. In our situation, the target is the orbital electrons

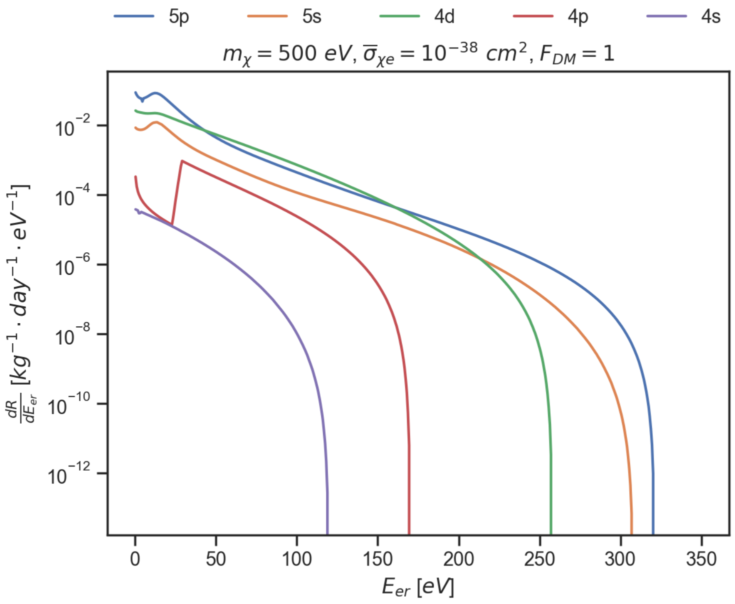

Figure 1.9: Differential rate for LDM-electron scattering in different orbitals. The LDM particle is asummed to be 500 eV and with a nominal cross-section $\overline{\sigma}_{\chi e} = 10^{-38}\ cm^2$. The interaction is assumed to happen via a heavy mediator ($F_{DM} = 1$).

of xenon atoms. The N_T for xenon atoms is $\sim 45.87\ kg^{-1}$, and for the orbital electrons, we need to multiply the number of electrons within each orbital.

The calculation of the differential rate for each orbital is summarized in the wimprates package [45]. Fig. 1.9 shows the rates of a LDM particle of mass 500 eV and a nominal cross-section $10^{-38}\ cm^2$ scattering off the two outermost shells through a heavy mediator ($F_{DM} = 1$).

1.3.2 Dark Photon

As mentioned in the WIMP miracle case (Sec. 1.2), the DM particle and the massive vector mediator form a dark sector. However, there is no reason to rule out the possibility that the mediator by itself constitutes the entirety of the DM population. One mechanism for such a mediator to exist is through a second $U(1)$ gauge group, namely $U(1)_D$. This additional symmetry would result in a new gauge field, A', which can interact with the SM particles via a kinetic mixing [40, 46]. Such a new vector boson can gain its mass ($m_{A'}$) through the Stückelberg mechanism [47] or the Higgs mechanism with an extra Higgs field [48]. The corresponding particle is called the Dark Photon (DP).

At low energy, the kinetic mixing between the DP and the SM particles is dominated by the mixing with the SM photon, with the relevant Lagrangian expressed as [48]:

$$\mathcal{L} \sim -\frac{1}{4}F'^{\mu\nu}F'_{\mu\nu} - \frac{\epsilon}{2}F^{\mu\nu}F'_{\mu\nu} + \frac{1}{2}m^2_{A'}A'^{\mu}A'_{\mu}, \tag{1.18}$$

where ϵ is the kinetic mixing strength, $F_{\mu\nu}$ and $F'_{\mu\nu}$ are the SM photon and DP tensors, respectively. The absorption cross-section of the DP by an SM electron ($\sigma_{A'}$) can be expressed by the photoelectric absorption cross-section of an SM photon of energy $m_{A'}$ ($\sigma_{PE}(E = m_{A'})$) as [48]

$$\sigma_{A'}(m_{A'})v_{A'} \approx \epsilon^2\sigma_{PE}(E = m_{A'}), \tag{1.19}$$

where $v_{A'}$ is the DP velocity. The values of $\sigma_{PE}(E)$ for different elements with a wide range of photon energies have been measured, for example, in Ref. [49]. Using Eqn. 1.17 but treating it as a mono-energetic peak, we can get the rate of interaction (R) as a function of $m_{A'}$:

$$R = N_T\frac{\rho_\chi}{m_{A'}}\epsilon^2\sigma_{PE}(E = m_{A'}). \tag{1.20}$$

Eqn. 1.19 is only correct if the mass of the DP particle is much larger than the first ionization energy if the medium, or otherwise polarizations of the medium would distort the interaction and an in-medium correction to the absorption rate is needed. As calculated in Ref. [50], with the longitudinal and transverse polarization functions $\Pi_{L,T}$, the rate of DP absorption after correction is:

$$R_{L,T} = -\frac{\epsilon^2 m^4_{A'}}{\left|m^2_{A'} - \Pi_{L,T}\right|^2}\Im\left(\Pi_{L,T}\right), \tag{1.21}$$

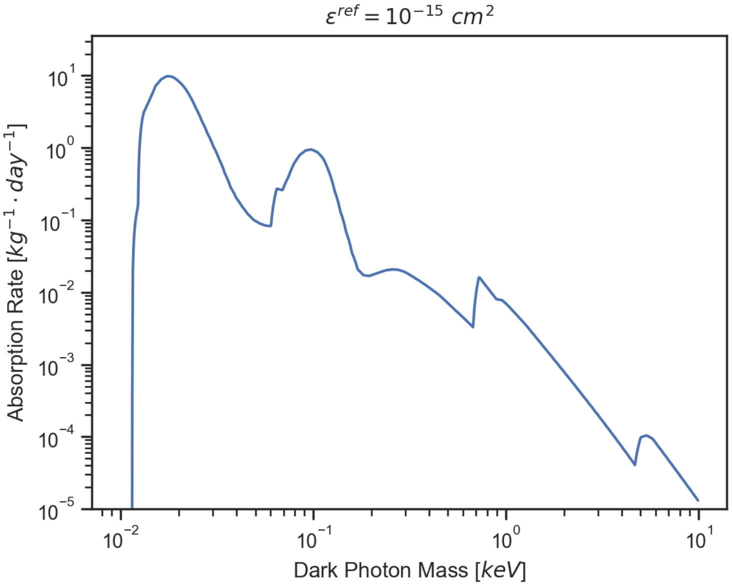

Figure 1.10: DP absorption rate as a function of DP mass. $\epsilon^{ref} = 10^{-15}$ was used. I used the same rate calculation as presented in Ref. [52].

where $\Im\left(\Pi_{L,T}\right)$ is the imaginary part of the polarization functions. Using the refractive index values of xenon tabulated in Ref. [49] and extrapolate to low-energy DP using the relation discussed in Ref. [51], Fig. 1.10 shows the absorption rate of DP particles as a function of the DP mass, with nominal mixing strength $\epsilon = 10^{-15}$. Despite the complicated expression, we can straightforwardly read from Eqn. 1.21 that given a DP mass, the absorption rate scales as the square of the mixing strength, i.e.

$$R \sim \epsilon^2.$$

1.3.3 Axion-like Particles

The original Axion was proposed by Roberto Peccei and Helen Quinn [53, 54] in the hope of solving the strong CP problem[5], which has a coupled particle mass m_a and its decay

---

[5] The formulation of the Quantum Chromodynamics does not manifestly preserve the charge conjugation symmetry and parity symmetry (CP). However, no violation of such symmetry has ever been observed in

constant f_a [34]

$$m_a = 5.691(51)\left(\frac{10^9\ GeV}{f_a}\right) meV. \tag{1.22}$$

For a decay constant long enough such that the axion can be a DM candidate, the corresponding axion mass is on the scale of μeV [55] and is beyond the reach of a particle detector like XENONnT.

In a more general sense, a group of similarly defined pseudo-scalar fields with decoupled masses and decay constants called axion-like particles (ALPs) is useful as potential DM candidates. A minimal Lagrangian defining the pseudoscalar field of ALP a interacting with the SM particles, in particular the coupling to the SM electron, can be expressed as [48]

$$\mathcal{L} \sim \frac{1}{2}\partial_\mu a \partial^\mu a - \frac{1}{2}m_a^2 a^2 + i g_{ae} a \bar{e}\gamma_5 e. \tag{1.23}$$

It can interact with electrons and be absorbed through the "axioelectric" effect. The cross-section of absorption σ_{AE} can be expressed in relation to the photoelectric cross-section σ_{PE} as [56, 57]

$$\sigma_{AE}(E) v_a \approx \sigma_{PE}(E) \frac{3}{4}\frac{g_{ae}^2}{4\pi\alpha}\frac{E^2}{m_e^2}\left(1 - \frac{1}{3}v_a^{\frac{2}{3}}\right), \tag{1.24}$$

where E and v_a are the APL's energy and velocity, and g_{ae} the coupling strength between ALP and the SM electron. For a non-relativistic ALP model, $E \simeq m_a$.

The formulation of σ_{AE} is similar to $\sigma_{A'}$ in the DP absorption scenario. The same in-medium correction is needed for the final absorption rate of the ALPs by the SM electrons in a detector. Fig. 1.11 shows the absorption rate of ALP particles as a function of the ALP mass, with nominal coupling strength $g_{ae} = 10^{-15}$. Again, given an ALP mass, the absorption rate scales as the square of the coupling strength, i.e.

$$R \sim g_{ae}^2.$$

---

interactions only involving strong interaction. This is the so-called strong CP problem.

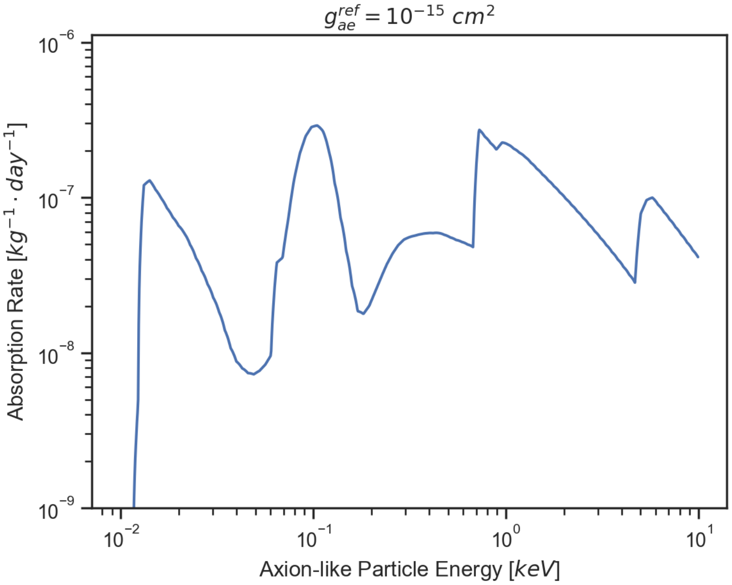

Figure 1.11: ALP absorption rate as a function of ALP energy. $g_{ae}^{ref} = 10^{-15}$ was used. I used the same rate calculation as presented in Ref. [52].

CHAPTER 2

THE XENONNT EXPERIMENT

XENON Collaboration has been dedicated to the search for a well-motivated DM particle model, the Weakly Interactive Massive Particles (WIMPs). A family of two-phase liquid xenon detectors, known as Time Projection Chamber (TPC), and their supporting infrastructures, were built and ran for over 15 years starting from XENON10 [58] to nowadays gigantic XENONnT [59]. Benefitting from considerable exposure and accurate event energy and position reconstruction, XENON achieved an ultra-low background rate and has set the most stringent limits for DM-nucleon cross sections.

2.1 XENONnT Detector

The XENONnT experiment is operated at Laboratori Nazionali del Gran Sasso (LNGS), located beneath the Gran Sasso mountain in Italy below 3600 m of water-equivalent rocks to shield it from cosmogenic background. The experimental setup is constituted by three nested detectors (see Fig. 2.1 right): the Liquid Xenon Time Projection Chamber (LXe TPC), the Neutron Veto (NV), and the Muon Veto (MV). The XENONnT detector is located in Hall B of INFN Laboratori Nazionali del Gran Sasso (LNGS) in Assergi, Italy, under the Gran Sasso mountain.

The two-phase Time Projection Chamber is the core detector designed to be sensitive to potential low-energy interactions of Dark Matter particles with the liquid xenon target. The latter encompasses ∼6.4 tons of xenon in the liquid phase above which a gaseous xenon pocket is maintained. This active volume, as shown in Fig. 2.1, is surrounded by a cylindrical 134 cm-high structure composed of 24 diamond-polished PTFE panels to enhance reflectivity. A total of 494 3 Hamamatsu R11410-21 Photomultiplier Tubes (PMTs), split into two arrays, read out the active volume from its top and bottom and detect the light produced within

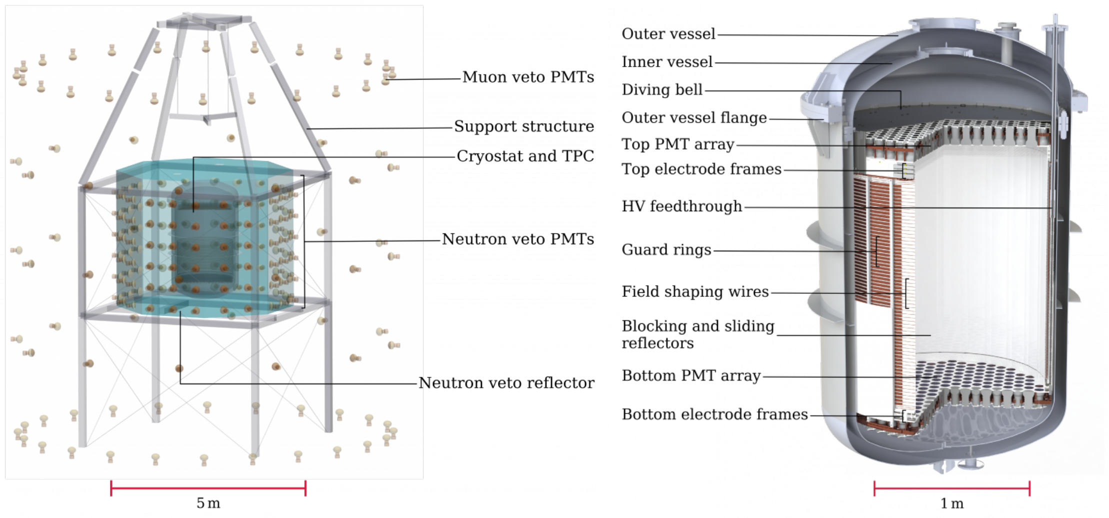

Figure 2.1: 3D rendering of XENONnT TPC (left) and NV (right) [61].

it (252 at the top and 242 at the bottom). A cathode parallel-wire grid, placed 60 *mm* above the bottom PMT array, and a gate grid, located 148.6 *cm* above it and 3 *mm* below the liquid-gas interface, define the drift electric field ($\mathcal{E}_d$). To minimize edge effects in the field, two concentric sets of copper field shaping rings (FSRs) surround the active volume (see Fig. 2.1 right). A third grid, the anode, is located in the gas phase, 8 *mm* above the gate and, together with the gate grid, allows to establish a strong extraction electric field ($\mathcal{E}_{ext}$) in the thin layer of liquid above the gate and a multiplication electric field ($\mathcal{E}_{mult}$) in the gas. Two additional grounded screening grids are placed 5.3 *mm* above the bottom PMT array and 40.7 *mm* below the top PMT array to protect the PMTs from strong electric fields. The grids are composed of parallel stainless steel (SS) wires stretched on metal SS frames. Besides the parallel wires, the gate and anode grids feature respectively 2 and 4 perpendicular wires that were added to minimize the wire-plane sagging. A photograph of a detail of the anode grid is shown in Fig. 2.2. Materials used to construct the detector were extensively assayed in order to select the most radiopure materials [60].

To maintain the xenon gas at its evaporation temperature and allow both phases to coexist, the TPC is inserted within a cryostat. A cryogenic and a purification plant are used

Figure 2.2: A detail of the anode grid. It is composed of parallel wires that are 5 *mm* apart. Besides them, four perpendicular wires (2 are shown in the picture) were added to mitigate sagging.

to continuously cool down and purify the xenon gas from electronegative impurities from material outgassing [62]. The system is also equipped with a krypton and radon cryogenic distillation column. The first is designed to be operated in batch mode and remove traces of the radioactive isotope ^{85}Kr from natural xenon before the physics run starts [63]. The second is operated online and allows for continuous removal of ^{222}Rn emanated from materials both in gaseous and liquid phase and mixing with the xenon gas [64, 65].

The cryostat is located at the center of a water tank of 10 *m* diameter and 10 *m* height and fixed in place by metal support (see Fig. 2.1 left). The water tank is split into two volumes and equipped with photomultipliers to be operated as Neutron and Muon Vetoes.

The Neutron Veto surrounds the cryostat and was designed to tag neutrons after their interaction inside the TPC. External or internal (from the TPC materials) radiogenic neutrons represent an extremely dangerous background since these neutral particles can produce Nuclear Recoils inside the TPC active volume, mimicking a WIMP signature. The NV region is encompassed by an octagonal-based structure composed of high reflectivity PTFE panels (that optically separate it from the Muon Veto) and read out by 120 Hamamatsu R5912-100-10 8 PMTs installed on the panels (see Fig. 2.1 left). When operated with pure water,

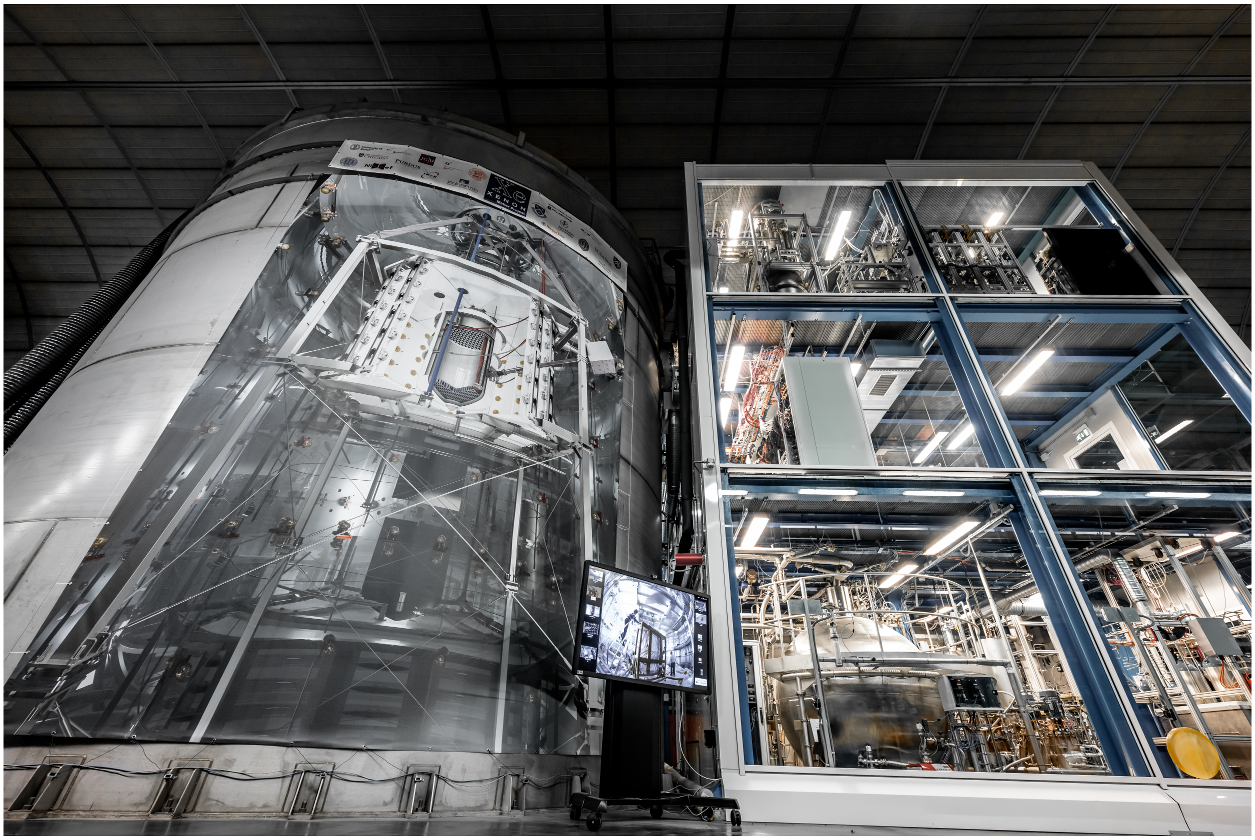

Figure 2.3: Photo of the XENONnT Experiment. Taken in the summer of 2022.

NV can tag neutrons by the emission of Cherenkov light associated when they are captured by hydrogen. This is the condition in which the NV was operated during XENONnT Science Run 0. At a later stage, to increase tagging efficiency, the water was doped with Gd-salt.

As shown in Fig. 2.1 on the left, the Muon Veto surrounds the NV. It is equipped with 84 Hamamatsu R5912ASSY 8 PMTs installed along the internal wall of the water tank, whose surface is covered with high-reflective 3M foil. This water Cherenkov detector is used to tag muons crossing the water tank and is potentially capable of tagging the Cherenkov light emission of cosmogenic neutrons and, hence, actively suppressing the neutron background.

A photo of the whole structure is shown in Fig. 2.3. The detector was commissioned in the Winter of 2021. The first science run, called Science Run 0 (SR0), started on May 3rd, 2021. It started with a complete set of calibrations including ^{220}Rn, $^{83\mathrm{m}}$Kr and AmBe. A

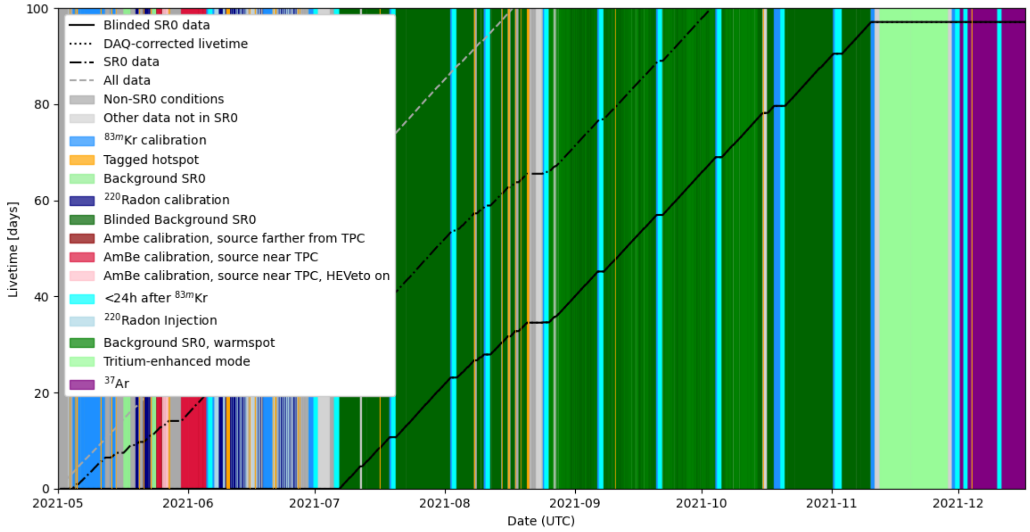

Figure 2.4: Data taking during SR0.

total of 97.1 days of low-background science data were acquired from July 6th to November 10th, 2021, with bi-weekly $^{83\mathrm{m}}$Kr calibration runs to track the behavior of the detector. The low-background science data were followed by two weeks of data taking acquired in similar conditions but bypassing the purification getter with the goal of enhancing traces of Tritium in the TPC if any. These two weeks are referred to as Tritium Enhanced Data (TED) runs. It turned out after analyses that no tritium rate increase – except purity drop – was detected during TED data, making them ideal to test the analysis presented in this work. Finally, an ^{37}Ar calibration was performed to study the response of the detector even at lower energies. Science Run 0 data were used to search for WIMPs and other Dark Matter models. During the SR0 period of XENONnT, the temperature of liquid xenon was kept at 176.84 $^{\circ}K$, and the pressure of gaseous xenon was maintained at around 2.48 atm. To date, no discovery has been made, but world-leading stringent constraints on a wide range of models were set [66, 67].

Science Run 0 was followed by other science runs, but in this work, we will only consider SR0. The data-taking periods and live-time accumulation is shown in Fig. 2.4.

2.2 The TPC Working Principle

When a particle crosses the TPC, it can deposit a fraction of its energy interacting with the xenon medium. More specifically, if the primary particle is neutral, as in the case of dark matter, the visible energy associated with its interaction can lead to:

- a Nuclear Recoil (NR): the primary neutral particle scatters off the xenon atom nucleus by interacting with its constituents. The recoiling nucleus acts as the primary ionizing particle, losing its kinetic energy by ionizing, exciting, and heating the liquid xenon medium. At the energies of interest, the resulting track has a typical dimension of less than 1 μm for NR in the range of 1-100 keV (estimated from Fig. 5 of Ref. [68]). This is the expected signature of a WIMP, but a neutron would generate a similar process, becoming a dominant background for the search;
- an Electron Recoil (ER): the primary neutral particle scatters off an orbital electron of the xenon atom. The recoiling electron ionizes and excites the liquid xenon medium. Unlike the NR case, the track is slightly more extended for ER in the range 1-100 keV, ranging from less than 1 μs to $400 \mu s$ [68]. Electron recoils are the typical signature for light-dark matter candidates, i.e., Axion-like particles.

The nature and energy of the ionizing particle (ER or NR) ultimately define the dimension and structure of the ionization track, leading (in the presence of a field) to different relative ratios of scintillation light and free ionization charge. Although electron recoils are intrinsically different from nuclear recoils, the statistical fluctuations associated with the low-energy regime can sometimes lead to very similar responses. For these reasons, the more abundant ERs associated with surviving gamma and beta contamination also become a dominant background for WIMP searches.

The de-excitation of the excited Xe atoms, called excimers (Xe^*), will produce a prompt scintillation light, called S1, that will bounce inside the TPC and eventually be detected by

PMTs. The ionization electrons, if the energy deposition happens inside the active volume of the TPC, will drift up to the gate under the effect of $\mathcal{E}_d$, from which they will be accelerated and extracted into gaseous Xe (GXe). In GXe, the electrons will create a secondary scintillation light, called S2, that is very localized and can be used to determine the (x, y) location of the energy deposition (detailed discussion in Sec. 3.1.3). Part of the ionization electrons may recombine with their positively charged counterparts if an insufficient $\mathcal{E}_d$ was presented, thus contributing to S1. Such recombination is directly related to the strength of $\mathcal{E}_d$, as a stronger drifting field separates the ionization electrons from the xenon ions more effectively, reducing the chances of the recombination between the two [69]. The decay of excimers and the process of recombination are described as:

$$Xe^* + Xe \to Xe_2^* \to 2Xe + \gamma, \tag{2.1}$$

$$\begin{aligned} &Xe^+ + Xe \to Xe_2^+ \\ &Xe_2^+ + e^- \to Xe^{**} + Xe \\ &Xe^{**} \to Xe^* + \text{heat} \\ &Xe^* + Xe \to Xe_2^* \to 2Xe + \gamma \end{aligned} \quad . \tag{2.2}$$

The time difference between S1 and S2, or drift time (t_d), is generally used to characterize the location z where the energy deposition occurs. A schematic graph of the energy deposition and the S1-S2 generation and detection process is shown in Fig. 2.5. Traditionally, the drift time is defined either by the time difference between the beginning of S1 and S2 signals or between the center of gravity[1] of the two. The difference between the two definitions is negligible because the duration of S1 and S2 signals[2] are much smaller than the drift time[3].

---

[1] The timestamp that separates the signal into two equal parts by area

[2] The duration of an S1 signal is in the order of a few hundred nanoseconds [70], and an S2 signal is typically less than $30\mu s$, more discussions in Ch. 3

[3] The maximum drift time in XENONnT TPC is about 2.3 ms [70]

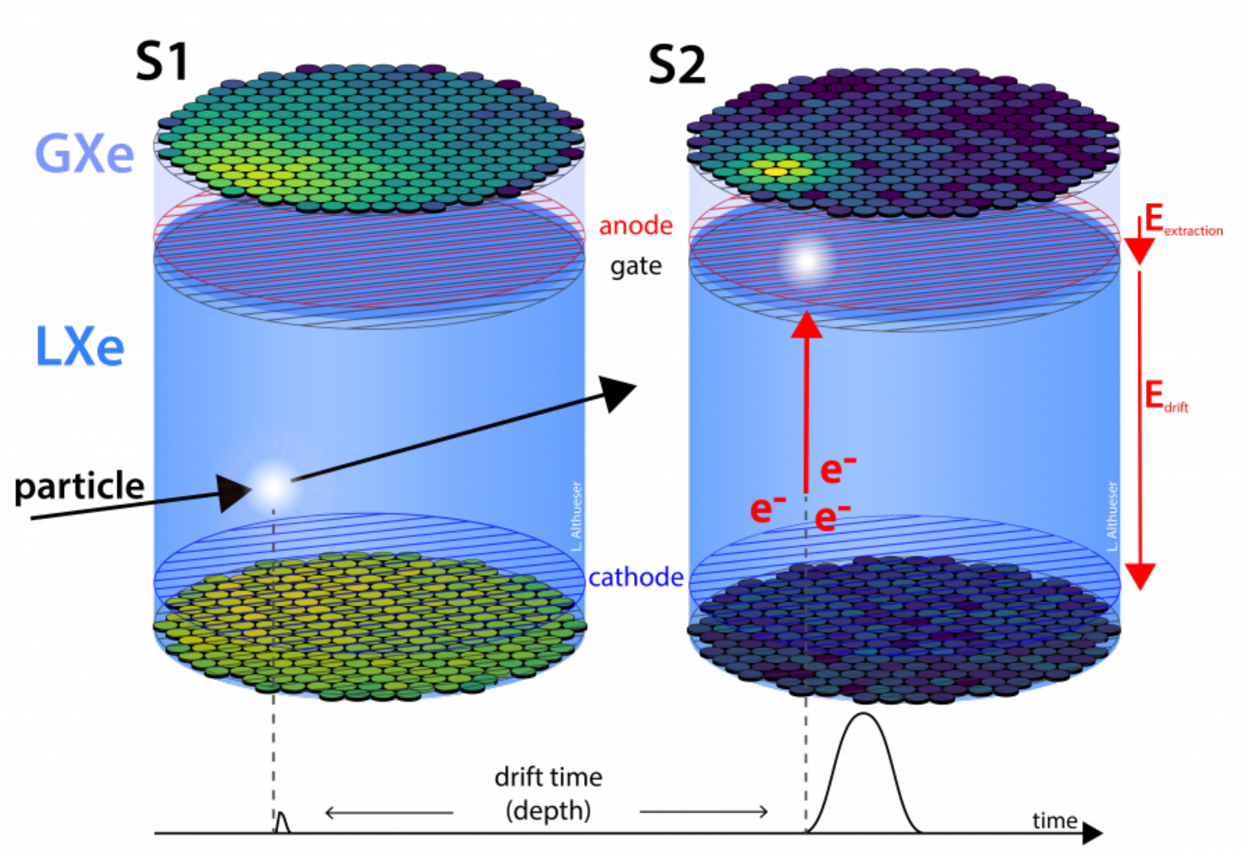

Figure 2.5: Illustration of an event from energy deposition to S1-S2 production. Picture by Dr. Lutz Althueser.

For an unambiguous definition, in this literature, I will use the first definition, which is the time difference between the beginning of the two signals.

The response of the top PMT array to an S2 signal, called the S2 hit pattern, features strong clustered patterns around the location where the electrons are extracted and accelerated in the gas, as depicted on the right of Fig. 2.5. Such a clustered pattern allows us to reconstruct the xy location of the electron extraction and, thus, the location of the S2 signal. After correcting with respect to the drifting field distortion [71], we can trace back the xy location of the interaction in the liquid. With the full 3-dimensional position reconstruction, we are able to optimize our signal-to-background ratio by fiducialization, i.e., using a volume within which we can exclude the majority of the backgrounds and thus improve the search

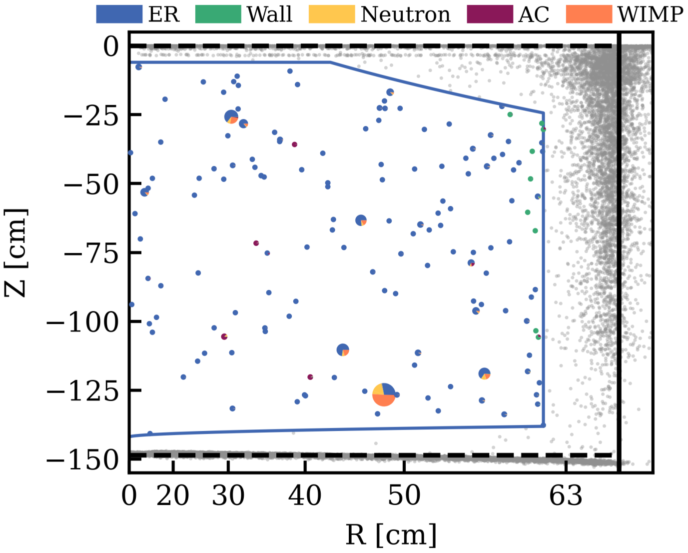

Figure 2.6: The FV (blue line) defined in the WIMP search [66], defined in the rz space. The two dashed horizontal lines mark the z positions of the cathode and anode. The boundary of the FV was carefully optimized to exclude the abundant radio-impurity backgrounds at the outskirt of the detector (the faint black dots clustered at the edge and top corner of the detector and at the bottom of the detector near the cathode). Based on the population within the FV, we performed the statistical inference based on the likelihood test and estimated the probability of observing a signal induced by WIMP-nucleon interaction. There was no significant excess observed during SR0 of XENONnT.

results for rare interactions. Such volume is called the fiducial volume (FV). As an illustration, the FV we used to search for WIMP Dark Matter Nuclear Recoil signals, overlaid with the final observed events, is shown in Fig. 2.6.

While most of the information can be found in Ref. [72], here I briefly introduce the process from energy deposition to S1 and S2 signals for both electronic and nuclear recoils.

2.2.1 Electronic Recoil

After an initial deposition of energy E, a total of N_q excimers and electron-ion pairs, collectively called quanta (and thus the subscript q), are generated. The distribution of N_q is described by Gaussian distribution, with a fano factor in its variance. Since N_q has to be an integer, it was floored from the Gaussian distribution (denoted as Norm).

$$N_q = \text{floor}\left(\text{Norm}\left(\frac{E}{W}, \sqrt{f\frac{E}{W}}\right)\right). \tag{2.3}$$

W is an empirical value that describes the average energy needed to produce a quanta. As measured with 1 MeV conversion electrons from ^{207}Bi [73], the expectation value of W is normally around 13.8eV/quanta. More recent measurements indicated a lower W at 11.2eV/quanta [74], with a possible explanation that the silicon photomultipliers (SiPMs) they used respond to the infrared light of xenon scintillation [75]. In XENONnT, the best-fitted value for W was 13.7 ± 0.2 eV/quanta [72].

The distribution of the sub-components (the excimers and the electron-ion pairs) is described by a binomial distribution (denoted as Binom) and expressed in terms of the number of electron-ion pairs as

$$N_i = \text{Binom}\left(N_q, \frac{1}{1+\left\langle\frac{N_{ex}}{N_i}\right\rangle}\right) \tag{2.4}$$

$$N_{ex} = N_q - N_i.$$

N_{ex} and N_i are the number of excimers and electron-ion pairs, respectively. The excimer-electron ratio term $\left\langle\frac{N_{ex}}{N_i}\right\rangle$ is treated as a variable and was measured to have a lower bound of 0.06 and an upper bound of 0.2 [73, 72]. With no further information, the distribution of this ratio term was assumed to be flat.

While N_{ex} directly contributes to S1, the electron-ion pairs undergo a recombination process. In XENONnT, we used a modified Thomas-Imel (TI) model [69, 72]. The expected recombination rate, given the energy deposition E, $\mathcal{E}_d$, W value and the excimer-charge ratio is expressed as

$$\langle r\rangle = \frac{1}{\exp\left(-\frac{E-q_0}{q_1}\right)+1}\left(1-\frac{\log\left(1+\langle N_i\rangle\varsigma\right)}{\langle N_i\rangle\varsigma}\right), \tag{2.5}$$

$$\varsigma = \frac{1}{4}\gamma_{er} e^{-\frac{E}{\omega}} \mathcal{E}_d^{\delta_{er}}, \tag{2.6}$$

$$\langle N_i \rangle = \frac{E}{W} \frac{1}{1 + \left\langle \frac{N_{ex}}{N_i} \right\rangle}, \tag{2.7}$$

with fluctuations in the recombination rate, interpreted as Gaussian standard deviation, as

$$\Delta r = q_2 \left(1 - e^{-\frac{E}{q_3}} \right), \tag{2.8}$$

where q_0, q_1, q_2, q_3, γ_{er}, ω_{er} and δ_{er} are free parameters to be fitted and E is the deposited energy. It is worth mentioning that the TI model was derived with the assumption that electron-ion pairs are uniformly distributed within a box. The ions were assumed to be fixed in position, i.e., they don't move and diffuse, while the charges only move under $\mathcal{E}_d$, and no diffusion was considered. This model works best if the spatial span of the recoil process, called track, is short. For long track recoils (typically a result of high energy depositions), the Doke/Birk's (DB) law [67] better describes the process as it was based on calculations of the rate of a train of electrons captured by fixed ions. As shown in Fig. 2.7 (Fig. 5 in Ref. [76]), the TI model fits experimental data well below $\sim$10 keV, while the DB law performs better above. Due to the difficulty of finding the exact switching point of these two models, an exponential term was added in Eqn. 2.6 to solve this discrepancy and suppress the prediction of the TI model at high energy depositions.

With a sampled recombination rate r from Norm($\langle r \rangle, \Delta r$), the final charge yield (CY) that contributes to S2 is then

$$N_e = \text{Binom}(N_i, 1 - r) \tag{2.9}$$

and the light yield (LY) that will contribute to S1 is

$$N_\gamma = N_{ex} + N_i - N_e = N_q - N_e. \tag{2.10}$$

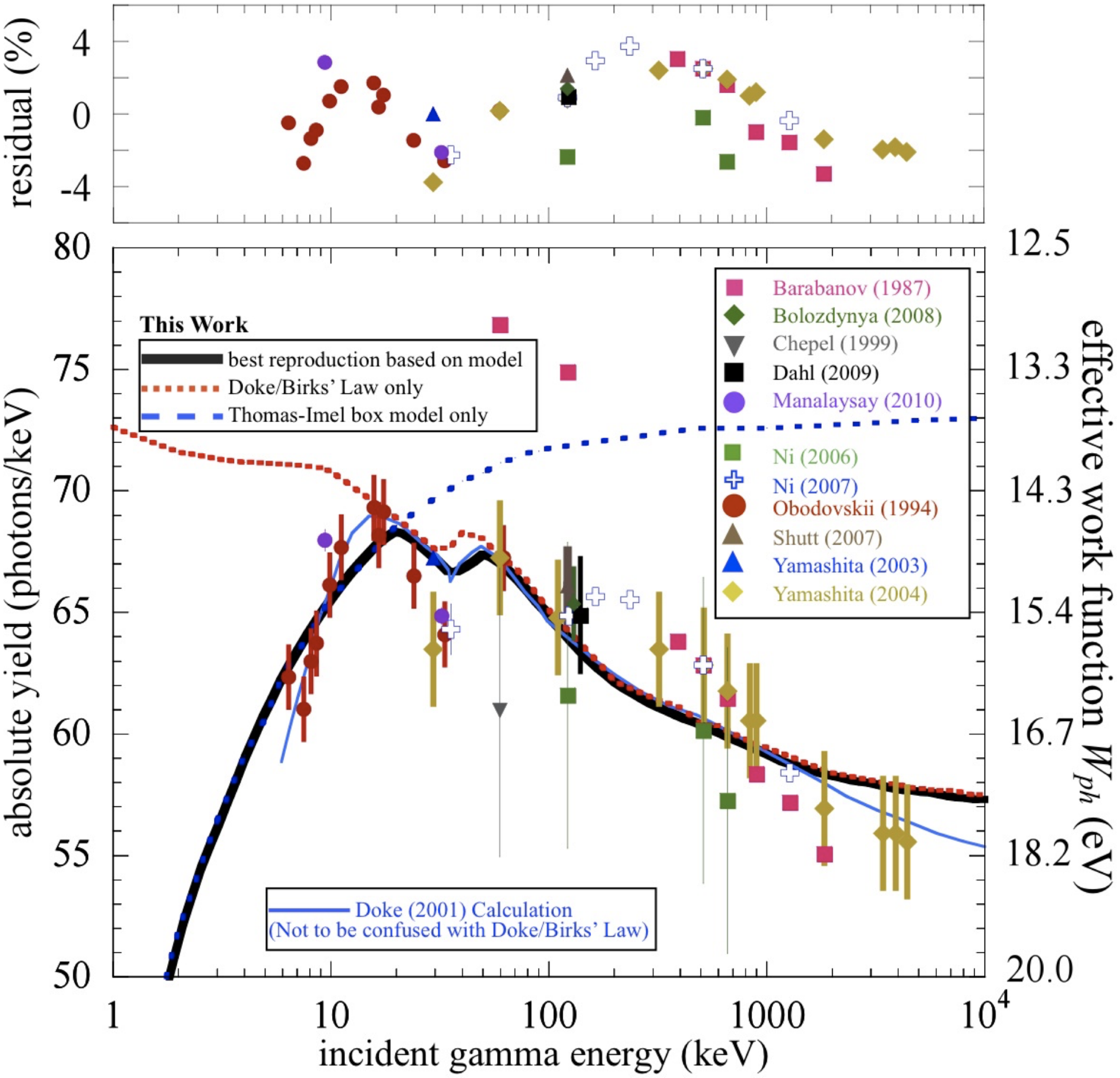

Figure 2.7: Birk/Doke model and TI model combined in NEST model, overlayed with experimental measurements. The blue dotted line is the TI model only, and the red dotted line is the Birk/Doke model only. The TI model is effective at low energy, while the Birk/Doke model works at higher energy. This is Figure. 5 in Ref. [76].

2.2.2 Nuclear Recoil

While NR is, for the most part, similar to the ER process, the major differences are that 1. there are two quenching steps, 2. the expectation of excimer-charge ratio has a different form, and 3. the recombination is described differently.

The two quenching steps will effectively reduce the CY and LY, compared to ER. First, when energy deposition happens, part of E will be converted into kinetic energy of Xe atom and thus lost. This is described by Lindhard Quenching factor (L) [77, 78]:

$$L = \frac{\kappa g(\epsilon)}{1 + \kappa g(\epsilon)}, \tag{2.11}$$

where κ is a proportionality constant between the electron stopping power and the velocity of the recoiling nucleus, and $g(\epsilon)$ is proportional to the ratio of electronic stopping power to nuclear-stopping power, defined as

$$\epsilon = \frac{11.5E}{keV} Z^{-\frac{7}{3}} \tag{2.12}$$

$$g(\epsilon) = 3\epsilon^{0.15} + 0.7\epsilon^{0.6} + \epsilon, \tag{2.13}$$

where $Z = 54$ is the atomic number of the Xe atom. Second, if excimer density is high, the inverse of step 2 in Eqn. 2.2 could happen through bi-excitonic interaction

$$Xe^* + Xe^* \rightarrow Xe_2^{**} \rightarrow Xe^+ + Xe + e^-. \tag{2.14}$$

This path will effectively turn Eqn. 2.1 to Eqn. 2.2. While effectively reducing the number of participating excimers by half and introducing more heat loss in step 3 of Eqn. 2.2, it will also provide extra charge yields if the electron-ion pairs do not recombine. Such quenching is called Penning Effect [79], and can be expressed as

$$f_l = \frac{1}{1 + \eta \epsilon^{\lambda}}, \tag{2.15}$$

where η and λ are free parameters to be fitted. A remark is that this excimer reduction quenching is assumed to only happen to N_{ex}, as the density of excimers introduced by the recombination of electron-ion pairs is not large enough.

The excimer-charge ratio for NR, instead of a uniform distribution, is parametrized as

$$\left\langle \frac{N_{ex}}{N_i} \right\rangle = \alpha \mathcal{E}_d^{-\zeta} \left(1 - e^{-\beta\epsilon}\right), \tag{2.16}$$

where α, β and ζ are free parameters to be fitted. Besides this different excimer-charge ratio, the definition of ς is also different in the recombination rate of NR from Eqn. 2.6, while the expression for $\langle r \rangle$ is the same as in Eqn. 2.5.

$$\varsigma = \gamma \mathcal{E}_d^{-\delta}. \tag{2.17}$$

The fluctuation of the recombination rate of NR is usually smaller and thus is ignored. The best-fitted ER and NR parameters are summarized in Tab. 2.1.

2.2.3 S1 and S2 Signals

From LY, the photons reflect around in the TPC and eventually are received by PMTs at the top and the bottom. Such reflections grant a position-dependent LCE that quantifies the attenuation from LY to S1 yield. Each photon the PMT receives will trigger a photoionization on the PMT cathode and produce photoelectrons (PE). With ∼20% chance, one photon can produce two PE in a PMT. Such a phenomenon is called Double Photoelectron (DPE) production. Each PE is then amplified in the PMT by a series of diodes, set at ascending

Parameters	Prior	Marginal Posterior	Unit
W	13.7 ± 0.2	$13.7^{+0.2}_{-0.2}$	eV
f	0.059	0.059	-
		ER parameters	
$\langle N_{ex}/N_i \rangle$	0.06-0.20	$0.13^{+0.04}_{-0.04}$	-
γ	free	$0.13^{+0.03}_{-0.02}$	-
δ	free	$0.34^{+0.07}_{-0.07}$	-
ω	free	57^{+15}_{-12}	keV
q_0	free	$1.32^{+0.17}_{-0.20}$	keV
q_1	free	$0.47^{+0.07}_{-0.05}$	keV
q_2	free	$0.030^{+0.002}_{-0.002}$	-
q_3	free	$0.47^{+0.40}_{-0.31}$	keV
		NR parameters	
ζ	0.047	0.047	-
δ	0.062	0.062	-
α	free	$0.92^{+0.07}_{-0.06}$	-
γ	free	$0.016^{+0.001}_{-0.001}$	-
β	239^{+56}_{-18}	334^{+40}_{-43}	-
κ	$0.139^{+0.006}_{-0.005}$	$0.138^{+0.005}_{-0.006}$	-
η	$3.3^{+10.6}_{-1.4}$	$10.0^{+6.8}_{-5.9}$	-
λ	$1.14^{+0.90}_{-0.18}$	$1.40^{+0.61}_{-0.38}$	-

Table 2.1: Prior and best fitted posterior values for NR and ER parameters [72].

voltages, and eventually collected on the PMT anode [80], causing a voltage drop. The collection of all voltage drops from the photons from this LY forms an S1 signal.

From CY, the free electrons first drift up in LXe. During this process, part of the electrons is lost to electronegative impurities in LXe and on the drifting path, which is described as an electron lifetime attenuation, expressed as an exponential function of the drift time t_d with an electron lifetime τ_e:

$$N_e^d = N_e \, e^{-\frac{t_d}{\tau_e}}, \tag{2.18}$$

where $N_{e,0}$ is the initial number of electrons (CY) inside the liquid. N_e^d is the number of electrons reaching the liquid surface after drifting for t_d time. In the SR0 of XENONnT, τ_e was consistently larger than 10 ms. After reaching the liquid surface, the electrons are extracted to GXe by the extraction field $\mathcal{E}_{ext}$ with an associated efficiency, namely the extraction efficiency (EE). The extraction efficiency depends largely on the magnitude of the extraction field strength [81], and in SR0, it was estimated to be around 0.54 [70] (explained later in Eqn. 2.22). The electron lifetime and the extraction attenuations are captured by a two-step binomial process:

$$N_e^d = \text{Binom}(N_e, e^{-\frac{t_d}{\tau_e}}) \tag{2.19}$$

$$N_e^{ext} = \text{Binom}(N_e^d, \text{EE}), \tag{2.20}$$

where N_e^{ext} is the number of electrons successfully extracted to GXe, respectively. Each extracted electron will then undergo the secondary scintillation process, during which it is accelerated by the extraction field $\mathcal{E}_{ext}$ in GXe and produces scintillation photons. The photons are then received by the PMTs with a position-dependent LCE, and the propagation of the signal thereafter follows the same path as discussed for the S1 signal.

To properly quantify the size of S1 and S2 signals, dedicated calibration is designed and carried out to measure the magnitude of the voltage drop corresponding to a single PE. While the details of this calibration are not of interest in this study, it is important to clarify that such magnitude is defined as the area of the voltage drop from the baseline, calculated by integrating the voltage drop along the time axis. To convert the unit of such integral ($[V \cdot s]$) into the unit of charge[4], the internal resistance of the PMT circuit is divided[5]. However, from the standpoint of a calibration practice, since the resistance is a constant, its exact value functions as a constant scaling of the voltage drop area. Therefore, the mean area of the voltage drop from a single photoelectron is defined to be 1 PE[6], where PE represents a unit of charge. Retrospectively, the amplitude of the original waveform is inverted by baseline subtraction and converted to the unit $[PE/ns]$. An example of waveforms of an S1-S2 pair is shown in Fig. 2.8. For this reason, the size of S1 and S2 signals is also referred to as **S1 and S2 area**. More details of this calibration can be found in Ref. [83, 84].

Unlike the S1 signals for which we can directly calculate the number of photons generated in liquid, the fundamental unit of S2s is the number of electrons extracted into GXe. The S2 area of a single electron, or equivalently the average amount of photoelectrons produced by a single electron during the secondary scintillation process, named single electron gain (SEG), bridges the number of electrons to the photoelectrons detected by the PMTs and is calibrated by selecting the S2s of one electron population from the data. The nominal values of SEG can be found in Tab. 2.2, and more discussions on the model of SEG can be found in Sec. 3.1.3.

There is a formulation that directly establishes a relation between S1/S2 areas and the initial energy deposition, bypassing the microphysical pictures of ER and NR processes, with two new variables g_1 $[PE/\gamma]$ and g_2 $[PE/e^-]$, representing the average PE response per photon and per electron generated in liquid, respectively. A canonical formula that

---

[4] Photoelectron, or PE, is a unit of charge, and to draw an equivalence between the two quantities, such conversion is necessary.

[5] $[V/\Omega \cdot s = A \cdot s = C]$

[6] In reality, voltage drops are recorded by digitizers, an analog-to-digital conversion device, in the unit of ADC counts. The model of digitizers used in XENONnT is V1724 by CAEN [82], featuring a 14-bit resolution over 2.25 peak-to-peak voltage range. Therefore, the calibration actually maps from the unit $[\mathrm{ADC} \cdot ns]$ to the unit of $[PE]$

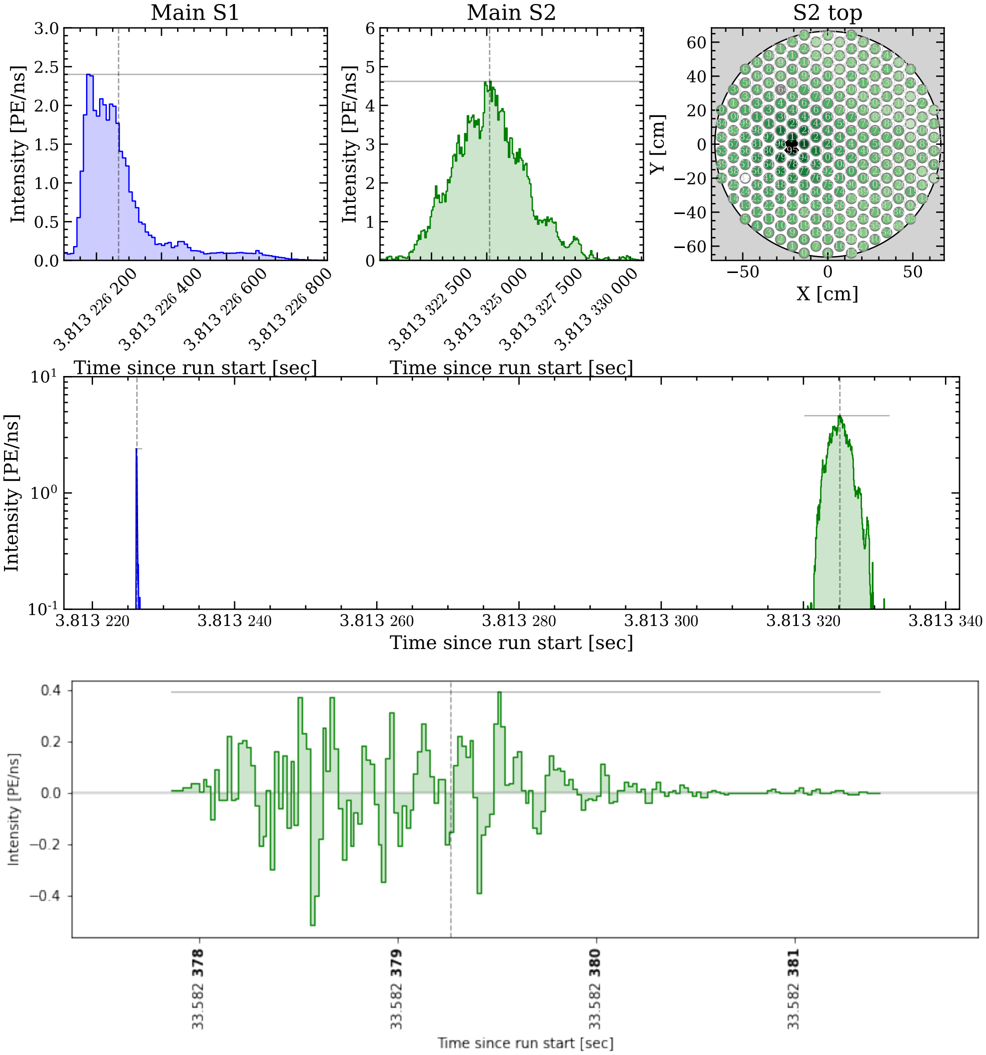

Figure 2.8: Example of waveforms of an S1-S2 pair recorded in XENONnT. The top right plot is the response of the top PMT array to the S2 signal, used for reconstructing the S2 xy positions, with a darker color indicating more light received. The gray vertical lines mark the center of gravity of the waveforms, and the gray horizontal lines mark the amplitude of the maximum of the waveforms. The time difference between the S1 and the S2 is shown in the bottom plot. At the bottom, an "unidentified" waveform that was classified as neither S2 nor S2 is shown. This waveform was generated mostly from electronic noises.

relates directly E, W, $S1$ and $S2$ is usually used:

$$E = W\left(\frac{\mathrm{cS1}}{g_1} + \frac{\mathrm{cS2}}{g2}\right), \tag{2.21}$$

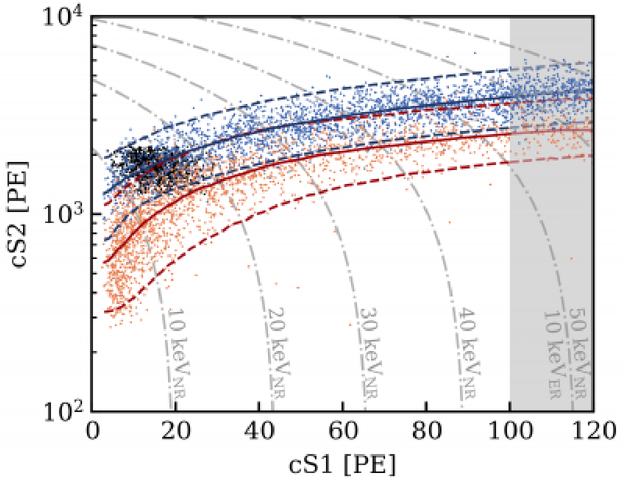

Figure 2.9: XENONnT SR0 ER/NR calibration results. The NR and ER bands are the orange and blue bands, respectively. ^{220}Rn was used for the ER band calibraiton and *AmBe* was used for NR. The solid lines are the center of the bands, and the dashed lines are the 1 σ ranges. The gray dashed lines mark the equivalent NR energy levels.

where c means corrected, which will become clear in the next section (Sec. 2.3). The values of g_1 and g_2 are obtained by fitting the Eqn. 2.21 to various mono-energetic radioactive sources and their corresponding S1-S2 signals, as explained in Ref. [70] and Ref. [85]. The values of g_1 and g_2 in SR0 of XENONnT were calculated to be 0.15 PE/γ and 16.45 PE/e^- [72], respectively. Because g_2 represents the average number of PE responses per electron generated in liquid, it differs from the value of SEG by the effect of extraction. Therefore, the extraction efficiency (EE) can be obtained by taking the division between the two

$$\text{EE} = \frac{g_2}{SEG}, \tag{2.22}$$

and we can obtain the value of EE to be 0.54.

At the end, the XENONnT SR0 ER/NR calibration is shown in Fig. 2.9. ^{220}Rn was used for the ER band calibraiton and *AmBe* was used for NR. The solid lines are the center of the bands, and the dashed lines are the 1 σ ranges. The gray dashed lines mark the equivalent NR energy levels.

2.3 Signal Corrections

In a typical TPC detector, energy depositions at different (x, y, z) locations result in different S1-S2 pairs, even if the same amount of energy is deposited into the medium. This is because of non-uniformity in detector response to the energy deposition caused by variations in the drifting electric field ($\mathcal{E}_d$), the extraction electric field ($\mathcal{E}_{ext}$), and the position-dependent light collection efficiency (LCE), etc. To accurately identify the nature of the interaction induced by the primary particle (NR vs. ER), the energy deposition and the relation between the sizes of S1 and S2 signals need to be precisely reconstructed. For this purpose, the non-uniformity induced by the detector responses needs to be flattened since it is not related to the nature of the interaction but an artifact of the unideal detector condition.

Such non-uniformity can be calibrated with mono-energetic sources. In XENONnT, we used $^{83\mathrm{m}}$Kr as our calibration source. $^{83\mathrm{m}}$Kr has a characteristic two-step decay that emits two photons with a half-life of $\sim$157 ns. The two steps each carry energies of $\sim$9.4 keV and 32.2 keV, respectively. Benefitted from the sharpness of S1s ($\sim$150 ns wide for the central 50% area range), such shortly gapped decays produce quite often two distinctive S1s, enabling precise event selections for signals from $^{83\mathrm{m}}$Kr just from such S1 time correlation besides other signal quality cuts. For convenient reference, these two S1s are called $\mathrm{S1_a}$ (32.2 keV) and $\mathrm{S1_b}$ (9.4 keV). However, due to the long duration of S2s (detailed discussion in Ch. 3), the two S2s from such two-step decays are normally merged, resulting in one S2 with a characteristic energy of 41.6 keV. Such topology is schematically shown in Fig. 2.10.

With a pure population of $^{83\mathrm{m}}$Kr and the premise that the same energy deposition should yield the same S1-S2 responses, corrections for S1 and S2 signals were studied and applied. This is well-documented in Ref. [70]. In this section, I will focus on the details of S2 corrections.

Given an energy deposition, the S2 signal yield is influenced by the following factors:

1. The strength of the drifting field $\mathcal{E}_d$ at the location of the energy deposition influ-

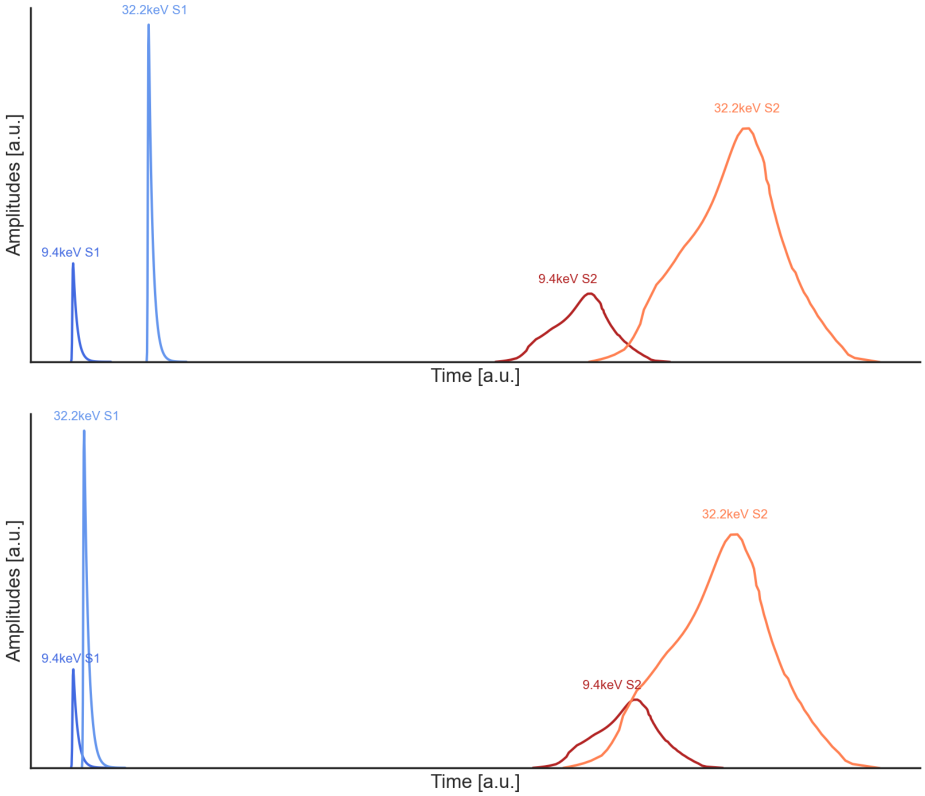

Figure 2.10: Illustration of $^{83\text{m}}$Kr S1s and S2s. While the two S1s are sometimes separated and can be distinguished due to the sharpness of the S1 shape, S2s from the two-step decay are normally overlapped and thus merged into an S1 equivalent to 41.6 keV deposition. Quite often, even the S1s are merged, giving an S1-S2 pair of 41.6 keV. Top: $^{83\text{m}}$Kr events with separable S1s; bottom: events with merged S1s. The axes are not to scale.

ences the charge yield. Unavoidably, non-uniform $\mathcal{E}_d$ in the drift region would cause a variation in the charge yield and, thus, the eventual S2 area;

2. The drift time t_d of the electron cloud determines the amount of electro-negative impurities the electrons can encounter, to which the electrons are attached and lost. The longer the drift time, the deeper the energy deposition is in the TPC, and a larger drifting path is covered. Consequently, a larger electron lifetime attenuation is expected;

3. The strength of the extraction field $\mathcal{E}_{ext}$ at the location where the electrons reach the liquid-gas interface influences the extraction efficiency and, therefore, the S2 area;

4. The light collection efficiency along the path of the secondary scintillation process of a certain electron determines the fraction of photons that can be received by PMTs.
5. The locality of photon emission during the secondary scintillation process, combined with the differences in the responses of individual PMT, can also induce non-uniformity in the S2 area.

To handle these factors, a 3-dimensional spatial correction is needed for S2 signals. The fluctuation in the strength of $\mathcal{E}_{ext}$ is a function of (x, y). The light collection efficiency and the locality of photon emission are both associated with the thin GXe region at the top of the detector[7] and can also be regarded as only dependent on (x, y). The drift time of the electron cloud is only z-dependent. The only factor that depends on (x, y, z) is the non-uniform charge yield due to the fluctuation in $\mathcal{E}_d$. However, in the SR0 of XENONnT, the effect on the charge yield due to the fluctuation in $\mathcal{E}_d$ across the whole drifting region was less than 8%, much smaller than the effect of the rest four factors. Thus, the influence of the fluctuation in $\mathcal{E}_d$ was ignored, and the 3-dimensional corrections are decoupled into (x, y) and z corrections. The development of these spatial corrections is discussed in Sec. 2.3.2.

Besides the spatial corrections, due to frequent high-intensity single electron bursts during the summer of 2021, the gate and anode electrodes were ramped down to protect the PMT arrays from intensive lights and back up after a few hours. This practice disturbed the equilibrium between gravity, electrostatic force, and wire tensions in the electrodes, resulting in dynamic responses up to three days after each ramp-up in the detector. The effects of such dynamics were observed as evolutions in the single electron gain (SEG) values and the number of extracted electrons in a $^{83\mathrm{m}}$Kr merged S2s. Therefore, dedicated corrections were developed to handle this time-dependent evolution and discussed in Sec. 2.3.1.

---

[7] around 5 mm for XENONnT

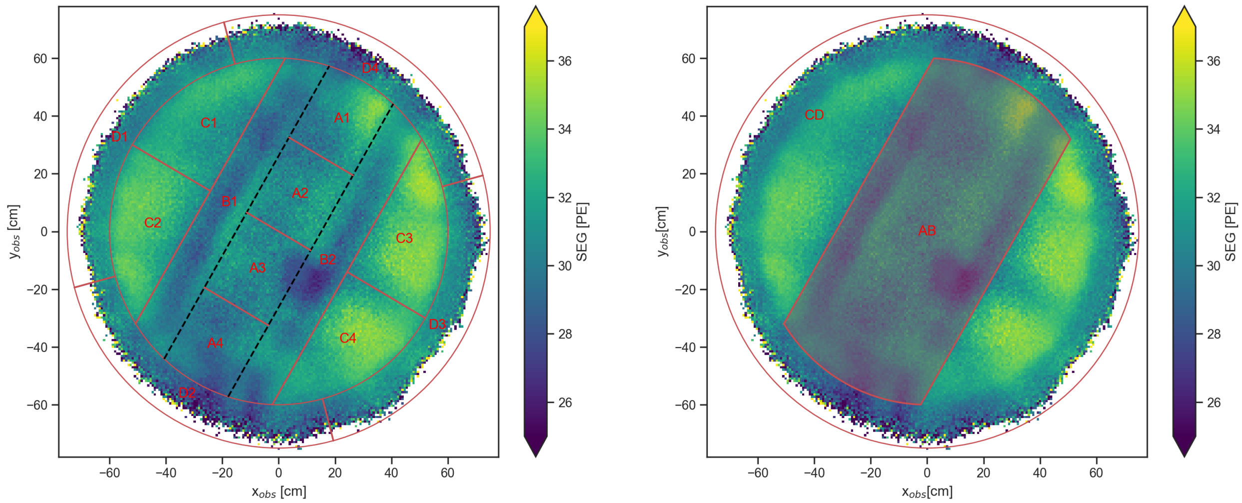

Figure 2.11: SEG xy distribution. The color map is SEG values at different locations. The black dashed lines mark the position of gate transverse wires. Left: fine binning strategy; right: coarse binning, as A and B partitions have similar trends, while C and D partitions show no sign of evolution; thus, they were merged.

2.3.1 Time Dependent Corrections for S2

SEG, by definition, is the S2 value of the single electron population, which can be obtained run-by-run for monitoring purposes. The exact SEG model will be discussed in Sec. 3.1.3. Due to the observed SEG expectation value difference in different regions of the TPC, I divided the TPC xy plane into ten partitions, as shown in Fig. 2.11 (left). SEG was calculated for each run (roughly 30 minutes long) within each partition, and the time evolutions throughout SR0 are shown in Fig. 2.16. It is pretty clear that the A and B partitions, which are at the center of the detector where the parallel wires are the longest, showed a clear correlation of SEG relaxation after each anode ramp-up (marked as vertical red dashed lines). In contrast, the C and D partitions didn't show such a trend. Due to the xy spatial correction on S2 that will be discussed in the next section, we didn't want to interfere too much with the spatial variation of SEG. Therefore, the A and B partitions, called AB partitions, were merged; the same was true for CD. Such merging is shown in Fig. 2.11 (right). Since no evolution was observed in the CD partition, only the AB partition was corrected for SEG.

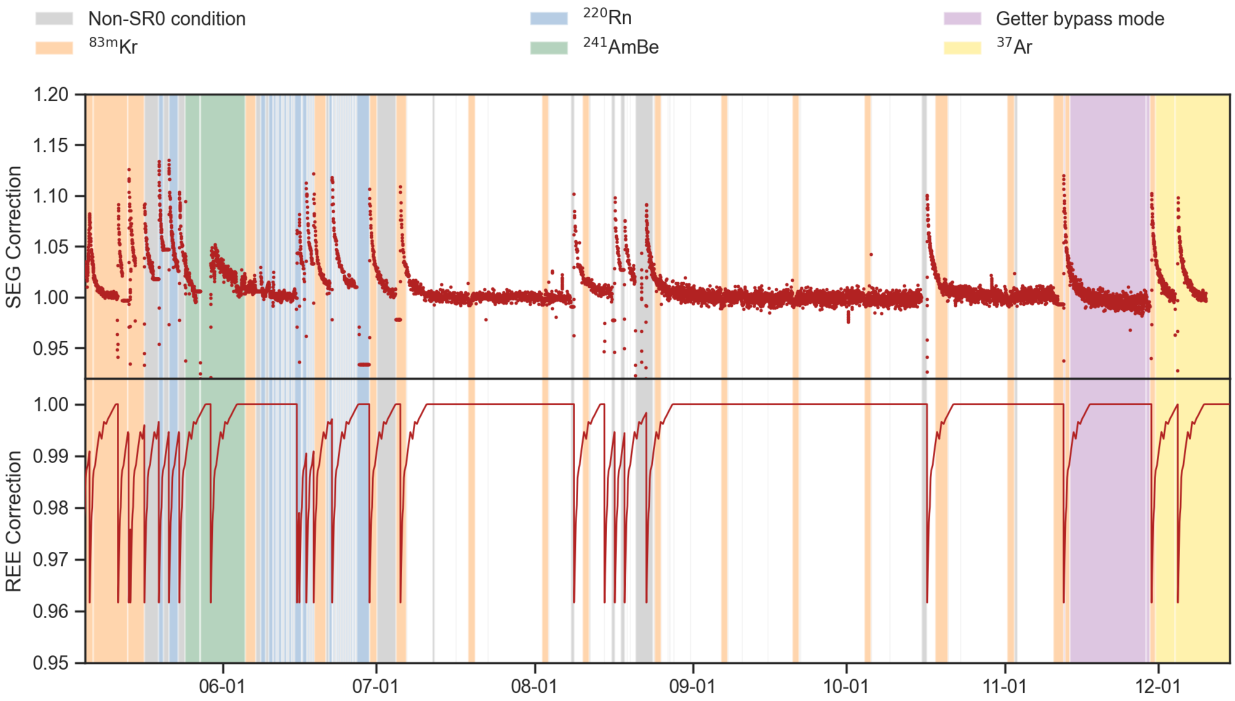

Figure 2.12: SEG and REE correction for AB partition.

Such correction is shown in Fig. 2.12 (top).

A period between 2021-07-05 and 2021-08-08 indicated in black arrows in Fig. 2.16, was chosen as the reference period for nominal SEG evaluation as it was the longest stable background data-taking period. The nominal SEG values were calculated by the number of SE observed and the SEG value from each run within this period:

$$\langle \text{SEG} \rangle = \frac{\sum\limits_j N_j \text{SEG}_j}{\sum\limits_j N_j}. \tag{2.23}$$

N_j is the number of entries, and j runs through each run in the reference period. Also, an estimation of the uncertainty of the nominal SEG can be calculated with

$$\sigma_{\langle \text{SEG} \rangle} = \sqrt{\frac{\sum N_j (\text{SEG}_j - \langle \text{SEG} \rangle)^2}{\frac{M-1}{M}\left(\sum N_j\right)}}, \tag{2.24}$$

where M is the number of runs in this reference period. For a proper description of the SE population, the standard deviation (std) of SEG also needs to be quantified from such a period. Due to a lack of established formula, a simple derivation is shown below.

$$\begin{aligned}
\langle\sigma\rangle_x &\equiv \sqrt{\frac{\sum\limits_j\sum\limits_i \left(x_{i,j}-\langle x\rangle\right)^2)}{\sum\limits_j N_j}} \\
&= \sqrt{\frac{\sum\limits_j\sum\limits_i \left(x_{i,j}-\langle x\rangle_j+\langle x\rangle_j-\langle x\rangle\right)^2}{\sum\limits_j N_j}} \\
&= \sqrt{\frac{\sum\limits_j\sum\limits_i \Big(\left(x_{i,j}-\langle x\rangle_j\right)^2+2\left(x_{i,j}-\langle x\rangle_j\right)\left(\langle x\rangle_j-\langle x\rangle\right)+\left(\langle x\rangle_j-\langle x\rangle\right)^2\Big)}{\sum\limits_j N_j}} \\
&= \sqrt{\frac{\sum\limits_j \sigma_j^2(N_j-1)+\sum\limits_j N_j(\langle x\rangle_j-\langle x\rangle)^2+2\sum\limits_j\sum\limits_i(x_{i,j}-\langle x\rangle_j)(\langle x\rangle_j-\langle x\rangle)}{\sum\limits_j N_j}} \\
&= \sqrt{\frac{\sum\limits_j \sigma_j^2(N_j-1)}{\sum\limits_j N_j}+\sigma_{\langle x\rangle}^2\frac{M+1}{M}+2\frac{\sum\limits_j\sum\limits_i(x_{i,j}-\langle x\rangle_j)(\langle x\rangle_j-\langle x\rangle)}{\sum\limits_j N_j}}. \qquad (2.25)
\end{aligned}$$

Index j runs across different populations and i across different data inside each population. $x_{i,j}$ here is a generic variable and indicates the i-th datapoint inside j-th population. $\langle x\rangle_j$ and σ_j are the mean value and std of $\{x_{i,j}\}$ inside j-th population. $\langle x\rangle$ is the overall mean. It is clear that the last term of Eqn. 2.25 yields 0 as both $\sum\limits_i(x_{i,j}-\langle x\rangle_j)$ and $\sum\limits_j(\langle x\rangle_j-\langle x\rangle)$ give 0. Replacing x with the SEG, plugging in Eqn. 2.24 for the second term, and σ_j with the standard deviation of SEG within each run, we can get an expression of the nominal

	$\langle\mathrm{SEG}\rangle$	$\sigma_{\langle\mathrm{SEG}\rangle}$	$\langle\sigma\rangle_{\mathrm{SEG}}$	$\sigma_{\langle\sigma\rangle_{\mathrm{SEG}}}$
Whole TPC	31.15	0.97	6.616	0.005
AB	30.09	0.09	7.351	0.003
CD	32.04	0.09	5.787	0.002

Table 2.2: SEG nominal values and nominal stds, with their uncertainties for the whole TPC, AB partition, and CD partition.

standard deviation of SEG:

$$\langle\sigma\rangle_{\mathrm{SEG}} = \sqrt{\frac{\sum_j \sigma_j^2 (N_j - 1)}{\sum_j N_j} + \frac{M-1}{M}\sigma^2_{\langle\mathrm{SEG}\rangle}}. \tag{2.26}$$

To complete the picture, the uncertainty of the nominal std, namely $\sigma_{\langle\sigma\rangle_{\mathrm{SEG}}}$, can be obtained by error propagation. I will omit the expression for this quantity. The relevant values of SEG are summarized in Tab. 2.2.

Since there are no objective ways to obtain EE, a relative extraction efficiency (REE) was calculated after spatially corrected (next section) S2s of $^{83\mathrm{m}}$Kr events and the SEG for each run. By dividing SEG from spatially corrected S2s, the expected number of electrons can be obtained from this mono-energetic source. However, it is a little more complicated than SEG correction, as we do not always have a calibration source. Therefore, modeling the REE trend is necessary. An empirical power law was adapted to fit such trends as

$$\mathrm{EE}(t) = c - \left(\frac{t-a}{d}\right)^b, \tag{2.27}$$

where t is the time delay from each ramp-up of anode mesh, and a, b, c, d are four free parameters. A sample of the fitting is shown in Fig. 2.13. Although not fully understood, with the hypothesis that such a trend is physically driven and should be roughly the same

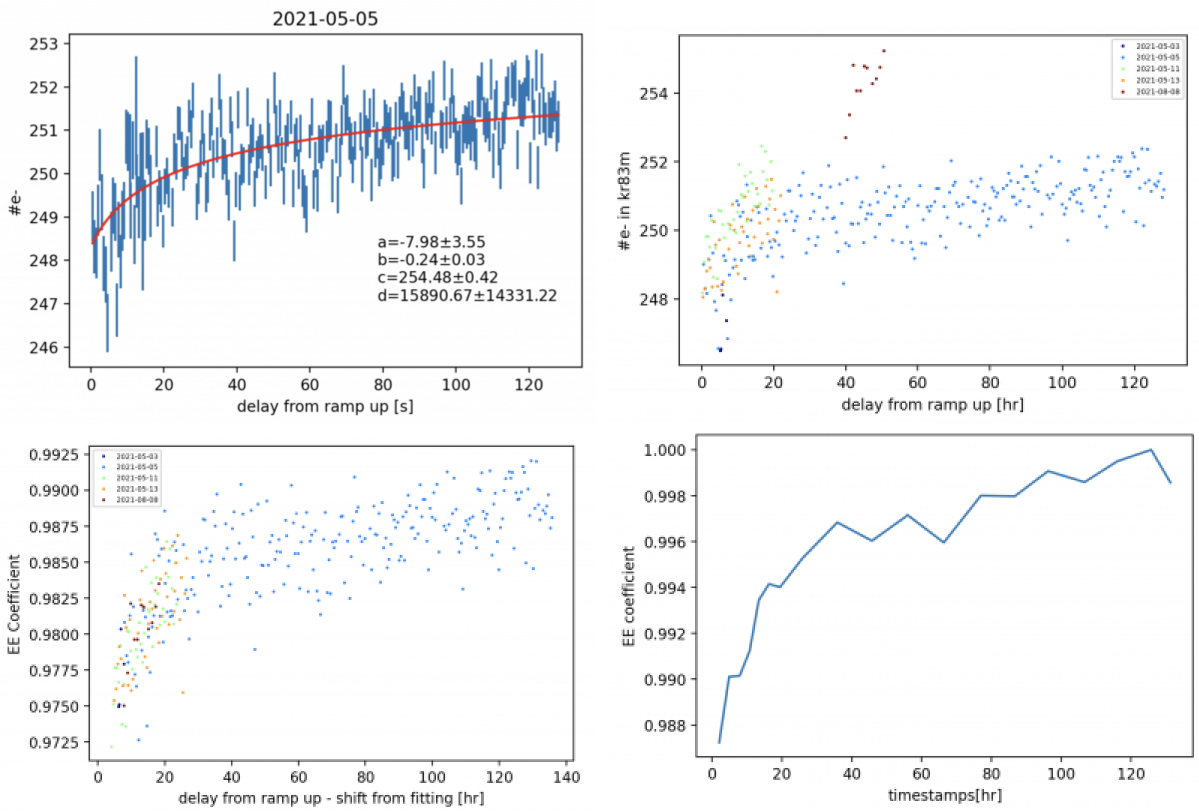

Figure 2.13: Example of fitting REE trend with a power law and stitching multiple ramp-up occasions into an empirical trend. Top left: sample fitting results of REE trends using $^{83\text{m}}$Kr runs; Top right: raw REE values as a function of delay time from the nearest ramp up of anode; bottom left: shifted REE values with respect to their fitted a's and c's; bottom right: smoothened REE trend, normalized with respect to the largest raw REE value after smoothening.

after each ramp-up, a and c parameters can be understood as relative time shifts and leveling. Throughout SR0, we had a total of 26 ramp-up occasions (red vertical lines in Fig. 2.16), and 5 of them had immediate $^{83\text{m}}$Kr calibrations, most of which were at the beginning of May 2021. A sample of REE evolution and a group of fitted parameters were obtained for these five ramp-ups. Then, the trends were shifted with respect to their fitted a's and c's to create a more consistent trend. This process is shown in steps in Fig. 2.13. Then, such a smoothened trend is extrapolated as a function after each ramp-up, with a delay time longer than three days set to 1, as shown in Fig. 2.12. Again, the correction factors in the CD partition were set to be one due to no evolution observed and thus were not plotted.

These two time-dependent corrections for S2s helped restore lots of background data from the durable effect of ramping electrodes, and restored data constitutes about 7.1% of total exposure.

2.3.2 Spatial Dependent Corrections for S2

The correction to the xy fluctuation is a conclusive data-driven coefficient map, called S2_cor_map(x_{obs}, y_{obs}). Because the fluctuations on xy are related to the location of electron extraction at the liquid surface, such correction is related to the observed locations (thus x_{obs}, y_{obs}). The z attenuation comes from the electron attachment to electro-negative impurities through drifting, as described in Eqn. 2.19 and can be expressed as a function of dt as

$$\mathrm{S2}(dt) = \mathrm{S2}_0 e^{-\frac{t_d}{\tau_e}}, \tag{2.28}$$

where τ_e is the electron lifetime. For the xy correction and z correction, the merged $^{83\mathrm{m}}$Kr S2s were used for map generation and electron lifetime fitting.

The fitting of electron lifetime is straightforward: within each slice of dt, calculate the mean value of S2s of $^{83\mathrm{m}}$Kr, then fit the obtained trend with Eqn. 2.28. An example is shown in Fig. 2.14. To monitor the purity inside the TPC, ^{37}Ar and 5.5 MeV α from emanated ^{222}Rn were also used as cross-checks. Especially since the α source is in the detector background and cannot be removed, it provides a vital monitoring capability outside calibration periods. One electron lifetime value was obtained for each 6 hours of data taking. The z correction, namely electron lifetime correction, is then using the observed S2s and dividing by such exponential.

Traditionally, S2_cor_map(x_{obs}, y_{obs}) was obtained simply by taking all S2s, applying the electron lifetime correction, binning them into xy blocks, calculating the mean values (or other statistical expectation values) within each xy bin, and normalize the resulted map with respect to the mean of the whole population. In this way, all observed S2s should

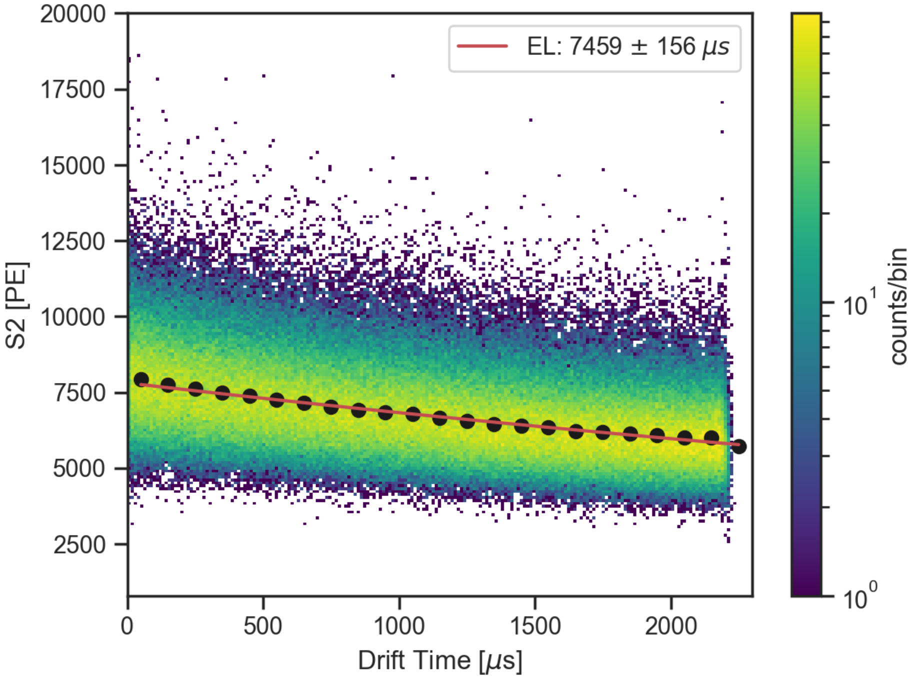

Figure 2.14: Example of electron lifetime fitting with $^{83\mathrm{m}}$Kr S2s.

divide such map based on their (x_{obs}, y_{obs}) locations to be corrected for secondary scintillation process-related fluctuations. However, the generation of such a map was a bit more complicated due to time-dependent evolutions discussed before, and a naive binning can no longer work because the absolute yield of S2s from a mono-energetic source has a time evolution component. This problem can be bypassed with a weighted map: within each run, the S2s from $^{83\mathrm{m}}$Kr events were binned and normalized to the mean value of the population in this run. This will result in numerous xy maps of relative S2 sizes evaluated at (x_{obs}, y_{obs}), $c_i(x_{obs}, y_{obs})$, where i represents each run. Then, these individual maps are combined as a weighted mean to give the final spatial correction map (S2_cor_map(x_{obs}, y_{obs})), with the number of events from each run $(N_i(x_{obs}, y_{obs}))$ as weight, as given in:

$$\text{S2\_cor\_map}(x_{obs}, y_{obs}) = \frac{\sum_i c_i(x_{obs}, y_{obs}) N_i(x_{obs}, y_{obs})}{\sum_i N_i(x_{obs}, y_{obs})}. \tag{2.29}$$

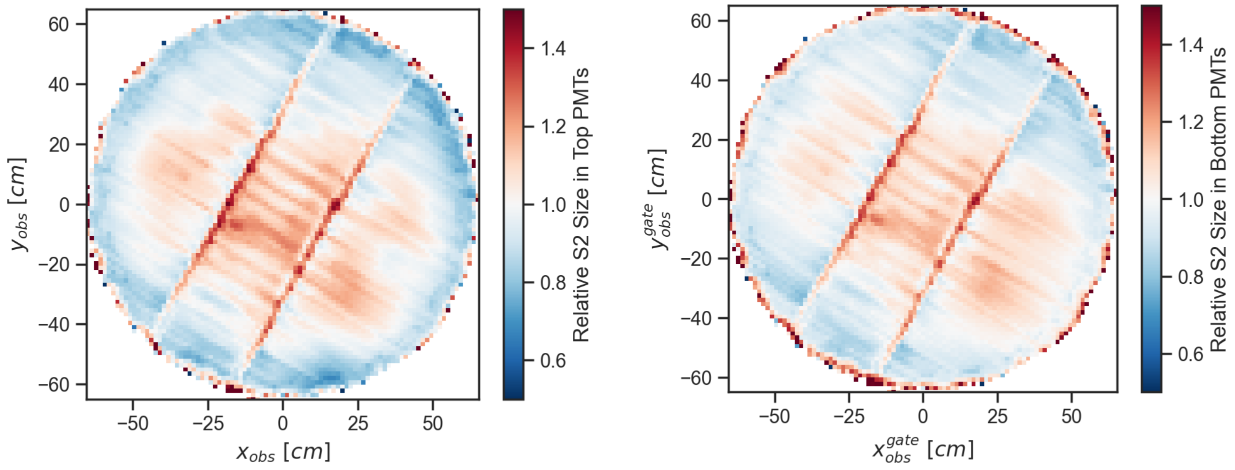

Figure 2.15: S2_cor_map(x_{obs}, y_{obs}) for the top (left) and bottom (right) PMT arrays.

There is one nuance about the entanglement between the electron lifetime correction and the S2_cor_map(x_{obs}, y_{obs}) correction: while doing the electron lifetime fitting, it was assumed that the xy correction has been applied, and vice versa for the xy map establishment. Although the two corrections are from different sources, one must happen before the other. An iteration process was adopted for decoupling the two, and the evolution of the xy map and electron lifetime were studied. As it was shown, no matter whether starting from a no-z-correction map or a no-xy-correction electron lifetime, after about eight iterations, both the map and electron lifetimes (reminder: electron lifetimes were obtained for every 6 hours) converge to precisely the same values. The currently used maps and electron lifetime values were the converged ones after iterations.

Two maps were generated for top and bottom PMT arrays, and their S2 contributions were corrected independently. The two maps applied to SR0 are shown in Fig. 2.15. Eventually, the corrected S2 (cS2) can be expressed as

$$\mathrm{cS2}(x_{obs}, y_{obs}, dt, t) = \frac{\mathrm{S2}(x_{obs}, y_{obs}, dt)e^{\frac{dt}{\tau(t)}}}{\mathrm{S2\_cor\_map}(x_{obs}, y_{obs})\mathrm{SEG}_c(t)\mathrm{REE}_c(t)}, \tag{2.30}$$

where the subscript c of SEG and REE means the normalized correction values.

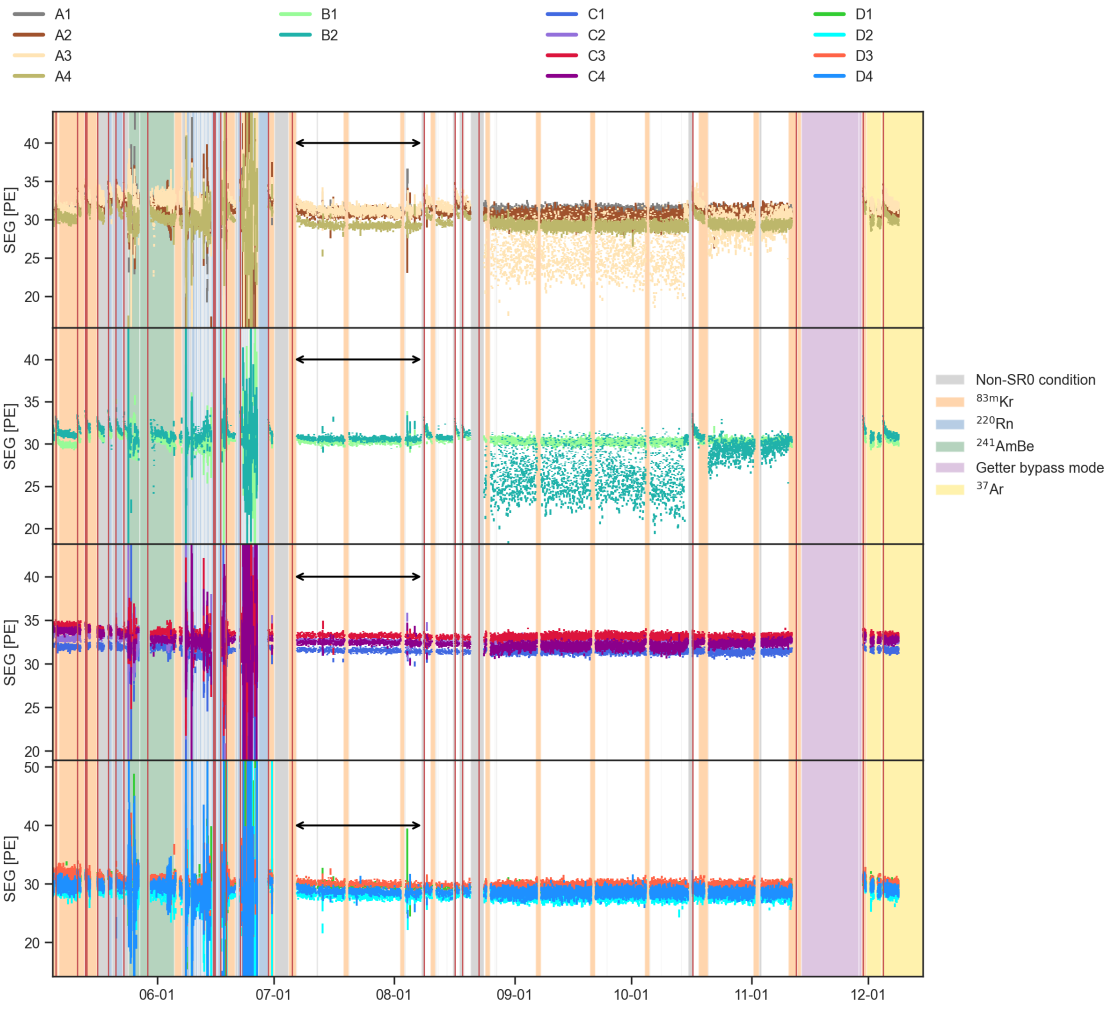

Figure 2.16: SEG evolution in each partition throughout SR0. The black arrows (same in all subplots) indicate the period where SEG correction reference values were set, as it was the longest stable background data-taking period.

The distribution of cS1-cS2 pairs of ^{83m}Kr population from SR0 calibration data is shown in Fig. 2.17.

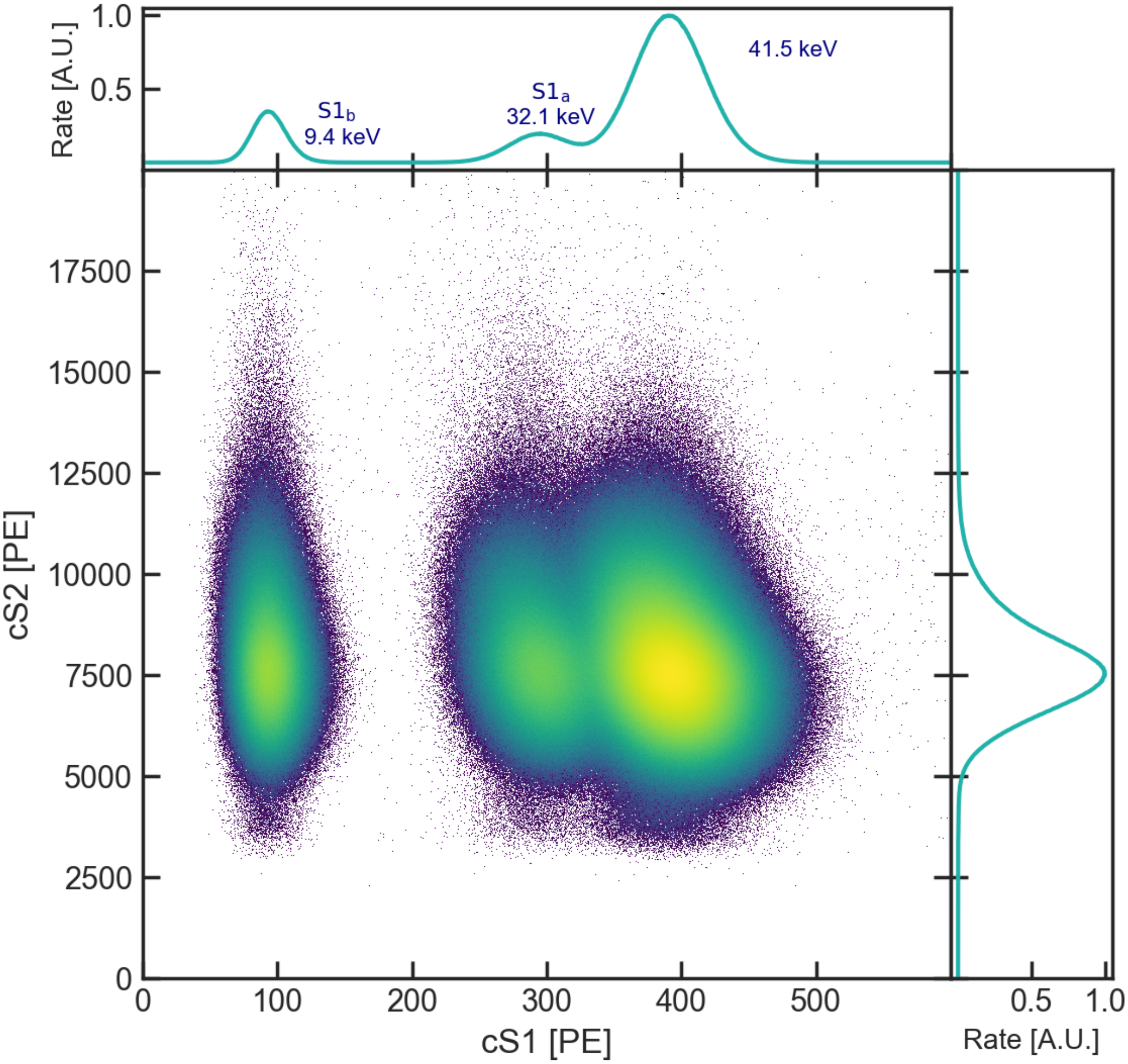

Figure 2.17: $^{83\text{m}}$Kr cS1$_\text{a}$ vs cS2$_\text{b}$ plots. Normally, we cannot see standalone S1$_\text{b}$ paired with the merged S2s. Therefore, this plot was produced with true S1$_\text{a}$-S2 pairs, true merged S1-S2 pairs, and the second largest S1s that accompany the identified S1$_\text{a}$'s as S1$_\text{b}$ population.

CHAPTER 3

MODELING THE S2 SIGNAL SHAPE

When electronic and nuclear recoils are induced within the active volume, excimers, and electron-ion pairs are produced along the ionization track [68] until their kinetic energy is fully transferred. As summarized in Sec. 2.2, the associated recombination and de-excitation lead to the prompt emission of UV photons, i.e., primary scintillation. On the other side, under the effect of the electric field $\mathcal{E}_d$, the ionization electrons surviving to recombination are drifted towards the liquid-gas interface and then extracted into gas by $\mathcal{E}_{ext}$ where they get accelerated (by $\mathcal{E}_{ext}$) to induce electroluminescence i.e. secondary scintillation (S2). The shape of the S2 signal is intimately related to all these processes. First, during drifting, the compact ionization electron cloud undergoes longitudinal and transverse diffusion [86]. **As shown in Fig. 3.1, longitudinal diffusion induces a spread of the cloud along the z (drift) direction, staggering the arrival times of the individual electrons at the liquid-gas interface.** The arrival time of individual electrons should be combined with the time profile of the light production mechanism, ultimately determining the emission of S2 photons during the electron acceleration in the gas pocket.

As described in Sec. 2.2, the dimensions of the tracks produced by low-energy ERs and NRs of interest are sub-millimeter and negligible with respect to the typical longitudinal diffusion observed in XENONnT. Therefore, from now on, the initial state of the electron cloud is assumed to be point-like.

In the rest of this chapter, I will discuss and model the S2 pulse shape, with particular emphasis on its time profile. In Sec. 3.1, I will establish a semi-analytical model for the S2 signal duration in two steps: first I will derive an analytical description of the shape of the electron cloud within S2 signals before entering the GXe (Sec. 3.1.1 and Sec. 3.1.2), followed by a Monte Carlo method incorporating the secondary scintillation process (Sec. 3.1.3). In Sec. 3.2, I will then build on the previous model and focus on the discrete nature of the

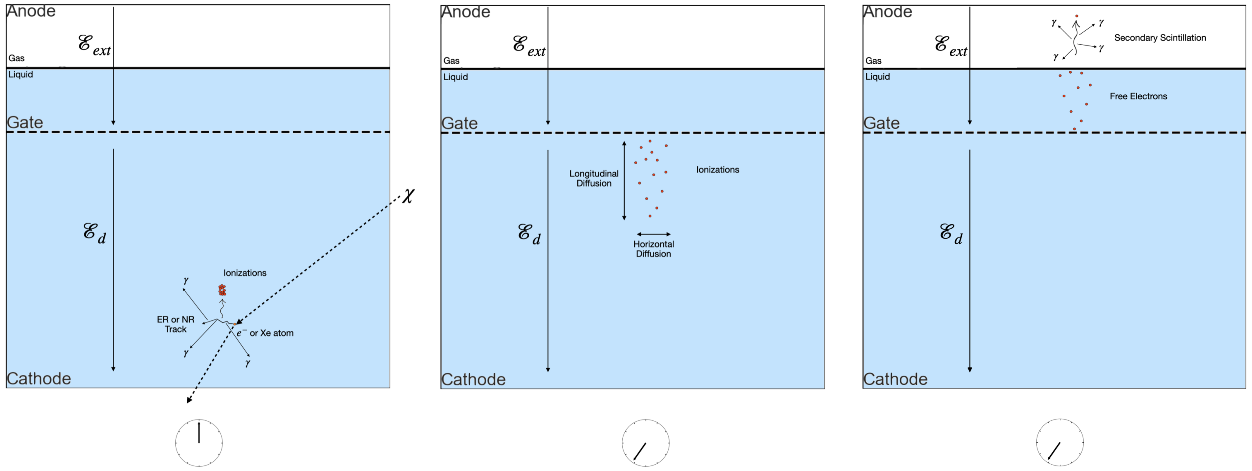

Figure 3.1: Illustration of electron production during scintillation (left), the diffusion of the electron cloud after drifting in LXe (center), and the secondary scintillation process of individual electrons (right). At low energy deposition, the dimensions of the track are negligible to the diffusion process, and therefore, the initial state of the electron cloud is assumed to be point-like. The plot is not to scale.

diffusion process, discussing how it can impact and bias the reconstruction of S2s. With the model of the diffusion process and understanding of the discreteness of the electron cloud, I will propose a new way to analyze the data to mitigate the bias. This will enable a more realistic description of the ultra-low energy regime where the small number of ionization electrons enhances the impact of discreteness.

3.1 Duration of the S2 Signal

According to the studies presented in Ref. [86], a point-like electron cloud that drifts in liquid xenon under the effect of an electric field $\mathcal{E}_d$ can be described by the following numerical spatial density:

$$n(\rho, z; T) = n_0 \frac{1}{4\pi D_H T} \exp\left(-\frac{\rho^2}{4 D_H T}\right) \times \frac{1}{\sqrt{4\pi D_L T}} \exp\left(-\frac{(z - \mu \mathcal{E} T)^2}{4 D_L T}\right), \tag{3.1}$$

where:

- n_0 is the initial (and total) number of drifting electrons. In our experiment, n_0 equals the initial charge yield attenuated by the electron lifetime and the extraction efficiency (Sec. 2.2.3);

- $\mathcal{E}$ is the external field under which the electron is drifted. In the SR0 of XENONnT, this corresponds to the drifting field $\mathcal{E}_d = 22.92\ V/cm$;

- D_H and D_L represent the coefficients of horizontal and longitudinal electron diffusion, respectively, quantified in units of cm^2/s. In XENONnT SR0, D_L was empirically determined to approximate 45 cm^2/s. Conversely, D_H has not been precisely quantified within the scope of XENONnT measurements. The exclusion of D_H from this analysis is reasoned in the following paragraphs;

- μ denotes the electron mobility coefficient, expressed in units of $cm^2/(V \cdot s)$. The product of μ and the electric field strength $\mathcal{E}$, denoted as $\mu\mathcal{E}$, characterizes the drift velocity (v_d): the mean velocity at which electrons propagate through the medium. This movement occurs under the influence of a constant electric field and as the electrons scatter off the medium's atoms. In the SR0 of XENONnT, v_d was evaluated to be 0.675 $mm/\mu s$ on average;

- T is the time the electron cloud drifts from the compact initial cluster. $T = 0$ corresponds to the timestamp when the point-like electron cloud is created. The quantity $\mu\mathcal{E}T$ marks the expected z location of the electron cloud (the location of the red vertical line in Fig. 3.2);

- (ρ, z) is the cylindrical coordinates. z is aligned with the direction of drift (longitudinal), and ρ is perpendicular to z in the xy plane (horizontal). Given $T > 0$, Eqn. 3.1 describes a 3-dimensional Gaussian distribution centered at $(0, \mu\mathcal{E}T)$, with standard deviations of $\sqrt{2D_H T}$ in ρ direction and $\sqrt{2D_L T}$ along z-axis. At $T = 0$, Eqn. 3.1 converges to a 3-dimensional Dirac Delta function $\delta(\rho, z)$, symbolizing the point-like

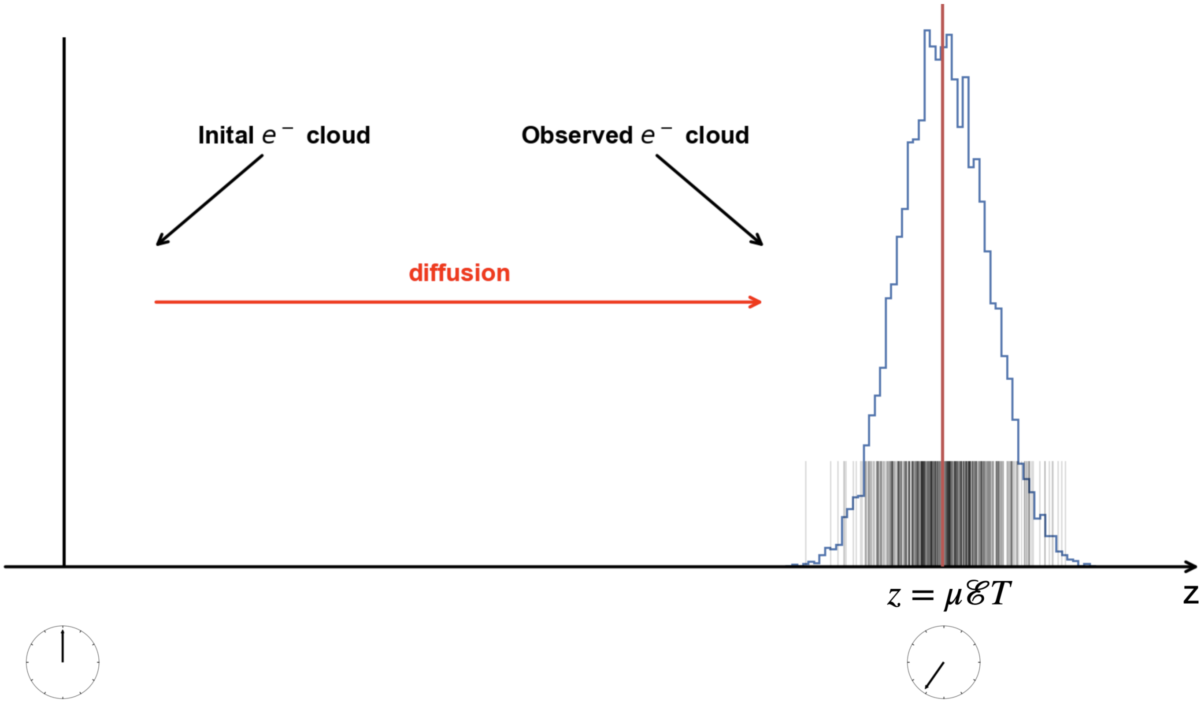

Figure 3.2: Illustration of a point-like electron cloud diffusing into a Gaussian cluster after drifting under an external field $\mathcal{E}$ in the longitudinal direction. The plot shows two snapshots of the z-distribution of the electrons, one at the energy deposition time and the other at a later time after drifting. The black lines are individual electrons, and the red vertical line indicates the expected location of the electrons $z = \mu\mathcal{E}_d T$. Starting from a point-like distribution, the electron cloud diffuses and is observed at a later time, with the counts' distribution in the blue histogram.

initial distribution of the electron cloud. Consequently, the coordinates (0,0) denote the inception point of the electron cloud, equivalently, the site of energy deposition.

Although D_L and D_H differ, and their exact correlation depends on the property of the medium, the two quantities are of the same order [86]. In the case of XENONnT, the maximum expected longitudinal and transverse diffusion obtained from Eqn. 3.2 for a point-like electron cloud generated at the bottom of the TPC active volume is of the order of 0.45 cm. Such value is at the same scale as the xy position reconstruction, and hence, transverse diffusion can be safely ignored [70]. On the opposite side, the resolution on the z-position reconstruction is much smaller; hence, longitudinal diffusion shall be considered.

It is worth stressing that the parameter T is defined as a generic time at which we want to evaluate the cloud diffusion. It corresponds to the timestamp at which the center of the 3D Gaussian distribution reaches $z = \mu\mathcal{E}T$. For the scope of developing the diffusion-only contribution to the S2 shape, we are interested in evaluating the diffusion that a point-like electron cloud will undergo before the S2 signal starts to be produced (we will focus in Sec. 3.1.3 on the impact of the light formation on the S2 shape). This means that, for each energy deposition, we should evaluate the longitudinal diffusion of the cloud at the moment T at which the center of the Gaussian reaches the z value corresponding to the liquid-gas interface. This is conceptually different from the mean of the drifting time of each electron in the cloud – when the number of electrons in the cloud is large, the latter can be a good estimator of T.

From an experimental standpoint, the observable that best approaches this time is the drift time t_d, defined as the time difference between the start of the detected S1 signal and the start of the detected S2 signal (see Sec. 2.2). In principle, T and t_d differ since the evaluation of t_d involves the light production mechanism of both S1 and S2 and the diffusion process itself for S2. Nevertheless, since the formation time of both S1 and S2 signals, in the order of a few hundred ns and tens of μs, respectively, is much faster than the typical T values, such difference is negligible, and the drift time (t_d) can be safely used as an estimator for T.

Implementing all the discussions above, Eqn. 3.1 can be simplified to

$$n(z; t_d) = \frac{n_0}{\sqrt{4\pi D_L t_d}} \exp\left(-\frac{(z - \mu\mathcal{E}_d t_d)^2}{4D_L t_d}\right). \tag{3.2}$$

An illustration of the impact of longitudinal diffusion on the spatial distribution of the electron cloud is sketched in Fig. 3.2, showing the z-distribution of the electrons both at the initial time when it is created as a very sharp cluster and at a later time after diffusion kicked in.

For each S2, the drift time t_d is fixed[1], and Eqn. 3.2 is effectively a 1-dimensional Gaussian along the z-axis with a shifted center at $\mu\mathcal{E}_d t_d$, instead of a wave function in which T is allowed to evolve. Therefore, to describe the shape of S2 signals, only the denominator of the exponential matters. Since S2 signals are recorded along the time axis in the unit of PE/ns (Fig. 2.5), the spatial parameter $(z - \mu\mathcal{E}_d t_d)$ is often replaced by $v_d t$, where t is a generic time variable and $v_d t$ characterizes the spatial deviation from $z = \mu\mathcal{E}_d t_d$. With this replacement, Eqn. 3.2 can be further reduced to

$$n(t; t_d) = \frac{n_0}{\sqrt{4\pi D_L t_d}} \exp\left(-\frac{(v_d t)^2}{4 D_L t_d}\right). \tag{3.3}$$

As discussed in Sec. 2.2.3, the S2 signal waveform is recorded as voltage drop over time (and normalized to charge per time in the unit of $[PE/ns]$, see Fig. 2.8). Therefore it is more intuitive to use t, instead of $v_d t$ as the parameter to describe the shape of S2 signals. From now on, I will refer to the S2 signal shape in the scope of this time parameter instead of the spatial parameters discussed thus far.

The standard deviation σ_n of the distribution in Eqn. 3.3,

$$\sigma_n = \sqrt{\frac{2 D_L t_d}{v_d^2}}, \tag{3.4}$$

plus proper modeling of the secondary scintillation process, can be used for large S2 signals to establish the relationship between S2 signal duration and the drift time. As discussed in Ref. [87], if we assume the secondary scintillation process is uniform and can be described by a boxcar function, the relation can be modeled as

$$\sigma_e = \sqrt{\sigma_n^2 + \sigma_0^2}. \tag{3.5}$$

---

[1] This drift time is for the electron cloud, not individual electrons

σ_e is defined as the time interval encompassing the central 68% (1 σ) area of an S2 signal. Given a waveform shown in Fig. 2.8[2], σ_e is determined by measuring the time difference between two points: one preceding and the other following the signal's center of gravity (indicated by the gray vertical line). These points are chosen such that the areas they enclose with the center, on either side, represent 34% of the signal's total area (thus sum up to 68% between the two points).

However, Eqn. 3.4 is valid only within the domain where the number of electrons in the electron cloud is sufficiently large, facilitating a distribution that approximates a Gaussian form as delineated in Eqn. 3.3. This model does not accurately capture the characteristics of the S2 signal's (diffusion-only) duration when the electron count is minimal, leading to significant deviations from the Gaussian profile for individual electron clouds. Additionally, the applicability of Eqn. 3.5 presupposes a uniform secondary scintillation process, an assumption that does not universally hold as evidenced in Fig. 3.5.

3.1.1 Diffusion-Driven S2 Signal Full Duration: The Ideal Case

Let's start by deriving the time gap between the extraction of the first and last electron in the electron cloud, which is intimately related to the S2 signal duration (I will embed the light production mechanism later in the chapter). Attenuation associated with the electron lifetime (τ_e) and extraction efficiency (EE) are ignored to simplify the calculation.

Let's define the probability density function of an electron reaching the liquid-gas interface (and subsequently, extracted)[3] at time t as[4] $\text{Prob}(t, \hat{\theta})$, with shape parameters $\hat{\theta}$. Let's assume that the first of N electrons belonging to an initially point-like electron cloud is

---

[2] While the discussion primarily addresses S2 signals, the principle applies equally to S1 signals.

[3] Here, I acknowledge the existence of electron trapping at the liquid surface and the delay time caused by the trapping. However, it is a much longer process ($> 200\mu s$ [88, 89]) and will lead to splitting of the electron cloud, which, to the first order, in the derivation of this section, can be treated as several independent events.

[4] same definition as in Eqn. 3.3 as a relative time, marking the deviation from the conceptual drifting time $T = t_d$

extracted in gas at $t = t_0$. In order to observe a total S2 duration equal to Δt, the electron cloud must meet the following criteria:

1. Exactly 1 electron is extracted at time $t_0 + \Delta t$:
   - the probability of observing the first electron at t_0 and the last one at $t_0 + \Delta t$, within an infinitesimal window dt_0, is given by the combined probability

     $$\text{Prob}(t_0, \hat{\theta}) \cdot \text{Prob}(t_0 + \Delta t, \hat{\theta})\ dt_0.$$

   - given N electrons, we have N choices for the first electron, and $N-1$ for the last electron.
2. All other electrons shall be extracted between $(t_0, t_0 + \Delta t)$:
   - the probability for this to happen can be expressed by the combined probability

     $$\prod_{i=1}^{N-2} \int_{t_0}^{t_0+\Delta t} dt_i\ \text{Prob}(t_i, \hat{\theta})$$

Combining all terms, the probability of observing a total duration equal to Δt given the first electron extracted at $t = t_0$ can be expressed by the following probability density function

$$\rho_{tot,0}(\Delta t | N, t_0, \hat{\theta}) = N(N-1) \cdot \text{Prob}(t_0, \hat{\theta}) \cdot \text{Prob}(t_0 + \Delta t, \hat{\theta}) dt_0 \int_{t_0}^{t_0+\Delta t} \prod_{i=1}^{N-2} dt_i \text{Prob}(t_i, \hat{\theta}) \tag{3.6}$$

$$= N(N-1) \cdot \text{Prob}(t_0, \hat{\theta}) \cdot \text{Prob}(t_0 + \Delta t, \hat{\theta}) dt_0 \left(A_{t_0}^{t_0+\Delta t}\right)^{N-2}, \tag{3.7}$$

where $A_{t_0}^{t_0+\Delta t}$ is the integral of the electron cloud density function $\text{Prob}(t, \hat{\theta})$ between t_0 and $t_0+\Delta t$ and $N-2$ is the number of electrons that are extracted in between the two boundaries.

Now, integrating over all possible t_0, the probability density function of observing Δt, given $\mathrm{Prob}(t, \hat{\theta})$, can be expressed as

$$\rho_{tot}(\Delta t|N, \hat{\theta}) = N(N-1) \int_{-\infty}^{\infty} dt_0 \; \mathrm{Prob}(t_0, \hat{\theta}) \cdot \mathrm{Prob}(t_0 + \Delta t, \hat{\theta}) \left(A_{t_0}^{t_0+\Delta t} \right)^{N-2} . \tag{3.8}$$

Equation 3.8 can be re-written, using the Gaussian of Eqn. 3.3 as electron cloud density function with $\hat{\theta} = \sigma$, as[5]

$$\rho_{tot}(\Delta t|N, \sigma) = N(N-1) \frac{1}{4\pi\sigma^2} \int_{-\infty}^{\infty} dt_0 \; e^{-\frac{(t_0)^2}{2\sigma^2}} e^{-\frac{(t_0+\Delta t)^2}{2\sigma^2}} \left(A_{t_0}^{t_0+\Delta t} \right)^{N-2} . \tag{3.9}$$

Changing the variable from t_0 to $t_0 - \frac{\Delta t}{2}$ helps to further merge terms and simplify the equation. Eventually, the probability density function of observing a total duration of Δt, given N electrons in a cloud and with a diffusion characterized by σ, can be expressed as:

$$\rho_{tot}(\Delta t|N, \sigma) = \frac{N(N-1) e^{-\frac{\Delta t^2}{4\sigma^2}}}{2\pi\sigma^2 2^{N-2}} \int_{-\infty}^{\infty} dt_0 \; e^{-\frac{t_0^2}{\sigma^2}} \left(A_{t_0-\frac{\Delta t}{2}}^{t_0+\frac{\Delta t}{2}} \right)^{N-2} , \tag{3.10}$$

with $A_{t_0-\frac{\Delta t}{2}}^{t_0+\frac{\Delta t}{2}}$ being expressed as a difference between two points on an error function:

$$A_{t_0-\frac{\Delta t}{2}}^{t_0+\frac{\Delta t}{2}} = \frac{1}{2} \left(Erf\left(\frac{t_0 + \frac{\Delta t}{2}}{\sqrt{2}\sigma} \right) - Erf\left(\frac{t_0 - \frac{\Delta t}{2}}{\sqrt{2}\sigma} \right) \right) . \tag{3.11}$$

Few considerations about Eqn. 3.10:

- While a closed form for ρ_{tot} was not found, we can easily solve Eqn. 3.10 numerically. Outcomes of such evaluation with an assumption of $\sigma = 30$ *a.u.* (arbitrary unit), calculated for different N values, are shown in Fig. 3.3. It was also checked that the

---

[5] Here I use a generic σ rather than σ_n of Eqn. 3.5 since: 1) the quantity described here by σ turns out to not be an observable (see Sec. 3.1.3) and 2) to lighten the nomenclatures.

formula, if integrated over Δt from 0 to infinity, yields 1 for different N values.

- For a $2e^-$ cloud, i.e. $N = 2$, the formula simplifies to $\frac{1}{\sigma\sqrt{\pi}} \exp\left(-\frac{\Delta t^2}{4\sigma^2}\right)$. This is a simple Gaussian, centered at $\Delta t = 0$ and with std $\sqrt{2}\sigma$. This is exactly what we would expect from subtracting two independent Gaussian variables. Since Δt can only be non-negative, the normalization factor $\frac{1}{\sigma\sqrt{\pi}}$ manifestly shows that such distribution should be single-sided;
- As N goes up, the area term plays a bigger role: the more we sample, the more the total distribution follows the actual diffusion Gaussian, which makes the total duration go to infinity.

3.1.2 Diffusion-Driven S2 Signal Percentile Duration

In the real detector, we typically cannot precisely evaluate the full duration of a signal due to a few unavoidable issues:

1. For large numbers of electrons, as pointed out at the end of the previous section, the S2-signal full duration goes to infinity. "Infinite" continuous data taking is not affordable;
2. Even accepting a limited maximum full duration, it is not trivial to precisely define the start and the end of an S2 signal. The sparse nature of low-energy signals overlapped to a "noisy"[6] environment, makes it hard to precisely determine the boundaries of a signal.

The above considerations imply that the full duration of the S2 signal (introduced in Sec. 3.1.1) is not a good experimental observable, and hence we should redefine in our model

---

[6] In this case, "noisy" refers to the fact that in a TPC, you can have accidental pile-up between the signal generated by energy deposition you are interested in and a spare emission of a single photoelectron or of a single electron as well as another physical energy deposition happening closely.

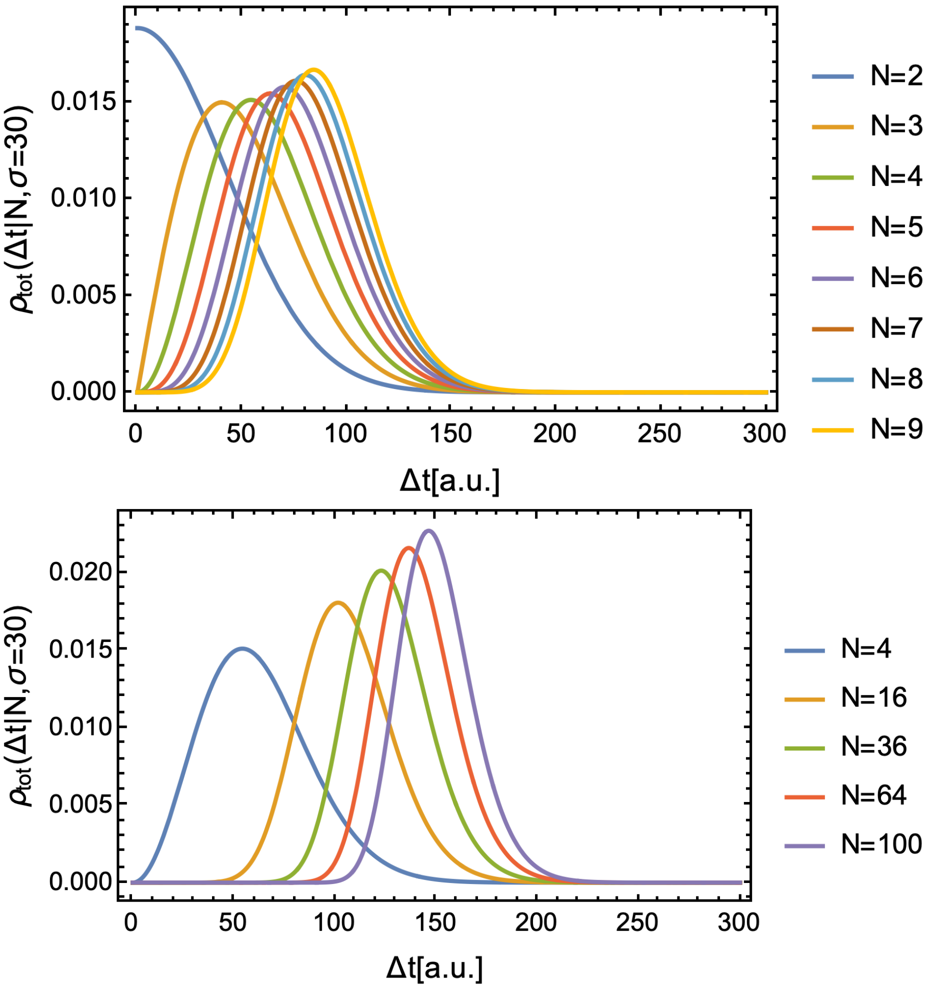

Figure 3.3: $\rho_{tot}(\Delta t|N, \sigma = 30)$ evaluated at different N. Top: values of the function at small N. Bottom: evaluated at large N

a new set of variables that will allow an easier comparison with the data. Although the exact start and end of the S2 signal can be fuzzy due to the more dispersed nature of the cloud at its boundaries (see Fig. 3.2), we can typically well identify experimentally the central bulk of the electron cloud since given the Gaussian profile of the cloud, a larger fraction of electrons will typically reach the gas pocket with similar arrival times. Each electron, while accelerating in the gas, will produce light, and the emitted photons, once detected, will tend to overlap in time, creating higher peaks in the sum waveforms, making them easier to identify. The variable used in the data to capture the shape of the S2 pulse around its maximum is referred to as r_{50p} (r_{90p}), representing the duration of the S2 signal containing, with respect to its center, 50% (90%) of its total area. For easy reference, r_{50p} (r_{90p}) is called "the range of the central 50% (90%) area"[7].

Let's start from a general percentile p, where r_p denotes the range of the central p area (with p=0.5 or 0.9 corresponds to the two cases mentioned above)[8]. For an S2 signal to attain a specific r_p value, it must fulfill certain conditions. Without the loss of generality, here I use Δt again, similar to its previous definition in Sec. 3.1.1 but with a key difference: it now signifies the time gap between the two very electrons that satisfy upcoming criteria, not just the first and last extracted electrons. Similar to the derivation of the full duration in the previous section, starting from an anchor timestamp t_0, for $r_p = \Delta t$, the ensemble of the electrons within the S2 signal has to have the following features:

1. Exactly one e^- is observed at t_0, and another at $t_0 + \Delta t$:
    - the probability of this to happen, once the combinatoric terms are accounted for is
    $$N(N-1) \cdot \text{Prob}(t_0, \hat{\theta}) \cdot \text{Prob}(t_0 + \Delta t, \hat{\theta})$$
2. Exactly $\frac{1-p}{2}N$ e^- are observed before t_0, and exactly $\frac{1-p}{2}N$ e^- are observed after $t_0 + \Delta t$:
    - The probability of each e^- arriving before t_0, in analogy to the previous section, is just the $\left(A_{-\infty}^{t_0}\right)^{\frac{1-p}{2}N}$. Similarly the probability of each e^- arriving after $t_0 + \Delta t$ is given by $\left(A_{t_0+\Delta t}^{\infty}\right)^{\frac{1-p}{2}N}$;
    - For the electrons observed before t_0, there are a total of $\binom{N-2}{\frac{1-p}{2}N}$ combinations;

---

[7] With this convention, σ_e defined in Eqn. 3.5 is called the range of the central 68% area

[8] Although r_p is defined with respect to S2 area, here we omit the light formation process. This simplification treats the secondary scintillation process as point-like, using SEG (PE/e^-)) as the S2 area's unit instead of PE

- For the electrons observed after $t_0 + \Delta t$, there are a total of $t\binom{N-2-\frac{1-p}{2}N}{\frac{1-p}{2}N} = \binom{\frac{1+p}{2}N-2}{\frac{1-p}{2}N}$ combinations.

3. The rest $(pN-2)$ e^- strictly in between the two boundaries (to ensure that counting the two electrons on the boundaries, there are a total pN electrons included to meet the definition of r_p):

   - The probability of this happening is another area term, raised to the corresponding power: $\left(A_{t_0}^{t_0+\Delta t}\right)^{pN-2}$
   - There is no combinatoric term because all the rest of the electrons should be in this step

Multiplying all terms together, we can get a similar expression as Eqn. 3.6:

$$\begin{aligned}\rho_{p,0}(r_p = \Delta t|N, \hat{\theta}, p, t_0) =& N(N-1)\binom{N-2}{\frac{1-p}{2}N}\binom{\frac{1+p}{2}N-2}{\frac{1-p}{2}N} \cdot \text{Prob}(t_0, \hat{\theta}) \cdot \text{Prob}(t_0+\Delta t, \hat{\theta})dt_0 \\ & \times \left(A_{-\infty}^{t_0}\right)^{\frac{1-p}{2}N} \left(A_{t_0+\Delta t}^{\infty}\right)^{\frac{1-p}{2}N} \left(A_{t_0}^{t_0+\Delta t}\right)^{pN-2}. \end{aligned} \tag{3.12}$$

The combinatoric factors can be combined as

$$N(N-1)\binom{N-2}{\frac{1-p}{2}N}\binom{\frac{1+p}{2}N-2}{\frac{1-p}{2}N} = \frac{N!}{\left(\left(\frac{1-p}{2}N\right)!\right)^2 (pN-2)!}. \tag{3.13}$$

Integrating over t_0 and introducing the Gaussian as the electron cloud density function returns the probability density of observing pN electrons within $[t_0, t_0+\Delta t]$ given a diffusion characterized by σ.

$$\rho_p(r_p = \Delta t|N, \sigma, p) = \frac{N!}{\left(\left(\frac{1-p}{2}N\right)!\right)^2 (pN-2)!} \frac{e^{-\frac{\Delta t^2}{4\sigma^2}}}{2\pi\sigma^2 2^{N-2}}$$

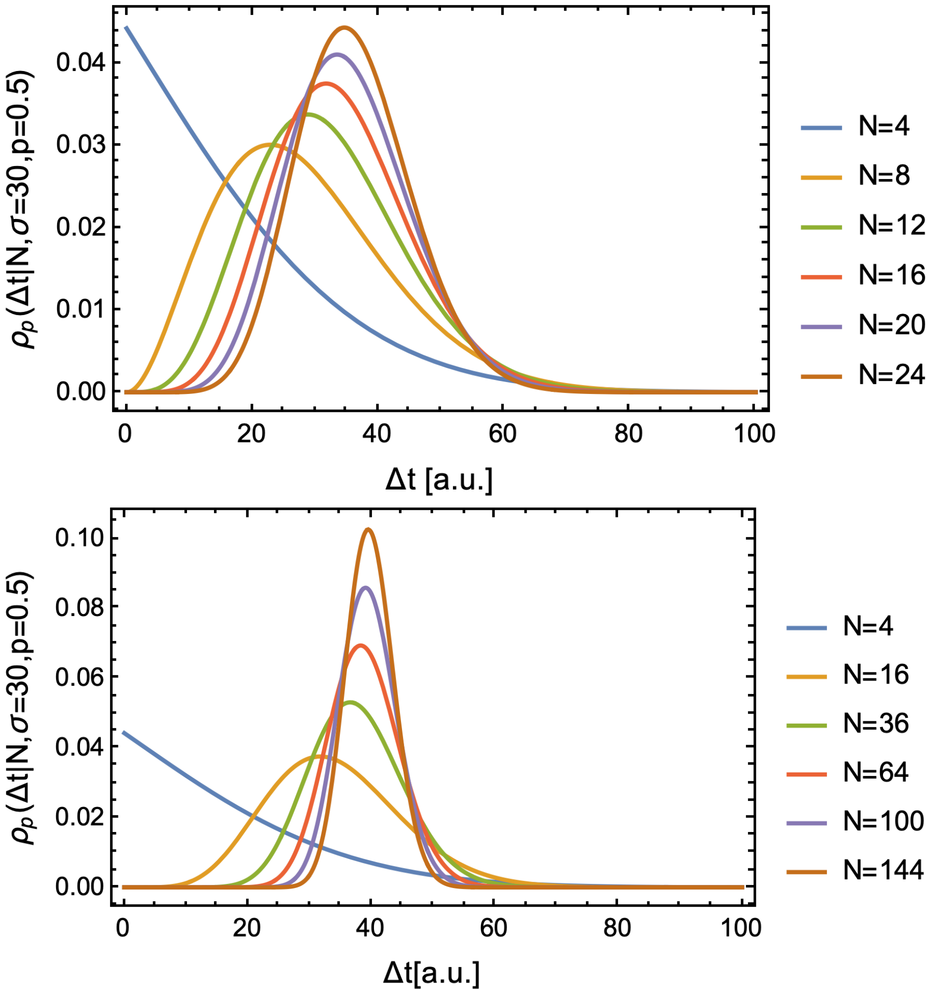

Figure 3.4: $\rho_p(\Delta t|N,\sigma=30,p=0.5)$ evaluated at different N. Top: values of the function at small N. Bottom: evaluated at large N.

$$\cdot \int_{-\infty}^{\infty} dt\, e^{-\frac{t^2}{\sigma^2}} \left(4A_{-\infty}^{t_0} A_{t_0+\Delta t}^{\infty}\right)^{\frac{1-p}{2}N} \left(2A_{t_0}^{t_0+\Delta t}\right)^{pN-2}. \tag{3.14}$$

The $\mathrm{Prob}(t_0,\hat{\theta})$ terms can be evaluated in the same way, and the area terms will result in similar expressions as Eqn. 3.11.

There is one trivial limitation to the choice of p, given N: since electrons are assumed to be point-like, they are not divisive, and thus $\frac{1-p}{2}N \in \mathbb{Z}^+$. Some numerical evaluations of Eqn. 3.14 are shown in Fig. 3.4. Unlike the total duration, the expectation of r_p, $\langle r_p \rangle$, doesn't go infinite as N increases. This is intuitive: the larger the N, the closer the electron cloud would resemble the underlying Gaussian (or some other) distribution. Thus, $\langle r_p \rangle$ should asymptotically approach the corresponding width that covers p percent of the area under such a distribution, while the farthest gap goes to infinity.

It should be noted that a numerical evaluation of the integration of Eqn. 3.14 gives 1 with an extensive range of testing parameter values (N, σ, p), which indicates that $\rho_p(\Delta t|N, \sigma, p)$ is a normalized probability density function.

3.1.3 Implementing The Single Electron Response

To reach a realistic description of the shape of the S2 signal, we need to convolve the electron cloud diffusion model with the secondary scintillation process. Each electron travels through the gas pocket under the effect of $\mathcal{E}_{mult}$ and, along its path, it induces the formations of excited dimers that lead to the emission of UV light[9].

The photon yield of this process is related to the strength of $\mathcal{E}_{mult}$, the length of the path traveled in the gas pocket, and the gas pressure. Using a formulation similar to the one introduced in Ref. [91, 92, 93], the number of photons per unit of the path can be expressed as:

$$\frac{dN_{ph}}{dz} = \left(a\frac{\mathcal{E}_{mult}(z)}{P} + b \right) P, \tag{3.15}$$

where N_{ph} is the number of emitted photons, z is the length of the path travelled in gas ($z = 0$ corresponds the liquid-gas interface) and P is the gas pressure. The constants a and b are free parameters empirically obtained from measurements (Fig. 3 in Ref. [92] and Fig. 6 in Ref. [93]).

Several other mechanisms affect the measurements of the secondary scintillation light such as the light collection efficiency [61], the PMT single photoelectron (SPE) response [94, 95], signal propagation in electronics, digitizer baseline fluctuations [82], and peak identifi-

---

[9] The decay time for the dimers in GXe is around 5 ns (singlet) and 100 ns (triplet) [90], and thus is ignored in this study

cation during data processing [70]. Some of these effects are position-dependent within the detector, and their net effect is that the Single Electron Gain (SEG), i.e., the number of S2 photoelectrons per extracted electron (PE/e^-), varies throughout the xy plane, leading to slightly different average values across it.

To properly account for all these effects in the model, I extracted from XENONnT data a few quantities that will be later used in Monte Carlo to produce realistic fluctuations associated with the various above-mentioned processes:

- A normalized waveform template corresponding to the average shape of the S2 signal produced by a single electron (see left plot of Fig. 3.5)[10]. Its features are very well understood and stem out from the convolution of the various effects involved in the S2 signal formation, i.e., excimers production throughout the electron path in the gas (before reaching the anode wire) and their successive decay;
- A two-dimensional map capturing the variation of the Single Electron Gain throughout the xy plane due to some of the position-dependent effects mentioned above, as depicted in Fig. 2.11. This map was further elaborated, and SEG in different macro-regions of the detector was defined;
- A two-dimensional map capturing the standard deviation of the Single Electron Gain throughout the xy plane. We will refer to this quantity as σ_{SEG}. In analogy with the SEG, the map was further elaborated. See Sec. 2.3.1 and Tab. 2.2.

For simplicity, the xy dependences are absorbed into the fluctuations of the SEG and σ_{SEG}. Their distributions are expressed as two Gaussians, centered at $\langle \text{SEG} \rangle$ and $\langle \sigma \rangle_{\text{SEG}}$, with standard deviations $\sigma_{\langle \text{SEG} \rangle}$ and $\sigma_{\langle \sigma \rangle_{\text{SEG}}}$, respectively. See Sec. 2.3.1 and Tab. 2.2 for the exact values, and Sec. 2.3.1 for the derivations.

---

[10] This template was generated by identifying in the tails of large S2 signals, the smallest peaks corresponding to the more sparse single electrons that, being extracted far from others can be easily identified. Such pieces of waveform were then aligned in time and averaged out to produce a typical time template.

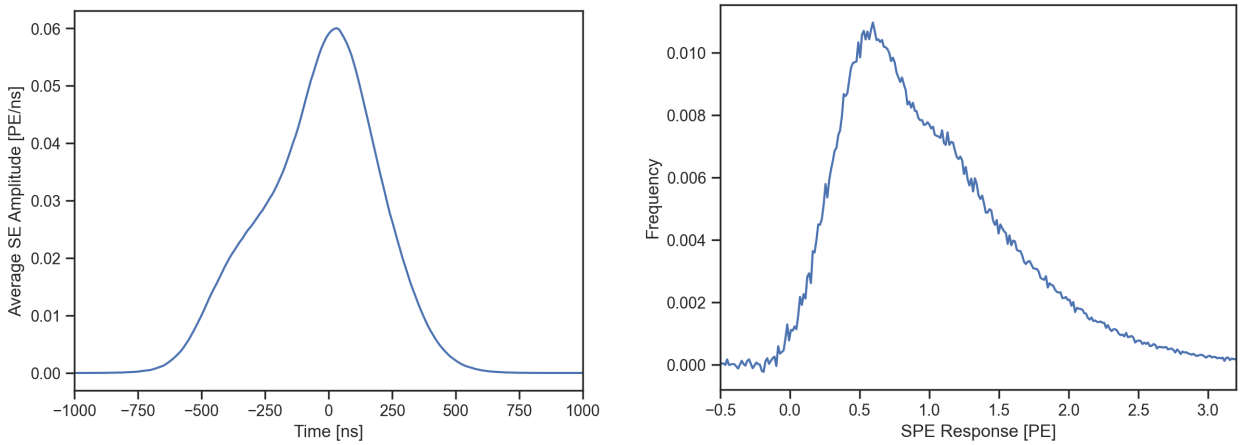

Figure 3.5: Left: average single electron waveform from SR0 background data; right: average SPE response across all PMTs normalized to 1. Notice that sometimes a photon can result in "negative" PMT responses because a photon might not trigger a photoelectron when hitting the PMT cathode, and the baseline fluctuation dominates and gives a negative yield.

The MC approach aims to reproduce synthetic data mimicking final S2 signal shapes, i.e., "waveforms" associated with ionization clouds produced in the liquid at different depths, diffusing while drifting through the xenon and extracted in the gas in a specific location (x_0, y_0) of the xy plane. These data are produced by executing the following procedure:

1. The arrival time of N electrons is sampled out of a generic Gaussian diffusion model (such Gaussian model, described by the standard deviation σ and centered at 0, will be given a physical meaning in the next section);

2. An (x_0, y_0) location is randomly selected and. Equivalently, a value of SEG is sampled from a Gaussian distribution, centered at $\langle \text{SEG} \rangle$ with standard deviation $\sigma_{\langle \text{SEG} \rangle}$. Similarly, a value of σ_{SEG} is sampled from its Gaussian distribution;

3. Given the SEG and $\sigma_{\langle \text{SEG} \rangle}$, a value of the number of expected photons from the electron[11] is sampled out from the associated Gaussian distribution;

---

[11] By definition, this can also be called the Single Electron Gain. However, by the definition of Sec. 2.3.1 and Tab. 2.2, the value of SEG for is a weighted value (Eqn. 2.23), and to obtain an instance of the expected number of photons from a simulated electron, we need to sample it out from a Gaussian.

4. Subsequently, the actual number of detected photons (or photoelectrons) generated for the very simulated electron, denoted N_γ, is sampled from a Poisson distribution with expectation equals the expected number of photons from the last step;
5. The detection time of each detected photon is sampled out from the single electron S2 signal template, which is treated as a probability density function (see Fig. 3.5 left);
6. As introduced in Sec. 2.2.3, each photoelectron results in a voltage drop in the PMTs and can vary in size. To incorporate such fluctuation, the size of each photoelectron is described by a normalized photoelectron template whose amplitude is scaled according to a charge value sampled out of the single photoelectron (SPE) distribution during the calibration period (see Fig. 3.5 right), describing the average charge response of the PMTs to an individual photon.

This simulation process aims to reproduce the shape of the S2 waveform for electron clouds. The combination of Step.3 and Step.4 is a combination of Poisson and Gaussian (Poisson&Gaussian) distribution, which can be expressed as

$$\mathrm{Prob}\left(N_\gamma = x; \mathrm{SEG}, \sigma\mathrm{SEG}\right) = \int_0^\infty dx' \mathrm{Poisson}(x, x') \mathrm{Gaussian}\left(x'; \mathrm{SEG}, \sigma\mathrm{SEG}\right). \tag{3.16}$$

The sampling of all electrons and summing up the contributions from every individual can be schematically expressed as

$$\mathrm{Prob}(\mathrm{SEG} = x; N_\gamma) = \int_0^\infty \left(\prod_{i=1}^{N_\gamma - 1} dx_i \; \mathrm{SPE}(x_i) \right) \mathrm{SPE}\left(x - \sum_{i=1}^{N_\gamma - 1} x_i \right). \tag{3.17}$$

As a first exercise, we can turn off the SE shape and SPE response to simulate the diffusion-only part of the model. Figure 3.4 shows the comparison between the distributions of r_{50p} obtained from the numerical solution of Eqn. 3.14 (solid lines) and those obtained

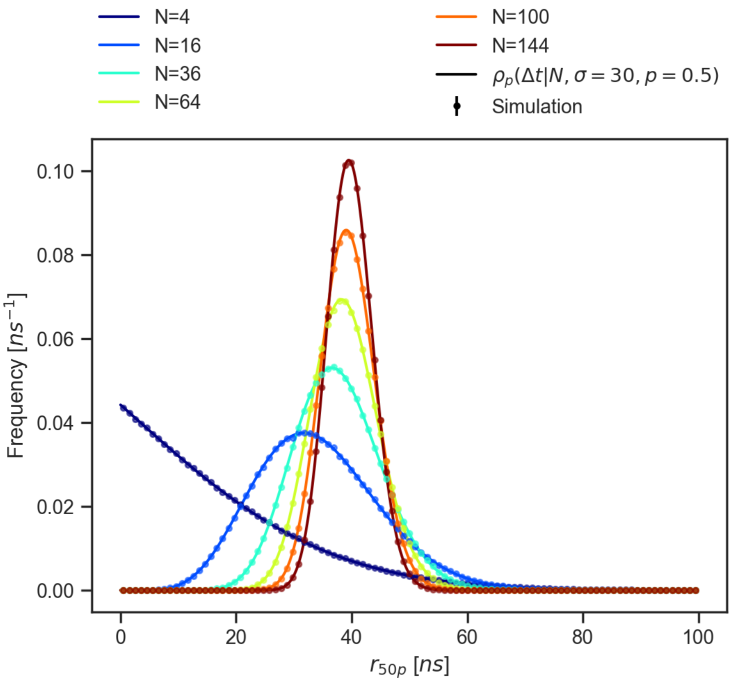

Figure 3.6: Comparison between Mathematica evaluations of Eqn. 3.14 (solid lines) and simulated populations (dots) at different N. For this specific simulation, the SE shape and SPE shape were assumed to be point-like.

analyzing the synthetic data from this MC (dots). The comparison spans electron clouds from 4 to 144 electrons and assumes a diffusion described by $\sigma = 50$ $a.u.$. The matching is excellent.

The r_{50p} duration distributions obtained by the full simulation, enabling SE shape and SPE response, are shown in Fig. 3.7, assuming for the diffusion a more realistic $\sigma = 5000$ ns, which roughly corresponds to the center of the XENONnT TPC.

3.1.4 Establishing Diffusion - Drift Time Relation

Sec. 3.1.3 describes a way of developing synthetic data that, beyond the formulations, can be used to extract the correlation between the duration, expressed in the form of r_{50p}, and the drift time. The idea here is to transform the MC simulation described in the previous section into a Markov Chain MC (MCMC), used to fit XENONnT calibration data and extract from

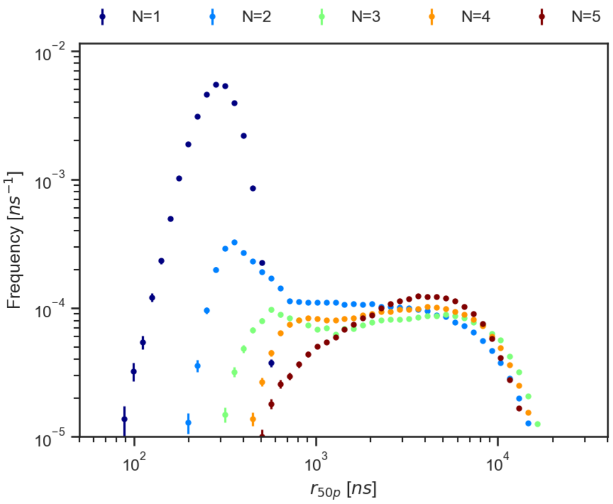

Figure 3.7: r_{50p} values from simulations of realistic electron cloud shape with SE shape and SPE responses (Fig. 3.5). Different N was simulated with a constant $\sigma = 5000$ ns.

the best fit the relation between r_{50p} and the drift time t_d. The data used for this study are those acquired while spiking the xenon gas with gaseous radio-isotopes,^{37}Ar and $^{83\text{m}}$Kr, that diffuse uniformly within the active volume. The ^{37}Ar radio-isotope decays through electron capture emitting, among the rest, x-rays associated to the K-shell (∼2.7 keV) and L-shell (∼0.26 keV) electron captures. The former decays are well within the reach of the detector, and being mono-energetic, they are easy to identify and select. Similarly, $^{83\text{m}}$Kr decays ($\sim 41.6\ keV$ from the merged two-step decay) lead to the emission of mono-energetic lines that are ideal for characterizing the detector response.

Fig. 3.8 shows the 2D histograms of the r_{50p} duration vs drift time t_d for both the $^{83\text{m}}$Kr interactions and the ^{37}Ar (K-shell) interactions. The figure also reports the r_{50p} duration histograms for a specific value of the drift time. As evident from the plot, the two populations feature much narrower duration for $^{83\text{m}}$Kr than for ^{37}Ar. If the model presented in Sec. 3.1.3 is correct, interactions occurring at the same depth in the detector, i.e. same drift time, shall undergo a diffusion process governed by the same identical $\sigma(t_d)$ (unique for all energies) and the different duration of the associated S2 signal shall stem out simply from the different numbers of electrons (N's) produced during the $^{83\text{m}}$Kr than for ^{37}Ar decays (smaller in the

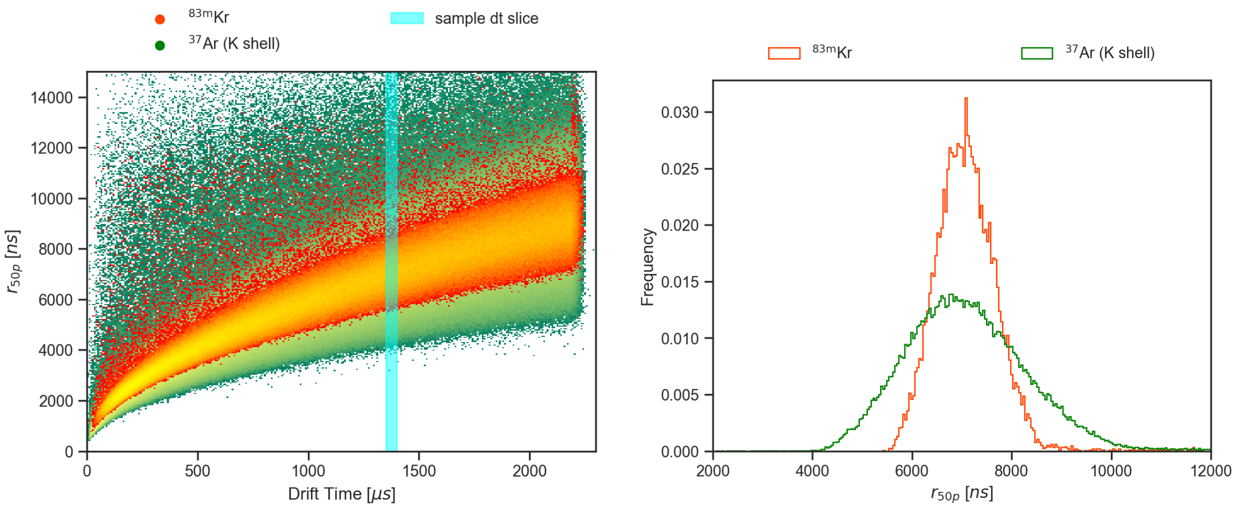

Figure 3.8: Left: the r_{50p} values of $^{83\mathrm{m}}$Kr and ^{37}Ar (K-shell) as functions of drift time; right: the r_{50p} values 1D distribution in the sampled drift time slice.

case of ^{37}Ar given the lower energy).

Given this observation, we can run our MCMC separately the on the $^{83\mathrm{m}}$Kr and ^{37}Ar data to confirm that the model properly describes the data and extract the desired dependence of the desired dependence of the diffusion from the drift time. The ingredients of this procedure are:

- The number of electrons in each slice of drift time ($N(t_d)$) for both populations can be easily obtained by the average S2 signal area in each slice of drift time divided by the corresponding single electron gain (the latter being independent of the drift time);
- The observed r_{50p} duration distribution in each slice of drift time can be extracted from the data as shown in Fig. 3.8.

The only unknown and free parameter of the MCMC is the diffusion constant in each slice of drift time, $\sigma(t_d)$. The left plot of Fig. 3.9 shows the r_{50p} duration distribution compared to the distribution from the model obtained with the σ best-fit value (for the specific t_d slice). The right plot shows the best-fit value of σ (dots) as function of the fitted t_d slice, both for $^{83\mathrm{m}}$Kr and ^{37}Ar. Although fitted independently, the two calibration data returns values

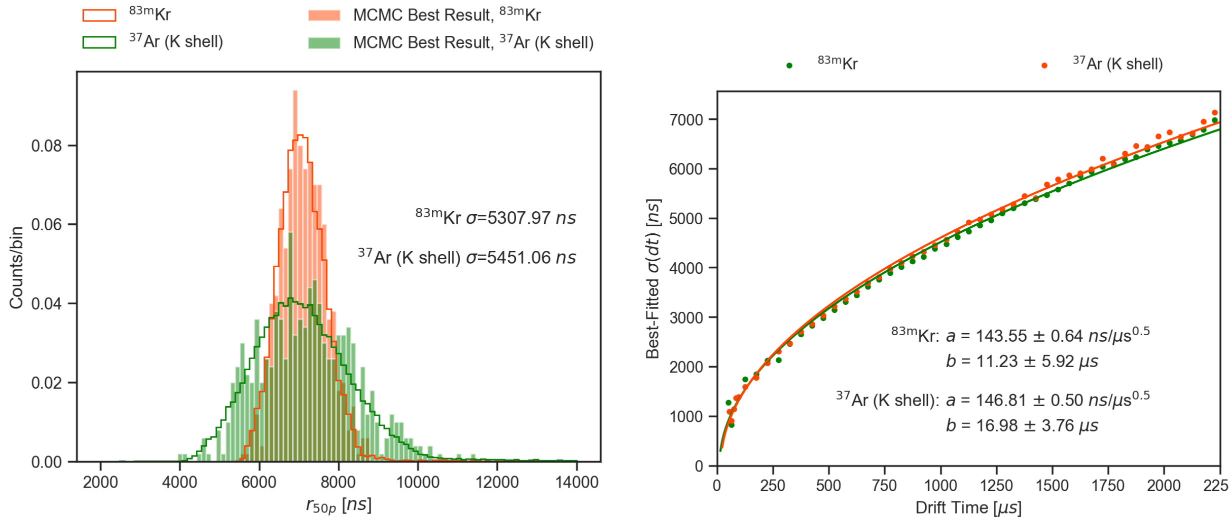

Figure 3.9: Left: best MCMC results of r_{50p} values vs real data for $^{83\text{m}}$Kr and ^{37}Ar (K-shell), and their corresponding best-fitted diffusion constant σ; right: $\sigma(t_d)$ and a square root fitting.

surprisingly similar, indicating that the assumption that the diffusion constant is a unique property of the detector holds properly.

The observed values of the diffusion constant as a function of the drift time can be fitted by

$$\sigma(t_d) = a\sqrt{t_d - b}, \tag{3.18}$$

where a and b are the free fit parameters. The parameter a has the unit of $ns/\sqrt{\mu s}$ and describes the increment of diffusion constant σ as a function of the square root of the drift time. The parameter b has the unit of μs. The value $t_d = b$ marks the time required for the electrons to drift from the gate to the liquid-gas interface (under the extraction field $\mathcal{E}_{ext}$, not the drifting field $\mathcal{E}_e$). Because the extraction field above the gate is much stronger than the drifting field, and the liquid above the gate is thin ($\sim 3\ mm$) compared to the drift region, we assumed during that time the electron cloud remains point-like and is described by the single electron shape shown on the left of Fig. 3.5.

The nominal values for a and b are taken as the mean values of the the two fits. The absolute difference can be taken as an estimate of the systematic uncertainty, while the individual uncertainties on the fitted parameters are combined as a statistical uncertainty:

$$\begin{aligned} a_{nom} &= 145.18 \pm 1.63 \text{ (sys)} \pm 0.81 \text{ (stat) } ns/\sqrt{\mu s} \\ b_{nom} &= 14.10 \pm 2.88 \text{ (sys)} \pm 7.01 \text{ (stat) } \mu s \end{aligned} . \tag{3.19}$$

With the square root correlation of Eqn. 3.18, the r_{50p} duration of S2 signals can be modeled for different numbers of electrons and used to develop data selection criteria (see Sec. 4.4). The modeled distributions of r_{50p} duration of S2 signals for the case of ionization cloud containing from 1 up to 9 e^- are shown in Fig. 3.10. As expected, r_{50p} duration of S2 signals composed of one electron is independent of the drifting. It is worth noting that for $N = 2$ a peak at small r_{50p} values is visible throughout the full drift time range. Intuitively, the time gap between the two electrons after drifting can be described by Eqn. 3.10 and is peaked at $\Delta t = 0$ for all σ's, as shown in Fig. 3.3. Although this function describes the total duration, the value of r_{50p} for a two-electron S2 signal must have partial contributions from both electron responses, the duration of which is then governed by the time gap between the two and should be peaked at 0, and the final shape should feature a peak resembling the r_{50p} duration of single electron S2s. As N goes larger, the r_{50p} vs drift time correlation converges to a nice band that can be described by a square root function, with the shape of the band well-described by a direct fitting of the band [70].

3.2 Time Gap Between Adjacent Electrons Inside the S2 Signal

The model presented up to now, although embedding as many realistic effects as possible, is glancing at one aspect that plays an important role in the case of small electron multiplicities. This has to do with the reconstruction algorithm that takes the recorded waveforms from the PMTs and tries to identify patterns that we call S1 and S2 signals. Such an algorithm is typically trained for interactions presenting both an S1 and S2, and hence, it typically

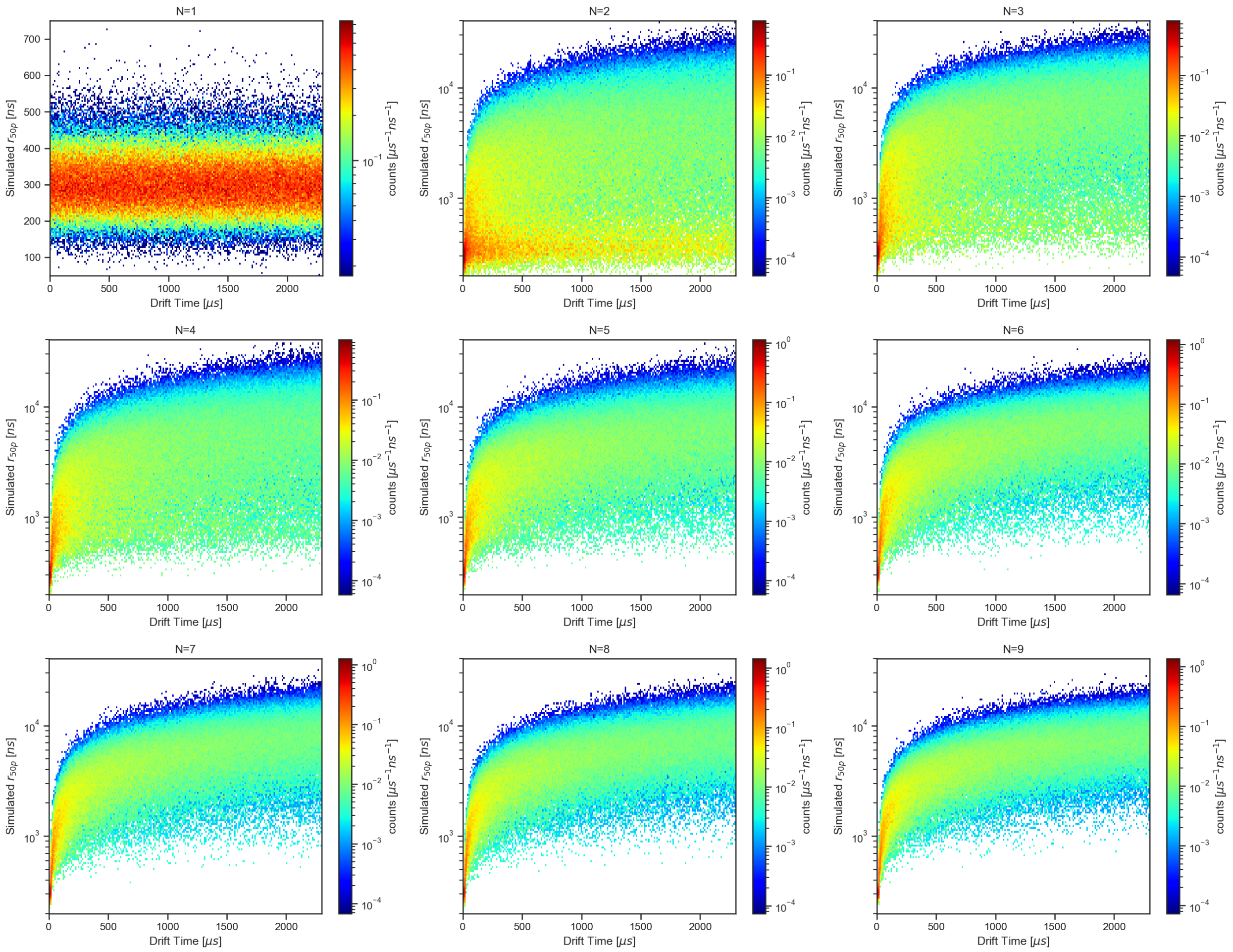

Figure 3.10: Simulated r_{50p} vs drift time of SE to $9e^-$ population with the square root correlation function Eqn. 3.19. With a constant σ in each drift time slice, the resulting r_{50p} distributions differ dramatically across different N's. Due to the use of log-scaled binning, the color bars are normalized to the size of each bin in the unit of $[\mu s^{-1} ns^{-1}]$.

performs better for S2 signals larger than the ones we are interested in here. Large S2 signals are generated by larger numbers of electrons, and the associated S2 photoelectrons tend to overlap in time and generate "connected" pulses rather than isolated ones. The algorithm starts failing when lower numbers of electrons (and hence of S2 photoelectrons) are involved, and empty gaps start to appear between the single electron S2 signals. For these cases, we need to put extra care and improve the performance of the algorithm to properly execute the merging of Single Electron S2 signals if they belong to a single low-energy deposition.

This signal merging process is illustrated in Fig. 3.11. As a first step, single pulses above

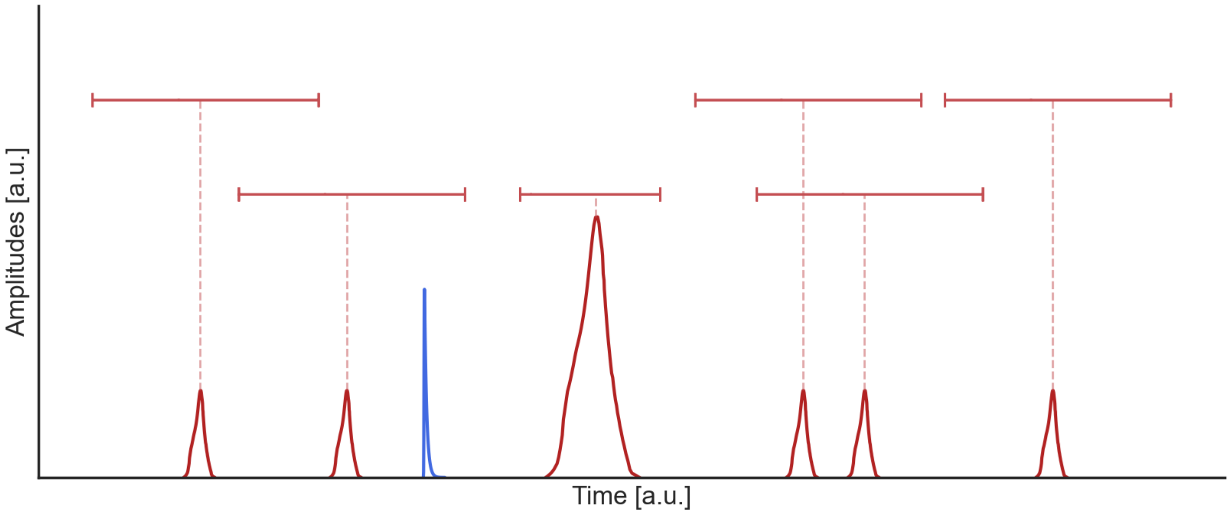

Figure 3.11: Illustration of pulse merging for building an S2 signal. Each small red spike indicates a cluster of light associated with an ionization signal. The horizontal segments indicate the merging window around each pulse. Note that the smaller the signal size, the larger the merging window. In the scenario shown in the picture, the 4th and 5th signals will be merged as one lies within the other's merging window. In contrast, all other signals remain separated and are treated by the standard algorithm as individual S2 signals associated with multiple energy depositions. The blue spike is an S1 that is neither merged to the ionization pulse in front of it nor is associated with a merging window to combine other pulses around it.

the threshold are identified by the reconstruction code and, based on the time profile, tagged as ionization signals or primary scintillation signals. Ionization signals that are near are then merged by the algorithm to form the S2 "peak" with a merging window correlated with the pulse sizes. There are several rules regarding this merging algorithm:

1. only ionization signals are merged (not signals whose time profile resembles the primary scintillation);
2. the larger the pulse size, the shorter the merging window;
3. small signals are merged into large signals but not the opposite, i.e., if a large S2 lies within the merging window of a nearby small S2, as long as the small S2 is outside the merging window of the large one, they will not be merged.

This procedure faces difficulties that are ultimately not solvable:

- there is no objective way of obtaining the true rate of S2s inside the detector, i.e., one cannot judge the extent of over-merging / under-merging simply by the number of reconstructed S2s;
- with the knowledge of the electron diffusion process presented in Sec. 3.1.4, it is clear that the merging window should be drift time-dependent, especially for small S2s. This cannot be implemented because:
  - before fully reconstructing the S2 peak and pairing it with the S1 peak, the drift time is not defined;
  - there is a large number of S2 signals without an associated S1. For these interactions, the drift time cannot be evaluated.

Utilizing the Monte Carlo method and the established diffusion correlation as discussed in Sec. 3.1.3 and Sec. 3.1.4, such merging practice can be studied and, to a certain degree, optimized. In this section, I will introduce a systematic method of establishing the merging strategy.

3.2.1 Optimizing The Merging Algorithm with the Diffusion Model

The basic idea is to set a proper merging window curve as a function of the signal size equipped with the diffusion relation discussed in Sec. 3.1.4. Based on the number of electrons N, gaps between individual electrons (groups) can be simulated, and merging windows can be properly adapted.

An illustration of the procedure followed to define the optimal merging window is shown in Fig. 3.12, in which, as an example, two S2 signals produced by 3 electrons produced in different regions of the TPC are simulated. For each simulated S2 signal, the maximum gap between the 3 electrons is stored. The procedure is repeatedly simulating the S2 signals for ionization clouds from 1 to up to 10000 e^-, spanning the 0-400,000 PE range in the S2 signal area. Given the impact of the drift time on the recorded maximum gap, two separate simulations are performed. In one, whose results are shown in the left plot of Fig. 3.13, the electron clouds are generated uniformly in the entire TPC active volume. In the other, shown on the right, the electron clouds are generated only near the cathode. As expected, the average maximum gap is larger for interactions coming predominately from the bottom of the TPC. This is more clear when comparing the two 99% percentile curves extracted from the left plot (green curve) and right plot (blue curve).

The difference between the blue and green curves shows that two different approaches could be used to improve the traditional merging window indicated in light blue in Fig. 3.13. Using the blue curve extracted from the model simulating interactions near the cathode would be the “conservative" approach, ensuring minimal under-merging cases. On the other side, using the green curve extracted from the model simulating interactions in the full TPC would be the “aggressive" approach, preventing over-merging but causing to split more often interactions from the cathode (more severely affected by diffusion). For the sake of the present S2-only analysis, we adopted the conservative approach, ignoring the over-merging issues because the S2s are large enough for traditional WIMP search to be away from the few-electron regime [66] (>200 PE – that is more than 6 electrons).

Fig. 3.13 is limited to a per-event level, and the crosstalks amongst events haven't been considered. This is the source of over-merging: electrons from different energy depositions are merged. Due to the ultra-low event rate in XENONnT detector [72], it is not crucial for big S2s, as it is rare to have two physical large S2s happening within their merging window, and it is not harmful if a few SE signals are merged inside. But this merging artifact is potentially detrimental in the S2-only studies, where the focus is on small S2s: if two physical events produce two SE S2s and they are merged, not only will we misidentify a 2 e^- event, but also the two original events are lost.

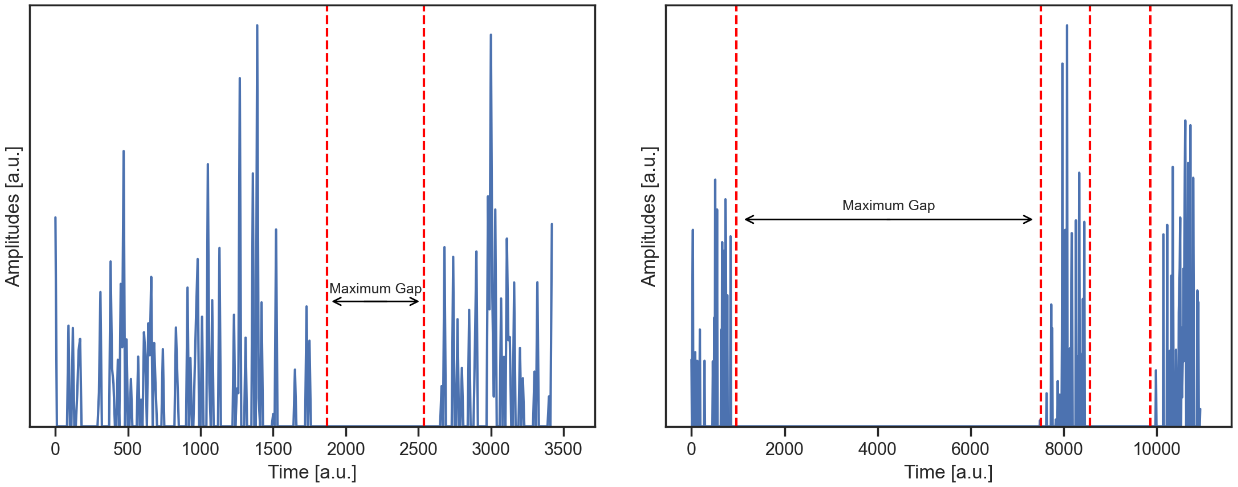

Figure 3.12: Two examples of simulated 3 e^{-} waveforms. Left: event happening at the top of the TPC with small diffusion; right event happening at the bottom of the TPC with large diffusion. Vertical red dashed lines are markers of the beginning and end of individual electrons/electron groups. The maximum gap is indicated with the black arrow.

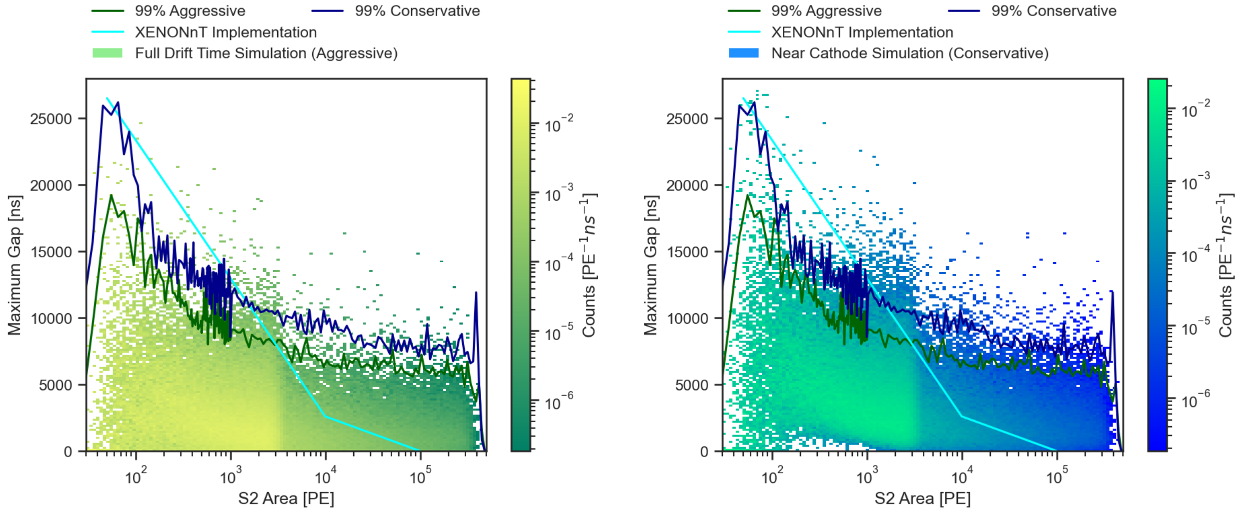

Figure 3.13: Maximum gaps within S2s of different sizes. Simulations were done with events throughout the full drift time (left) and only near the cathode (right). In both figures, the 99 percentile lines of both simulations are plotted as comparisons to the full distributions. The cyan curve is the XENONnT merging curve. Due to the limited simulations across a large S2 size range, the simulations contain more entries with S2s between 1 e^{-} and 100^{-}, and for larger S2s, I used log-binning. This resulted in the artificial "boundary" near 3000 PE.

Here, I give a quick quantitative estimation of such merging. From a TED run of 30

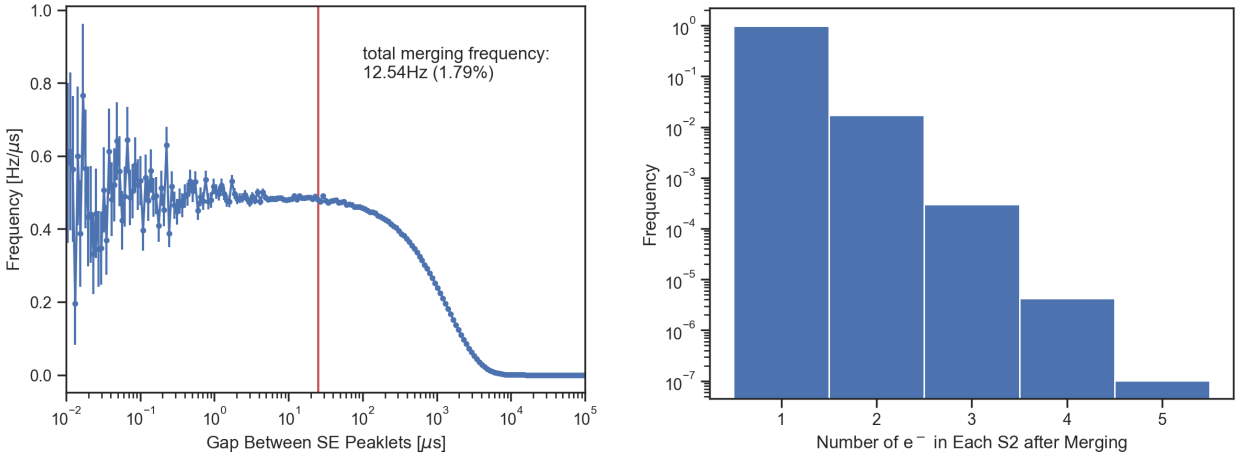

Figure 3.14: Results of simulation of 700 Hz independent all-SE peaklets. Left: Simulated distribution of gaps between adjacent peaklets; right: number of electrons in each recognized S2 after merging with 25 μs window. The red vertical line is the XENONnT merging window for S2s at SE size.

minutes in SR0, the rate of inseparable waveform pieces (called peaklets)[12] with sizes less than 300 PE (roughly 10 e^-) is ∼700 Hz. Assuming they all come from independent sources and ignoring their intrinsic durations, i.e., treating all peaklets as point-like SEs, a quick estimation of gaps between adjacent peaklets is shown in the left plot of Fig. 3.14, with the red vertical line marking the merging window of ∼100PE S2s. Because all peaklets are uncorrelated and follow a Poisson distribution, the distribution of the gaps follows an expected exponential distribution. With the XENONnT merging window, 12.54 Hz (1.79%) SE peaklets will be merged and wrongly form larger S2s. The merging results in this simplified scenario are shown in the right plot of Fig. 3.14. Out of the merged 1.79% peaklets, most form 2 e^- S2s, and some form larger ones. One critical remark is that, after merging, a non-existent large S2 emerged, and the SE components were lost.

A more interesting and chaotic simulation is to assume that all peaklets come from 2 e^- events and incorporate the diffusion process. Of course, in this scenario, the total rate of

---

[12] Inseparable means there are no clear clusters within the waveform. e.g., each piece between the red dashed lines (or between the red dashed lines and the beginning/end of the waveform) in Fig. 3.12 would count as an inseparable waveform piece, or peaklets.

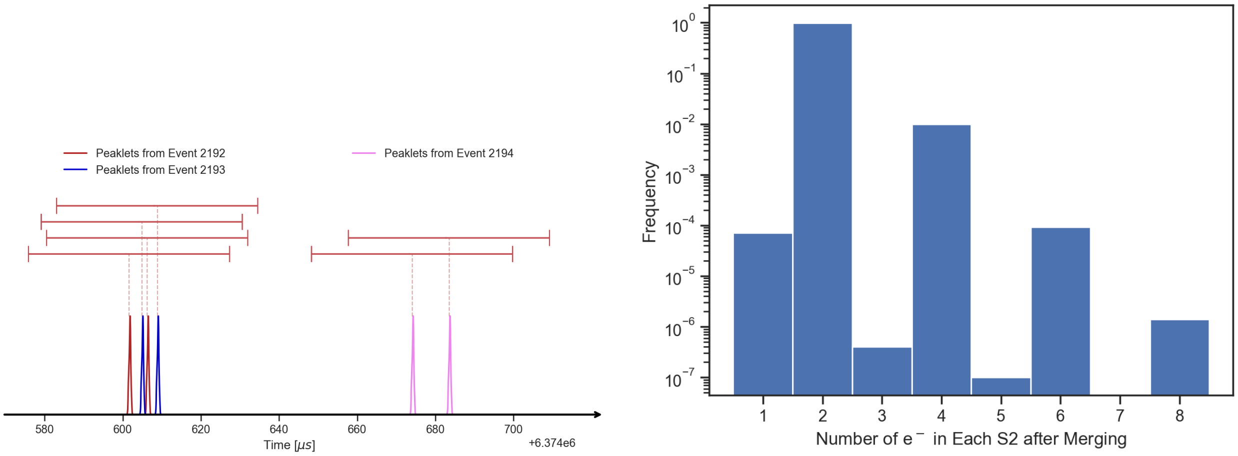

Figure 3.15: Results of simulation of 350 Hz independent all-2 e^- peaklets. Left: illustration of crosstalks between events due to the diffusion process during drifting. The two peaklets (of two electrons) from two closed-by events are observed alternatingly, causing wrong recognition of event reconstructions. The horizontal lines are peaklet merging windows centered at each observed "SE" signal ($\sim 25\mu s$). Right: number of electrons in each recognized S2 after merging with 25 μs window.

events should be halved to 350 Hz. The events were sampled randomly throughout the entire drift region with the diffusion relation (Eqn. 3.18 with nominal values from Eqn. 3.19). The individual signals (2 electrons from one event) are sorted by their observed time. To better understand the procedure, a piece of real simulation is shown in the left plot of Fig. 3.15, with samely colored peaks indicating signals from the same events. The red horizontal bars centered at each peaklet are the merging windows. This piece is specially picked to show because of the overlap of two 2 e^- events. The results of the merging of nearby peaklets are shown in the right plot of Fig. 3.15. Because the merging windows were designed at 99% of the diffusion distribution, some 2 e^- events from the bottom of the detector can be split and recognized as two independent S2s (events). Moreover, crosstalks beyond merging between events happen as odd-numbered e^- S2s emerge with minimal frequencies.

There is a more severe problem: the merging window is assumed to be dependent on the actual size of the event. In real data, only peaklets are observed firsthand, and there is no way to estimate the actual size of the event before merging peaklets up. Thus, in practice, the merging window was decided based on the size of the peaklets, which is an unavoidable compromise.

In conclusion, with the two simple simulations under idealized assumptions, mergings of events that produce only a few electrons cause a few percent loss of observations and a systematic bias of shifting the expected S2s spectrum larger. This observation leads to the proposal of the next section.

3.2.2 Decomposing S2s: A Proposal of An Unbiased Approach

The source of the dilemma introduced in Sec. 3.2.1 is exactly the merging practice. While it is physically motivated that signals inside the detector should be assembled to form "events", why can't we simply use the unmerged signals for analyses? That is, instead of trying ambiguously to reconstruct the original complete S2s, utilizing the expectation of the diffusion model to profile the peaklets. To swap from reconstructed events to peaklets only, the following changes in the streamlining of analyses need to be done:

1. For signal characteristics (for example, the Dark Matter - electron scattering rate as a function of ER energy), there needs to be one more step after the process discussed in Sec. 2.2 that converts energy to S1-S2 yields: the diffusion relation needs to be implemented to decompose the S2s into peaklets;
2. From the data side, only naturally connected signals should be counted towards one peaklet, and no further merging needs to be conducted.

To illustrate the idea, I will focus on the S2-only analysis perspective, where S1s are ignored, and the focus is on the smallest S2 signals between SE and 5 e^{-}. Let's assume there is an ideal new particle model that has an entirely flat characteristic energy spectrum in the unit of $[kg^{-1} \cdot day^{-1} \cdot keV^{-1}]$. Furthermore, it has a nominal rate of 1 event per

$[kg \cdot day \cdot keV]$ at some nominal cross-section:

$$R = 1\ kg^{-1} \cdot day^{-1} \cdot keV^{-1}, \tag{3.20}$$

where R is the rate of ABSMP-electron interaction. From the process described in Sec. 2.2, the expected CY at this nominal cross-section can be expressed using a simplified binomial process as shown in Eqn. 3.21

$$R_{ne}(N) = R \int_0^\infty dE \text{ Binomial}\left(N; N_0 = \text{floor}\left(\frac{E}{W}\right), p = \frac{1}{1 + \left\langle \frac{N_{ex}}{N_i} \right\rangle}\right), \tag{3.21}$$

where $R_{ne}(N)$ is the rate of an interaction producing a CY of N electrons. Ignoring the electron lifetime attenuation (Eqn. 2.19) and extraction efficiency attenuations (Eqn. 2.20) discussed in Sec. 2.3, the expected S2 spectrum in the unit of number of electrons observed is 0.015 per $kg \cdot day$. Now, the atomization requires further anatomy of these events. While the SE population is unaffected, larger S2s will likely separate into multiple small S2s. For a simple implementation of such practice:

- Within each event, if the gaps between electrons are smaller than SE width ($r_{100p} \sim 2\mu s$), they are merged as one peaklet, with the number of merged electrons as N;
- Otherwise, signals from each electron are regarded as individual peaklets of SE;
- Because of the ultra-low event rate and a much smaller "merging window" compared to the discussion in Sec. 3.2.1 ($2\mu s$ vs $25\mu s$), the mergings across different events are ignored.

Fig. 3.16 shows a simulation result up to 100 e^-. A boost in small S2s is observed, especially in the SE population, as many S2s composed of a few electrons after the diffusion process have separable waveforms. There is a deficiency in large S2s as the rate of peaklets drops below the true event rate because:

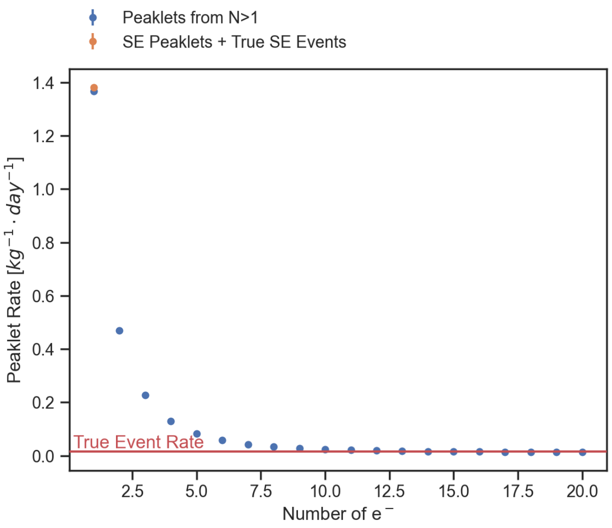

Figure 3.16: Rates of observing peaklets of N electrons with a flat interaction rate of 0.015 events per $kg \cdot day$. Since the SE population cannot be further split, contributions towards the rate spectrum from $N > 1$ are plotted in blue dots, and the individual bin of SE events is added to the first bin in yellow. The simulation was done up to 100 e^-.

1. They are broken into smaller S2s and boosting their bins, thus reducing the count in their bin;
2. Simulation terminated at 100 e^-, so there are not enough larger S2s to be broken up and fill these bins.

Surprisingly, the spectrum of true events is turned from flat to a peak at SE simply from the atomization process. With the rates used in the example, the contribution in the SE bin from $N > 1$ events is much larger than the actual true rate of the SE event. With an infinitely flat signal spectrum, the rate of observing any N peaklet would eventually go to infinity. In real-world models, there is always some roll-off at some point to prevent this from happening.

More complicated detector conditions can be implemented with a more comprehensive simulation to make the effect of this atomization practice more realistic. In conclusion, this method bypasses the dilemma of uncontrolled merging discussed in Sec. 3.2.1, which can be much more dangerous than what was depicted in Fig. 3.14 and Fig. 3.15 as there are all sorts of correlated junk signal productions when some physical event happens.

CHAPTER 4

S2-ONLY (FEW ELECTRON) ANALYSIS

In an LXe TPC, the simultaneous measurement of the prompt scintillation light (S1) and the delayed ionization signal (S2) allows for precise 3D position reconstruction of the energy deposition. However, this is possible only if the interaction generates S1 and S2 signals above their corresponding detection thresholds.

Thanks to the charge-to-light amplification mechanism occurring in gas, one ionization quanta – one single free electron – produces on average an S2 signal of about 32 PE (Tab. 2.2), well above the S2 light detection threshold. On the other side, for S1 signals, the light quanta – a single UV photon – often escapes detection due to the non-unitary light collection efficiency and PMT efficiency. Finally, for typical particles of interest, the relative ratio of photons to free ionization electrons is such that, while the energy of the deposition decreases, the S1 signal is the first to fall below the detection threshold. This behavior is evident in the ER/NR band of Fig. 2.9: on the left end of both the ER and NR bands, while the cS1 signals approaches 0 PE, the cS2 signals have an average value of about $\sim$ 1000 PE ($\approx$30 e^-) and $\sim$ 600 PE ($\approx$19 e^-) for ER and NR respectively. To be more quantitative, the light yield per unit of deposited energy is significantly smaller than the charge yield, as shown in Fig. 4.1 for various reference ER energies[1].

Beyond the aspects mentioned above related to the xenon micro-physics and the detector response, the detection efficiencies of S1 and S2 signals near the threshold are also impacted by the interplay between their different time evolution and the performance of the peak identification algorithm. The results of this complex process are shown in Fig.. 4.2. For S1 signals, the efficiency reaches 100% at about ten detected photons; for S2 signals, such value is reached around five detected photons ($\approx$5 PE). Considering that, as mentioned above,

---

[1] Notice that in Fig. 4.1, the charge yield has the unit of PE/keV, different from the unit e^-/keV defined in Sec. 2.2.1.

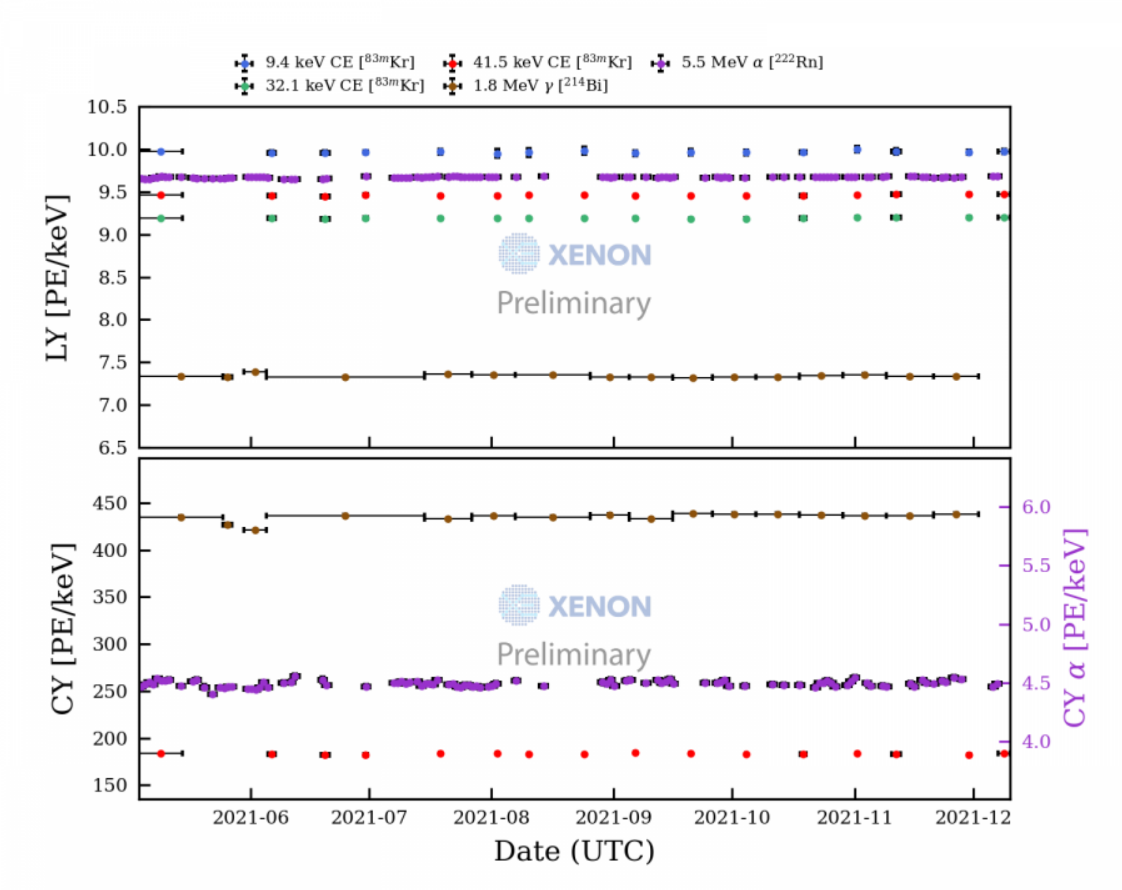

Figure 4.1: LY and CY evolution throughout SR0. Despite being stable, the LY (~ 9.7 PE$/keV$, measured with 5.5 MeV ^{222}Rn α) is much lower than the CY (~ 250 PE$/keV$).

each e^- produces an S2 signal of 32 PE on average, and it is safe to assume that ionization signals of even a single electron – as long as the electron survives the drift in the liquid and is successfully extracted into the gas – can be detected with close to 100% detection efficiency. The above considerations are at the basis of the so-called S2-only analyses, where the requirement for detecting the S1 is dropped in favor of the capability of reducing the ultimate energy threshold of the detector. But this does not come without drawbacks. Not requiring the detection of S1 means losing the z coordinate of the interaction normally extracted from the time delay of the S1 and S2 signal. This prevents us from applying position-dependent corrections, like the electron lifetime correction discussed in Sec. 2.3, with the net effect of degrading the detector energy resolution and forcing us to incorporate

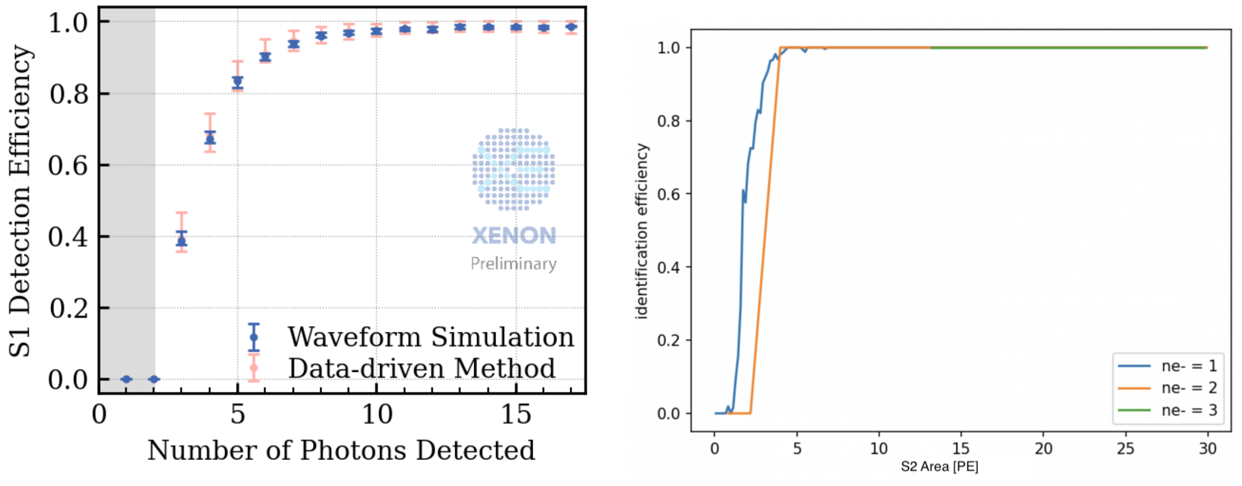

Figure 4.2: S1 and S2 detection efficiency in the unit of PE. S1 detection efficiency approaches 100% at 10 PE and S2 at 5 PE

such nuisances into the detector response models rather than correcting for them. The absence of the z coordinate also prevents defining boundaries of the fiducial volume (see Sec. 2.2) along the drift direction (while we can still fiducialize in the x-y plane). At the same time, as shown by this work, the benefits are also evident, and S2-only analyses allow us to extend the physics reach of the detector and its sensitivity to light DM.

The analysis presented in this work focuses on the lowest regime of S2 signals corresponding to ionization signals of up to five electrons extracted in the gas. Incorporating the Single Electron Gain and its standard deviations listed in Tab. 2.2, this corresponds to a region of interest in the S2 space from 10 to 174 PE[2]. To differentiate from the more traditional S2-only analyses, which typically focus on larger S2 signals and consider interactions through both NR and ER channels, this analysis is often referred to as the *few-electron analysis*. Challenges arise in this ultra-low energy regime:

---

[2] The choice of 10 PE as the lower bound, instead of 0 PE, is because the "S2s" from random pileups of lone-hits, a type of single photon response within single PMTs, dominates the region below 10PE, as shown in Fig. 4.4. The exact sources of lone-hits are still unclear, but such a population is certainly not the S2 signals of under-fluctuated single electrons. It will be clear after the discussion about statistical inferences in Sec. 4.6 that the exact value of the bounds of the few-electron analysis does not matter as long as we do not include dominant un-modeled backgrounds in our final dataset. Thus, 10 PE is a sufficiently good separation point between the pileup population and the true Single Electron S2s

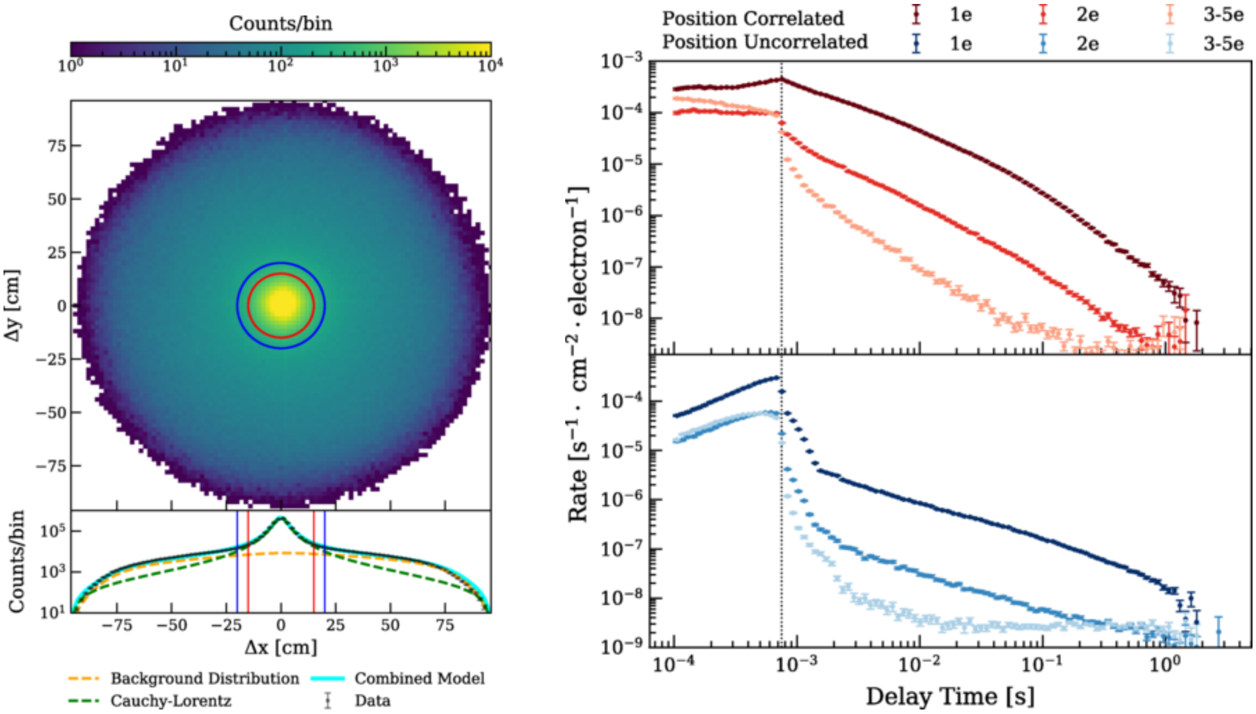

Figure 4.3: Spatial (left) and time (right) correlations between small S2s and their preceding large S2s as observed in XENON1T [52]. In the left plot, the 2D histogram shows a clear peak near $\Delta x = \Delta y = 0\ cm$, indicating a strong spatial correlation between the small S2s and their preceding large S2s. Such correlation is straightforwardly shown in a direct comparison between the spatial difference distribution of purely random pairing between small S2s and large S2s (the orange dashed line in the bottom panel) and the distribution from data (black dots with errorbars, with two fittings from assumed functions in yellow and green). The small S2s within a position-correlated radius, indicated with the red circle, are considered position-correlated DEs, and the ones outside the blue circle are the position-uncorrelated small S2s. In the right plot, time delayed from preceding large S2s of both the position-correlated DEs and uncorrelated small S2s of sizes 1 to 3 e^-'s are plotted. The gray vertical line indicates the one full drift time in XENON1T. While the rates of the position-correlated DEs (red dots at the top) exhibit strong decreasing trends as the time delay from the preceding large S2s increases, the rates of the position-uncorrelated small S2s (blue dots at the bottom) are relatively constant. (While there is a decreasing trend in the blue dots, due to the log-scale of the y-axis, the dependence of the rates of delay time from preceding Primary S2s is much weaker for the position-uncorrelated small S2s compared to the position-correlated DEs).

- The existence of a substantial instrumental background. As depicted in Fig. 4.3, it has been observed [52] that, after large S2 signals, there is a train of much smaller S2 signals that are spatially correlated with it, i.e., the primary large S2 signal and the following small S2 signals have a similar (x, y). These spatially correlated small S2 signals can last for seconds after large S2 signals and are generally small ($< 10\ e^-$), ending up in the ROI for this search. The rate of these secondary S2s is strongly related to the arrival time of the primary large S2 signal and its amplitude. The larger the primary S2, the higher the rate of small S2s. The larger the delay with respect to the primary S2, the smaller the rate of small S2s. This indicates that such delayed small S2s are an artifact produced by the first primary S2 and do not correspond to independent low-energy depositions. This component is hereafter referred to as Delayed Electrons (DE), and we will present in Sec. 4.1 known origins for these electrons. Therefore, to analyze the smallest S2s in our detector, such a small S2 population needs to be properly removed or accurately modeled as a background;

- The limitations of the S1-S2 signal classification. The reconstruction algorithms developed to identify the S1 and S2 peaks in the waveforms were not optimized for ultra-small S2 signals. The standard peak classification has three categories: "S1", "S2", and "unidentified". The identification of S1 and S2 signals, examples of which are shown in Fig. 2.8 is performed based on the time profile of the light signals (see Sec. 2.2.1, Sec.2.2.2, Sec.2.2.3), with the S1 peaks being typically narrow and spiked while S2 peaks being broader and relatively flat [70, 85]. Reconstructed peaks not matching the above criterion, one example of which is shown in Fig. 2.8 at the bottom, are labeled as "unidentified". While performing well enough for S1-S2 analysis, this classification strategy is based solely on the characteristics of individual waveforms and doesn't consider correlation amongst adjacent peaks. To properly characterize the spatial and time correlations mentioned in the first point, a systematic infrastructure for defining such correlations needs to be built over the traditional classification;

- The requirement of precise modeling of the shape of S2 signals in the detector. As discussed extensively in Ch. 3, when analyzing waveforms, a merging step is implemented to combine nearby "peaklets"[3] and form peaks that we call S2s. Such a merging step was tuned and optimized for the traditional S1-S2 studies in which the size of S2 signals is large and far from the discrete regime, and it was designed to ensure minimal under-merging in those energy regions. But, as explained in Sec. 3.2.1, this leads to some over-merging, i.e., we cannot distinguish a 2 e^- peak from a wrongly constructed peak of two independent single e^- peaks. Such an effect can be modeled with the results of the independent study of the diffusion of the electron cloud in liquid and its impact on S2 signal shape, as discussed in Ch. 3.

In the scope of the few-electron study, since we are differentiating the so-called "large S2s" and the smaller ones, the boundary between the small S2 and large S2 was set at 10 e^-. Incorporating the Single Electron Gain and its standard deviation listed in Tab. 2.2, the boundary is set at 340 PE. The reason for choosing 10 e^- as the boundary is that since we are focusing on the S2s consisting of 1 e^- to 5 e^-, to ensure that the leakages of under-fluctuated S2s consisting of larger than 5 e^- are properly accounted for into our signal models within our region of interest, we need to include S2s comprised of up to 10 e^-.

In the rest of this chapter, I will discuss the efforts to address the challenges listed above and the details of the few-electron analysis. More specifically, in Sec. 4.2, I will introduce a new peak classification infrastructure (named *subtyping*) based on time and size correlations between peaks and their nearby neighbors that expands the traditional S1-S2 classification into multiple physically motivated subcategories. In Sec. 4.3, I will introduce an algorithm that restores the number of electrons from waveforms of S2 signals in order to be used with the model of S2 signal shape developed in Sec. 3.1.3[4]. In Sec. 4.4, I will first introduce a standard set of selection criteria for S2 signals to select legit S2 signals and then a peak selection criteria designed to minimize the background. The selection criteria are developed

---

[3] A waveform that is indivisible, full definition and discussion in Sec. 3.2.1

[4] The number of electron (N) dependence in Eqn.3.14 indicates the requirement of this parameter, which is not readily available from traditional analysis framework

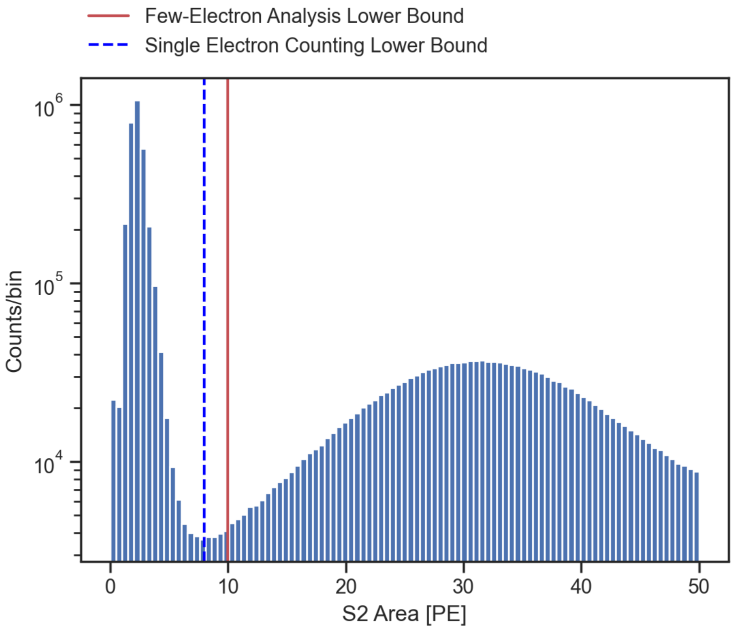

Figure 4.4: S2 area distribution of 10 TED runs without data selection. The vertical line marks the lower bound of the few-electron analysis at 10 PE. While the Single Electron population is visible on the right of the red line (centered at around 32 PE), there are two prominent populations on the left-hand side: the peak near 0 PE is the baseline fluctuation population, and the one centered at around 2 PE is pileups of lone-hits. The blue dashed line indicates the lower bound for counting 1 e^- discussed in Sec. 4.3

using the TED dataset, i.e., unblinded data acquired in conditions similar to those of the physics runs. In Sec. 4.5, a new dedicated XENONnT detector response model is used to describe the S2 signal spectra from a set of DM candidates and BSM hypothesis. Finally, in Sec. 4.6, I will perform the statistical inference on the data and, applying the Yellin Optimal Interval, present preliminary[5] constraints on three new physics channels: light Dark Matter interacting via electron scattering, Dark Photon absorption, and Axion-like Particle absorption. The results refer to the TED data, but the analysis will soon be extended to the full SR0 data, which is still blinded.

---

[5] At the time this thesis was written, we are at the final stage of the unblinding of XENONnT SR0 scientific data. These results were obtained from the TED data in an unblinded manner.

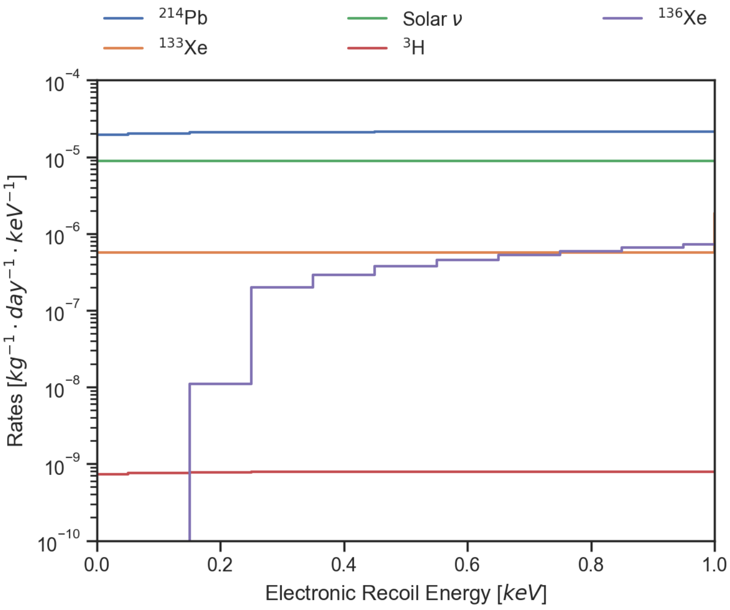

Figure 4.5: Event rates of radioactive impurities inside the detector and Solar neutrinos, as a function of ER energy.

4.1 Origin of Small S2 Signals

Two types of backgrounds affect the few-electron analysis producing S2 signal within the ROI: ultra-low energy physical interactions from radioactive contaminants and neutrinos as well as "instrumental" sources responsible for the emission spurious electrons even in absence of an actual interaction within the active volume.

The amount of radioactive contaminants within the XENONnT detector and solar neutrinos interacting with xenon orbital electrons responsible for energy deposition of more than 1 keV was precisely measured in the context of the DM searches presented in Ref. [66] and Ref. [67]. The extrapolation of those radioactive components to energies below 1 keV, as well as the signals from neutrinos, are shown in Fig. 4.5. The isotopes that contribute the most are ^{136}Xe, ^{214}Pb, ^{133}Xe and ^{3}H [67], which undergo β^{-} decays and generate the the electronic recoil.

On the other hand, due to a lack of z information, the volume cannot be fiducialized along the drift axis, causing Compton scatterings from gammas emitted near the top and the bottom of the detector not to be removed. Besides, the small S2s from interactions through the NR channel, i.e., from neutrons or neutrinos (through CEνNS [96, 97]), cannot be distinguished from the small S2s from interactions in the ER channel since, in the absence of S1s, there is no way to discriminate NR and ER.

Furthermore, there was mention of the lights generated when the positively charged ions (Xe^+, Xe_2^+) reach the cathode, mimicking S2 signals [98]. Efforts were made to search for such a signal in the XENONnT detector. However, due to its slow drifting speed (because the ions are much heavier than the electrons), the time correlation between such a signal and the S1 and S2 generated from the same energy deposition is too blurry to be spotted, and we didn't find direct evidence of such signal. Nevertheless, I document it here as a potential contamination source, acknowledging that we know very little about such a source.

In addition to the physical low-energy depositions mentioned above, various instrumental effects can produce spurious electrons generating small S2 signals.

The first one is called the Fowler-Nordheim electron emission or field electron emission [99, 100] from metal surfaces. While this emission would happen both on the wires and on the grid frames, the dangerous emitted electrons are those that can be emitted inside the active volume and, hence, those from the wires. The electron emission rate depends on the electric field value around the wire [101]. In XENONnT, the radius of the cathode wire is $\sim 150\ \mu m$, and the radius of the gate wire is $\sim 100\ \mu s$. With nominal field strength around the wires to be $\sim 200\ kV/cm$ for the cathode and $\sim 60\ kV/cm$ for the gate, we expect conservatively the rate of the spurious electron emission to be less than 210 Hz as reported in Ref. [101]. Nevertheless, this rate is hard to quantify and represents a background inside our ROI that will generate single electrons not correlated in space and time with other interactions within the TPC, making them an irreducible background.

For all the above-mentioned reasons, it is extremely challenging to have a trustworthy and fully comprehensive model for the physical backgrounds. Consequently, the few-electron analysis aims to set strong constraints on theoretical models in the form of upper limits. Similar conclusions are true also for the instrumental background that we will describe below. However, for some of its components, i.e., delayed electrons, we were able to develop data selection criteria leveraging their spatial and time correlation with neighbor interactions that allowed us to improve the signal-to-background and enhance the physics reach of this search.

A second broad category of instrumental background dominates over all other components due to long trains of small S2s produced right after a preceding large S1 or S2 signal. These small S2s, often referred as *delayed electrons* presents the following features:

- their rate is maximum immediately after a preceding large signal and starts to drop after one full drift time, which is the time needed by electrons produced at the cathode to reach the liquid/gas interface.
- after one full drift time, the rate continues to drop but with a much longer decay time, and small S2s can extend up to seconds after the preceding large S2s.
- a large fraction of these delayed electrons presents an x-y position that is compatible with that of the preceding large S2.

These features were observed in the XENON1T single electron population, as depicted in Fig. 4.3. Numerous studies on the nature of these single-to-a-few electron background were conducted, both in large experiments (XENON [93, 52], LZ [102], DarkSide [39] and PandaX [103]) and in small local labs (Ref. [104, 105, 88, 89]). Several explanations with convincing evidence were proposed:

- when a large S1 and S2 occurs, it can induce, at some level, photoionization. When large S1 or S2 photons travel inside the detector, they can hit surfaces (i.e., metal wires) or electronegative impurities in the LXe and induce single electron emissions. The emitted electrons are then drifted by the electric field towards the liquid/gas interface, generating small S2s. Since the time required for the photon to hit the electrode or electronegative impurities (in the order of ns) is negligible compared to the full drift time (in the order of μs to ms), the bulk of the electrons from photoionization are observed within one full drift time from the preceding large signals. The rate of emission is moderate; otherwise, the detector would not operate correctly, but it is still not negligible for the single electron analysis. Also, small S2s can produce photoionization, but the smaller the number of photons emitted, the smaller the rate of emitted electrons. This process implies a strong time correlation with the primary larger signal but no spatial correlation;

- as shown in Ref. [88, 89] a fraction of the electrons produced during an energy deposition can remain temporarily trapped at the liquid/gas interface, leading to a delayed emission of the electrons in the gas, causing spurious small S2s even milliseconds after the original S2. Such a background is strongly related to the intensity of the extraction field, $\mathcal{E}_{ext}$, responsible for accelerating the electrons and providing them the right amount of vertical momentum to overcome the potential barrier at the interface. Given a large ensemble of electrons reaching the interface, some of them will be immediately extracted in gas, and some others will have to be re-accelerated more and more until they are emitted, leading to a longer extraction time. The extraction efficiency as a function of the $\mathcal{E}_{ext}$ value is described in Ref. [81]. At XENONnT working configuration $\mathcal{E}_{ext}$ is set at $\sim 3.9\ kV/cm$, leading to an average extraction efficiency of about ~ 0.54 (Sec. 2.2.3). This process implies both a time correlation and a strong space correlation with the primary larger signal.

These two explanations are both physically well-motivated and capable of explaining a large fraction of the observed features. However, they both fail to justify the component of small S2 showing up at the few seconds scale. A promising explanation for such long delayed electrons, initially described in Ref. [88, 89], is that electrons, while drifting towards the interface, can get temporarily trapped by electronegative impurities, forming a metastable object that will release the electron at a much later time. Although the releasing mechanism is not fully understood, such a hypothesis seems strongly corroborated by my analysis of XENONnT data:

- XENONnT data indicates that the rate of small S2s beyond the photoionization regime - at time delays larger than one full drift after the primary large S2 - is strongly correlated to the length of the path length traveled by the electron cloud of the primary S2 travels (hence to the drift time of the primary S2). The left plot of Fig. 4.6 illustrates this correlation. Specifically, a higher average rate of late delayed electrons is observed for primary S2 signals with larger drift times. This, combined with the observations that such delayed electrons share the same x-y of the primary S2, strongly supports the hypothesis that they might be attached along their drift path and re-emitted at a later.

- The right plot of Fig. 4.6 shows another expected behavior: the rate of these late delayed electrons, once normalized with the primary S2 amplitude and averaged out in the full drift time, is constant and does not depend on the primary S2 amplitude. This observation corroborates the hypothesis that the drifting electrons have a constant attachment probability per unit of drift length.

Delayed electrons from photoionization, trapping at the liquid/gas surface, and impurity attachment are the dominant backgrounds to this search. The bulk of these few-electron analysis aims to characterize such background and suppress it by vetoing, in a smart way, time periods (after a large S1 or S2) and spatial region of the detector based on the primary signal position (this is not possible for primary S1). A schematic illustration showing the three components of the DE population can be found in Fig. 4.7.

In summary, the radioactive impurities, the Solar neutrino, and the field electron emission backgrounds are subdominant compared to the DEs. Thus, we focused our effort on

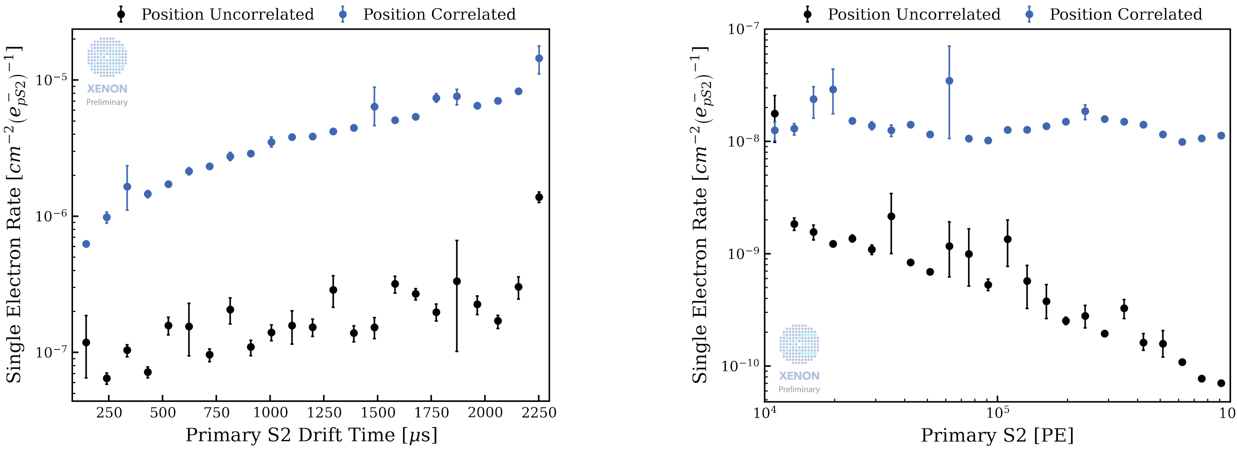

Figure 4.6: These plots were obtained with the complex procedure described later in this chapter. While it is complicated to justify the units without having presented the full treatment, we reported them here to share the main outcomes. The vertical axis of both plots is normalized to the total electron count of the corresponding primary S2s (e^-_{pS2s}) and per unit of surface (this will be more clear later). Since the rates depend on the time delay from the primary S2, we selected small S2 within a fixed window from three full drift times to 10 s to ensure to select the late delayed electrons (i.e. no photoionization). The small S2s are split into two groups, *position uncorrelated* and *position correlated*, according to the relative distance between their x-y and the x-y of the primary large S2. *Left:* positioned correlated small S2s have a much higher rate, and their rate increases with the drift time of the primary S2, i.e., with the path traveled by the ionization cloud of the primary interaction *Right:* the rate of position-correlated small S2s is independent of the size of S2 (which is not the case in the position-uncorrelated population.)

effective removal strategies for this DE background. The field electron emission background is hard to quantify once the detector is built, and the impact, although estimated to be minimal, remained unknown to us. Therefore, the few-electron analysis does not have a full background model and thus is only capable of setting an upper limit on BSM models.

4.2 Data Analysis Framework: Peak Subtyping

Limited by the electron drift velocity in liquid xenon, the corresponding S2 after an S1 should be observed within the maximum drift time allowed by the TPC depth (namely, the

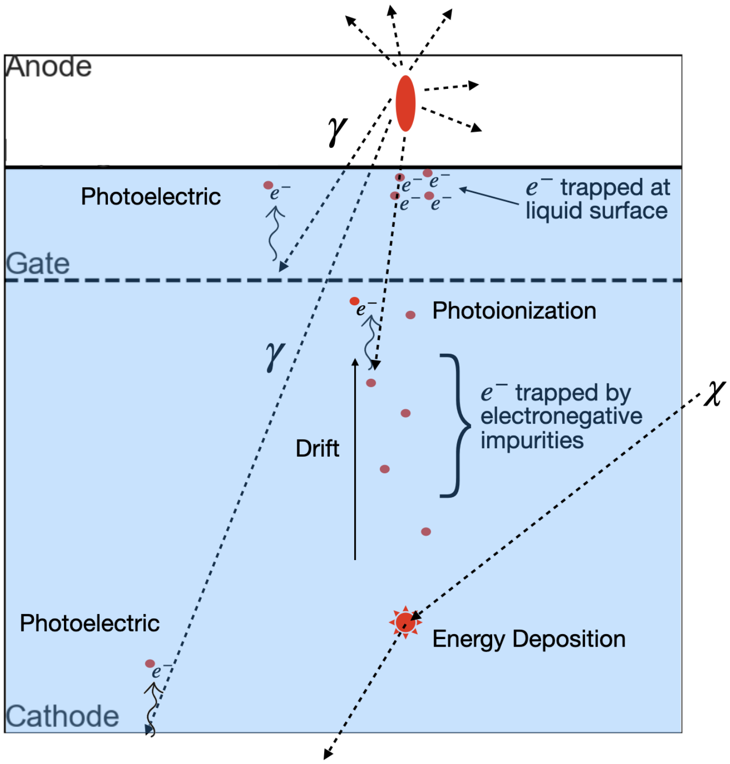

Figure 4.7: Illustration of the photoionization/photoelectric effect following an S2, the delayed release of electrons trapped at the liquid-gas interface, and the hypothetical spontaneous release of electrons trapped by electronegative impurities.

full drift time). Therefore, from each S1, all S2s within 1.2 full drift time[6] afterward are scanned, with the largest S2 above 10 e^- registered as the primary S2 (pS2), which means it is regarded as the corresponding S2s from the same energy deposition as the S1. Notice that only the large S2s are recognized as pS2s. If there are some small S2s within one full drift time from an S1, they are not classified as pS2s as they are regarded as incapable of creating DE trains[7]. Suppose such pS2 exists for the S1, motivated by the well-known photoelectric

---

[6] Using 1.2 instead of exactly one full drift time is to allow uncertainties in drifting velocity and event reconstructions. First, the drifting field is inevitably non-uniform, especially near the edge of the TPC, rendering a different drifting velocity of the electron cloud and, thus, a different time required for an electron to drift from the bottom of the TPC. Second, as discussed in Sec. 2.2, the definition of "drift time" has an ambiguity with respect to the definition of observation time of S1 and S2. As a reminder, in this thesis, the drift time is defined to be the time difference between the beginning time of a pair of S1 and S2

[7] This practice effectively ignores the correct S1-S2 pairing if the S2 is below 10 e^-. However, this is not a concern in the few-electron analysis, as the S2s of this size are regarded as not capable of generating

and photoionization process introduced in Sec. 4.1, the scan window is extended to 2.4 full drift times after this pS2 (same reason for not using exactly two full drift time). All S2s between the initial S1 and the end of the scan window are sorted as follows:

- If the S2 is smaller than either half the size of the pS2 or 10 e^-:
    - If the S2 is before the pS2, it is classified as photoionization induced by S1, namely S1PH;
    - If the S2 is after the pS2, it is classified as induced by S2, namely S2PH;
- If the S2 is larger than both half the size of the pS2 and 10 e^-:
    - If the S2 is before the pS2, it is classified as other large S2 after an S1, namely S1olS2;
    - If the S2 is after the pS2, it is classified as other large S2 after an S1, namely S2olS2.

If no pS2 is identified for an S1, all S2s after such an S1 and within one full drift time will be classified as S1PH, and such an S1 will be labeled as a lone S1, that is, a loneS1.

This step iterates through all S1s, which means if two S1s coincide, the latter might overwrite the classification of the first. I enforced that pS2s will not be rewritten as S1(S2)olS2. Another nuance is that small S2s have a non-negligible chance of being misclassified as S1s. To bookkeep this fact and enable further studies, loneS1s smaller than half the Single Electron Gain (31.9 PE) are labeled as small loneS1s, namely sloneS1s. And their associated S1PHs are relabeled slS1PHs accordingly.

After exhausting all S1s and their associated S2s, all that is left are S1-less S2s that could originate from several sources: 1. the S2 is from an energy deposition event, but the S1 is too weak and not detected; 2. the energy deposition happened too close to the gate or even

---

delayed electron tails shown in Fig. 4.3 and thus will not contaminate the population of our interest above the gate, that the S1 and S2 are too closed in time and merged; 3. the S2 is from some electron emissions, like electrode emission or DEs, and not from energy depositions; 4. some other edge cases where S1s are lost with some preceding S2s, or misclassified as S2s [67]. All these S2s are sorted as follows:

1. Starting from the first unsorted S2:
    - If it is an small S2 (smaller than 10 e^{-}), motivated by the misclassification of S1s, establish a scan window of 1.2 full drift time;
        - If there is a pS2 spotted within the window ($> 10\ e^{-}$), label this small S2 fake S2, as if it is an S1 but misidentified as an S2. Then repeat the operation for the S1-pS2 pair, with the exception that now the S1olS2 and S1PH are named fakeS2olS2 and fakeS2PH;
        - If there is no pS2 spotted, label this small S2 as sS2;
    - If it is an large S2 (larger than 10 e^{-}), label it as a lonepS2:
        - Scan 2 full drift time after it, and label all S2s smaller than half the size of this lonepS2 or 10 e^{-} S2PHs, all S2s larger than both half the size of this lonepS2 and 10 e^{-} S2olS2s;
2. Jump to the next unsorted S2 and start again;

The above iteration should exhaust all remaining S2s. As a summary, all subtyping nomenclatures and their corresponding codes are shown in Tab. 4.1. While all subtypings are physically motivated and worth extensive exploration, in the scope of the few-electron analysis, we focused on the small S2s that are sufficiently separated from any preceding large S2s (sS2, index 21). In order to model the Delayed Electron population mentioned in the introduction and shown in Fig. 4.3, we considered all primary S2s (pS2, index 22, and lonepS2, index 25) to study their correlations with the sS2 population. In the rest of the chapter, I will refer to all primary S2s with index 22 or 25 as "pS2" and all small S2s with index 21 as "sS2". Notice that the photoionization electrons mentioned in Sec. 4.1 are effectively vetoed by excluding the S1PH and S2PH populations, as we used the conservative two full drift time window to incorporate the iterative behavior of the photoionization process.

4.3 Retrieving The Number of Electrons From Waveforms

The parameter r_{50p}, or more usually called the S2 width, and its relation with the drift time of an S2 is usually used to separate S2s generated in the drifting region from S2s constructed from pileups of noises[8]. As extensively discussed in Sec. 3.1.3 and shown in Fig. 3.10, the S2 width has a nontrivial dependence on the number of electrons (N) inside the electron cloud of an S2 signal. Such a number is not directly observable inside a TPC, as the secondary scintillation process turns each extracted electron into a train of photons, and waveforms of S2 signals are recorded in the form of voltage drops (discussed in Sec. 2.2.3) and expressed in the unit of PE/ns. To use the models derived in Ch. 3, we need to reconstruct the number of electrons from S2 waveforms.

The method of retrieving the number of electrons from S2 waveforms involves two steps: the quantization of the original S2 waveform, which means breaking the waveform into pieces and counting single electron contributions, which turns each piece of the original waveform into the number of electrons. The quantization step follows an intuitive waveform breaking-up idea:

1. The waveform is smoothened with a moving average window of length 2 μs,[9] as shown in Fig. 4.8 As explained above, each electron is converted into a train of photons

---

[8] More often, the relation between the S2 width and the drift time is used to choose the good S1-S2 pairs from accidental coincidences [67, 66]. The inverse of such a relation can also be used to infer the z-position of an event [106]. However, as illustrated in Fig. 3.10, such inverse-relation is not usable for the S2s consisting of a small number of electrons

[9] The moving average is equivalent to a low-pass filter. The 2 μs window length was chosen to be closer to the average full duration of the S2s of a single electron, as shown in Fig. 3.5

Subtypes	Codes	Descriptions
Unidentified	0	Unidentified peaks
S1	11	S1s with pS2s identified
loneS1	12	S1s without pS2s identified and with a size > 0.5 SEG
sloneS1	13	S1s without pS2s identified and with a size < 0.5 SEG
sS2	21	sS2s that are not within 2 full drift time after or 1.2 full drift time before a large S2
pS2	22	large S2s identified after an S1 or a fakeS2
lonepS2	25	large S2s without an identified preceding S1 and a fakeS2, and not identified as olS2s
S1olS2	261	large S2s between S1 and pS2, with area larger than half the area of the pS2
S2olS2	262	large S2s within 2 full drift time after a pS2 or a lonepS2, with area larger than half the areas of the pS2
S1PH^1	271	S2s between S1 and pS2 that are either sS2s or large S2s smaller than half the size of the pS2
S1PH^2	271	sS2s within 1.2 full drift time after loneS1
S2PH	272	S2s within 2 full drift time after a pS2 or a lonepS2 that are either sS2s or large S2s smaller than half the size of the pS2
slS1PH	273	S1PH after a sloneS1
fakeS2	28	sS2s with a large S2 spotted within 1.2 full drift time
fakeS2olS2	29	S1olS2 but between a fakeS2 and a pS2
fakeS2PH	20	S1PH but between a fakeS2 and a pS2

Table 4.1: Summary of subtypes. The missing indices, 23 and 24, were historical subtypes not used for scientific purposes.

through the secondary scintillation process. Thus, the waveform of its S2 signal is spiky. This smoothening step is to avoid the valleys between individual photons to cause over-breaking of the waveform;

2. Whenever the smoothened waveform passes through a chosen threshold, the timestamp is marked as either the "returning to baseline" point or the "leaving baseline" point. These points, as the names indicate, mark the beginnings or ends of subsets of the waveform[10], shown as the red dashed vertical lines in Fig. 4.8. The threshold was set at 0.0001 PE/ns as it was tested to be low enough that the smoothened waveform properly returns to the baseline below this value, and it is not too low that minor fluctuations in the baseline can cross it

After the quantization step, within each subset of the waveforms, the counting step is simply taking the area[11] and dividing it by the Single Electron Gain. To better account for the under-fluctuations of the S2s of single electrons, one electron is counted towards an S2 if the area of a subset is larger than 8 PE.[12] An example result of the quantization and counting of a waveform is shown in Fig. 4.9, in which 5 e^-'s are reconstructed from an S2 waveform.

4.3.1 Quantifying The Biases In The Reconstructed Number of Electrons

The reconstruction algorithm described above provides a new parameter space called the reconstructed number of electrons, denoted $N_{e,rec}$. This parameter is inherently different

---

[10] It is worth mentioning that because of the way that the waveforms are stored, the beginning of a waveform always starts above the baseline and thus is never registered as a "leaving baseline" point by this algorithm. However, because of extra placeholders at the end of the waveforms, the end of each waveform is always registered as a "return to baseline" point. Thus, starting from the beginning of the waveform, the first marked timestep would be a "returning to baseline" point, and the waveform piece between the beginning and this first marker will be regarded as the first subset of this waveform. Then, the waveform piece between the second and the third marker will be regarded as the second subset, and so on

[11] integration of the amplitude over the duration

[12] As shown in Fig. 4.4 in the introduction, the boundary between the lone-hit pileups and the S2s of single electrons is at 8 PE

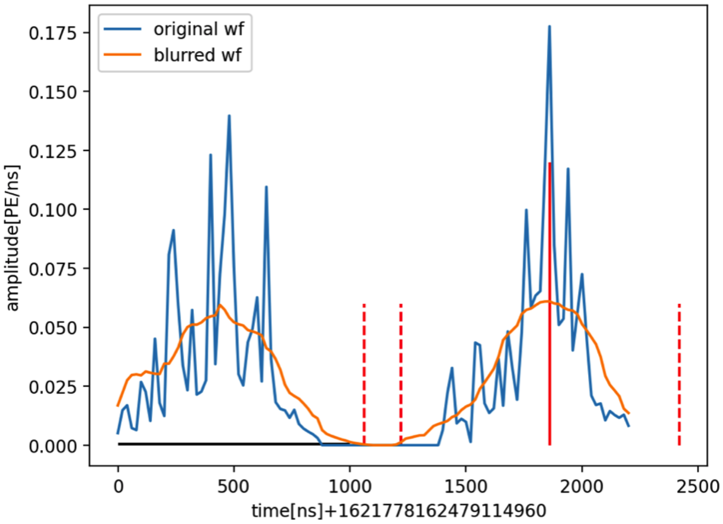

Figure 4.8: An example of the steps of quantizing an S2 waveform. The blue spiky waveform is the original waveform of the S2 signal, and the orange one is after smoothening. The red vertical lines are the "returning to" and "leaving" baseline points. The x-axis is the relative time of the waveform with respect to the beginning of itself plus the epoch time of the beginning.

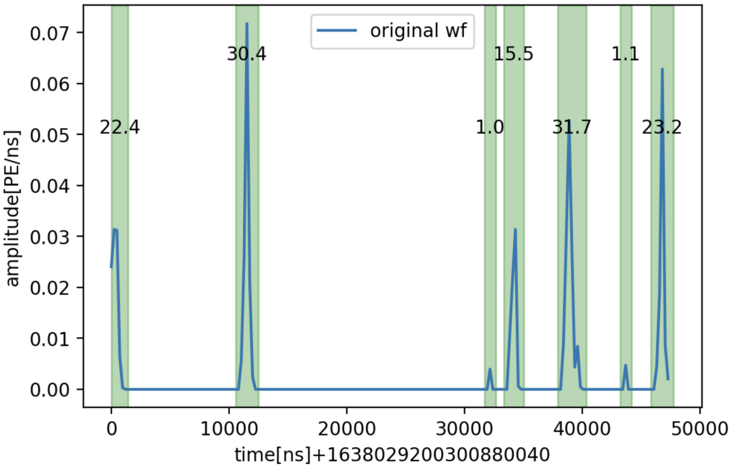

Figure 4.9: An example result of the quantization and counting of a waveform. The green shaded region marks each identified subset, and the values are the areas within. The waveform shown in this plot is assigned a total of 5 e^{-}.

from the true number of electrons of an observed S2 (denoted $N_{e,true}$ respectively):

- As shown in Fig. 3.10, at the top of the TPC, diffusion of the electron cloud is minimal, and very often, the resulted S2s are very compact in duration and do not have visible separable subsets. For such compact S2s, the quantization process does not work, and only the counting step takes effect. On the contrary, the S2s from the bottom of the TPC tend to be more diffused and thus will more often result in separable waveforms. Thus, the efficiency of this reconstruction algorithm is z-dependent;

- Within each subset of a waveform, due to the relatively large standard deviation of the single electron gain (Tab. 2.2), we cannot tell if a subset of the waveform is from two under-fluctuated e^-'s, merged, or an over-fluctuated e^-. With the method of counting step being a simple rounding (except for the lower bound of the single electron at 8 PE), such misclassification needs to be properly quantified;

- In some edge cases, the waveform of a single electron can be slightly gapped, resulting in a false counting of extra subsets of its waveform. Depending on the exact values of the area within each subset, the $N_{e,rec}$ can be 0, 1, 2, or larger.

Here, I take the S2s from two electrons, i.e., $N_{e,true} = 2$, as an example to discuss all possible scenarios qualitatively. We can start the discussion in segments of the S2 area (of the sum of the two electrons):

- if both e^-'s under-fluctuate and the S2 area is less than 8 PE, i.e., the sum of the photoelectrons from the two electrons is less than 8 PE, it will be identified as 0 e^-, i.e., $N_{e,rec} = 0$, no matter the waveform is merged or has visible separation;

- if the total area is in [8,16) PE:
  - if the waveforms of the two electrons are visibly separated, and their individual subset of waveforms have further separations, the areas of all subsets might fall below the 8 PE threshold, resulting in $N_{e,rec} = 0$;
  - however, as long as one subset has an area larger than 8 PE, $N_{e,rec} = 1$;
  - if the waveforms of the two electrons are merged, $N_{e,rec} = 1$;

- if the total area is in [16,24) PE, similar to the cases above:
  - if the waveforms of the two electrons are merged, $N_{e,rec} = 1$;
  - if the waveform is separated into more than two subsets, there is a probability of all subsets falling below 8 PE, rendering an $N_{e,rec} = 0$; at the same time, there is also a probability of having exactly one subset above 8 PE and all the rest below it, rendering an $N_{e,rec} = 1$;
  - different from the case above, now there can be two subsets above the 8 PE threshold, yielding an $N_{e,rec} = 2$ for the S2;
- if the total area is in [24,32) PE: besides the scenarios discussed above that can happen for the S2s in this area range, there can be a maximum of three subsets above the 8 PE threshold and an $N_{e,rec} = 3$;
- $\cdots$

As a summary, qualitatively, for an S2 with area A, there can be at most floor($A/8$) reconstructed number of electrons, and conceptually at a minimum of 0.

To quantitatively measure the reconstruction biases also involving the diffusion of the drifting process, we can use the same simulation procedure discussed in Sec. 3.1.3 to generate z (drift time)-dependent S2 waveforms with fixed numbers of electrons, i.e., with fixed $N_{e,true}$. Then we can apply the reconstruction algorithm to the simulated waveforms[13] and analyze the results. Two example simulated waveforms of $N_{e,true} = 3$ are shown in Fig. 3.12, and as predicted above, in the plot on the left, the waveforms of two electrons are merged and inseparable, while the third is visibly separated. On the other hand, in the plot on the right, all three electrons are reasonably separated and properly reconstructed. Again, using $N_{e,true} = 2$ population as an example, Fig. 4.10 shows the reconstruction results in four

---

[13] The red dashed lines in Fig. 3.12 are exactly obtained with this reconstruction algorithm

slices of the full drift time (0 to 2300 μs), expressed in the frequencies of getting different $N_{e,rec}$'s[14]. The results match the expectation from the qualitative analysis above: at the top of the TPC (top left), due to a minimal diffusion process, lots of the S2 waveforms are compact, resulting in a relatively high rate of misclassified $N_{e,rec} = 1$ for the under-fluctuated S2s; on the contrary, at the bottom of the TPC (bottom right), benefitted from the diffusion process, the waveforms of the two individual electrons are more likely to be separated, and the quantization process functioned well in this situation, rendering a much lower misclassified $N_{e,rec} = 1$ rate. However, the longer diffusion process and the more separated waveforms do not benefit the misclassification rates for the over-fluctuated S2s, as the $N_{e,rec} > 2$ rates (yellow histograms) are relatively constant throughout the TPC.

In the scope of the few-electron analysis (or, in general, the S2-only analysis), we don't have the drift time information for the S2s. Therefore, the best we can do is use an average reconstruction bias, i.e., ignoring the drift time dependence of the reconstruction bias. The results are shown in Fig. 4.11 (and the rest, up to $N_{e,true} = 9$, are shown in Appendix. A). As will be discussed in more detail in Sec. 4.5.2, the frequencies in this figure will be turned into matrices of a tensor representation of the detector response model.

Ideally, we should use $N_{e,true}$; however, because $N_{e,true}$ is not observable, whenever we develop quantities that depend on the number of electrons, $N_{e,rec}$ is used. Such differences triggered the development of the Tensor representation for the detector response model in Sec. 4.5.2.

4.4 Data Selection And Exposure Calculation

To select a good subset of data in which we can search for interactions beyond the Standard Model (BSM), dedicated event selection criteria, more often referred to as *cuts*, were developed to distinguish interaction-induced S2s from pileups of S2s, pileups of noises that mimic

---

[14] The reconstruction results of $N_{e,true} = 1$ to 9 are summarized in the Appendix. A.

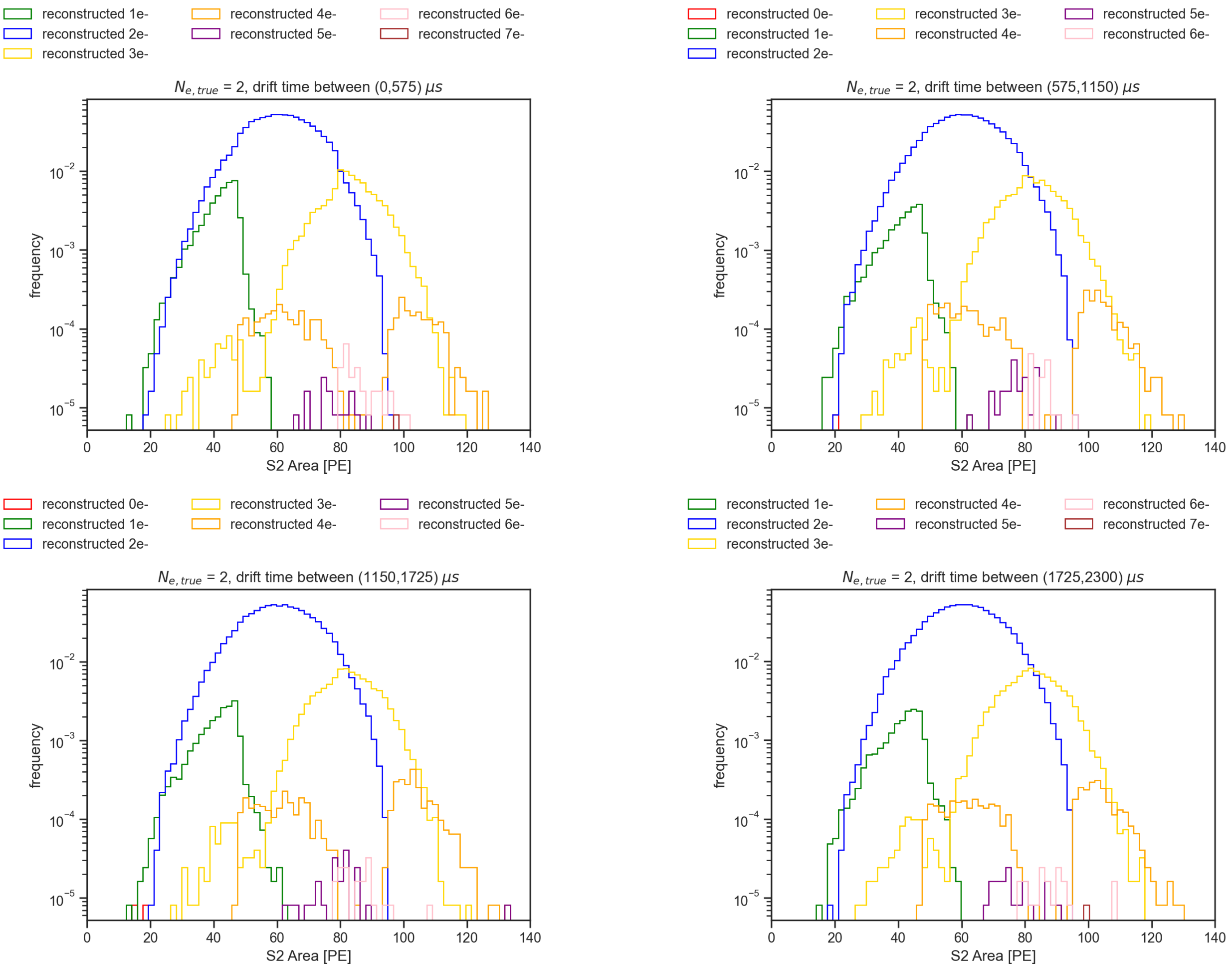

Figure 4.10: Frequencies of getting different values of $N_{e,rec}$ with S2s from a fixed $N_{etrue} = 2$, i.e., composed of exactly two electrons, generated at different depth (drift time). At the top of the TPC (top left), due to a minimal diffusion process, lots of the S2 waveforms are compact, resulting in a relatively high rate of misclassified $N_{e,rec} = 1$ for the under-fluctuated S2s. On the contrary, at the bottom of the TPC (bottom right), benefitted from the diffusion process, the waveforms of the two individual electrons are more likely to be separated, and the quantization process functioned well in this situation, rendering a much lower misclassified $N_{e,rec} = 1$ rate. However, the longer diffusion process and the more separated waveforms do not benefit the misclassification rates for the over-fluctuated S2s, as the $N_{e,rec} > 2$ rates (yellow histograms) are relatively constant throughout the TPC.

S2s, S2s contaminated by noises or misidentifications. Because of the use of the reconstruction algorithm discussed in Sec. 4.3, we have three parameter spaces that we apply cuts in the true number of electrons ($N_{e,true}$), the reconstructed number of electrons ($N_{e,rec}$), and the S2 area. The reason for having these three parameters is discussed in Sec. 4.5.2. Because

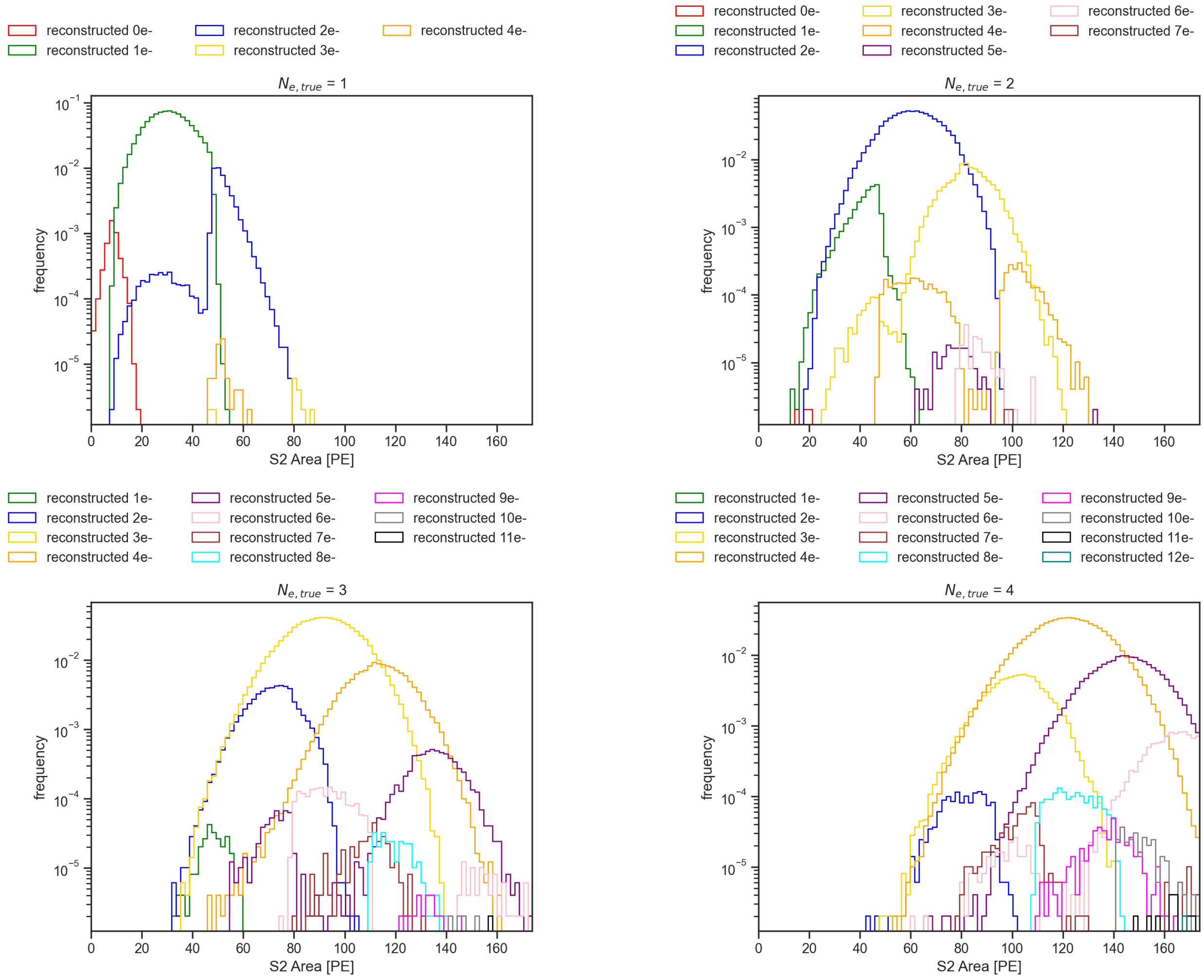

Figure 4.11: The frequencies of of getting different values of $N_{e,rec}$ with S2s from $N_{e,true} = 1$ to 4, averaging over the whole drifting region. For larger $N_{e,true}$'s, the results are summarized in Appendix. A.

of the interplay among the three parameter spaces, we need to estimate the cut acceptances, defined as the fraction of good S2 peaks accepted by the cut, for each cut with respect to its relevant parameter space.

On the other hand, the exposure is defined as the mass of liquid xenon defined by the fiducial area (A_f) and the height of the TPC (H) exposed for the total exposure time (t_{exp}).

With ρ_{LXe} the mass density of liquid xenon, the exposure can be expressed as

$$\rho_{LXe} \times A_f H \ \times t_{exp}. \tag{4.1}$$

ρ_{LXe} was measured to be 2.86 g/cm^3 during XENONnT SR0, and $L = 148.6\ cm$. The optimization of exposure is intricate for the few-electron analysis. Because we do not have a full description [15] of our background, we optimized our background-to-noise ratio by tuning the total amount of the final sS2 population, with which we set our limits on BSM interactions, and the total exposure, which determines the total amount of BSM interactions we expect to observe within our detector with a given interaction strength. The tuning between these two parameters is achieved with proper choices of R_f and t_{exp}, the latter of which is determined by summing up the exposure time after each pS2 that passed the cuts and allowed by the delay time cut thresholds (more details later in this section).

We applied cuts to both sS2 and pS2 populations. As discussed in Sec. 4.4.1, while the cuts applied to sS2s remove the sS2s directly, the ones applied to pS2s remove the pS2s, the sS2 between the removed pS2 and its next pS2, and the exposure time between the two pS2s. In this section, I will summarize all the cuts we applied in this analysis and their cut acceptances on small sS2s. Because the cuts on pS2s effectively reduce the total exposure time, we don't include the cut acceptances for them. These cuts were developed against the TED datasets. After that, I will describe the method for calculating the total exposure after applying the cuts, particularly the Delay Time Cut and the Position Correlation Cut. The application of the cut acceptances to their corresponding parameter spaces will be introduced in Sec. 4.5.2.

---

[15] As discussed in Sec. 3.2.2, it is ultimately not distinguishable between pileups of single electron noises from true multi-electron S2s. Beyond this, single electron events from physical interactions are identical to the single electron backgrounds – both are observed as single electron S2s, and it is challenging to map out all sources for such tiny signals. This is a key bottleneck of this few-electron analysis. Some efforts are discussed in Ch. 5 beyond the scope of this analysis

4.4.1 Standard Procedure for Primary-S2-related Data Selection

One key to the few-electron analysis is correctly associating sS2s and pS2s and mapping out the spatial and time correlations. To do that, sS2s and their nearest (in time) preceding pS2s need to be paired up for later studies. One intricate problem arises when cuts are applied to the pS2 population, as illustrated in Fig. 4.12, that the sS2s (DEs and S2PH) associated with the removed ones will be wrongly paired to their previous pS2s, causing them to fall into the position-uncorrelated population and leading to biases in the modeling of the spatial and time correlations. To mitigate such bias, I introduce the standard operation procedure of the cut handling:

- For each pS2 that fails the cuts:
  - all sS2s between this removed pS2 and the next pS2 are removed to avoid wrong pairings between the sS2s and the pS2s before the removed one;
  - the exposure time between this removed pS2 and the next pS2 is also removed. After removing this pS2 that fails the selection criteria and its associating sS2s, they are excluded from the model-building process for the spatial and time correlations between the sS2s and pS2s. Thus, the final established models of the correlations and the peak selection criteria derived from these models might not describe the correlation between the removed populations. Therefore, the exposure after the removed pS2 until the next pS2 that passes the selection criteria should be excluded from the analysis, the same as the sS2 population within;
- For sS2s that fail the cuts, only the sS2s themselves are removed.

4.4.2 Data Selection Criteria (Cuts)

The development of cuts on sS2 and pS2 populations follows identical procedures. However, different sets of cuts were applied to the two populations, summarized in Tab. 4.2. For

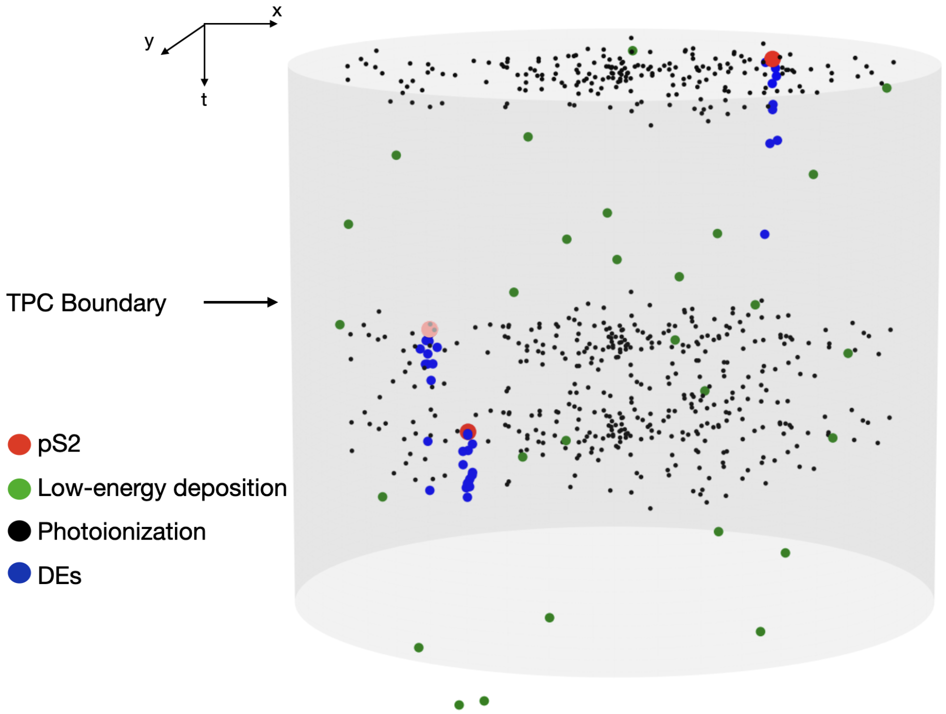

Figure 4.12: An illustration of three pS2s (red), their correlated sS2s, including photoionization/photoelectric electrons (S2PH, black) and the DEs (blue), and numerous low-energy depositions sS2s (green). As an example, if the second pS2 is removed by some peak selection criterion (the transparent red dot), its correlated DEs (the following blue dots) and S2PHs (the black dots) will be wrongly associated with the first pS2. Therefore, when removing the second pS2, its associated sS2s and S2PHs must be removed together.

sS2s, we designed stringent cuts to ensure the removal of all unphysical S2s, with proper estimation of cut acceptances to be applied to the BSM interaction spectra expectations in Sec. 4.5.3. For pS2s, a subset of cuts was applied to include as many pS2s as possible while ensuring only pS2s of good quality are included in the spatial and time correlation modeling.

Cut #1: Run Selection

We focused on the science data taken during the Science Run 0 (SR0) of XENONnT and used the data from the Tritium-Enhanced period (TED) for calibration purposes. During the TED period, the getter was bypassed, but otherwise, the detector was kept in the same condition as during the science data-taking period. There are a total of 14.31 days of TED

sS2s	S2 Region of Interest	
	Fiducial Radius	
	S2 N Contributing Channel Cut	
	After Pulse Cut	
	Position-Correlation Cut	
	Time-Correlation Cut	
	S2 Width Cut	pS2s
	S2 Area Fraction Top Cut	
	S2 Hit Pattern Cut	

Table 4.2: Summary of cuts and whether they are applied to sS2 or pS2 populations.

data and 97.09 days of science data. Because we don't have a full background model, the few-electron analysis is background-limited, which means increasing the exposure will simultaneously increase the number of background events. For this reason, we decided to unblind only part of the science runs for our search, keeping the rest blinded for future improvements. We unblinded an equal amount of the science data as the TED runs between September and December of 2021, during which the detector was at its highest purity (thus the longest electron lifetime t_e, which means more signals, especially the ones composed of single-to-a-few electrons, from the bottom of the detector will survive the drifting process and be detected). We also avoided up to three days after the anode ramp-up period [70], during which the Single Electron Gain and the extraction efficiency were not stable.

Cut #2: S2 Region of Interest

As mentioned in the introduction of this chapter, we focused on the ER channels that can create S2s between 1 e^- and 5 e^-, which corresponds to S2 areas between 10 PE and 174 PE. The 10 PE lower bound was decided to avoid the lone-hit pileups, and the 174 PE upper bound was chosen to include the 5 e^- population up to one sigma above the mean, given the standard deviation of the Single Electron Gain in Tab. 2.2.

Cut #3: Fiducial Area

Due to a lack of z information, we can only set a fiducial area defined by a fiducial radius and the full height of the TPC. We used the TED data to optimize the fiducial radius that provides the best constraints on the dark matter electron scattering cross-section. While the procedure will be discussed in Sec. 4.6, the exact value we used was 39.5 cm, significantly smaller than the radius of the TPC (66.4 cm).

Because of the lack of z information, we cannot correct peak position with respect to the known distortion in the drifting field $\mathcal{E}_d$ [70]. Without such distortion correction, the reconstructed detector geometry is skewed, and we can observe a clear contraction of the r distribution at the bottom of the TPC from the uniformly distributed $^{83\text{m}}$Kr events, as shown in Fig. 4.13. Marked as a gray vertical line in Fig. 4.13, the fiducial radius effectively includes more xenon liquid at the bottom of the detector than at the top. As estimated from the $^{83\text{m}}$Kr population, a correction factor of 1.19 was applied to the total mass of liquid xenon within the fiducial radius.

As mentioned in Sec. 2.3, high-intensity single electron bursts happened randomly in time during SR0 periods, sometimes forcing us to ramp down the anode and gate voltages. Such a population exists persistently during the data-taking period throughout the SR0 and affects a localized region in the xy plane. We excluded the high-intensity single electron bursts by removing two disks, centered at (8,-15) and (7,-16), with a radius of 10 cm. Besides, the transverse wire regions were also excluded from our fiducial area, as the single electron and extraction behaviors in those regions are drastically different from the rest of the TPC as a result of the distortion in $\mathcal{E}_{ext}$ and $\mathcal{E}_{mult}$ caused by the transverse wires. Compared to the wire regions defined for larger S2s, we excluded broader regions as the S2s of single electrons, due to their small S2 size, have a worse position-reconstruction precision [70]. The excluded regions and the final fiducial area are shown in Fig. 4.14. The total value of the fiducial area is $\sim 2768\ cm^2$, corresponding to a total liquid xenon mass of 1.4 t (with the correction

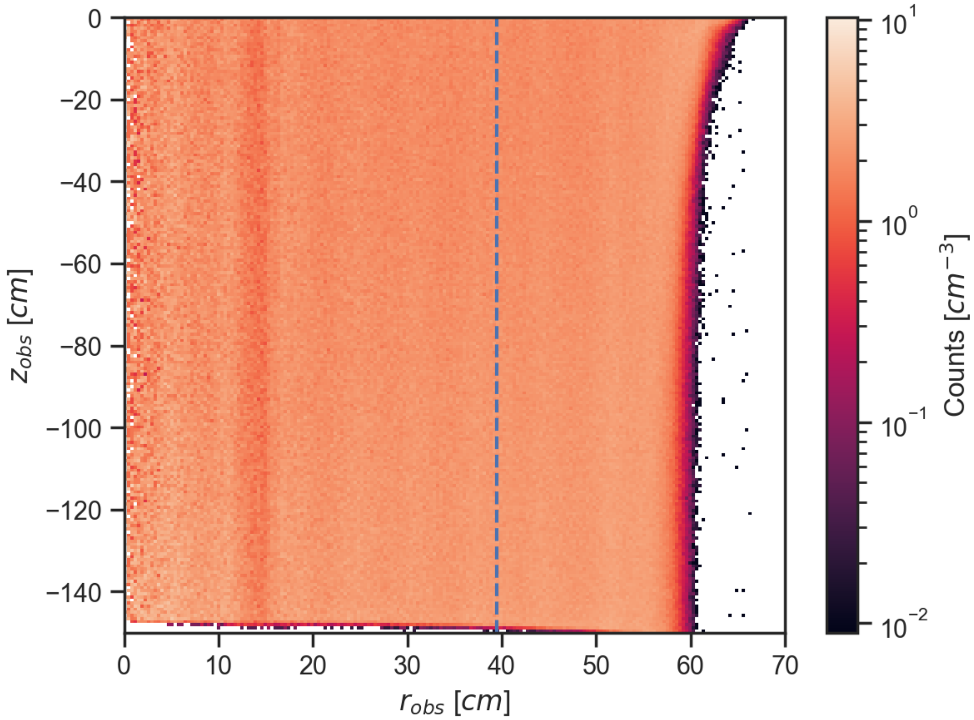

Figure 4.13: The $r - z$ distribution of $^{83\mathrm{m}}$Kr events in the TPC. The vertical dashed line marks the location of the fiducial radius. Because $^{83\mathrm{m}}$Kr is diffused inside the liquid xenon, it is assumed to be uniformly distributed, and the contraction at the bottom of the TPC results from the distortion in the drifting field. The dark band on the right-hand side marks the boundary of the TPC.

factor discussed above).

Cut #4: S2 Width

The S2 width cut aims to remove S2 signals that are wider than the maximum that the diffusion process allows. As a sanity cut, S2s with tiny widths are also removed. Because we don't have the z information, the full power of the model developed in Sec. 3.1.3 and shown in Fig. 3.10 cannot be utilized. Here, we ignore the drift time dependence of the S2 pulse shape and simulate a sufficient amount of S2 pulse shapes for each number of electrons ($N_{e,true}$) evenly sampled from the whole drift region (drift time between 0 and 2300 μs) using the model explained in Sec. 3.1.3. The top and bottom 1% of the populations are

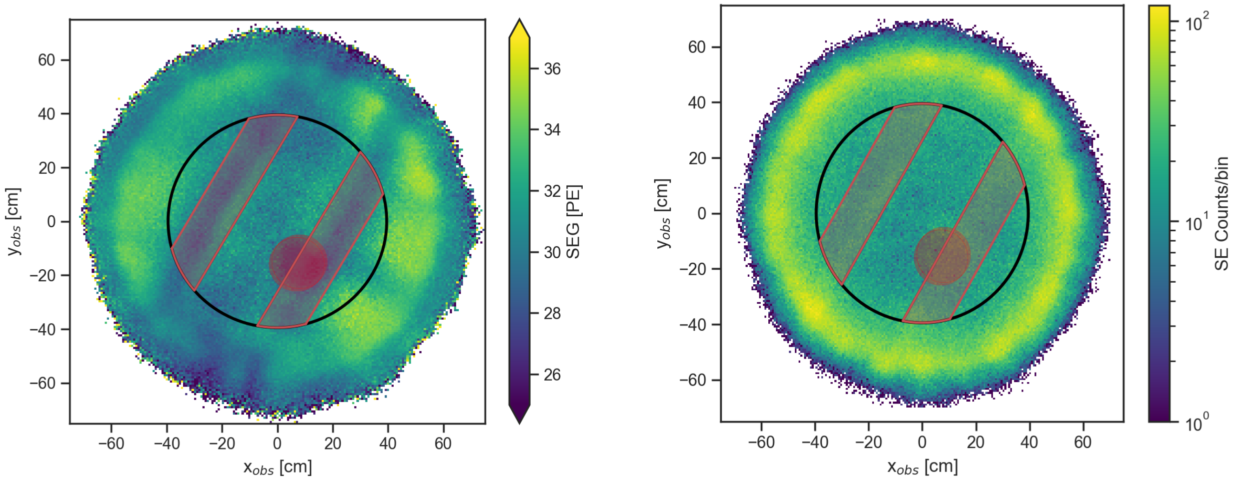

Figure 4.14: The fiducial area defined for the few-electron analysis. We excluded two transverse wire regions (the red-shaded stripes) and the high single electron intensity region (the red-shaded circles). The fiducial radius of 39.5 *cm* is indicated as the black circle. The 2D histograms on the left are the average Single Electron Gain values at a different position, and on the right is the number of single electron S2s.

excluded from our data. The simulated S2 width distribution and the designated locations of cuts for $N_{e,true} = 1$ to 4 are shown in Fig. 4.15. The distributions and cuts for $N_{e,true}$ up to 10 are summarized in Appendix. B.

Then, with the reconstruction algorithm introduced in Sec. 4.3, we can apply the cut boundaries to the real data in $N_{e,rec}$ space. The result is shown in Fig. 4.16. Since the cut is developed in each $N_{e,true}$, the cut acceptances are taken as 98% for all $N_{e,true}$ values and applied to the true number of electron parameter space. The discrepancies between $N_{e,rec}$ and $N_{e,true}$ are incorporated by the detector response mode that will be discussed in Sev. 4.5.2, based on the bias calculation in Sec. 4.3.1.

This cut is also applied to the pS2 population. We simulated and calculated the cut thresholds for up to $N_{e,true} = 99$. Because the S2 width distribution varies very little with respect to the number of electrons for large S2s, as can be told from $N = 8$ and $N = 9$ cases in Fig. 3.10, we used the cut thresholds from $N_{e,true} = 99$ for all larger S2s.

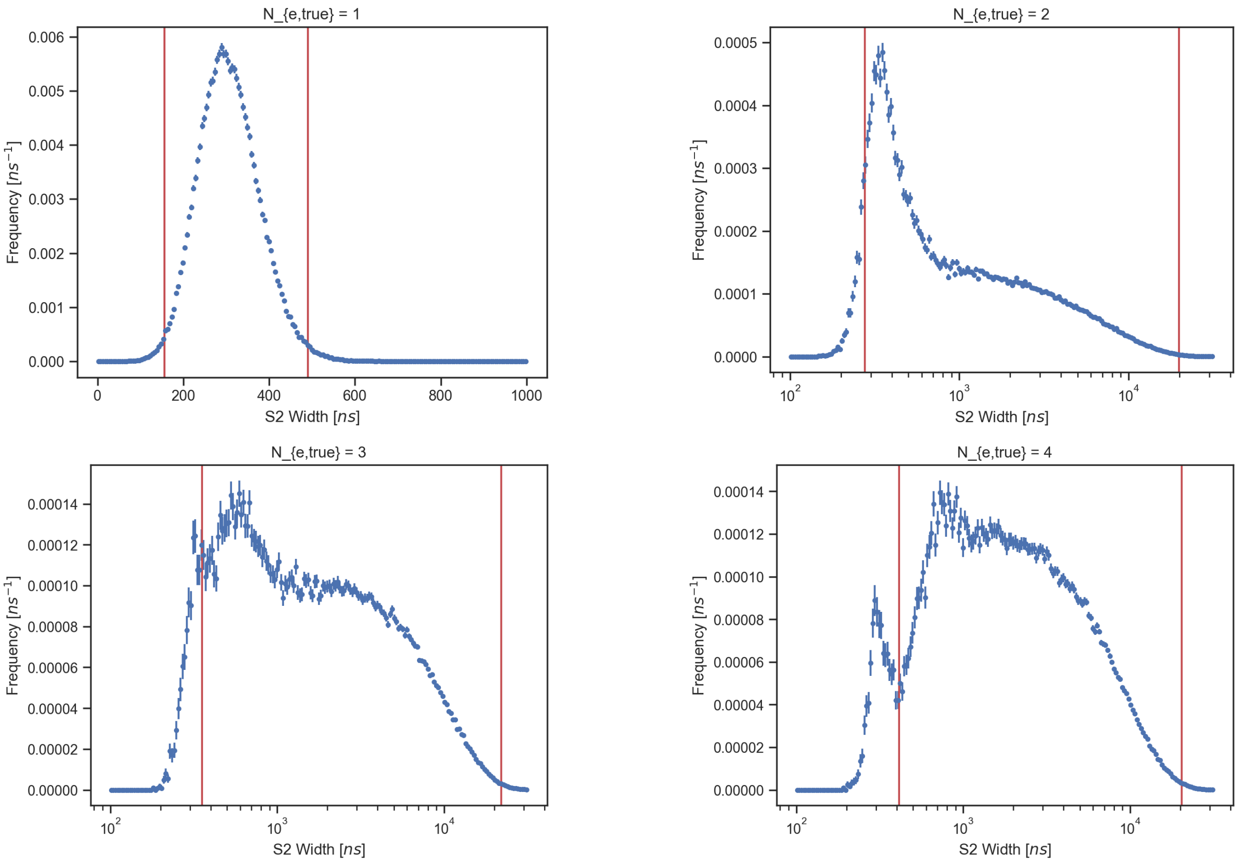

Figure 4.15: S2 width distribution of S2 signals with $N_{e,true} = 1$ to 4 and their corresponding top and bottom 1% cuts. It is worth noting that the peaks below the bottom 1% cut threshold (the red lines on the left in each plot) in $N_{e,true} = 3$ and 4 (and larger, summarized in Appendix. B) are results of a positive b value from the fitting of Eqn. 3.18 to the S2 width (r_{50p})-drift time relation, documented in Eqn. 3.19. For drift time below b, the diffusion σ is taken to be 0, and the S2 width is equivalent to that of a single electron S2.

Cut #5: S2 Area Fraction Top

The S2 area fraction top (aft) is defined as the fraction of the S2 area contribution of the top PMT arrays with respect to the total value. This parameter is important for distinguishing misclassified S1s from real S2s. Due to the proximity of the gas gap in which S2s are converted to photons, the expectation of S2 aft is significantly larger than that of the S1s, for which the photons are generated in the liquid and relatively closer to the bottom PMTs. Also, there are known top PMTs that experience higher after-pulse (more description in the After Pulse cut section) rates compared to the bottom ones [80], which can create fake S2s

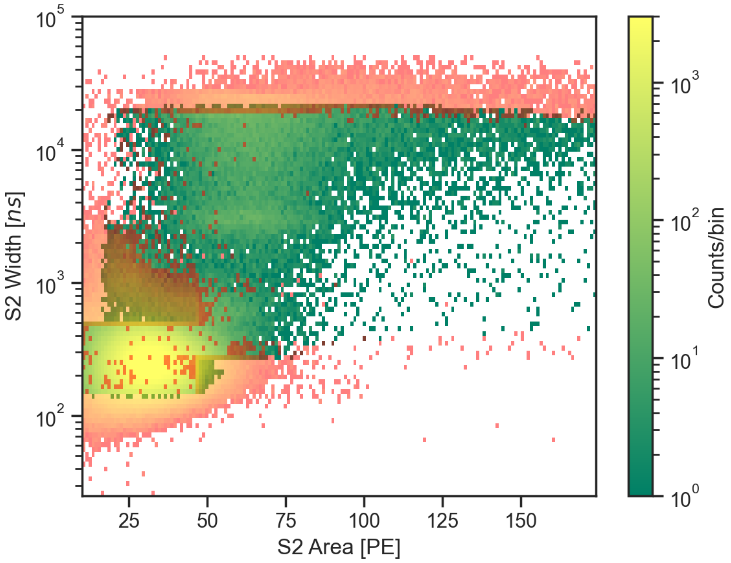

Figure 4.16: Applying the $N_{e,true}$-dependent S2 width cut on real data through $N_{e,rec}$ with no other cuts applied. The shaded red population is excluded, and the green population is the sS2s that pass the cut. 20 TED datasets are shown in this plot.

with exceptionally high S2 aft values.

Such a parameter, to the first order, can be described by a continuous binomial distribution because for each detected photon, there are only two choices: either by a top PMT or a bottom PMT. The expectation of S2 aft is estimated at 0.75 with S2s between 10^5 and 10^6 PE. This region of S2s is chosen for the estimation of S2 aft because 1. the S2s are large enough that the patterns of PMT responses are statistically stable, and 2. the S2s are not too large that the PMTs saturate and bias the estimation of the S2 aft. Then, with different values of the S2 area, the 1% and 99% thresholds are calculated with respect to the continuous binomial distribution and set as cut boundaries. These two boundaries are then used as the cut thresholds for both sS2s and pS2s.

PMTs are slightly different from each other in terms of the response to a detected photon, which induces an xy fluctuation in the real S2 aft values, as photons generated at different locations will more likely be received by the PMTs in that region. To incorporate such

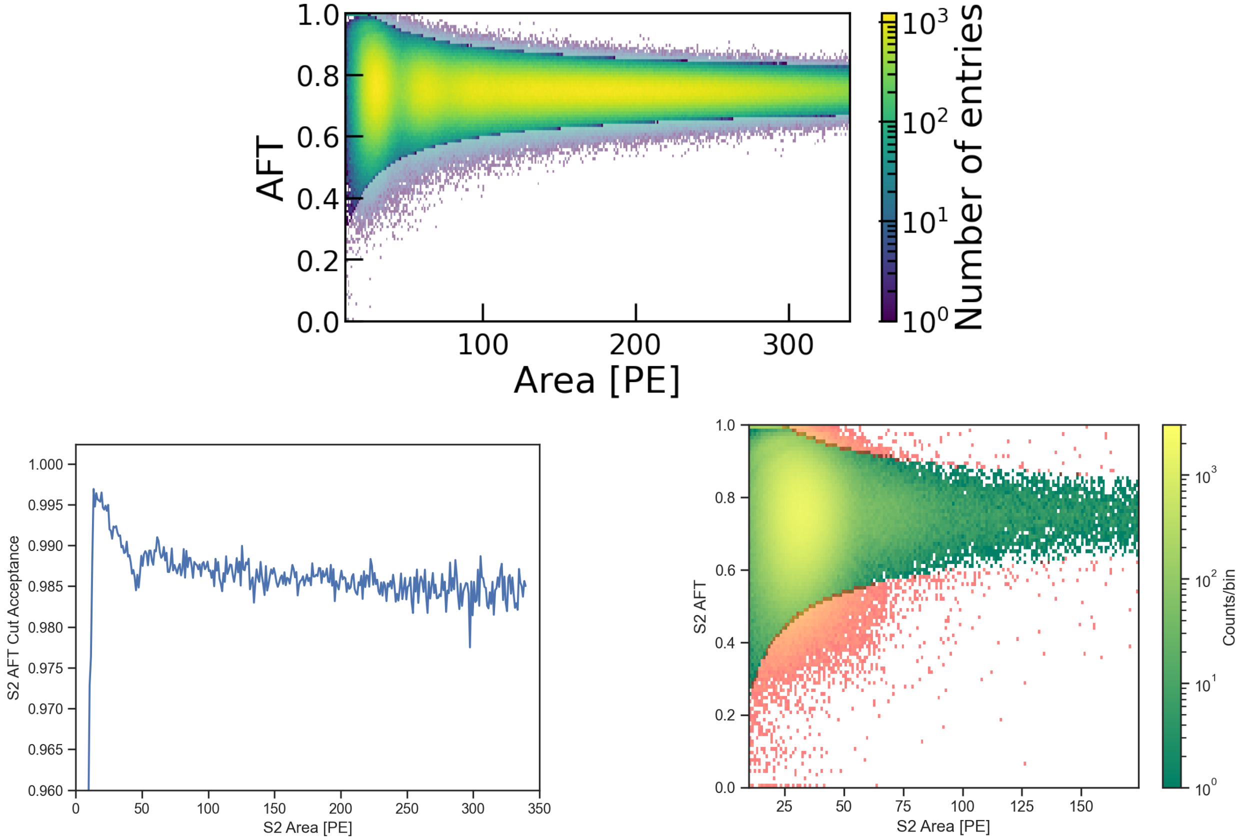

Figure 4.17: Top: simulated S2 aft vs. S2 area. The shaded regions are excluded. The plot is taken from Dr. Jacques Pienaar's study note. Bottom left: cut acceptance for S2 aft cut vs. S2 area, calculated by Dr. Jacques Pienaar. Bottom right: Applying S2 aft cut on real peaks identified as sS2, with no other cut applied. The red-shaded regions are excluded. 20 TED datasets are shown in the bottom right plot.

fluctuation, the cut acceptances are estimated with a full chain simulation program[16] [107] by computing the ratio of the simulated S2s that pass the cut in each slice of S2 area. The simulated results, the cut boundaries, and the cut acceptance as a function of the S2 area are shown in Fig. 4.17.

To emphasize, the S2 aft cut acceptance is applied to the S2 area parameter space, as it depends on the number of photons generated instead of the number of electrons inside an

---

[16] This full chain simulation program is different from, and much more complete and complicated than the detector response model discussed in Sec. 4.5. For a minimum comparison, the full chain simulation takes into consideration the propagation of each photon and calculates the probability of it hitting each individual PMT, whereas, in the detector response model, we only consider the final S2 area yield, with information like S2 aft and S2 width captured by efficiencies

S2 signal.

Cut #6: S2 Hit Pattern

Due to the proximity of the gaseous xenon layer – where the electrons are converted to photons, generating S2 signals – to the top PMT array, the responses of the **top PMT** to S2 signals exhibit distinct, localized patterns, referred to as "S2 hit patterns", as illustrated in Fig. 2.8. To differentiate between a localized S2 signal and overlapping S2 signals from various *xy* positions (pileups), we assigned a machine-learning-based, data-driven likelihood value to each S2 signal. Although a detailed discussion of the machine-learning algorithm is outside the scope of this analysis, I will provide an overview of how this parameter was developed and the criteria for its application.

One way to establish the expectation of S2 hit patterns is by utilizing the S2s of $^{83\mathrm{m}}$Kr and looking at their average behaviors. At each (x_{obs}, y_{obs}) location, we can obtain an expected fraction of light received by each top PMT by taking the average across all S2s. The result of this practice is a map that translates a spatial location to the expected response of each top PMT, denoted $f_{s2hp}(x, y)$:

$$\begin{aligned} f_{s2hp} &: \mathbb{R}^2 \to [0,1]^{252} \\ &(x, y) \mapsto \text{expected fraction of light received by each top PMT} \end{aligned} . \tag{4.2}$$

An example of the data-driven $f_{s2hp}(x, y)$ evaluated at a specific (x, y) location is shown in Fig. 4.18, along with an example of S2 hit pattern from one $^{83\mathrm{m}}$Kr S2.

Using the function $f_{s2hp}(x, y)$, we can determine the expected contribution of each top PMT to any given S2 signal observed at coordinates (x, y). Suppose a top PMT, indexed by i, contributes a fraction k_i to the area of an observed S2, while the expected fractional contribution from this PMT, based on the S2's position, is denoted as $f_{s2hp}(x, y)_i$. For simplicity, let's refer to $f_{s2hp}(x, y)_i$ as λ_i, noting that both k_i and λ_i depend on the S2's

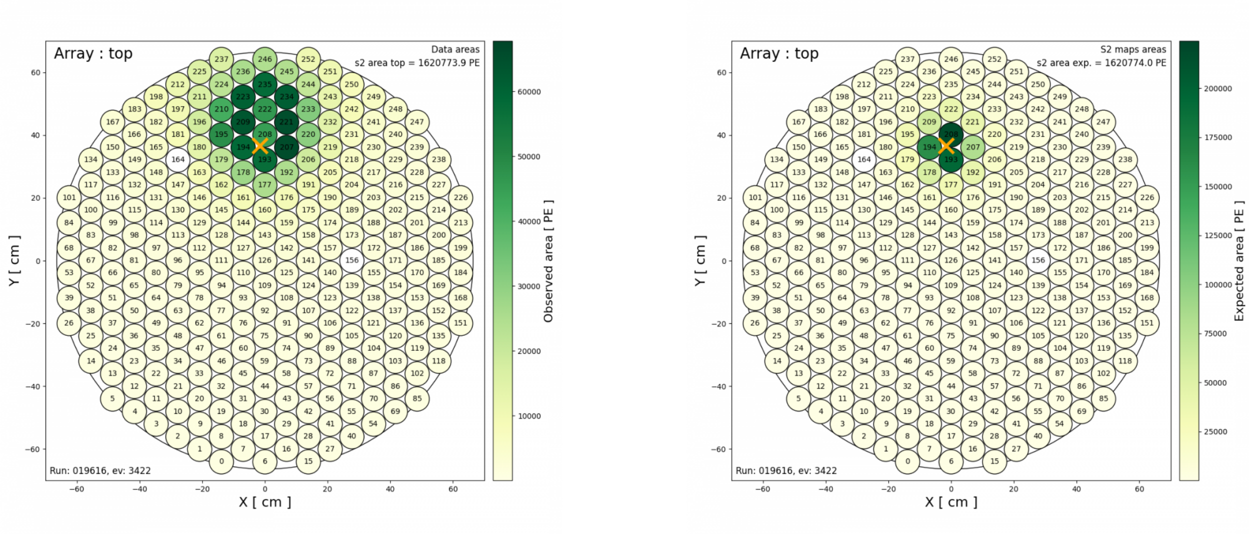

Figure 4.18: An example of S2 hit pattern from one $^{83\mathrm{m}}$Kr S2 observed at (58.80,-0.82) cm (left) and the $f_{s2hp}(x, y)$ evaluated at the same location (right), scaled to the total area of the observed $^{83\mathrm{m}}$Kr S2 on the left. $f_{s2hp}(x, y)$ was obtained by averaging a sufficient amount of $^{83\mathrm{m}}$Kr S2 hit patterns similar to the one shown at the top. The plots are from a study note by Dr.Andrii Terliuk and Dr.Giovanni Volta.

location.[17] From here, we define a log-likelihood function ($\log L$) that leverages the Poisson likelihood, adjusted by a data-driven expansion to account for variability. This expansion introduces a per-PMT width σ_i to the model,[18] facilitating a more nuanced comparison between observed and expected S2 contributions[19]:

$$\log L = \sum_{i=1}^{252} \left[[f(k_i; \lambda_i) - f(\lambda_i; \lambda_i)] \frac{\lambda_i}{g(\lambda_i; \sigma_i, \gamma_i)} - \frac{1}{2} \log(2\pi \; g(\lambda_i; \sigma_i, \gamma_i)) \right], \tag{4.3}$$

---

[17] This means that k_i and λ_i vary with position.

[18] σ_i is also influenced by the S2's position, indicating its dependency on location.

[19] Formula from a study note of Shenyang Shi, a collaborator in XENON Collaboration

where $f(k;\lambda)$ is a modified Poisson log-likelihood function, defined as

$$\begin{gathered} f(k;\lambda) = k\log(\lambda) - \log\Gamma(k+1) - \lambda \\ \Gamma(x) = \int\limits_0^\infty t^{x-1}e^{-t}dt \end{gathered}\quad, \tag{4.4}$$

and $g(\lambda;\sigma,\gamma)$ is the data-driven broadening function, defined as

$$g(\lambda;\sigma,\gamma) = 1.2\lambda + (\sigma\lambda^\gamma)^2 + 0.2. \tag{4.5}$$

In our analysis, the S2 hit patterns function $f_{s2hp}(x,y)$ is modeled by fitting the $^{83\mathrm{m}}$Kr S2 locations and their hit patterns with the Convolutional Neuron Network (CNN), instead of taking the average behaviors of $^{83\mathrm{m}}$Kr S2s.

To develop the cut, we further defined the Reduced-χ^2 with N degrees of freedom as

$$\chi^2/N = -2\log L. \tag{4.6}$$

After filtering out S2 signals affected by after-pulses[20] or those associated with distinctly separated PMT clusters[21], we isolated a subset of S2 signals from the TED dataset, presumed to be free of pileup effects. We then analyzed this subset by calculating the χ^2/N metric for each S2 signal. For different S2 area segments, we determined the points of 98% acceptance. These points were subsequently smoothed across the S2 area spectrum to establish our S2 hit pattern discrimination criterion. This cut is applied to both sS2 and pS2 populations.

Given the smoothing process, we specifically calculated the acceptance rate based on the

---

[20] The exclusion of S2 signals compromised by after-pulses involved monitoring the maximum contribution from any single PMT. After-pulses originate within the PMTs themselves; thus, an S2 signal contaminated by an after-pulse is likely to exhibit an unusually high contribution from a single PMT.

[21] We identified and removed S2 signals associated with spatially isolated PMT clusters by assessing the deviation of these clusters from the signal's "barycentre", which is determined by the weighted average position of the S2 signal.

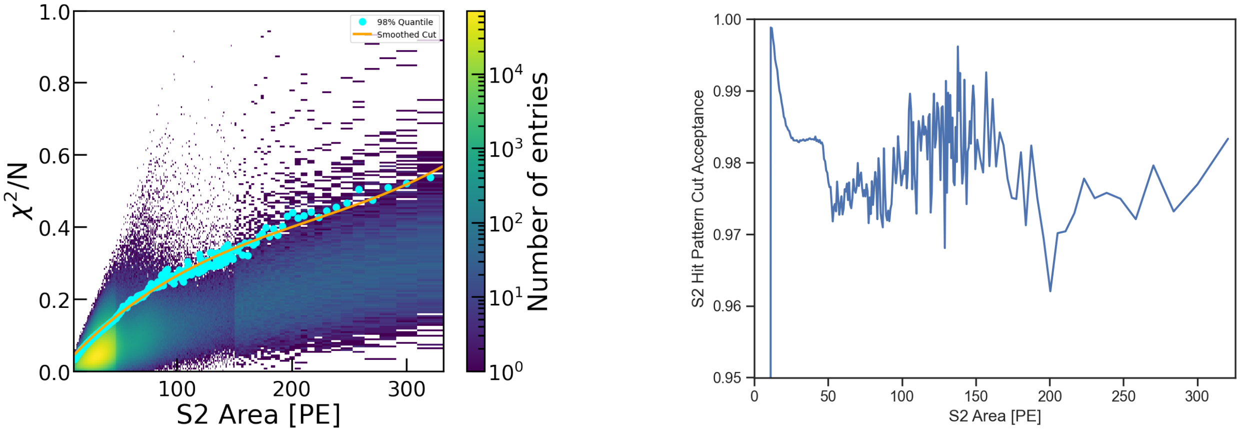

Figure 4.19: Left: Reduced-χ^2 vs. S2 area with Reduced-χ^2 calculated from the CNN generated log-likelihood function. The cyan dots are the 98% acceptance points in each slice of the S2 area, and the orange line is the smoothened S2 hit pattern cut threshold. The non-uniform binning was due to the lack of statistics at the larger S2 area region. The plot is taken from Dr. Jacques Pienaar's study note. Right: S2 hit pattern cut acceptance computed with the smoothened cut threshold. This plot is recreated based on Dr. Jacques Pienaar's study.

refined cut threshold. The relationship between χ^2/N and S2 area, alongside the defined cut thresholds, and the final acceptance rates are shown in Fig. 4.19. The final data selection result on 20 TED datasets is shown in Fig. 4.20.

To emphasize, the cut acceptance should be applied to the S2 area parameter space.

Cut #7: S2 N Contributing Channels

The S2 N Contributing Channels, as the name indicates, is defined as the number of PMTs contributing to an S2 signal. As shown in Fig. 4.21, there are two populations mixed inside the population of small S2s with large amounts of contributing PMTs, where on average each PMT contributes less than 1 PE. This cut aims to remove noises that were classified as small S2s but with an unreasonably large number of triggered PMTs.

Further checks showed that both populations are mostly sinusoidal noises similar to the one shown in Fig. 2.8 at the bottom. It was found that there is a time correlation between the occurrence of waveforms inside population 2 and data transferring from the digitizer's

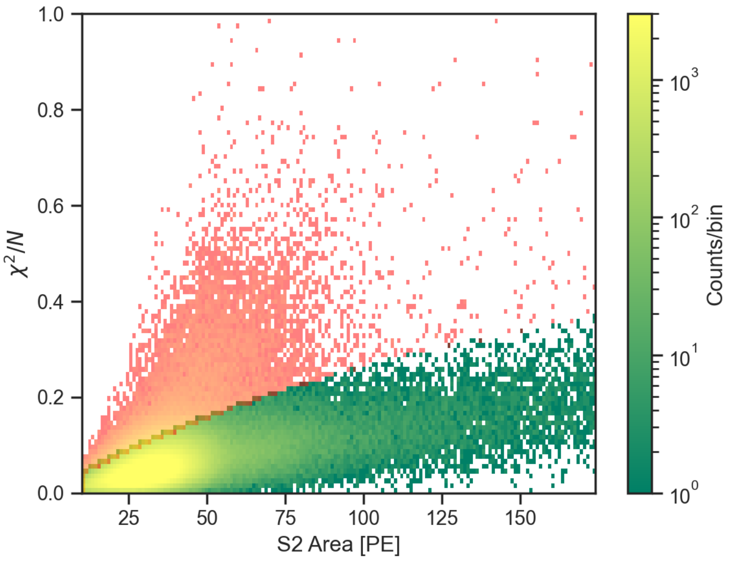

Figure 4.20: Applying S2 hit pattern cut on real peaks identified as sS2, with no other cut applied. The red-shaded regions are excluded. 20 TED datasets are shown in the bottom right plot.

internal storage to the computer hard drive. Thus, such noise might be related to the jittering of the electronics. On the other hand, waveforms inside population 1 are distributed quite evenly in our datasets. The origin of population 1 remains a mystery, but for the scope of the few-electron analysis, both populations can be safely removed as they are not from physical interactions inside the detector. For this reason, the cut acceptance was assumed to be 1, i.e., no S2s from energy deposition would be removed from this cut. The cut was defined as the red line shown in Fig. 4.21, expressed as

$$\text{S2 area} = 0.8 \times \text{N Channel} + 20. \tag{4.7}$$

The noises of both populations 1 and 2 are small in area. Therefore, this cut was only applied to the sS2 population.

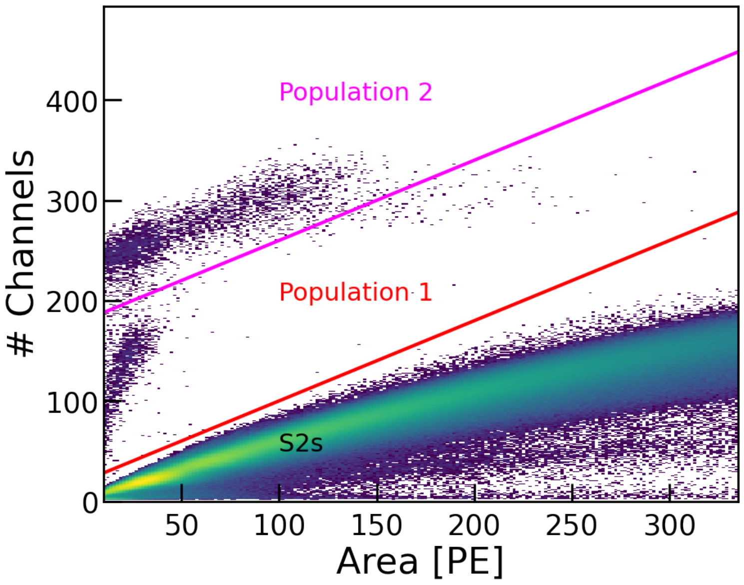

Figure 4.21: Number of contributing channels vs S2 area. The labeled populations 1 and 2 are both sinusoidal waveforms, similar to the one shown in Fig. 2.8. The cut is defined as the red line. Plot from Dr. Jacques Pienaar's study note.

Cut #8: After Pulses

After-pulse refers to any kind of PMT pulse generated inside a PMT that is delayed in time by an actual detected photon. There are various types of after-pulses. One example is that some PMTs suffered from minor leakage and the gases that leaked in. Such gases can be ionized by the initial photoelectrons from actual detected photons and form positive ions, like H^+, He^+, etc. These ions then drift between PMT diodes and cause photoelectron emissions when they hit one. This type of after-pulse features a constant time delay from a preceding S1 or S2 signal. The sizes of after-pulses vs. the characteristic delay time from preceding signals of various ions that are known to cause after-pulses are shown in Fig. 4.22[22].

After-pulses pose a significant risk to single-electron S2 signals. As Fig. 4.23 shows, they can be mistakenly identified by the reconstruction algorithm (Sec. 4.3) as an extra electron, inadvertently increasing the reconstructed electron count, $N_{e,rec}$, from 1 to 2. Consequently,

---

[22] There are two low-intensity after-pulses, the A1 and A2 populations, that do not feature characteristic delay time from preceding signals. The source of these two populations remains unknown. However, due to their low intensity and lack of features, we will ignore them for this analysis

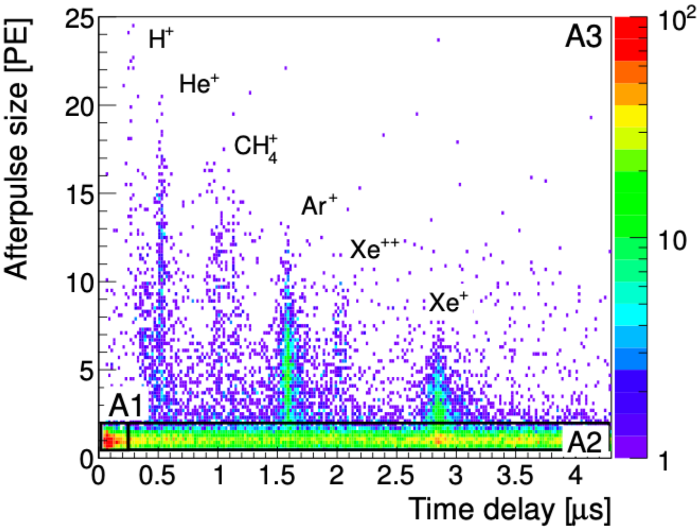

Figure 4.22: After pulse area vs. the characteristic delay times from previous S1/S2 signals of different ions. The delay time is related to the charge-mass ratio of the ion. This plot was taken from Luisa Hotzsch's study note.

such an S2 signal affected by after-pulses might erroneously pass other cuts, for example, the S2 width criteria set for single-electron signals, as the thresholds for single electron S2s are much more lenient for signals from 2 electrons due to diffusion effects, as depicted in Fig. 3.10 and Fig. 4.15. While larger S2 signals may also encounter this issue, the impact is less pronounced. This is because the S2 width criteria for $N_{e,true} > 1$ are similar, and thus, the presence of an after-pulse within a larger S2 signal does not significantly alter its survival rate as it does with single-electron S2 signals.

Using the after-pulse's characteristic time delayed from the preceding signal, a dedicated cut for the single-electron S2s inflicted by after-pulses was designed with the byproduct of the Quantization process of the reconstruction algorithm discussed in Sec. 4.3. As shown in Fig. 4.23, with the two identified "single electron" pieces (clearly, the second one is an after-pulse) within a waveform, we can calculate the time gap between the end of the first piece and the beginning of the second, as indicated by the black arrow. It was found that there are two distinctive clusters in the space of this time gap vs. the S2 area, as shown in

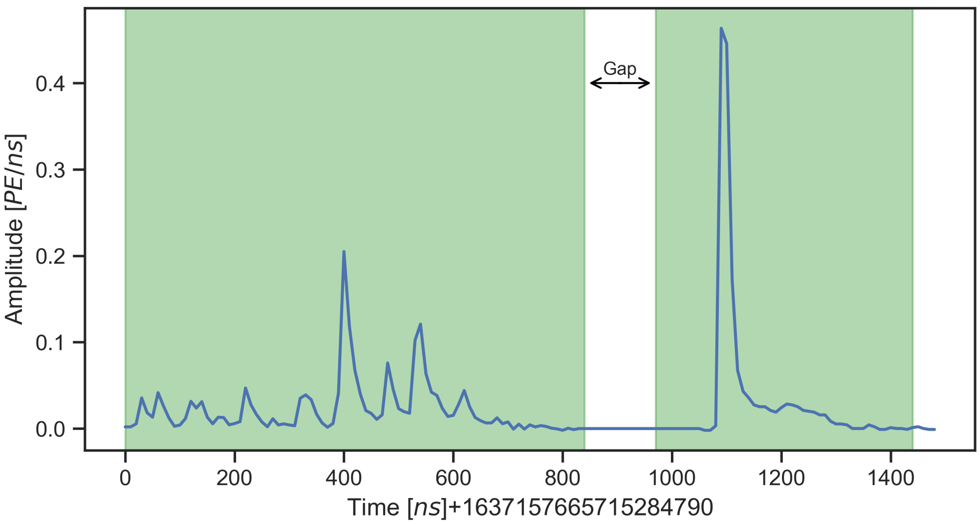

Figure 4.23: An example waveform of the S2 of a single electron followed by an after-pulse. The green regions are the identified subsets of the waveform by the reconstruction algorithm introduced in Sec. 4.3. The gap between the two identified regions is used to design the cut against single electron S2s contaminated by after-pulses.

Fig. 4.24 on the left. The single electron S2s contaminated with an after-pulse corresponds to the population in the cluster at the bottom corner, featuring a relatively small gap value, whereas the true multi-electron S2s are in the top cluster (the clean single electron S2s would not appear on this plot because there would be no identified second piece). We simply drew a straight line in the time gap vs S2 area space that separates the bottom corner from the main population, indicated as the red line in the left plot of Fig. 4.24. (It appears to be a curve on a log-linear plot).

Because the after pulses are small in area, and their waveforms can be separated only for small S2s like the ones from single electrons, this cut is not applicable to large S2s. Thus, this cut is only applied to sS2s.

Similar to the cut acceptance estimation for the S2 width cut, we ignored the drift time dependence of the S2 pulse shape and simulated a sufficient amount of S2 pulse shapes for each number of electrons ($N_{e,true}$) evenly sampled from the whole drift region, between 0 and 2300 μs, using the model explained in Sec. 3.1.3. Then, by using the reconstruction

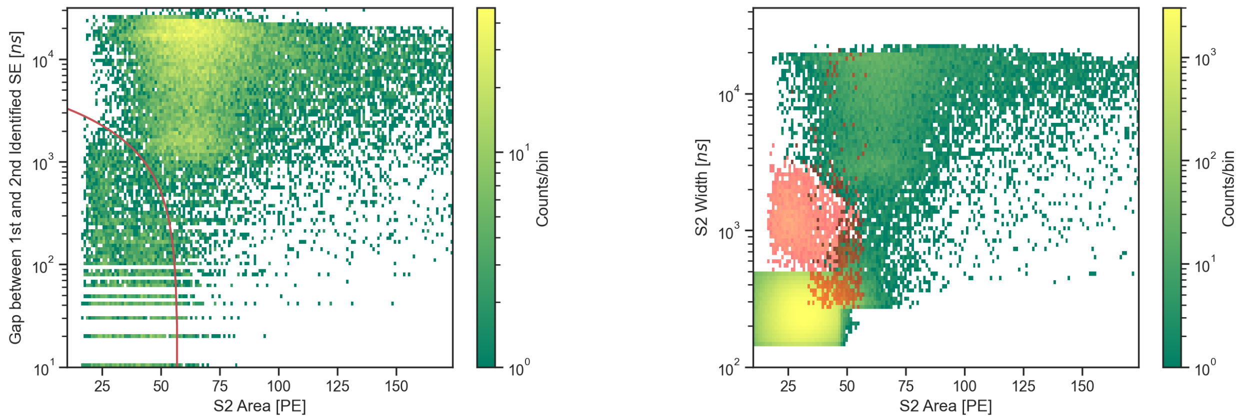

Figure 4.24: Left: the time gap between two identified "single electron" pieces as shown in Fig. 4.23 vs. S2 area for the S2s. The red line is the cut boundary, and the peak is excluded if it is below the line. Right: after applying all other cuts discussed previously, the results of applying the after-pulse cut. The red population passed all previously discussed cuts and is excluded by the after-pulse cut. Clearly, the excluded population features a much larger S2 width than the single electron S2s and a much smaller S2 area than the true two-electron S2s. 20 TED datasets are shown in two plots. Both plots are motivated by Dr. Jacques Pienaar's study.

algorithm, we can calculate the time gap between two identified single electron pieces[23] without the after-pulse contamination. Then, we applied the cut and estimated the fraction that passed the cut. This would give us the fraction of S2s removed by this cut without after-pulse contamination, i.e. good S2s. The results of applying the cut on simulated data with $N_{e,rec} = 2$ and 3 are shown in Fig. 4.25. As the simulation showed, except for $N_{e,rec} = 2$ and 3 populations, the cut doesn't remove any peaks from the populations with other $N_{e,rec}$ values.

The cut acceptances are summarized in Tab. 4.3. These acceptances should be applied to the reconstructed number of electron parameter space.

---

[23] As a reminder, it was reasoned in Sec. 4.3.1 that the two identified pieces are not necessarily the waveforms corresponding to two electrons. Therefore, it is necessary to estimate the cut acceptance with the simulation

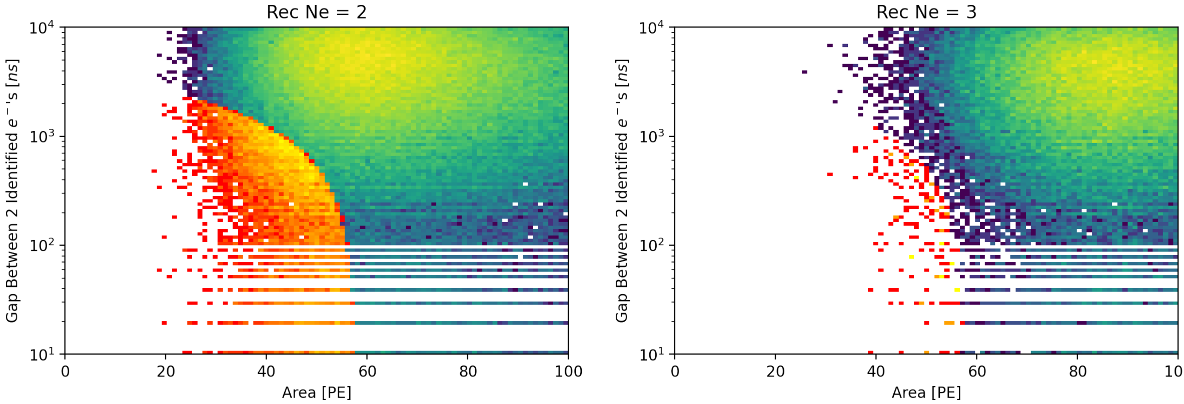

Figure 4.25: Results of applying the after-pulse cut on simulated S2 signals with $N_{e,rec} = 2$ and 3. For other $N_{e,rec}$ values, no peak was removed.

$N_{e,rec}$	2	3	Other values
Acceptance	0.964	0.998	1

Table 4.3: Cut acceptances for the after-pulse cut for each value of $N_{e,rec}$.

Cut #9: Primary S2 Shadow

If two pS2s occur close together in time, the DEs triggered by the first pS2 can be detected after the second pS2 has been observed. This overlapping effect is illustrated in Fig. 4.26: the dashed lines show the expected DE rate as a function of delay time from the pS2s, the large dashed triangles represent the pS2s, and the small solid triangles signify the DEs generated by the pS2s, matched by color. In the examples given, after associating sS2s (only DEs in the case here) with their preceding pS2s, DEs and pS2s of different colors are paired together. These pairs exhibit no temporal or spatial separation correlations between the DEs and pS2s, resulting in what are known as accidental coincidences or ACs. These ACs can skew the accurate estimation of the true spatial and temporal correlations between DEs and pS2s. An example of the distribution of spatial separations of ACs is shown in Fig. 4.28 on the right.

A close inspection of the situation told us that only the DE population of the latter

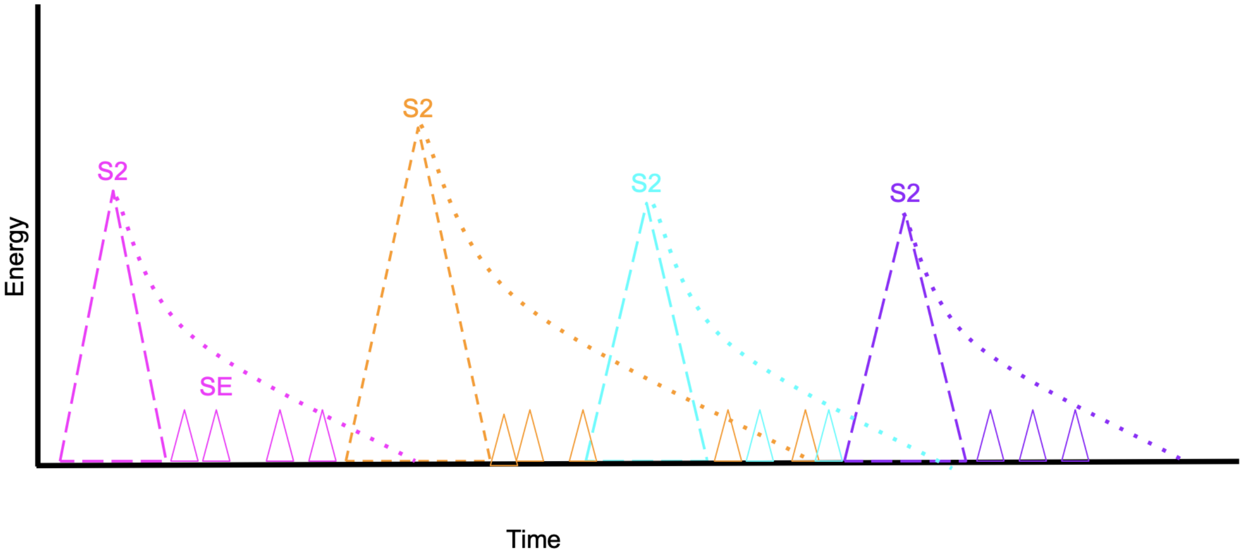

Figure 4.26: Illustration of overlap of DE tails from pS2s that are close in time. The plot was taken from Dr. Jacques Pienaar's study note.

pS2 is contaminated by the existence of the DEs from the first one, while the DEs of the first pS2, although they lose part of their population to the ACs, are paired correctly with their corresponding pS2 and can be used to study the underlying correlations. Therefore, we designed a cut targeting the pS2s that are contaminated by their predecessors. Such contamination is called the Primary S2 Shadow as if the first pS2 casts a shadow onto the second one.

In various studies [104, 105, 52], it has been observed that the frequency of delayed electrons adheres to a power-law distribution in relation to the time elapsed since pS2 events, characterized by an exponent less than -1. It's worth noting that other research, such as experiments conducted by LUX [102] and several smaller-scale detectors [88, 89], have documented an exponential dependency. Here, we used the power-law model. Adopting a conservative approach[24] by choosing -1 as the exponent that suggests a more gradual reduction in the rate of delayed electrons – thereby implying a larger area of overlap than

---

[24] Since removing pS2s doesn't bias our final population of sS2s, within which we establish constraints, it doesn't matter if we cut away slightly more pS2s when preparing the data. The effect of excluding pS2s would be reducing the allowed exposure time.

what is reported in the referenced literature – and acknowledging a direct proportional relationship with the magnitude of the antecedent pS2 (evidence in Fig. 4.6, right), enables the calculation of the proportion of delayed electrons present within a predetermined interval following each pS2. This calculation incorporates effects from all preceding pS2 events. With the interval defined between 2 ms and 200 ms after the considered pS2, such a proportion, named Shadow Fraction, is defined for the i-th pS2 with area $S2_i$ and observed at t_i as

$$\text{Shadow Fraction} = \frac{\int\limits_{t_i+2\ ms}^{t_i+200\ ms} S2_i t^{-1} dt}{\sum\limits_{k<i} \int\limits_{t_i+2\ ms}^{t_i+200\ ms} S2_k t^{-1} dt + \int\limits_{t_i+2\ ms}^{t_i+200\ ms} S2_i t^{-1} dt}. \tag{4.8}$$

For a realistic computing time, we limited the summation to pS2s within 5 s before the considered pS2. Intuitively, The smaller the shadow fraction value, the more overlaps the pS2 experiences, either because there are lots of pS2s before it within a short time window or it is after a significantly larger pS2s. Ideally, if there is no other pS2 within 5 s preceding this pS2, then the shadow value of it should be 1. The distribution of the shadow fraction is shown in Fig. 4.27. There is a natural separation point at 0.04 in the distribution. Further studies showed that the pS2s with a shadow fraction less than 0.04 are mostly large photoionization/photoelectric that is slightly beyond the threshold of 10 e^-, and thus are misclassified by the peak-subtyping algorithm discussed in Sec. 4.2 as pS2s instead of S2PHs. The pS2s with a shadow fraction larger than 0.04 were found to be regular S2s. We took this 0.04 as the cut threshold and excluded pS2s with shadow fraction values less than that.

As mentioned in Sec. 4.4.1, when removing pS2s by cuts, the whole population of sS2 and the exposure time between the removed pS2s and their succeeding ones are removed. Thus, this Primary S2 Shadow cut is an exposure cut, which reduces the total exposure by effectively "blinding" the whole detector for a duration of time. For this type of cut, we don't need to include the cut acceptance (or equivalently, for this period of exposure time, the cut

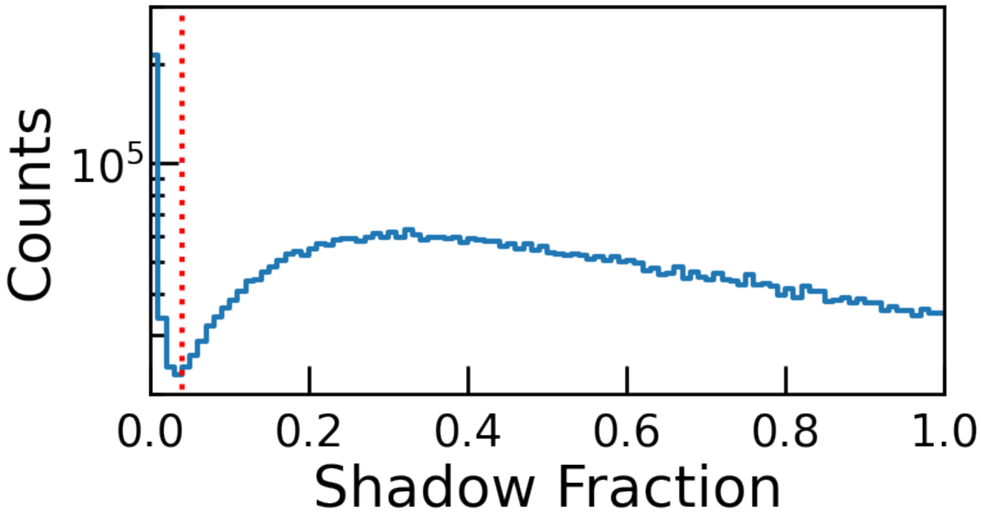

Figure 4.27: The distribution of the shadow fraction of pS2s. The smaller the value, the more overlaps the pS2 experiences (either there are lots of pS2s before it within a short time window, or it is after a significantly larger pS2s). There is a natural separation point at 0.04, and it was taken as the cut threshold. The plot was taken from Dr. Jacques Pienaar's study note.

acceptance is 0 because all good S2s are removed by this type of cut).

Cut #10: Position-Correlated Small S2s

After pairing the sS2s with their preceding pS2s and applying all the cuts discussed above (as a reminder, the proper way of handling cuts is discussed in Sec. 4.4.1: sS2s failing the cuts are removed directly, and the pS2s failed the cut are removed, along with their paired sS2s and the exposure window), we can study the displacements of the sS2s from their preceding pS2s, denoted (Δx, Δy), and the distances between the two, denoted Δr. The distributions of (Δx, Δy) is shown in Fig. 4.28 on the left. Similar to the observation in the XENON1T (Fig. 4.3 left), there is a prominent peak around $\Delta x = \Delta y = 0$, confirming the existence of the DE population. As a comparison, the distribution of $(\Delta x, \Delta y)$ of pairings between randomly sampled sS2s and pS2s are shown on the right, which doesn't show such a concentrated distribution near the origin. We need to remove such a population to improve

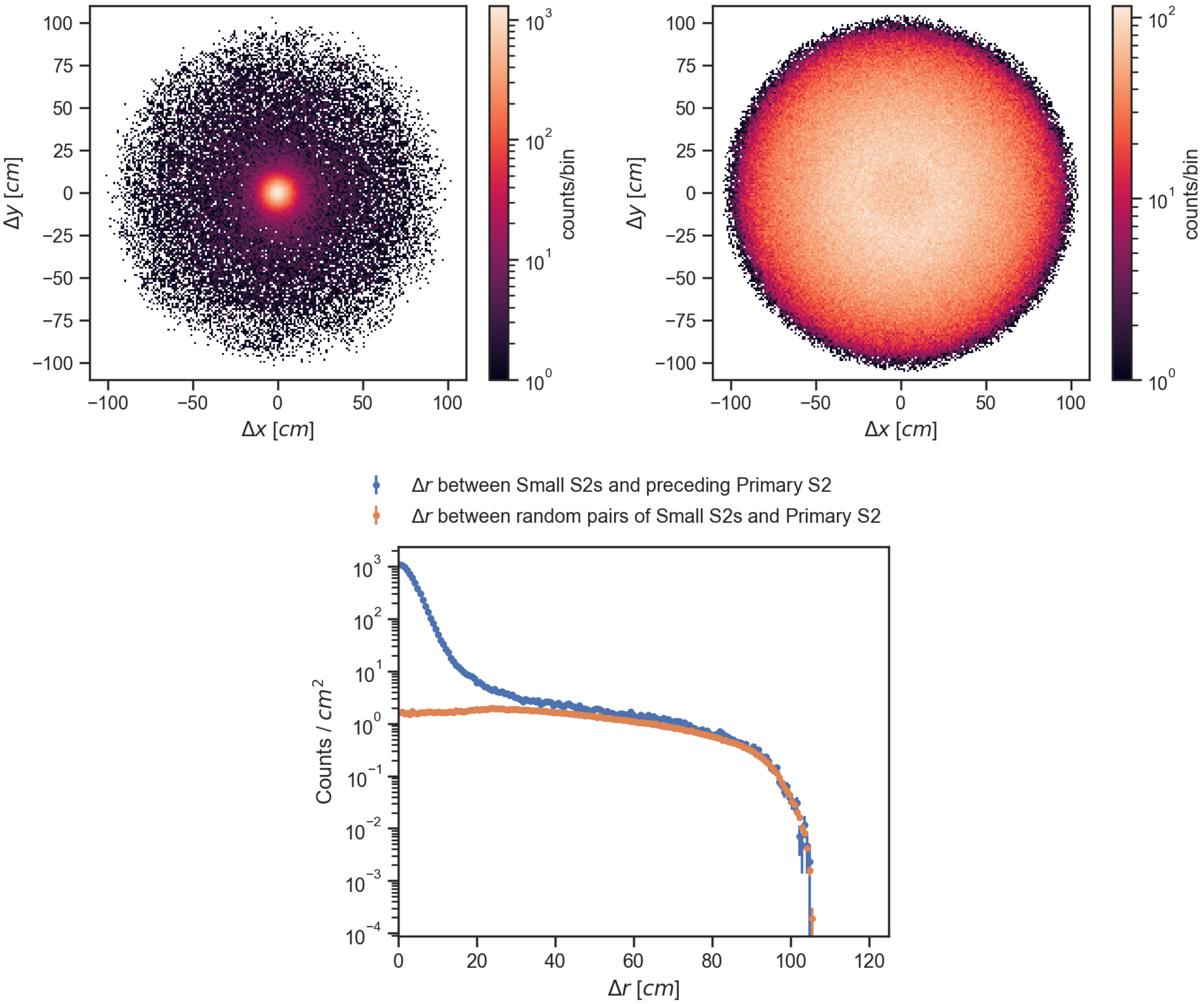

Figure 4.28: Distribution of (Δx, Δy) in between sS2s and their preceding pS2s in TED data (top left) and pairings of randomly sampled sS2s and pS2s with 10^6 entries (top right). The comparison in Δr between real data and random pairing simulation is shown at the bottom. The Δr distribution of the random pairing simulation is obtained from a total of 10^6 entries and normalized to match the amplitude of the real data. Notice that because the fiducial radius was defined at 39.5 *cm* and applied only to the sS2 population, the maximum Δr between an sS2 and a pS2 is the sum of the radius of TPC and the fiducial radius (~ 105 *cm*).

our signal-to-noise ratio for the Few-Electron analysis. This cut is named the position-correlation cut and was developed by discriminating the position-correlated DE population and the position-uncorrelated background.

To model the spatial correlation between the sS2s and the pS2s accounting for both a correlated DE population and an uncorrelated background (radioactive impurities, spurious electron emissions, etc.) population, we defined the distance gap $\Delta r = \sqrt{(\Delta x)^2 + (\Delta y)^2}$ and fitted the distribution of it with the sum of a Gaussian function and the model of the uncorrelated population. The spatial correlation between DEs and the pS2s is captured by the standard deviation, or σ, of the Gaussian in the unit of cm, as it describes how dispersed the DEs are from their progenitors. The model of the uncorrelated population, namely the uncorrelated model, was obtained by computing the Δr distribution of the pairings between randomly sampled sS2s and pS2s depicted in the right plot of Fig. 4.28. With a free amplitude factor a for the Gaussian and a scaling factor b of the uncorrelated model, the distribution of Δr can be expressed as

$$\text{Distribution of } \Delta r = a \cdot e^{-\frac{(\Delta r)^2}{2\sigma^2}} + b \cdot (\text{Uncorrelated Model}), \tag{4.9}$$

where a, σ and b are free parameters to fit. Notice that this distribution is not normalized and is not a probability density function. An example of the fitting is shown in Fig. 4.29.

We examined the dependence of σ with the size of the pS2s, the size of the sS2s, and the time gap between sS2s and pS2s. As shown in Fig. 4.30, no strong correlation was observed between the spatial dispersion of the DEs and the signal size of the preceding pS2s or the time delayed. However, the fitted σ's are inversely correlated with the size of the sS2s, as shown in Fig. 4.31. This is expected because of the reduced position reconstruction precision at low-energy S2 [70][25].

To remove the DEs while keeping most of the uncorrelated population for the dark matter search, we chose the cut threshold for each slice of sS2 area such that 99% of the DE population, described by the Gaussian component, is removed. Such cut threshold is called the position-correlation radius (r_c), within which we consider the sS2 population is

---

[25] The position reconstruction for S2s was developed with machine-learning based models. The precision of the reconstruction model depends on the size of the S2 signal. In our ROI, the radial uncertainties of the reconstructed xy positions range from ~ 5 cm near the 10 PE threshold to ~ 1 cm at 174 PE. More details can be found in the cited literature

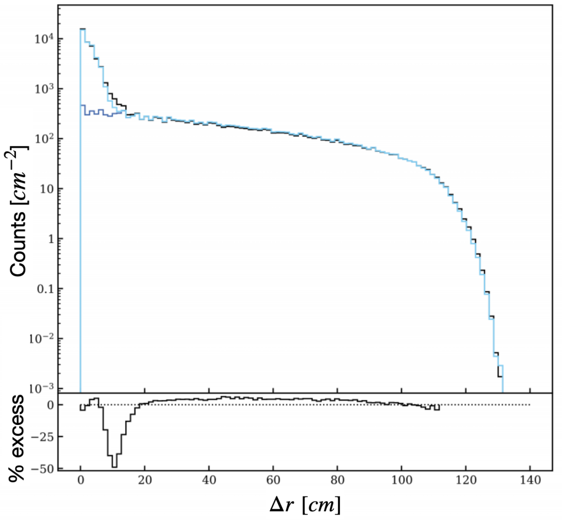

Figure 4.29: Fitting of the Δr distribution with a Gaussian function plus the uncorrelated model. On the top, the black histogram is the distribution of Δr observed in data, the deep blue one is the distribution of the uncorrelated population, scaled by the fitted scaling factor b, and the light blue one is the fitting result. At the bottom, the percentage difference between the distribution of Δr and the fitted results are shown. The plot was taken from Noah Hood's study note.

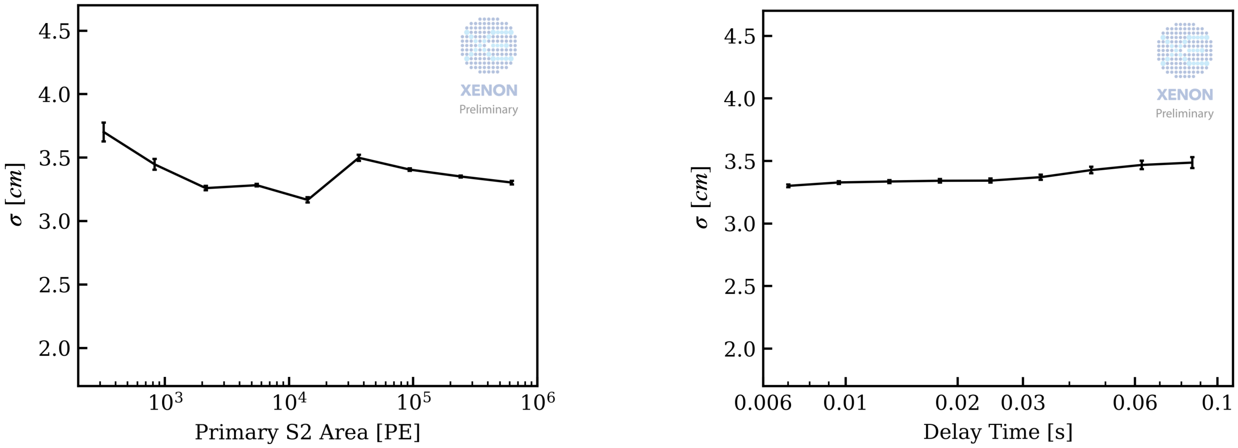

Figure 4.30: We fitted the Gaussian σ for different sub-populations. Left: the fitting was performed in each bin of the pS2 area. Right: the fitting was done with respect to the sS2 population inside each bin of the delay time from their progenitors. No clear dependence was found in these two parameter spaces. The plots were prepared by Noah Hood.

dominated by the DEs that are spatially correlated with the preceding pS2s. The value of r_c, as a function of the size of the sS2, is shown in Fig. 4.32. Due to a lack of statistics for larger sS2s beyond the 174 PE, and the curve flattens at large areas, for sS2s between 174 PE and

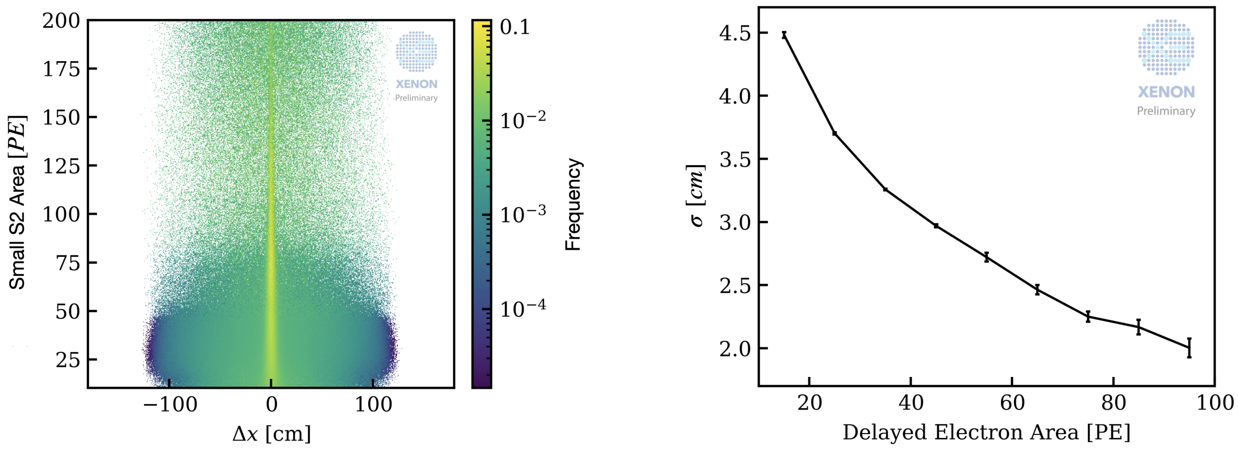

Figure 4.31: Left: the distribution of Δx in each bin of the sS2 area. The amplitude of each bin was normalized within each slice of the sS2 area. A clear narrowing can be seen as the sS2 becomes larger. Right: the fitted σ inside each sS2 area bin. The plots were prepared by Noah Hood.

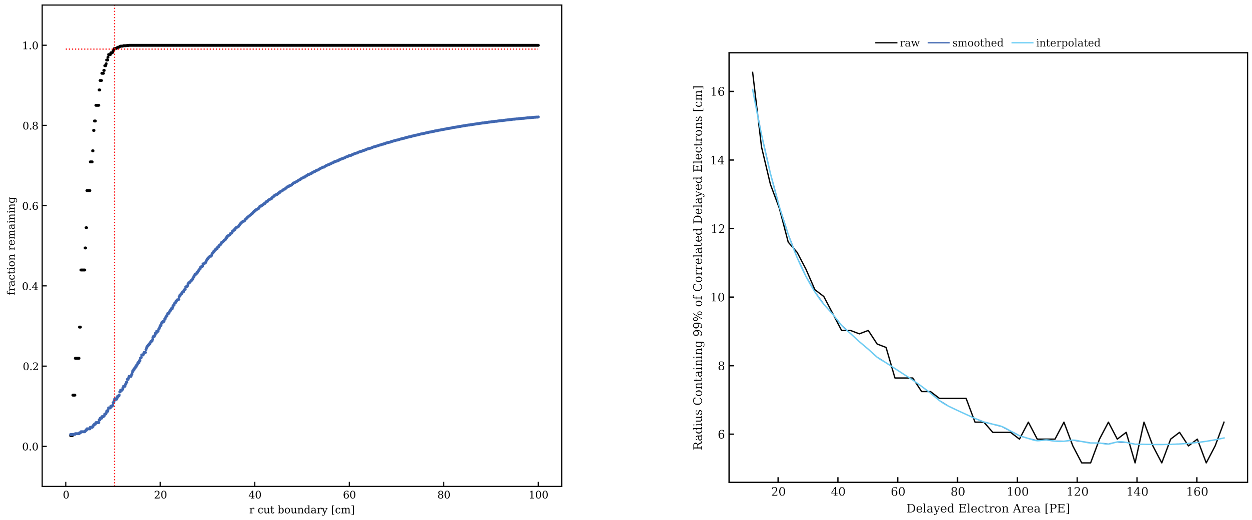

Figure 4.32: Left: an example of setting the position-correlation radius with the fitted Gaussian description of the DE population. The vertical red dashed line indicates the 99% exclusion radius for the DEs. In this example, around 10% of the position-uncorrelated sS2 population is excluded. Right: the 99% DE exclusion threshold as a function of the size of sS2 signals. The black line is the values derived from fitted σ's within each bin of the sS2 area, and the blue line is the smoothened curve. We adopted the blue line as our position-correlation cut threshold. For sS2s above 174 PE, we took the last value of the smoothened curve and extrapolated. The plots were taken from Noah Hood's study note.

340 PE, we simply took the last data point of the smoothened curve and extrapolated.

This cut effectively reduces the fiducial area for each pS2 since it removes a cylindrical volume of liquid xenon, and due to a lack of z information, the full height of the TPC needs to be vetoed. The location and the bottom area of this cylinder is defined by the xy position of each pS2 and r_c. The left plot of Fig. 4.33 shows the concept of removing the area (cylinder) around a pS2 at the origin (the black dot) with $r_c = 10\ cm$, looking down from the top of the detector. The red-shaded region is vetoed to suppress the DE events related to this pS2. For easy reference, we define the region inside the fiducial area and outside the vetoed disk (the blue region in Fig. 4.33) the *Reduced Fiducial Area*, namely RFA. Due to the irregular shape of RFA (and it depends on the position of the pS2), to accurately estimate it for each pS2, we used a Monte Carlo method that samples a large number of random points inside the square containing the RFA and calculate the fraction that lies within the RFA. We used 10^5 points for this simulation and estimated to yield uncertainties of less than 2% on individual RFA estimation. Such uncertainty is further suppressed as we compute the RFA for thousands of pS2s.

Along the time axis, this cylindrical liquid xenon volume is vetoed until the next pS2, as depicted in Fig. 4.34. I will leave the discussion of this operation to the next section, in which I will introduce the time-correlation cut.

In summary, the position-correlation cut is an exposure cut. It removes a cylinder of radius r_c and the full TPC height around each pS2 (this provides the removed liquid xenon mass) for a duration between the considered pS2 and the next one (this provides the exposure time). The correlation-radius r_c is sS2 area dependent; thus, for each value of sS2 area, we cut away different amounts of exposure. Similar to the three parameter spaces ($N_{e,true}$, $N_{e,rec}$ and S2 area) that the cut acceptances need to be applied to deliberately, this sS2 area-dependent exposure also needs to be applied to its corresponding parameter space, and that is the S2 area space. The full exposure calculation also involves discussion in the time-correlation section, but to better illustrate this sS2 area dependence, the total exposure for reconstructed-three-electron ($N_{e,rec} = 3$) sS2s as a function of sS2 area is shown in Fig. 4.35.

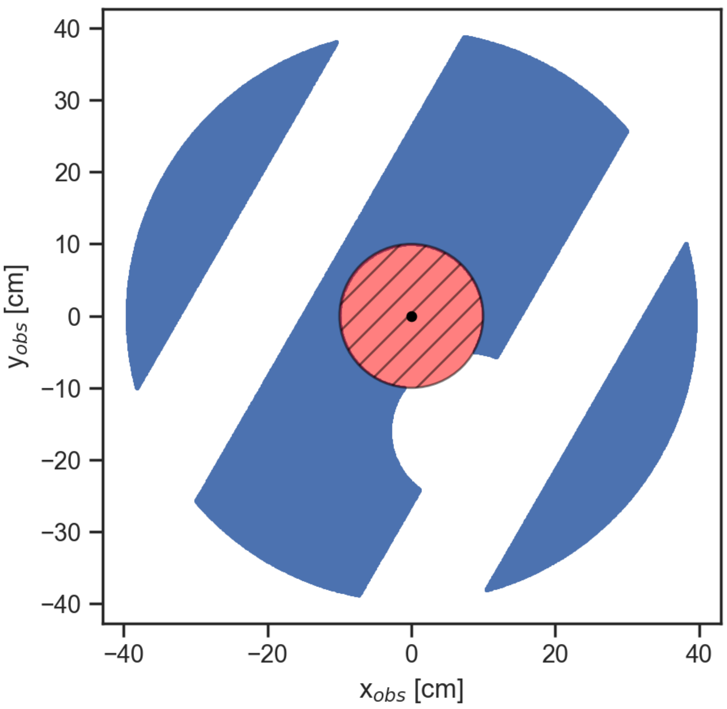

Figure 4.33: Example of vetoed region (red) around a pS2 at (0,0) with $r_c = 10\ cm$, and its relation with the fiducial area. The liquid xenon volume of the full height of the TPC under this vetoed region is excluded from our exposure calculation. The Reduced Fiducial Area (RFA) is the blue region.

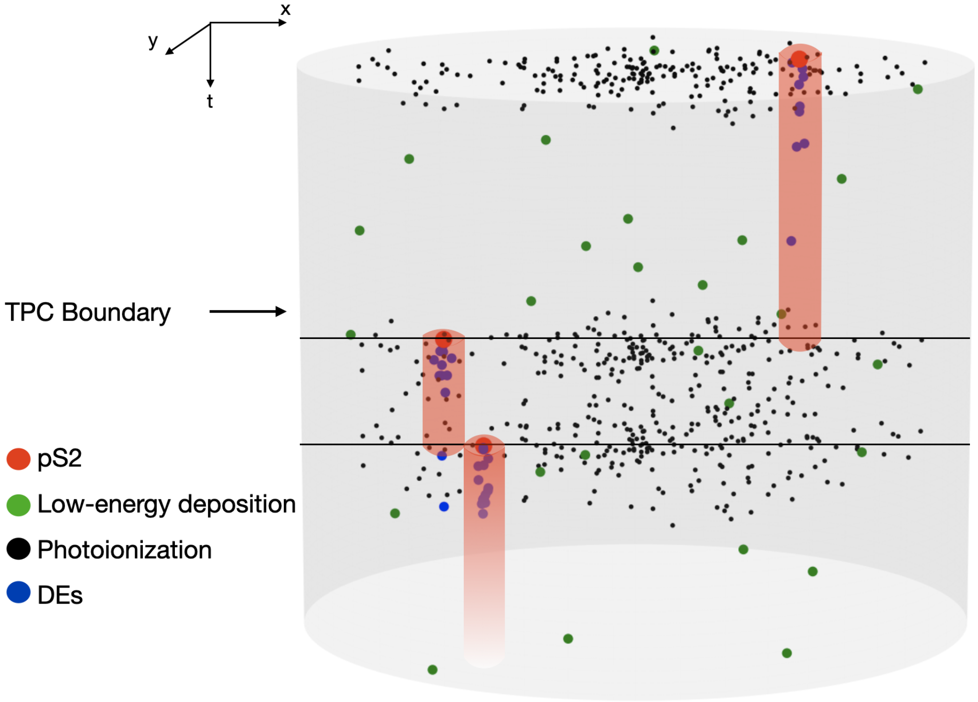

Figure 4.34: Vetoing of the position-correlation cylinder along the time axis. Depicted in (x, y, t) coordinates, the whole cylinder under each pS2 with radius r_c (the cross-sections of the cylinders in the plot) is removed for the whole period until the next pS2 (the height of the cylinders). As vividly shown, DEs from the second pS2 leaked into the exposure time of the third and are not removed by this position-correlation cut. This population is the main target of the time-correlation cut, discussed in the next section.

Cut #11: Time-Correlated Small S2s

While the majority of DEs will be removed effectively with the position-correlation cut, DEs still leak because the time vetoing of the cylinder is limited by the time gap between two pS2s. Efforts have been made to mitigate this leakage through the Primary S2 Shadow cut have been made, as exemplified by the potential removal of the third pS2 in Figure 4.34, which was close to the second pS2, along with the leaked DEs of the second pS2. However, the complete elimination of such leakage remains challenging. As will be demonstrated in this section, the DE rate decreases with the time gap between DEs and their progenitors. Therefore, detecting a small mixture of DEs from the tail end of one pS2 to the onset of the next one is difficult, especially after implementing the Primary S2 Shadow cut. Nevertheless,

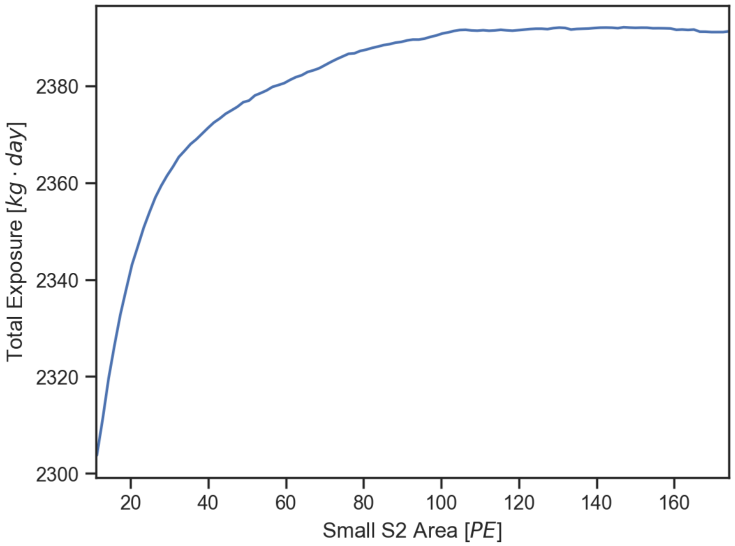

Figure 4.35: Total exposure as a function of sS2 area for three reconstructed electrons ($N_{e,rec} = 3$) sS2s calculated from TED dataset. The full calculation involves the vetoing strategy discussed in the Time-Correlated Small S2s section, which grants the exposure value the $N_{e,rec}$ dependence.

the existence of such remnants cannot be disregarded and must be acknowledged as a type of background. This residual background exists within the position-uncorrelated population, and we need to cautiously handle it to maximize the signal-to-background ratio through a thorough investigation of the time profile of such DE population.

When studying the distributions of time gaps between sS2s and pS2s, biases occur because the *time gap between two pS2s* limits the largest delay time that can be observed. Such an effect is illustrated in Fig. 4.12 and leads to two biases:

- After each pS2, the furthest sS2 that can be observed is limited to the time gap between this pS2 and the next.

To solve this bias, a "live-time score" (s_l) was assigned to each sS2 as the following:

1. For a certain sS2, mark the time gap between it and its preceding pS2 (Δt);
2. For the whole pool of pS2s (that passed the data selection), count the **total amount of time gap between pS2s** that is larger than Δt, and define the inverse of this

value as the live-time score (s_l)

This live-time score represents the chance of observing an sS2 in an infinitesimal time slot $(\Delta t, \Delta t + dt)$ after a pS2 if the gap between two adjacent pS2s is large enough to allow it. Then, instead of counting the number of sS2s observed within $(\Delta t, \Delta t + dt)$, we can sum up the probability of observing an sS2 within this window, and this quantity is not biased by the distribution of gaps between pS2s. Notice that the unit of the sum of live-time score within $(\Delta t, \Delta t + dt)$ should read "*the expected rate of sS2s per pS2 observed*". Thus, the unit of the sum of live-time scores is *per pS2*, represented as $(pS2)^{-1}$. Such *per pS2* can be easily translated into the usual unit Hz of rate by multiplying the rate of pS2s, or into the usual unit of total count by multiplying the total amount of pS2s, etc.[26]. For simplicity, I will still refer to the sum of live-time within each time window as "rate", with the unit of $(ps2)^{-1}$. As a comparison, the un-normalized distribution of time gaps between sS2s and their preceding pS2s and the unbiased delayed electron rate per pS2 are shown in Fig. 4.36 on the left and right, respectively, with all the cuts, except for the position-correlation cut, applied to both sS2s and pS2s.

With this unbiased measurement of the sS2 rate as a function of delay time from the preceding pS2s, we can look into the time profiles of the position-correlated and uncorrelated sS2s by applying the position-correlation cut discussed in the previous section. In Fig. 4.37, besides the sS2s, I also included the S2PH (see Sec. 4.2) in the plot to illustrate the regions that is dominated by the photoionization/photoelectric electrons induced by S2 signals (delay time from preceding pS2s < 1 full drift time). Besides the live-time score, the rate of sS2s are normalized with respect to an extra area normalization:

- The position-correlated sS2s are defined as the ones observed within the position-correlation disk of radius r_c (as a reminder, r_c depends on the sS2 area) and centered

---

[26] In Sec. 4.1, the unit of e^-_{pS2} is an extra normalization with respect to the number of electrons inside the pS2. The area normalization cm^{-2} will be explained shortly.

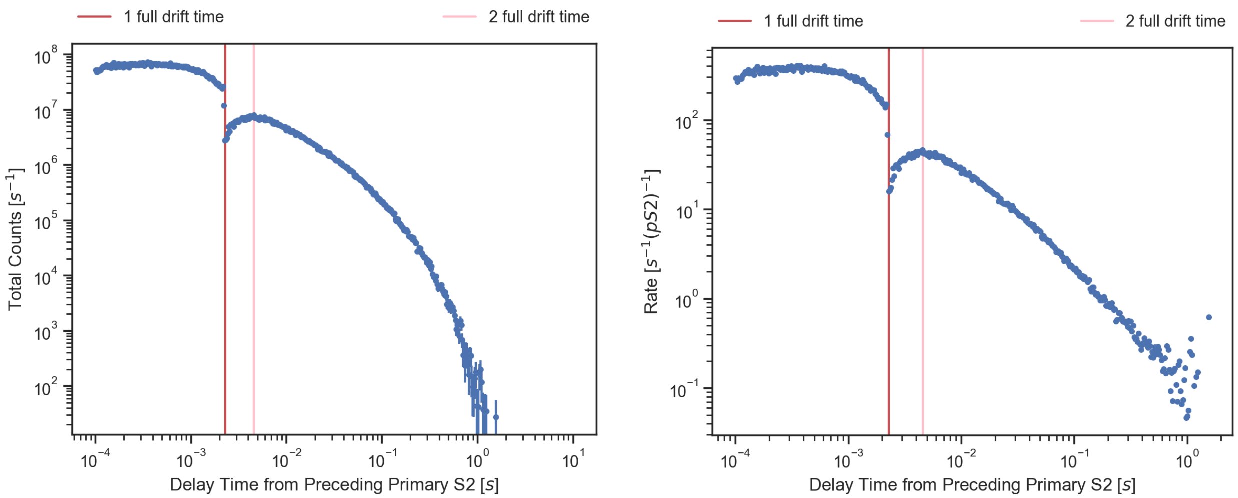

Figure 4.36: Un-normalized total counts of time gap of sS2s from their preceding pS2s from 50 TED runs (left) and the probability of observing an sS2 as a function of delay time after an pS2 (right). All cuts were applied except the position-correlation cut. The s^{-1} unit in the y-axes came from bin-width normalization with respect to the log-binning of x-axes.

at the preceding pS2 location. Therefore, the area on the liquid-gas interface where we observe the position-correlated sS2s is the overlapped region between the position-correlation disk and the fiducial area. For simplicity, we didn't consider the complicated geometry of the fiducial area but only calculated the overlapped area between the position-correlation disk of pS2s and the disk defined by the fiducial radius (39.5 cm). One example is the shaded region in Fig. 4.33. Thus, for a position-correlated sS2, the area normalization factor is the inverse of the area of the corresponding position-correlation disk;

- For the position-uncorrelated sS2s, they are the opposite of the position-correlated ones, and thus, the area normalization is (1 - the inverse of the area of the corresponding position-correlation disk). One example is the blue region outside the shaded region in Fig. 4.33 (again, for simplicity, we didn't subtract the complicated white region that was excluded for the transverse wire and high SE intensity regions).

Fig. 4.37 shows the rates of the position-correlated and uncorrelated sS2s as a function of delay time from the preceding pS2s after the area normalization and with the live-time score implementation. Indeed, the implementation of the position-correlation cut successfully removed a substantial part of the DE population, leaving only a trace of the leakages discussed at the beginning of this section. The high rate of the position-uncorrelated population within one full drift time corresponds to the photoionization/photoelectric electrons, as expected from the electron drifting mechanism inside the TPC (thus concentrated within one full drift time) and the isotropic photon emission (thus position-uncorrelated, or weakly correlated with their preceding pS2s). The rate of the position-uncorrelated sS2s drops significantly and immediately after one full drift time, marking the end of the photoionization dominant regime (we did not observe a significant iterative behavior of the photoionization electrons).

On the other hand, the position-correlated trend exhibits a weird pattern within two full drift time. There are hypotheses about such behavior, like the biases caused by the arbitrary separation between S2PH and S2olS2 (see Sec. 4.2), but none was satisfactory to explain such weird behavior. More studies are being conducted at the time this thesis is written, and their results will shine more light on the future improvement of this analysis. However, for the scope of this analysis, such population is removed by the position-correlation cut and the definition of sS2 (as a reminder, below 2.4 full drift time, the small S2s are defined as S2PH, see Sec. 4.2), and does not contaminate our ROI.

As mentioned at the beginning of this section, the rate of the DEs (position-correlated sS2s beyond two full drift time) decreases as the delay time from the preceding pS2s increases. At the tail of the DEs, the rate is comparable to the rate of the position-uncorrelated population right after the photoionization-dominant region. Moreover, the distribution of the time gaps between two independent and random (the population doesn't carry a feature itself, like monotonically decreasing) populations, e.g. the irreducible radioactive background and the pS2s, or sS2s from DM interactions and the pS2s, should be flat as depicted in

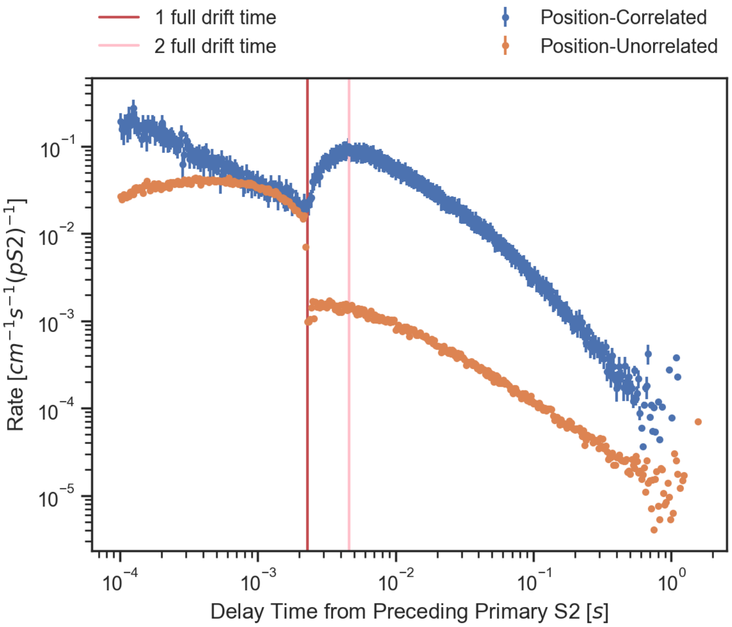

Figure 4.37: Rates of sS2s as a function of the delay time from the preceding pS2s for both position-correlated and uncorrelated populations, normalized with respect to the position-correlation (uncorrelation) disks. The vertical lines mark the locations where the delay from the pS2s equals one full drift time and two full drift time. The s^{-1} unit comes from the bin-width normalization, and the $(pS2)^{-1}$ comes from the live-time score summation.

Fig. 5.5, whereas the trend of the position-uncorrelated sS2s is not. All these prove the existence of DE leakage. Currently, such leakage is not reducible, as we are capped by the sS2-pS2 pairing strategy. While some efforts are discussed in Ch. 5, which is beyond the scope of the current few-electron analysis, we chose to remove a significant exposure time after each pS2 to increase the signal-to-noise ratio and optimize the final dataset for the constraint setting.

The removal of exposure time is applied on the delay time (from preceding pS2) space, named the delay time cut. It removes a fixed amount of time (thus the exposure) after each pS2. The removal amount was optimized with respect to two-parameter spaces, as listed below:

1. As depicted in Fig. 4.6 on the right, the expected DE rate is proportional to the size of the corresponding pS2 (the plot shows that, on average, the same fraction of

electrons from the preceding pS2s becomes DEs for pS2s of all sizes). Therefore, we studied the position-uncorrelated sS2 trends with different sizes of preceding pS2s. More specifically, we chose five pS2 intervals between [340, 100000, 180000, 280000, 440000, 4000000] PE;

2. It was found that for DEs of different $N_{e,rec}$'s, the trends are different. Therefore, for each value of $N_{e,rec}$ from 1 to 10, we studied the position-uncorrelated sS2 trends.

The optimization of signal-to-noise ratio follows a simple logic [52]: the more delay time we cut away after each pS2, the less exposure we would be left with and thus the less expected interactions from BSM interactions; in the meanwhile a smaller portion of DE leakage would be mixed into the final dataset, leaving us a cleaner final sS2 population to set constraints on the expected interactions from BSM physics. The procedures of this optimization were divided into two categories for sS2s with different $N_{e,rec}$:

- For $N_{e,rec} = 1$ and 2, the rate trends of the position-uncorrelated sS2s in all pS2 bins are always decreasing, hinting at a dominant DE leakage even at a large delay time. Because we don't have the full background model, we optimized the delay time cut thresholds by maximizing the ratio between the exposure (in the unit of $[kg \cdot day]$, linearly related to the total number of events from BSM interactions) and the 90% Confidence Level (CL) Poisson Upper Limit (UL) based on the final amount of sS2 (n) (position-uncorrelated and after all cuts):

  $$\frac{\text{Exposure}}{90\%\text{ CL UL}|_n}$$

  The calculation of the 90% CL UL can be found in Appendix. D. To estimate the rate of position-uncorrelated sS2s, we fitted the tail of the rate vs delay time trend with a power law function with amplitude A and power γ:

$$A \cdot t^{\gamma}$$

and extrapolated the fitted function. An example can be found in the top plot of Fig. 4.38 where we fitted the rate trend of position-uncorrelated sS2s for $N_{e,rec} = 1$ and with pS2s with area in [340,1e5] PE. The expected amount of sS2s (n) can be obtained by integrating the fitted power law over the allowed exposure time window: for each pS2, the allowed exposure time window is defined as the time window between the delay time cut threshold and the next pS2. The 90% CL UL then can be calculated from this n and expressed as a function of the delay time cut threshold, as shown in Fig. 4.39 on the top. Similarly, we can calculate the total exposure by multiplying the number of pS2s in each pS2 bin by the length of the allowed exposure time window and the mass of liquid xenon under the fiducial area, as shown in the middle plot of Fig. 4.39. Eventually, taking the ratio of the two and we can find the optimal delay time cut threshold for each $N_{e,rec}$ inside each pS2 bin.

- For large $N_{e,rec}$'s, we observed a flat rate region after the decreasing trend of rate, as shown in the bottom plot of Fig. 4.38 in which the position-uncorrelated sS2s of $N_{e,rec} = 3$ is plotted, hinting at the diminish of the DE leakage in the position-uncorrelated population. This implies that all the backgrounds in this region are forming random pairs with their preceding pS2s[27]. We then fitted the tail of the DE leakage trend with an exponential with scaling A and exponent $1/\tau$ plus a flat background B (t is the delay time from the preceding pS2s):

$$A \cdot e^{-\frac{t}{\tau}} + B$$

---

[27] As will be discussed in Sec. 5.3, such a flat rate spectrum doesn't necessarily imply a DE-free region.

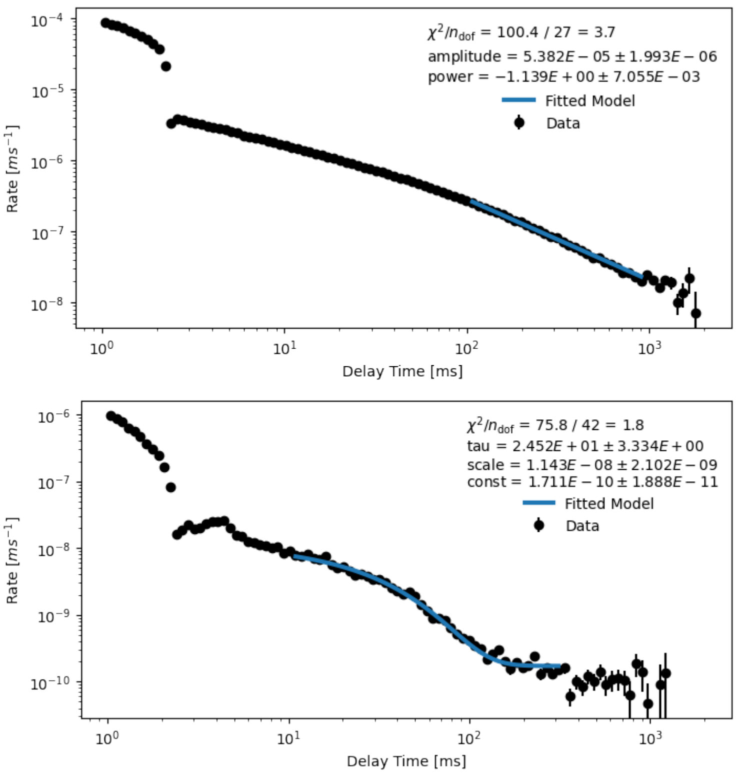

Figure 4.38: Example of fitting the tails of position-uncorrelated sS2 trend vs delay time from the preceding pS2s. Top: fitting the power law to the tail of sS2s with $N_{e,rec} = 1$ and in the pS2 bin of [340,1e5] PE. The blue fitted line is then extrapolated to estimate the expected rate of position-uncorrelated sS2s. Bottom: fitting the tail of the DE leakage trend with an exponential (tau and scale in the plot) plus a flat background (const in the plot). To be conservative, we took the delay time cut at ten times the fitted τ values from the exponential (so for this fitting, the delay time cut for sS2s of $N_{e,rec} = 3$ was set at 0.245 s). The plots were taken from Dr. Jacques Pienaar's study note.

and took conservatively ten times the fitted τ value as the delay time cut threshold.

Due to the lack of statistics, for $N_{e,rec} = 3$ to 5, we could not separate the population into the five pS2 bins, and thus an overall fitting was carried out. For $N_{e,rec} = 6$ to 10, we couldn't even distinguish the number of electrons for sS2, and thus a single binning with $N_{e,rec}$ between 6 and 10, and all the pS2 values were used with one fitting. The optimal delay time cut for sS2s with $N_{e,rec}$ from 1 to 10 and inside the 5 pS2 bins are summarized in Tab. 4.4. The relevant cut development plots are summarized in Appendix. C.

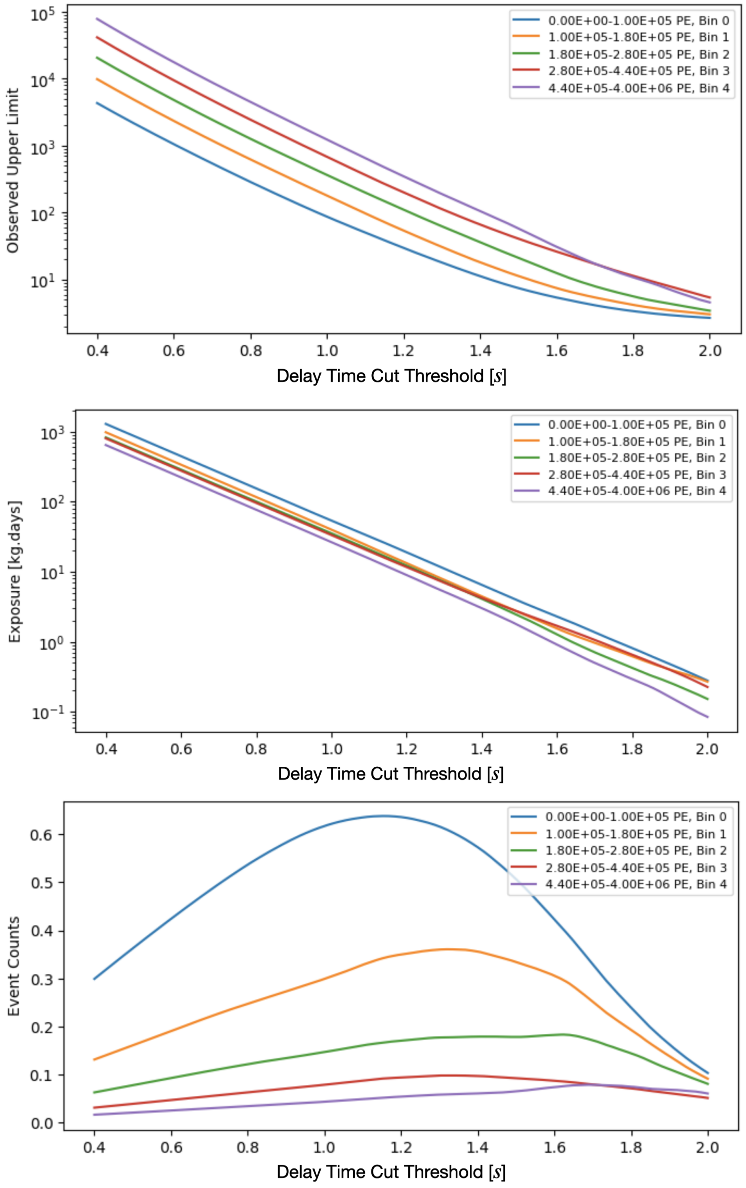

Figure 4.39: Delay time cut threshold optimization for sS2s with $N_{e,rec} = 1$ in the five pS2 bins. Top: the 90% CL UL calculated from the expected total amount of position-uncorrelated sS2s vs the delay time cut threshold. Middle: the total exposure based on the number of pS2s within each pS2 bin vs the delay time cut threshold. Bottom: the ratio of the two, with which the maximum point for each curve is taken as the delay time cut threshold for sS2s with $N_{e,rec} = 1$ in that pS2 bin. The plots were taken from Dr. Jacques Pienaar's study note.

Cut Threshold [s]		Primary S2 Area Bins [PE]				
		[340, $1e5$]	[$1e5$, $1.8e5$]	[$1.8e5$, $2.8e5$]	[$2.8e5$, $4.4e5$]	[$4.4e5$, $4e6$]
$N_{e,rec}$	1	1.160	1.328	1.624	1.320	1.696
	2	0.568	0.656	0.644	0.760	0.920
	3	0.245				
	4	0.229				
	5	0.239				
	6-10	0.232				

Table 4.4: Optimized delay time cut threshold to different pS2 sizes and sS2s of different $N_{e,rec}$'s. For sS2s with $N_{e,rec}$ between 3 and 5, there were not enough statistics to probe the distribution in each pS2 area bin. For $N_{e,rec}$ between 6 and 10, the statistics became even less, and we could only treat the population as one. The table was taken from Dr. Jacques Pienaar's study note.

4.4.3 Exposure Calculation

The concept of exposure has been mentioned and calculated in the previous sections. However, after all the dedications to the cuts, especially the position-correlation cut and the delay time cut, have been cleared, it is worth summarizing it here clearly for easy reference.

Fig. 4.40 depicts the application of the position-correlation cut, the delay time cut, and the resulting exposure on a section of the detector running time (simulated for illustration purposes only). Around the three illustrating pS2s, first, the position-correlation cylinders (mass) are removed for the time spans between them and their next pS2s. Then, the whole detector (mass) is removed for the time span defined by the delay time cut threshold. The unshaded white region labeled at the center of the figure is the survived exposure (mass × time), within which we search for the BSM interaction signals using the survived sS2 populations.

One key aspect – and the only one – of the exposure calculation Fig. 4.40 fails to show is the $N_{e,rec}$ and sS2 area dependences (when computing the exposure after each pS2, the pS2 will lie within one of the five pS2 bins, and thus this dependence is automatically resolved when iterating over all pS2s). For the position-correlation cut, the cut radius r_c is sS2 area

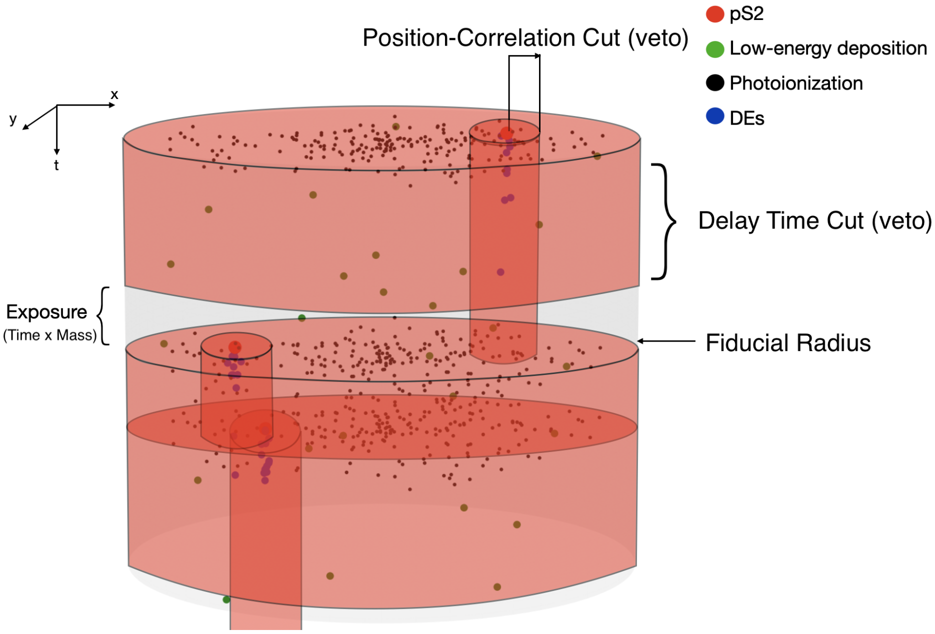

Figure 4.40: Illustration of the position-correlation cut and the delay time cut. After each pS2, the position-correlated cylinder is removed for the time span between it and the next pS2. Moreover, the time slot after each pS2, up to the delay time cut threshold, is also removed. In this very configuration, the only exposure we will be searching for BSM interaction signals is the white region labeled as "exposure", using the survived sS2 signals within.

dependent. This means at the same location – or more specifically, the same distance from a preceding pS2 – whether an S2 signal from a hypothetical interaction will be removed or not depends on the signal size, and a larger S2 signal is less likely to be removed than a smaller one because r_c is smaller for larger S2s (Fig. 4.32). Similarly, the delay time cut threshold is $N_{e,rec}$ dependent, i.e., at the same delay time from a preceding pS2, a larger S2 composed of (actually, reconstructed as) more electrons might survive the delay time cut while a smaller one might not, because the delay time cut threshold is, in general, smaller for larger S2s than the smaller ones. Therefore, the exposure calculated should bear these two dependences and become a matrix, as shown in Fig. 4.41.

This matrix will be applied to the detector response model, discussed in Sec. 4.5.2.

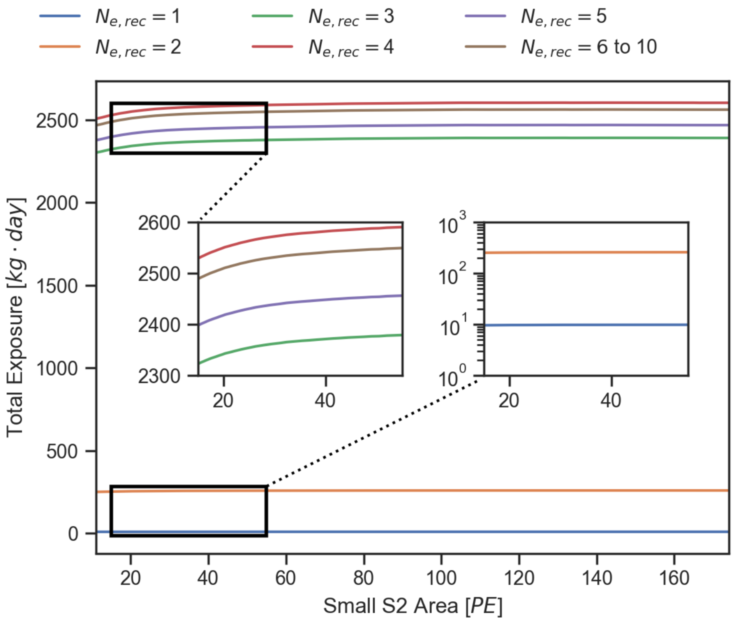

Figure 4.41: Total exposure calculated from TED datasets, with all cuts (on pS2), the position-correlation cut and delay time cut applied. Two zoomed-in plots focus the $N_{e,rec} = 1$ and 2, and $N_{e,rec} > 2$.

$N_{e,rec}$	1	2	3	4	5	6 - 10
Exposure [$kg \cdot day$]	9.8	258.7	2389.1	2604.0	2469.2	2562.5

Table 4.5: Exposures for different $N_{e,rec}$'s.

4.4.4 Summary

After implementing all the cuts discussed in Sec. 4.4, the peaks survived for the whole TED period is shown in Fig. 4.42.

The total exposure, although represented as a matrix in Fig. 4.41, can still be expressed as real numbers if we weigh it with the Single Electron Gain PDFs (discussed in Sec. 4.5.2). The total exposures (for the TED period) for each value of $N_{e,rec}$ is summarized in Tab. 4.5.

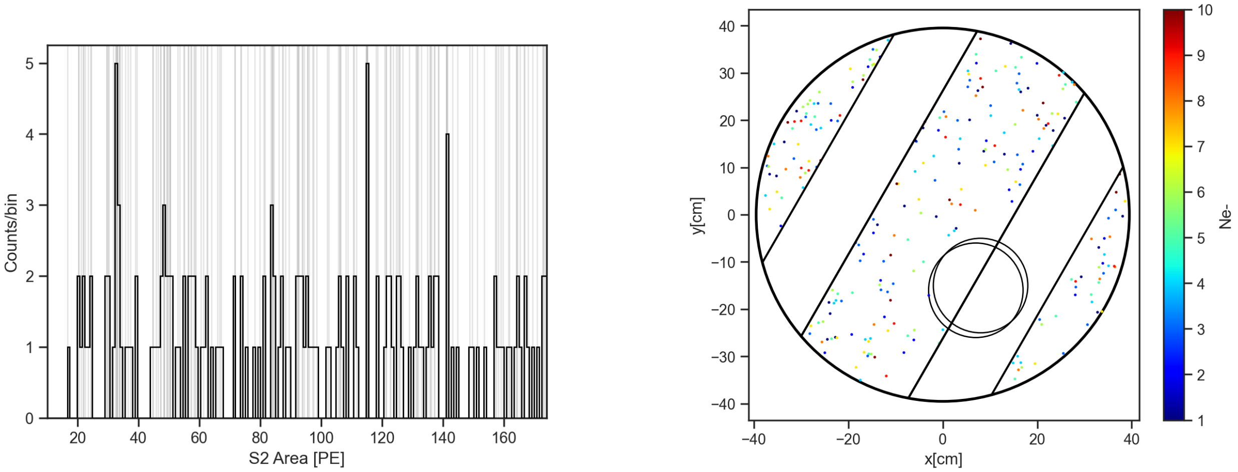

Figure 4.42: The final distribution of peaks in S2 area space (left) and xy space, overlapped with the fiducial area. The vertical lines are the individual S2 area values of the remained S2 peaks.

4.5 Detector Response Model

To obtain the expected S2 spectra from physics beyond the Standard Model, we need the response model of our detector, which converts the energy deposition from an incoming particle to the final S2 area. In the few-electron analysis, we only consider interactions through the ER channel. The microphysics of ER and from electrons to S2 signals have been discussed in Sec. 2.2. As described by the TI-model, at low-energy ER, the recombination rate is approximately 0, as shown in Fig. 4.43. Therefore, we assumed zero-recombination and adopted a fast two-step binomial process to convert ER energy to the final number of extracted electrons (following the definitions in Sec. 2.2.1, Eqn. 2.7, and Sec. 2.2.3) described as:

$$\begin{gathered} N_e = \mathrm{Binom}\left(\mathrm{floor}\left(\frac{E}{W}\right), \frac{1}{1+\left\langle \frac{N_{ex}}{N_i} \right\rangle}\right), \\ N_e^{ext} = \mathrm{Binom}(N_e, \mathrm{EE}\cdot\langle\mathrm{EL}\rangle) \end{gathered} \tag{4.10}$$

where:

- N_e is the number of free electrons generated at the energy deposition site, subsequently drifted up to the liquid surface;

- N_e^{ext} is the number of electrons successfully reaching the liquid surface and extracted into the gas;
- E is the initial kinetic energy of the primary ionization particle. In our case, the primary ionization particle is the ionization electron;
- W is the average energy needed to produce an excimer/an electron-ion pair. We took the value 13.7 $eV/quanta$ from Tab. 2.1;
- $\left\langle \frac{N_{ex}}{N_i} \right\rangle$ is the expected production ratio between excimer and electron-ion pair. It was taken as a uniform distribution between 0.06 and 0.2. We took the average of 0.13 as our nominal value;
- EE is the average extraction efficiency. During SR0 of XENONnT, the average extraction efficiency was evaluated to be 0.54;
- EL is the average electron lifetime attenuation, defined as

  $$\frac{1}{148.6} \int_{0}^{148.6} e^{-\frac{z}{v_d \langle \tau \rangle}} dz$$

  where $v_d = 0.0675\ cm/\mu s$ is the electron drift velocity, and $\langle \tau \rangle$ is the average electron lifetime during the considered time period. The variable z, although being integrated over, should be expressed in the unit of cm so the limits of the integral represent the top and the bottom of the detector. For TED datasets $\langle \tau \rangle \simeq 8.8\ ms$, and the value of EL is ~ 0.88.

What's left is a numerical mechanism that turns the number of extracted electrons to the S2 area. Mostly, we used the single electron gain values reported in Tab. 2.2 and the Poisson&Gaussian model introduced in Sec. 3.1.3. However, there are several details

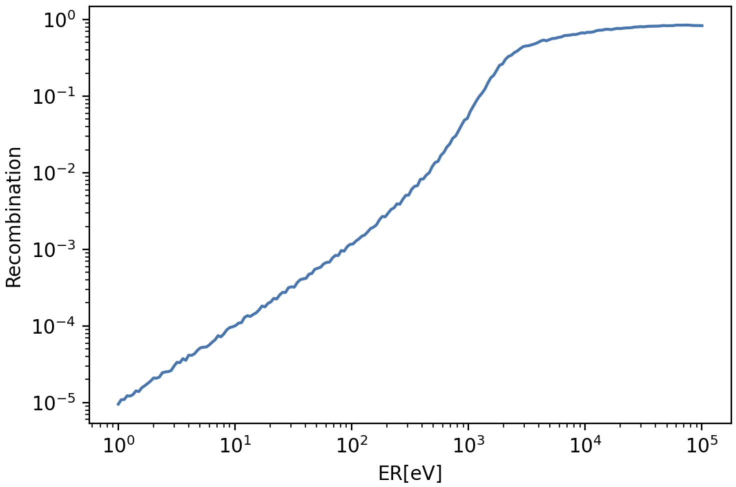

Figure 4.43: Recombination rate vs energy deposited through the ER channel.

that need to be well-documented, including the aforementioned differences between $N_{e,rec}$, the number of electrons reconstructed from S2 waveforms, and $N_{e,rtue}$, the true number of electrons constituting the S2. Before discussing this important aspect of the detector response model, I will first quantify the data-processing biases (Sec. 4.5.1). Then, I will apply such bias as a correction to the Poisson&Gaussian model and develop the detector response model, incorporating the three parameter spaces ($N_{e,true}$, $N_{e,rec}$, and S2 area) where the cuts are developed and depend on (Sec. 4.5.2).

4.5.1 Reconstruction Bias on S2 Signal Area

Recalling Sec. 2.2.3, the S2 signals are recorded in the format of voltage drops over time, in the unit of *ADC/sample*, for which *sample* is the time resolution of the digitizer. For the specific digitizer we used in XENONnT (CAEN V1724), 1 $sample = 10\ ns$. Then, a waveform processing pipeline [108, 109] reads the recorded waveform drop, recognizes pulses within, groups pulses into peaks, and eventually calculates relevant peak properties and classifies them into "S1", "S2", or "unidentified". The exact detail of such a processing pipeline is not the focus of this analysis and more details can be found in the two cited public

GitHub repositories. However, there are several sources of biases that are worth mentioning inside this pipeline:

- The pulses are identified with a "hit-finding threshold", which means the ADC value has to momentarily pass such a threshold for the pulse to be identified and processed. Depending on the exact situations inside the PMT and the transmission of electrons between diodes, each detected photon will result in different voltage drops. Therefore, some photons might be detected by the PMT (i.e., generated photoelectrons at the photo-cathode) but not recognized by the processor, leading to a loss in the final S2 area, and in some extreme cases, the loss of the whole S2;
- After recognizing pulses, the processor groups them up with a merging window to form "peaklets", as first defined in Sec. 3.2.1. Following the same rationale of the discussions in the same section, such merging practice might lead to over-merging in some cases and under-merging in others, which is ultimately unsolvable;
- For "peaklets" that are close in time and bear the shape characteristics of an S2 signal (wide and flat), they are merged together to form peaks. Discussions about this practice can be found in Sec. 3.2.1. Under the scope of the few-electron analysis, the final peak rate is extremely low, and the over-merging or under-merging biases discussed in the mentioned section do not concern us.

To quantify the biases induced during the peak processing pipeline within the ROI of the few-electron analysis, we used a dedicated waveform simulator called WFSim [107], which was designed to simulate realistic signal formations and PMT responses for both S1 and S2 signals based on both model-driven [110, 111, 112, 113] and data-driven detector characterization parameters. S2s composed of 1 to 10 e^{-}'s were simulated and fed through the peak processing pipeline. The results are twofold:

1. The S2 identification efficiency, defined as the rate of successfully identifying the S2

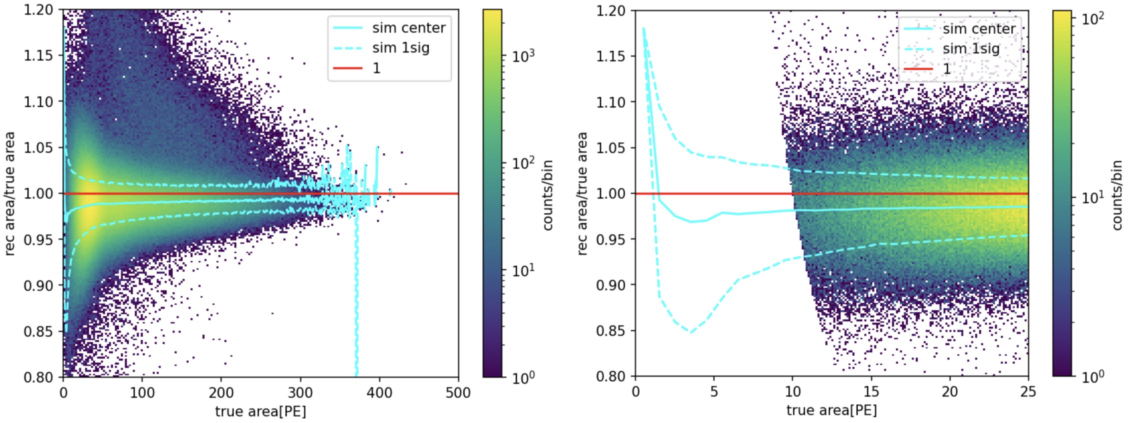

Figure 4.44: S2 reconstruction bias, calculated as the ratio of the simulated number of photoelectrons triggered in the PMT (true area) and the reconstructed S2 area in the unit of PE (rec area). On the right, I zoomed in to the lower boundary of the ROI, which is defined at the reconstructed S2 area equals 10 PE (notice that the 10 PE threshold should be defined in the true area space).

peak and reconstructing as an S2 signal (instead of misclassifying as S1 or unidentified), as a function of the S2 area (reconstructed by the pipeline) is shown in Fig. 4.2. Above ~ 5 PE, all S2s were successfully identified and classified. Thus, the identification efficiency is treated as 1 inside our ROI;

2. The S2 reconstruction bias, defined as the ratio between the reconstructed S2 area and the initial number of photoelectrons is shown in Fig. 4.44. The reconstruction bias within our ROI is systematically reducing the S2 areas and is less than 3%, with an added S2 area fluctuation of less than 5%.

The S2 reconstruction bias curves reported in Fig. 4.44 cannot be directly applied to our detector response model. When doing the simulation, the best estimator for the average number of photons a single electron can produce is the actual measured SEG value, reported in Tab. 2.2. However, the actual measured SEG is already "reconstructed", i.e., the value itself already bears the reconstruction bias inside, and applying such a bias would be double-counting the effect. To handle such nuance, we then normalized the bias curve and the associated fluctuation curves with the reconstruction bias at SEG (31.9 PE) being 1, as

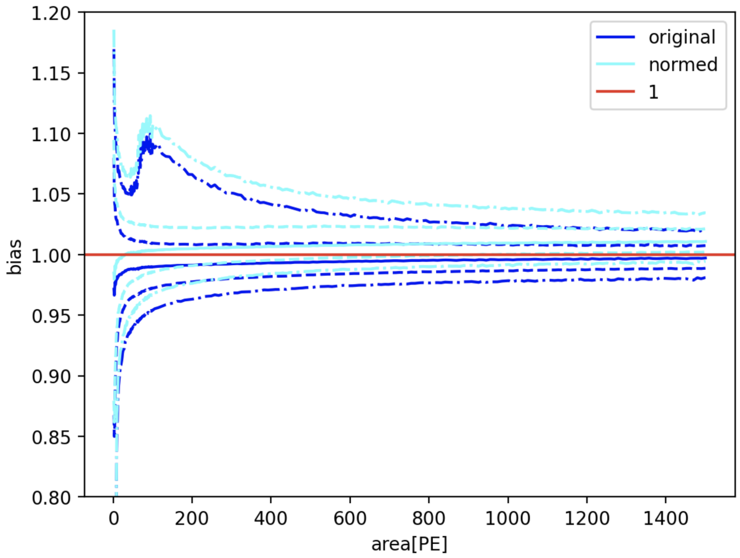

Figure 4.45: Normalized S2 reconstruction bias (cyan) vs the original S2 reconstruction bias. The normalization was set at SEG such that the bias should be evaluated to 1 at S2 area = 31.9 PE.

shown in Fig. 4.45. Then, S2s smaller than 31.9 PE would be biased down, and the larger ones would be biased up.

4.5.2 Tensor Representation of The Detector Response Model

As introduced in the S2 Width cut discussion in Sec. 4.4, in order to properly describe the S2 pulse shape using the model developed in Ch. 3, we need the know the number of electrons consisting of each S2. However, after extraction, electrons are turned into photons and, subsequently, voltage drops in the PMTs, through which we lose the "counting" capability of each individual electron. To reconstruct the number of electrons from S2 waveforms, an algorithm was developed and discussed in Sec. 4.3. However, as mentioned in the very section, the reconstructed number of electrons, or $N_{e,rec}$, is not necessarily the same as the number of electrons extracted for an S2, for which the latter we refer to as the true number of electrons, or $N_{e,true}$. The reconstruction biases are discussed in detail in Sec. 4.3.1. To build a robust detector response model and apply all the cut acceptances correctly for the final prediction of expected S2 area spectra from novel BSM models, such nuance needs to be handled with care.

With the $N_{e,rec}$ reconstruction algorithm in place, the full road map from energy deposition to the final S2 area spectrum is illustrated in Fig. 4.46:

1. Starting from the rate of energy depositions as a function of energy deposited through ER channel, usually in the unit of $[kg^{-1}day^{-1}]$ (or $[ton^{-1}year^{-1}]$), we can compute the rate of observing the true number of electrons (the number of electrons extracted into GXe, $N_{e,true}$) using the two-step binomial process discussed at the beginning of this section. The result of this step is the rate of observing S2s with each $N_{e,true}$, in the unit of $[kg^{-1}day^{-1}]$;

2. After obtaining the rate of observing S2s with each $N_{e,true}$, the cut acceptance of S2 Width Cut is applied. From the perspective of each individual energy deposition, the cut acceptance is simply a binomial process determining whether the S2 signal with its $N_{e,true}$ passes the cut or not. For a rate, the cut acceptance would simply be an attenuation factor. The result of this step should be an attenuated rate of observing S2 signals with each $N_{e,true}$, in the unit of $[kg^{-1}day^{-1}]$;

3. Based on the reconstruction bias discussed in Sec. 4.3.1, S2s with a certain $N_{e,true}$ can be reconstructed into different $N_{e,rec}$ based on the actual shape and size of its waveform. Such misclassification is documented in Appendix. A. Such reconstruction bias, in the form of a tensor, converts the rate of observing S2s with a certain $N_{e,true}$ to the rate of observing S2s with a certain $N_{e,rec}$ in the unit of $[kg^{-1}day^{-1}]$. This triggers the development of the *Tensor Representation* of the detector response model. I will defer the full discussion of such implementation to slightly later after introducing the S2 area;

4. Building from the rate of observing S2s with a certain $N_{e,rec}$, we apply the cut accep-

tances of the after pulse cut, and also the time-axis of the exposure calculation. The time axis of the exposure is determined by the delay time cut threshold, which in turn depends on $N_{e,rec}$. is represented as each individual curve of Fig. 4.41. Clearly, this time component (or the dependence on $N_{e,rec}$) cannot be decoupled from the mass component (or the dependence on the S2 area). Nevertheless, I will bypass this obstacle and finish the road map, leaving the discussion of this to the introduction of the tensor representation;

5. Next, we need to convert the rate to the total expected number of observations in the S2 area space. However, such practice is tricky: the Single Electron Response model (the Poisson&Gaussian described in Sec. 3.1.3 functions on each physical electron, i.e., it should be applied to the true number of electron axis. But we also need to incorporate the cut acceptances and the time axis of the exposure, which are applied to the reconstructed number of the electron axis. Therefore, we need to alter the original Single Electron Response model with the reconstruction biases, as shown in Fig. 4.47. With this conversion matrix, the rate of observing S2s with a certain $N_{e,rec}$ (again, with the conceptual dilemma of applying the time-axis to the rate) can be converted to the rate of observing S2s with a certain S2 area;

6. Eventually, we can apply the acceptances that depend on the S2 area to the final spectrum, including those of the S2 Hit Pattern cut and the S2 aft cut. The region of interest is also defined in the S2 area space. The final component is the mass (or spatial) axis of the exposure calculation, as shown in each curve of Fig. 4.41. At the end of this step we would get the expected number of observations with S2s of a certain area.

Since we cannot decouple the mass and time components of the exposure, and the acceptances of cuts need to be applied properly, we developed a tensor representation for the

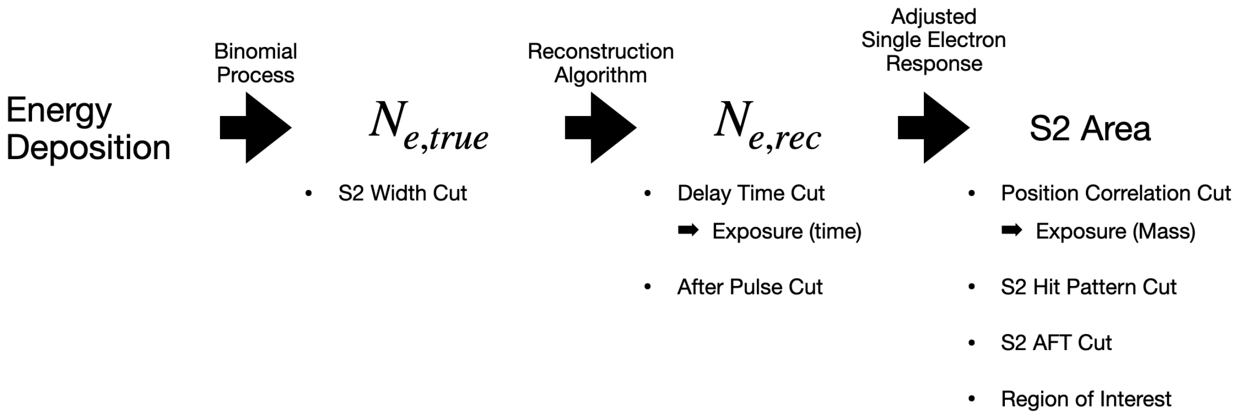

Figure 4.46: Flowchart of the detector response model. The processes above the arrows indicate the models we used to transition from the previous parameter space to the next one. The bullet points below each parameter space indicate the relevant cuts developed under them, for which the acceptances should be applied to the same parameter spaces.

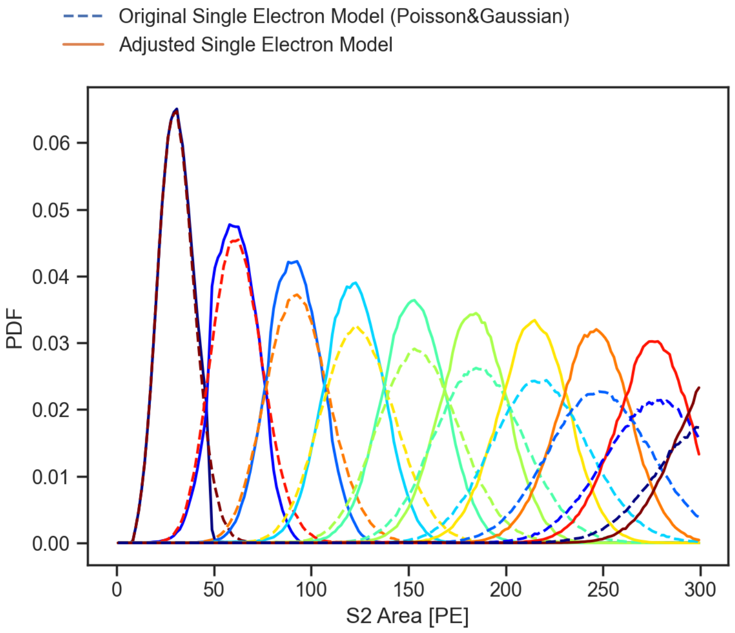

Figure 4.47: Single Electron Model. The solid lines are the Poisson&Gaussian model for each value of $N_{e,true}$. The dashed lines are the ones altered by the tensor (obtained by convoluting the solid curve with the curves in Appendix. A respectively then summing up the resulted spectra of the same $N_{e,rec}$). Calling back to the intro section of this chapter, although we focused on the ROI of (10, 174) PE, nominally corresponding to 1 e^{-} to 5 e^{-} S2s, the S2 area spectrum from up to 10 e^{-} can have small contributions to the ROI. Thus, when doing the models and cut acceptances, we included up to 10 e^{-} population.

detector response model, expressed as:

$$(\mathcal{N}_{PE})^{\sigma} = (A_t \circ \mathcal{N}_t)^{\mu} \left(\mathrm{Diag}(E^T \cdot \mathcal{M}) \circ A_r\right)_{\nu} \mathcal{T}_{\mu}^{\nu,\sigma} \circ (A_{PE})^{\sigma}, \tag{4.11}$$

where

- The σ index runs across all the bins of S2 area. In our analysis, instead of using continuous S2 area values, we used binned spectrum with equal bin widths for fast computation;
- The μ index runs across the true number of electron axis, i.e. $N_{e,true} = 1$ to 10;
- The ν index runs across $N_{e,rec} = 1$ to 10;
- The symbol $\circ$ represents element-wise product, e.g., $(a, b) \circ (c, d) = (ac, bd)$;
- $(\mathcal{N}_{PE})^{\sigma}$ is the expected number of observations of S2 signal with an area σ (equivalently the bin center of the σ-th S2 area bin);
- $\mathcal{T}_{\mu}^{\nu,\sigma}$ is the tensor. Illustratively, each μ value represents the reconstruction bias plot with $N_{e,true} = \mu$ in Appendix. A, each ν value represents a probability density function (PDF) with $N_{e,rec} = \nu$ in that plot, and each σ corresponds to the value of the PDF at S2 area $= \sigma$;
- $\mathcal{M}$ is a matrix representing the Single Electron model (Poisson&Gaussian). Illustratively, each row of it represents a PDF of a value of $N_{e,true}$ (each curve in Fig. 4.47);
- E is the exposure matrix that depends on $N_{e,rec}$ (time) and S2 area (mass). Arranged similarly to $\mathcal{M}$, each row of it represents a curve of a $N_{e,rec}$ value in Fig. 4.41. Thus the diagonal of $E^T \cdot \mathcal{M}$ is the exposure for each $N_{e,rec}$;
- $(A_t)^{\mu}$ is the cut acceptance depending on the true number of electrons, evaluated at $N_{e,true} = \mu$. $(\mathcal{N}_t)^{\mu}$ is the expected number of observations of S2 signal with $N_{e,true} =$

μ. The product of the two is the attenuated expected number of observing an S2 with $N_{e,true} = \mu$;

- $(A_r)_\nu$ is the cut acceptance depending on the reconstructed number of electrons, evaluated at $N_{e,rec} = \nu$. The term $\Big(\text{Diag}(E^T \cdot \mathcal{M}) \circ A_r\Big)_\nu$ represents the attenuated exposure for each $N_{e,rec}$. Notice that instead of absorbing the cut acceptance attenuation to the number of observations like in the case of $N_{e,true}$, here we absorbed it to the exposure, which is equivalent;
- $(A_{PE})^\sigma$ is the cut acceptance depending on the S2 area, evaluated at area $= \sigma$;
- Same and staggered indices are contracted. Specifically, μ and ν are contracted, while σ is only involved in the element-wise product. Therefore, the result of $(\mathcal{N}_{PE})^\sigma$ is the expected number of observation spectrum in the S2 area space, in the unit of $[PE^{-1}]$.

This tensor representation handles the cut acceptance in the three correlated parameter spaces ($N_{e,true}$, $N_{e,rec}$ and S2 area) in a covariant way. The s2 reconstruction bias from the peak processing pipeline, discussed in Sec. 4.5.1, is absorbed in the tensor term ($\mathcal{T}$) and the matrix term ($\mathcal{M}$).

4.5.3 The Model of the BSM Interactions

With the BSM models introduced in Sec. 1.3, we can feed the expected recoil energy spectra through the detector response model and get the expected S2 area spectra with some nominal interaction strengths. There are several extra treatments that need to be mentioned:

1. While implementing the differential rate as shown in Fig. 1.9 into Eqn. 4.10, we also need to account for the initial electron (the primary ionization particle) that is inducing the ER process. Since we are ignoring the recombination process, the initial electron should always survive and become a part of the initial electron cloud, i.e., we need to add 1 to N_e before accounting for the drifting and extraction attenuations;

Shell	$5p^6$	$5s^2$	$4d^{10}$	$4p^6$	$4s^2$
Additional Quanta	0	0	4	6	3

Table 4.6: Additional quanta results from the cascade process of electrons from outer shells falling to the vacancies of different shells. Only the most conservative additional quanta are recorded here. Table taken from Ref. [38].

2. As depicted in Fig. 1.9, LDM can scatter off electrons from all orbitals, with a decreasing rate for the inner shells as they have higher binding energy. Effectively, we only considered the interactions with the two outermost shells of the xenon atom (s and p shells). If a p shell electron is excited, there can be a sequence of cascade of s shell electrons to fill in the vacancy. Such a process, in addition to the ER process and the primary ionization electron, can induce further quanta and, subsequently, additional electrons. In this work. we quote the conservative additional quanta proposed in Ref. [38], and the exact values are summarized in Tab. 4.6. These additional quanta are added to the ER quanta yield $N_q = \text{floor}\,(E/W)$.

3. A similar bonus quanta can also happen to the absorption of DP or ALPs. In this case, while the binding energy is deducted from the energy remaining for the ER process, bonus quanta can benefit the final charge yield if the interaction is with electrons on an inner shell;

4. At the moment this thesis was written, we only considered absorptions of DP and ALP by the electrons on the outermost shell with equal probability for each orbital electron. Despite the bonus quanta introduced above, considering the absorption by outermost shell electrons gives us an optimistic signal yield.

The expected S2 spectra for the three BSM models are summarized in Fig. 4.48. Due to (and benefited from) the massive increase of the total exposure from $N_{e,rec} = 1$ to $N_{e,rec} = 2$ (20 times as listed in Tab. 4.5), the number of expected observations from interactions that

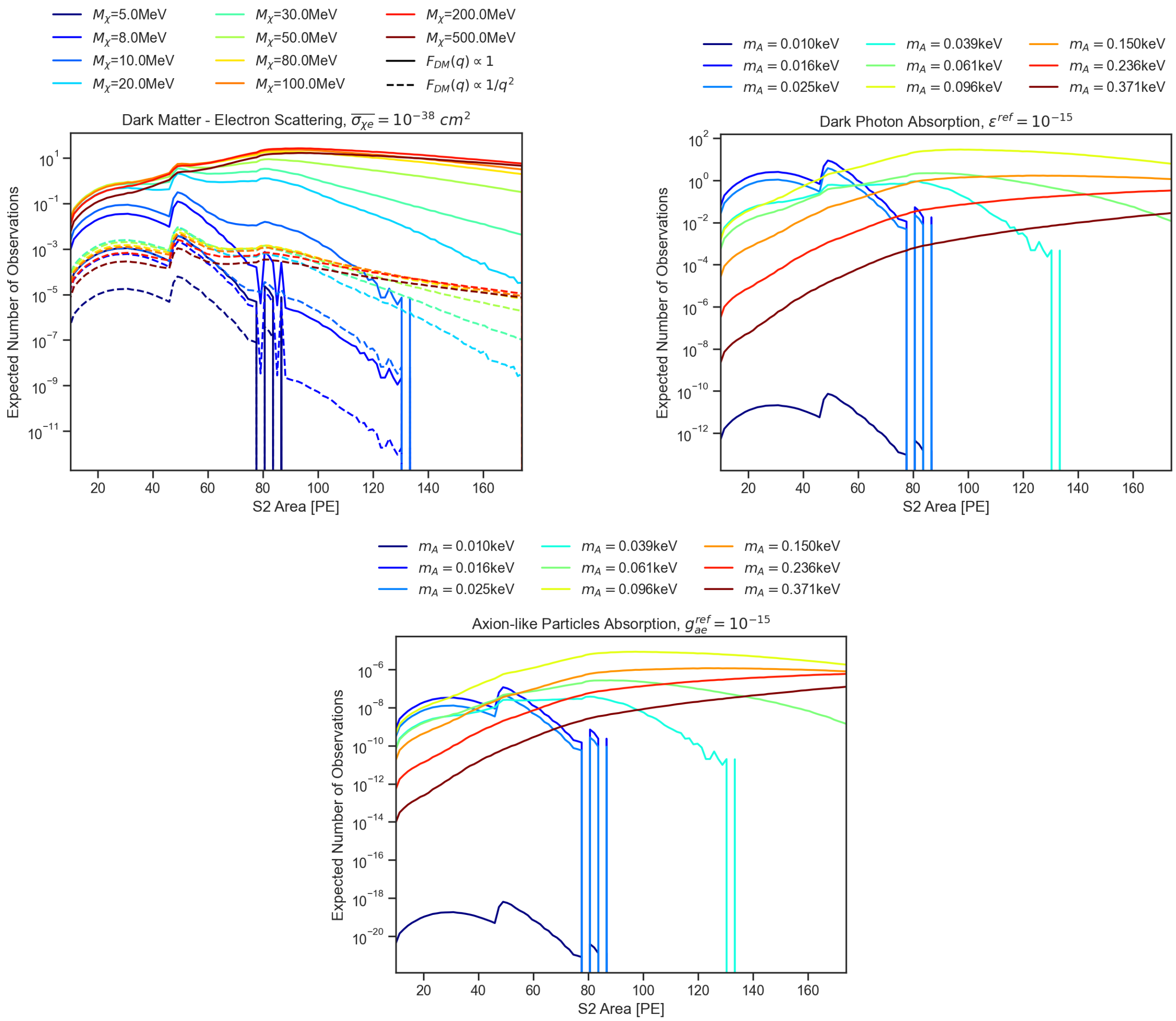

Figure 4.48: Expected S2 area spectra from different BSM physics interactions at nominal interaction strengths (under TED exposure).

produces two electrons [28] are boosted significantly, resulting in the cusps near S2 area = 40 PE. Similarly, the cusps near S2 area = 80 PE are also resulted from the increase of the total exposure from $N_{e,rec} = 2$ to $N_{e,rec} = 3$ (10 times from the table). While the resolution of S2s with sizes down to single electron allows us to probe interactions that deposit minimal energies to the xenon orbital electrons, such a boost in the expectation spectra allows us to set more stringent limits to the models that allow higher energy interactions.

---

[28] To be precise, produces a certain S2s that are reconstructed as two electrons, i.e., $N_{e,rec} = 2$.

The DM-electron scattering energy spectra transition smoothly from low-mass DM particles to higher-masse ones, shifting the expected S2 spectra gradually to have a larger weight on the S2s with a larger number of electrons. Thus, within the range of DM masses we considered, the huge total exposure for $N_{e,rec} > 1$ benefits all models, especially for the light masses because the originally low-rate region is boosted. The same statement is true also for the DP particles with low masses, or ALPs with low masses.

On the other hand, the peak of the expected S2 area spectra for DP with higher masses (and similarly, ALP with higher energy) is beyond our ROI, and we are only capturing the tail of the whole distribution. Although the tails still get a boost in the total expected number of observations, the missing peak inside our ROI would make us less competitive with respect to the experiments with an ROI covering the location of the peak, e.g., the traditional S2-only analysis where the ROI is beyond 5 e^-.

4.6 The Statistical Inference Framework

Thus far, I have illustrated the efforts to mitigate the substantial background called the Delayed Electrons (DEs), a remnant from large S2s that contaminates the ROI of the few-electron analysis between 1 e^- and 5 e^-. The final dataset and the exposures were fine-tuned to provide the cleanest space in the detector and time during SR0 of XENONnT for the search of physics Beyond the Standard Model. Nevertheless, as mentioned in Sec. 4.1, there are still traces of independent backgrounds remaining, for which accurate quantification is hard. Therefore, we have to acknowledge that part – if not all – of the remained S2 population shown in Fig. 4.42 might be from contributions of all sources that are not quantified. To cope with such an unknown contribution, a conservative approach of an upper limit (UL)-only inference was adopted.

We used Yellin's Optimal Interval Method introduced in Ref. [114] as our statistical tool for setting the UL. To understand it, first, we need to introduce the Maximum Gap Method, which is also introduced in Ref. [114]. Here, I will briefly introduce the methods.

4.6.1 Maximum Gap Method

The Maximum Gap Method, as the name indicates, looks at the gaps between observed events where no observation is recorded (regions between the vertical lines in the left plot of Fig. 4.42) and calculates the maximum probability of no observation allowed by the physics model we would like to test. Without the loss of generality, let's use a generic Model A with a parameter of interest σ (e.g., the light dark matter model with the dark matter electron scattering cross section $\sigma_{\chi e}$), which predicts an expected number of observations in the S2 area space (e.g., any one line in Fig. 4.48). Let's use the nomenclature introduced in Eqn. 4.11 and express the expected number of events from interactions predicted by Model A as a function of S2 area, as $\mathcal{N}_{PE}(S2)$ $[PE^{-1}]$. Then within the gap between the i-th and $(i+1)$-th data point, the total number (x_i) of expected events can be obtained by

$$x_i = \int\limits_{S2_i}^{S2_{i+1}} \mathcal{N}_{PE}(S2)\, dS2, \tag{4.12}$$

and the maximum of all x_i is named the "maximum gap", denoted as x. Such a process is illustrated in Fig. 4.49. Notice that by definition, our $\mathcal{N}_{PE}(S2)$ has the unit of counts/PE, and thus is equivalent to the dN/dE in the figure taken from Ref. [114].

The value of x is directly influenced by the parameter σ. If the chosen σ value allows interactions predicted by Model A to happen frequently, i.e., we would have calculated a large x, it is quite unlikely to observe 0 events within the gap that the x is computed from. From this fact, we can reject values of σ with the values of x and thus set upper limits. As reasoned in Ref. [114], the distribution of this variable x, independent from the shape of $\mathcal{N}_{PE}(S2)$, is always uniformly distributed with unity density. Also, with a fixed ROI, the total expected number of events, μ, is also independent of the $\mathcal{N}_{PE}(S2)$ shape. Thus, we

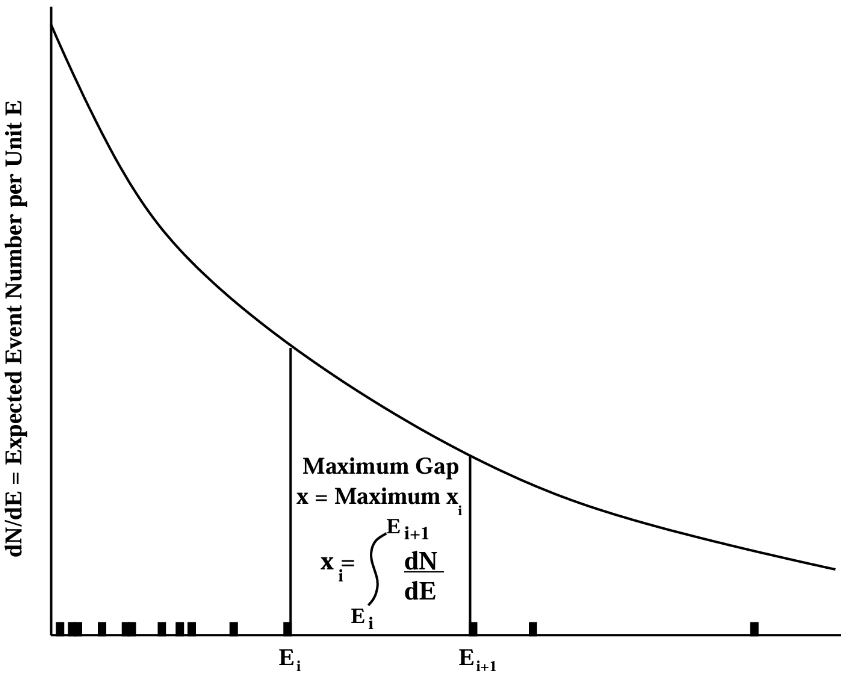

Figure 4.49: Illustration of the maximum gap method. In our case, E is the S2 area, dN/dE is the $\mathcal{N}_{PE}(S2)$. Figure taken from Ref. [114].

can reject the hypothesis (Model A with specific σ value being true) with confidence level (CL) C_0:

$$C_0(x,\mu) = \sum_{k=0}^{m} \frac{(kx-\mu)^k e^{-kx}}{k!} \left(1 + \frac{k}{\mu - kx}\right). \tag{4.13}$$

The full derivation of Eqn. 4.13 can be found in Appendix.A of Ref. [114]. To find the desired 90% CL UL, we just tune the σ value such that μ and x gives a $C_0(x,\mu)$ at 0.9.

4.6.2 Optimal Interval Method with Pmax

The Optimal Interval Method goes beyond the Maximum Gap Method and only looks at gaps between adjacent observations (thus, the 0-event gaps). In the Optimal Interval Method, all possible gaps are investigated. For the gaps containing n observed events, we can obtain a Maximum Gap value x_n (the x found Maximum Gap Method would be x_0 by this definition). Then, we need to compare the set of x_n's. A penalty term is needed to disfavor the large

n values because otherwise, the gap with the largest x_n would be the whole ROI. In our analysis, we adopted a method called Pmax, which utilizes the Poisson p-value (actually, 1 - the p-value) for the penalty term, defined as:

$$T_{pmax} = \max_{\text{all } n} \left(\sum_{k>n} \left(\frac{(x_n)^k}{k!} e^{-x_n} \right) \right). \tag{4.14}$$

The determination of CL is achieved by Monte Carlo. For a sufficiently large amount of σ values sampled, we simulate the event distribution predicted by Model A with the sampled σ and compute T_{pamx} value. Then the 90 percentile value of T_{pmax} and its corresponding σ value is taken as the 90% CL UL. More details regarding the Pmax variables can be found in Ref. [115].

4.7 Constraints On Physics Beyond the Standard Model

Here, I report the preliminary limits on the cross-section of Dark Matter electron scattering through heavy and light mediators, the kinetic mixing between the dark photon and the SM photon, and the coupling strength between Axion-like particles with the SM electron. These preliminary results were obtained from the TED dataset. We are aiming to unblind the science runs of SR0 soon.

For the LDM-electron scattering cross section, we achieved world-leading results in the LDM mass range of (7, 25) MeV for the interaction that happens through a heavy mediator and (20, 100) MeV for the light mediator. For the dark photon absorption, we achieved leading results in the UL of the kinetic mixing parameter in the boson mass range of (0.01, 0.2) keV. In a similar range (in the unit of energy), we set the most stringent limit for the Axion-like particle-electron coupling strength. Such stringent constraints benefited mostly from our huge target mass, high liquid purity, and high detection efficiency down to single electrons. We were able to probe theoretically an energy deposition as low

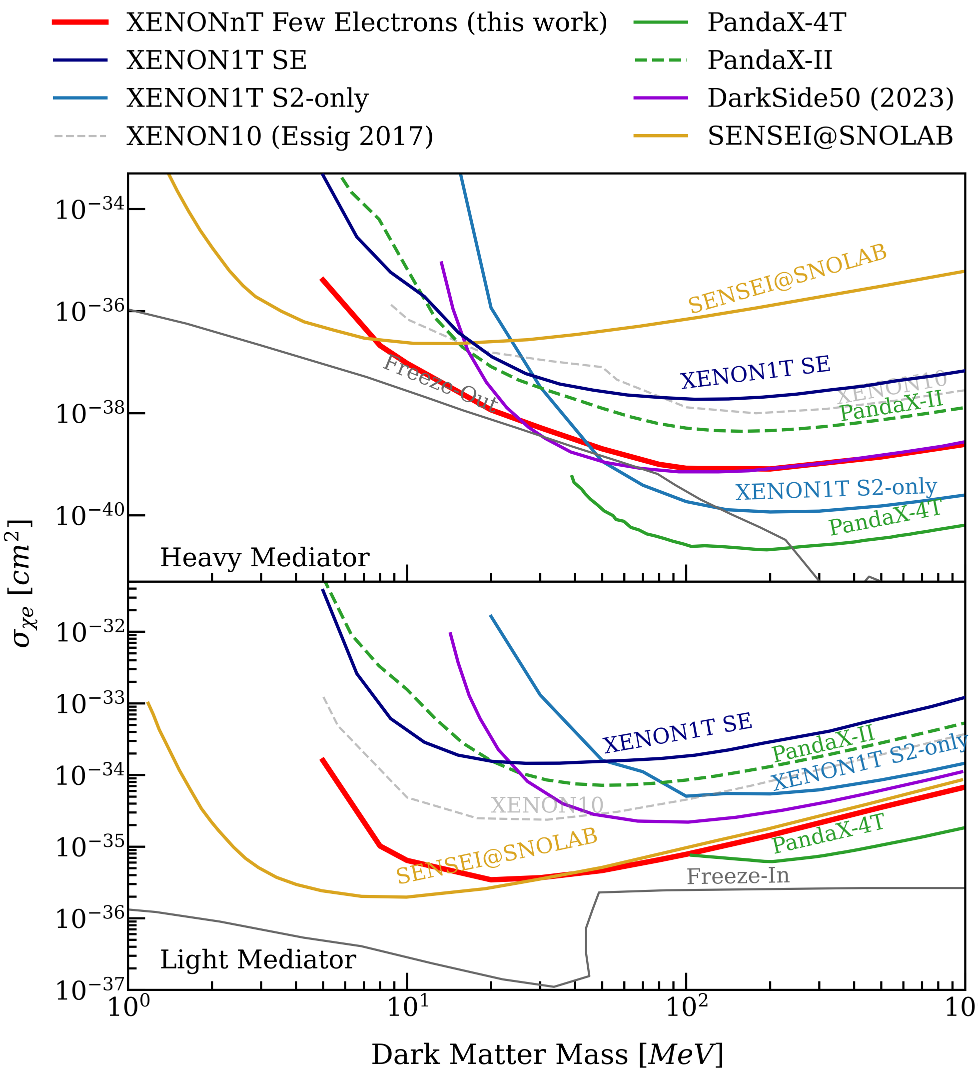

Figure 4.50: Upper limits of DM - electron cross-section $\sigma_{\chi e}$ with heavy mediator (top) and light mediator (bottom) assumptions. The results of this analysis are shown in red.

as $\sim 9.276\ eV$ [116], the band gap of liquid xenon, with which the xenon atom can be just ionized and the electron can be potentially detected[29].

However, the minimum energy required to produce an electron in liquid xenon (the band gap at $9.276\ eV$) and the kinetic energy required for the ionization electron to be multiplied through electronic recoil ($\sim 13.7\ eV$ per quanta with ~ 0.88 of the cases such quanta is an

---

[29] If the deposited energy is just above the band gap, the ionization electron would be kicked out with almost 0 kinetic energy, and thus does not trigger the ER process. However, the very ionization electron can drift up and be detected

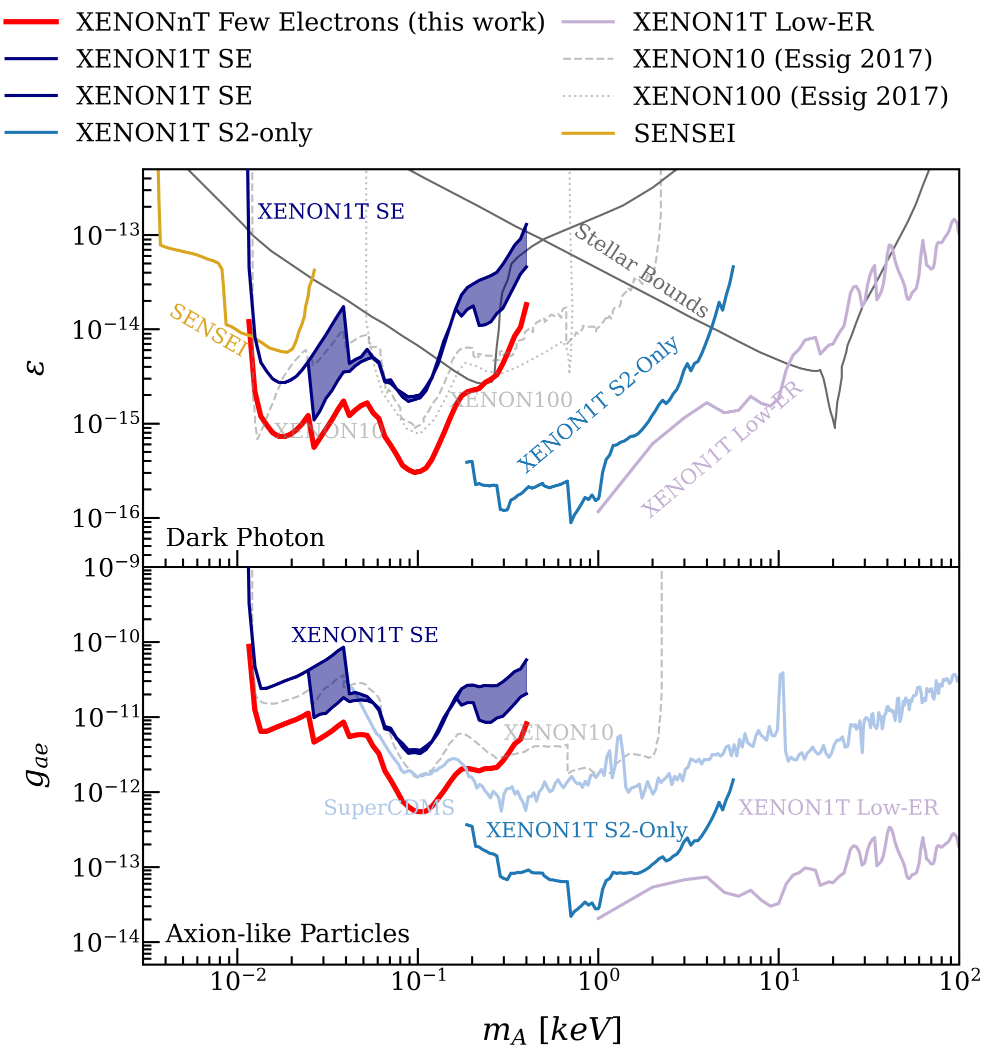

Figure 4.51: Upper limits of dark photon kinetic mixing strength (ϵ) with the SM photon (top) and the coupling strength between Axion-like Particles and the SM electron (g_{ae}) (bottom). The results of this analysis are shown in red.

electron) made us not competitive to the detectors featuring a much smaller energy expense for interactions that deposit less energy. For example, the skipper CCD technology used in Sensei [117] and DAMIC-M [118] features triggering energy as low as 4 eV [119], which makes them sensitive to interactions with much lighter dark matter particles, with which the interaction would be too weak to create ionization signals in a typical liquid xenon detector.

On the other hand, for interactions that deposit more energy, i.e., heavier dark matter masses, more massive vector bosons, and ALP with higher energy, we are limited by the lack of a full background model. Analyses from other experiments, like PandaX-4T [120], or other channels within XENON Collaboration, like the traditional S2-only analysis [106], either assumed full background model by excluding the lowest part of their ROI or performed partial background subtraction.

Looking back at the whole analysis framework, there are several points that we can improve for future studies:

- The delay time cut removes a tremendous amount of exposure, which intuitively is unnecessary. From the illustration of Fig. 4.40, for the purpose of removing the Delayed Electrons that are position correlated, we could simply remove a cylinder extending beyond the time gap between two primary S2s. This potentially can help us retrieve a considerable amount of exposure, thus increasing our sensitivity. An effort in this direction is elaborated in Ch. 5;
- As mentioned in Sec. 4.1, there are lots of background sources that can contaminate our ROI, for which we didn't quantify because proper removal of the dominant DE background was more rewarding. With dedicated modeling for the part – if not all can be modeled – of such background sources, we could further suppress the final event rate;
- The ambiguities of peak reconstruction discussed in Sec. 3.2.2 is unavoidable in the data processing pipeline. Such a proposal can be tested against data and might improve the results by getting rid of the biases in peaklet merging.

CHAPTER 5

A NEW MODEL FOR TIME CORRELATED BACKGROUND

One major task of the few-electron analysis discussed in Ch. 4 was to remove the DE (delayed electron) population. However, with the method described in Sec. 4.4 (more specifically, the time and spatial correlation vetos) the final strategy of DE removal was based on optimizing the signal-to-background ratio. Such a strategy, while effective, is hardly satisfactory because we can never claim a full removal of the DEs and assign cut acceptances. This unknown contribution of DEs limited the few-electron analysis to be background-limited and have no power to claim discovery[1].

In this chapter, I will introduce a method for obtaining a description of the time profile of these delayed electrons independently of their origin. In Sec. 5.1, I will set up a new framework involving a generic set of definitions and a new method of pairing up small S2s (sS2s) and primary S2s (pS2s) that creates an analyzable structure. In Sec. 5.2, I will discuss the situation in which only random pairings can happen, assuming no DE population in the detector, and derive analytical expressions for the spatial and time correlations between sS2s, from independent small energy depositions or irreducible backgrounds, and pS2s. In Sec. 5.3, I will turn to discuss the other scenario, where only pS2s and their DEs exist in the detector, with no other independent event creating sS2s, and derive analytical expressions for the correlations. Finally, in Sec. 5.4, I will combine the discussions and propose two strategies to establish a model-independent time correlation function.

---

[1] Also, I acknowledge the other not quantified sources of irreducible backgrounds. However, those are from sources we might be able to measure or estimate, either using projections from the S1-S2 analyses or by measurements of detector components. In contrast, the DE population is related to an unknown mechanism in the liquid that could very much vary from detector to detector, and thus, it is hard to quantify or be inferred from results of dedicated small-scale investigations.

5.1 New Framework Setup

The real situation is schematically shown in Fig. 5.1. Three major components need to be considered (besides noises and junk signals that can be safely removed with quality cuts):

1. pS2s: large physical S2s that has the potential to deposit small amount of e^- in LXe;
2. DEs: the delayed electrons associated with pS2s, featuring strong time and spatial correlations with their pS2s;
3. Signals: in this chapter, I define it as small S2s from either real energy deposition or independent irreducible backgrounds.

I will use small S2s (sS2s) to refer to both DEs and signals for simple nomenclature.

First, I introduce a new practice for matching up pS2s and sS2s: for each sS2, scan backward in time with a fixed window and sort the pS2s inside this window by their spatial distance from this sS2. We also need to define the relevant parameters. First, a *spatial correlation function*, $P_r(r)$, has to be assumed, which describes the spatial diffusion of DEs to their pS2 as a probability function. Also, we have to assume a *time correlation function*, $P_t(t)$, that describes the distribution of DEs after their pS2 as a probability function. Notice that r and t are the **distance and time gap between an sS2 and its paired pS2**. R_{fa} is a radius within which we analyze sS2s[2], and to simplify the calculation, such R_{fa} is assumed to be much smaller than the detector radius (R_d), within which pS2s can happen (more explanation later). Furthermore, we have to assume some constants: *rate of pS2* f_p, *rate of DE* f_{DE}, and *rate of signal* f_s. One last parameter we will need is the *scanning window*, w, which is from each DE how far back in time we search for pS2 to pair with.

To facilitate the derivations, here I assumed no pS2 size dependence, no DE size dependence, and no detector condition variations for the two correlation functions and rates of the

---

[2] It is exactly the definition of the Fiducial Area (FA), elaborated in Sec. 4.4. For simplicity, the FA is assumed to be a disk without punctures with radius R_{fa}.

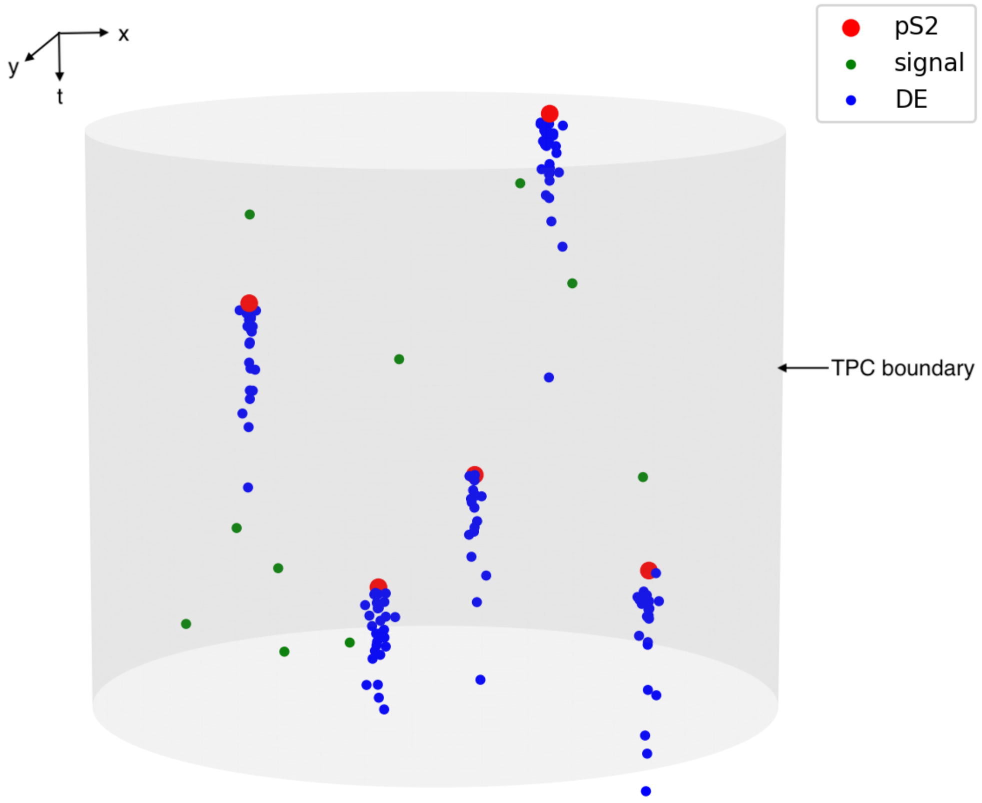

Figure 5.1: Drawing of pS2s (red) and their DE (blue) trends in TPC, together with uncorrelated signals (green). The leakage from pS2s into the later ones will be recognized as "uncorrelated" signals most of the time. Also, the uncorrelated signals will boost the estimation of the DE trend. It is worth mentioning that the height of the TPC, z, is a fourth dimension not shown in this plot, while the vertical direction in the plot is time.

relevant populations, as all these are worthy parameters to look into after some simple model is established. Also, the pS2s distribution is assumed to be random and uniform. After we pair up sS2s and pS2s and arrange the pS2s with their distances from the sS2s, we can take the nearest pS2s seen by an sS2 as an example. Three scenarios can happen:

1. the considered sS2 is a DE, and it is correctly paired with its pS2;
2. the considered sS2 is a DE, but it is wrongly paired with some other pS2;
3. the considered sS2 is a signal, and it is wrongly paired with some preceding pS2.

The latter two situations can similarly be accidental coincidences (AC). These three scenarios can be propagated to higher orders of paired pS2s. It is necessary to notice that **not only the signals can form AC by default, but also DEs**.

These set the foundation for analyses that will be explored in later sections.

5.2 Random Pairing between Signals and Primary S2s

The pairings between the signals and pS2s are simply matching two random populations inside two concentric circles (reminder, pS2s can happen within the full TPC radius R_d while sS2s are constrained inside a smaller FA R_{fa}). Therefore observing the nearest pS2 before a given signal at distance r, with a scan window w, can be understood as

1. observe 1 pS2 within an rdr annulus. If we have m pS2s in the scan window, we have m choices to be the nearest pS2, which is $m\frac{\mathcal{R}(r;x,y)rdr}{\pi R_d^2}$, where $\mathcal{R}(r;x,y)$ is a function that calculates the angle of the segment of a circle centered at (x, y) (location of the signal) with radius r inside TPC. It is a measure depending on (r, x, y) when doing integrations. For easy reference I define $\mathcal{D}r(r;x,y) = \mathcal{R}(r;x,y)rdr$;

2. observe 0 pS2 within r;

3. observe all the rest outside r, which can be simply expressed as the reciprocal of the area of TPC subtracted by a circle of radius r. $\left(1 - \frac{A_I(r;x,y)}{\pi R_d^2}\right)^{m-1}$, where $A_I(r;x,y)$ is a function that calculates the intersection area of a circle centered at (x, y) with radius r with TPC;

4. Finally we assign the probability of observing m pS2s within w and sum over all possible situations: $\sum\limits_{m\geq 1} \text{Poisson}(m; f_p w)$.

The TPC is always assumed to be a circle centered at (0,0) with radius R_d. Combining the steps above, an expression for observing the nearest pS2 at a distance r can be expressed as

$$\begin{aligned} &\rho_{s,r}(r;x,y;1,w)\mathcal{D}r(r;x,y) = \sum_{m\geq 1} m\text{Poisson}(m;f_p w)\frac{\mathcal{D}r(r;x,y)}{\pi R_d^2}\left(1-\frac{A_I(r;x,y)}{\pi R_d^2}\right)^{m-1} \\ \Rightarrow &\rho_{s,r}(r;x,y;1,w) = \sum_{m\geq 1} m\text{Poisson}(m;f_p w)\frac{1}{\pi R_d^2}\left(1-\frac{A_I(r;x,y)}{\pi R_d^2}\right)^{m-1}. \end{aligned} \tag{5.1}$$

$\rho_{s,r}(r;x,y;1,w)$ is the probability of observing the nearest pS2 given a signal at (x,y) at a distance r, with a scan window w. The 1 here indicates "nearest", or spatially the first pS2, compared to later pS2s with higher orders. An example of $\mathcal{R}(r;x,y)$ and $A_I(r;x,y)$ is shown in Fig. 5.2. Notice that $\rho_{s,r}(r;x,y;1,w)$ doesn't directly depend on $\mathcal{R}(r;x,y)$. If we assume R_d to be sufficiently large ($R_d \geq r + R_{fa}$), the two functions can be simplified to

$$\begin{aligned} \mathcal{R}(r;x,y) &= 2\pi \\ A_I(r;x,y) &= \pi r^2. \end{aligned} \tag{5.2}$$

This assumption is a good approximation if R_{fa} is set to be extremely small, i.e., we choose a very small FA. And Eqn. 5.1 can be simplified to

$$\rho_{s,r}(r;1,w) = \sum_{m\geq 1} m\text{Poisson}(m;f_p w)\frac{1}{\pi R_d^2}\left(1-\frac{r^2}{R_d^2}\right)^{m-1}. \tag{5.3}$$

It is worth mentioning that Eqn. 5.1 is not a normalized probability density function, i.e., the integration over r might be smaller than one because there might be a case that there is zero pS2 before a given signal. **This formula describes a probability of paired population**. This will be true for all ρ functions in this section.

As for the time gap between a signal and its nearest pS2, since pS2 is completely random from the viewpoint of signals, the distribution of such gap is simply the probability of

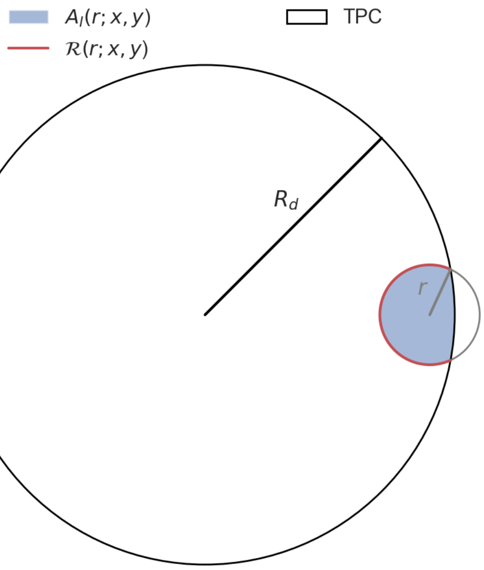

Figure 5.2: Illustration of $\mathcal{R}(r;x,y)$ and $A_I(r;x,y)$ with a signal happening at the edge.

observing a pS2 within an infinitesimal timepiece dt out of the full window w. In a scenario where multiple pS2s are observed because pS2s are independent events, anyone can be the nearest to this signal. Thus, the distribution of the time gap is independent of n, except for the probability of observing n pS2s within w as a prior. An illustration is shown in Fig. 5.3. The probability of observing the nearest pS2 in an infinitesimal delay time tdt can be expressed as

$$\rho_{s,t}(t;1,w)dt = \frac{dt}{w}\sum_{m\geq 1}\text{Poisson}(m;f_p w). \tag{5.4}$$

The distribution of spatially farther pS2s can be derived with a similar logic. While the generalization of $\rho_{s,t}(t;n,w)dt$ is simply limiting the occasion that allows an observation of n-th pS2, expressed as

$$\rho_{s,t}(t;n,w)dt = \frac{dt}{w}\sum_{m\geq n}\text{Poisson}(m;f_p w). \tag{5.5}$$

The generalization of $\rho_{s,r}(r;x,y;n,w)$ needs to consider the distribution of pS2s inside r:

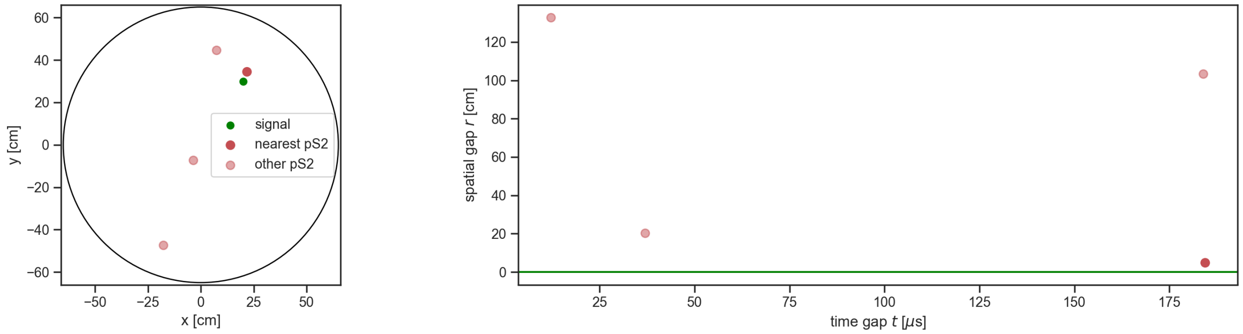

Figure 5.3: Example of spatial and temporal correlation between a signal and pS2s within w window before it. Left: the green dot indicates the (x, y) location of a signal, and the solid red dot is its nearest pS2 within a scan window w before the signal. Other shallower red dots are other pS2s in this window. Right: the green line is the reference location of the signal $(r = 0)$.

1. observe 1 pS2 within a rdr: $m\frac{\mathcal{D}r(r;x,y)}{\pi R_d^2}$ given m observed pS2s;
2. observe $n-1$ pS2 within r: $\frac{(m-1)!}{(n-1)!(m-n)!}\left(\frac{A_I(r;x,y)}{\pi R_d^2}\right)^{n-1}$;
3. observe all the rest outside r: $\left(1-\frac{A_I(r;x,y)}{\pi R_d^2}\right)^{m-n}$;
4. Finally we assign the probability of observing m pS2s within w and sum over all possible situations: $\sum\limits_{m\geq n}$ Poisson$(m; f_p w)$.

Combining the terms gives

$$\begin{aligned}
\rho_{s,r}(r;x,y;n,w)\mathcal{D}r(r;x,y)(r;x,y) = &\sum_{m\geq n}\text{Poisson}(m;f_p w)\frac{\mathcal{D}r(r;x,y)}{\pi R_d^2}\\
&\times\frac{m!}{(n-1)!(m-n)!}\left(\frac{A_I(r;x,y)}{\pi R_d^2}\right)^{n-1}\\
&\left(1-\frac{A_I(r;x,y)}{\pi R_d^2}\right)^{m-n}\\
\Rightarrow \rho_{s,r}(r;x,y;n,w) = &\sum_{m\geq n}\text{Poisson}(m;f_p w)\frac{1}{\pi R_d^2}\\
&\times\frac{m!}{(n-1)!(m-n)!}\left(\frac{A_I(r;x,y)}{\pi R_d^2}\right)^{n-1}\left(1-\frac{A_I(r;x,y)}{\pi R_d^2}\right)^{m-n}.
\end{aligned}\tag{5.6}$$

Taking $n = 1$ in Eqn.5.6 and Eqn. 5.5 reduces them into Eqn. 5.1 and Eqn. 5.4. This concludes the calculation of both spatial and time gap distributions of signals matching with pS2s. A few remarks:

1. because both signals and pS2s are independent, and there is no correlation between the distribution of spatial gap r and time gap t;
2. the time gap distribution $\rho_{s,t}(t; n, w)$ is independent of t and is a flat line. This is true for arbitrary choice of n.

It is hard to estimate Eqn. 5.6 in full form. But after implementing Eqn. 5.2, it is much more simplified and can be analyzed in Mathematica [121]. Notice that now Eqn. 5.6 is independent of (x, y). With $R_d = 65$ cm and $f_p = 6$ Hz, Fig. 5.4 shows values of $\rho_{s,r}(r; n = 1, w = 1\ s)$.The larger the n value, the further the average expectation of spatial gap is. Also, the longer the scan window w is, the shorter the minimum spatial gap between the signal and a pS2s is because more pS2s would be within the window. Remember the prior effectiveness of Eqn. 5.2 requires $R_d > r + R_{fa}$, which means at large $r \simeq R_d$, independent of the choice of R_{fa}, Eqn. 5.2 would not be a good approximation to Eqn. 5.6. Eventually, as a summary, the probability of observing the n-th pS2 having a spatial and time gap at (r, t) from random signal-pS2 pairs within a time window w can be expressed as

$$\begin{aligned}\rho_s(r, t; x, y; n, w) =& \frac{1}{w\pi R_d^2} \sum_{m \geq n} \text{Poisson}(m; f_p w) \\ & \times \frac{m!}{n!(m-n)!} \left(\frac{A_I(r; x, y)}{\pi R_d^2} \right)^{n-1} \left(1 - \frac{A_I(r; x, y)}{\pi R_d^2} \right)^{m-n} .\end{aligned} \tag{5.7}$$

It is important to notice that the summations overall contributing m in Eqn. 5.5 and Eqn. 5.6 are universal, so they are merged into one for Eqn. 5.7. However, when decoupling the spatial and temporal parts, such iteration needs to be returned to properly handle "not-observed pairs".

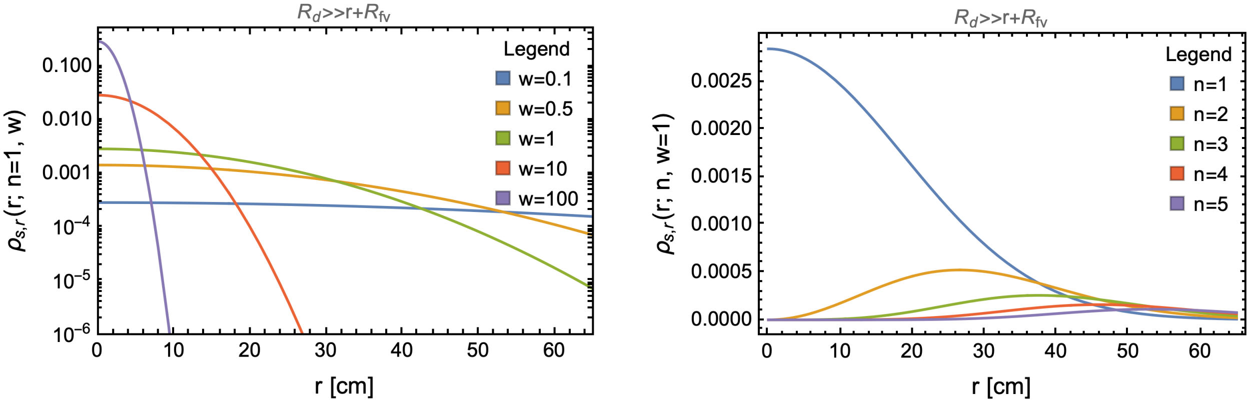

Figure 5.4: Evaluation of $\rho_{s,r}(r;x,y;n,w)$ with Eqn. 5.2 implemented. Left: Fixing $n=1$ and scan different w; right: fixing $w=1$ s and scan a few different n. The larger the n, the further the average expectation of spatial gap is. The longer the scan window w is, the shorter the minimum spatial gap between the signal and a pS2s is because more pS2s would be within the window.

MC is straightforward to construct for such a procedure. We can simply simulate two independent populations of pS2s and signals with different rates f_p and f_s and conduct the practice of matching pS2s before signals in ascending order of spatial gap. Intuitively, we should expect for each n-th nearest pS2 an average f_s/f_p number of signals, up to a factor of no observation (1 - the Poisson term in Eqn. 5.5). With $f_p = 4.7$ Hz, $f_s = 1.6$ Hz, $R_{fa} = 53.5$ cm and $R_d = 65$ cm (estimated from XENON SR0 TED runs), the results of this MC is shown in Fig. 5.5. The time gap distributions are flat and independent from t as predicted. Moreover, if corrected by division with respect to the coefficient $\frac{1}{w}\sum_{m\geq n}\text{Poisson}(m;f_p w)$ in Eqn. 5.5, the expected f_s/f_p rate can be restored, both for different w and different n, as shown in Fig. 5.6. The distribution of r is shown in Fig. 5.7. Compared with Fig. 5.4, simulation and mathematical evaluation results are very similar. The requirement that $R_d \gg R_{fa} + r$ is not assumed in the MC results, making it closer to a real-world detector setup than the depictions in Fig. 5.4.

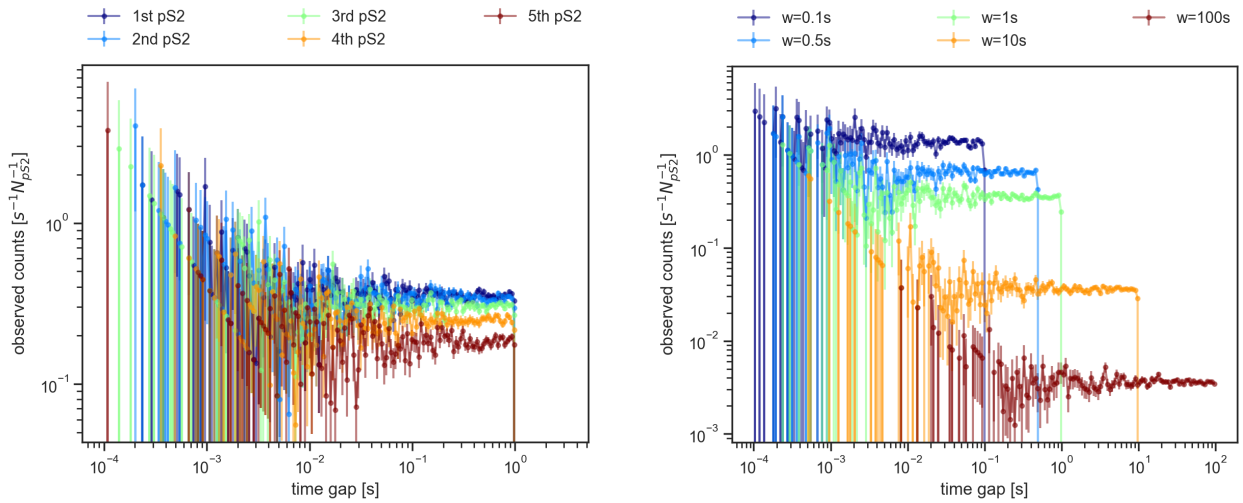

Figure 5.5: Time gap distribution from pairings between simulated signals and pS2s. Left: time gap distribution of 1st to 10th pS2 with a fixed $w = 1$ s; right: time gap distribution of 1st pS2 with different w's.

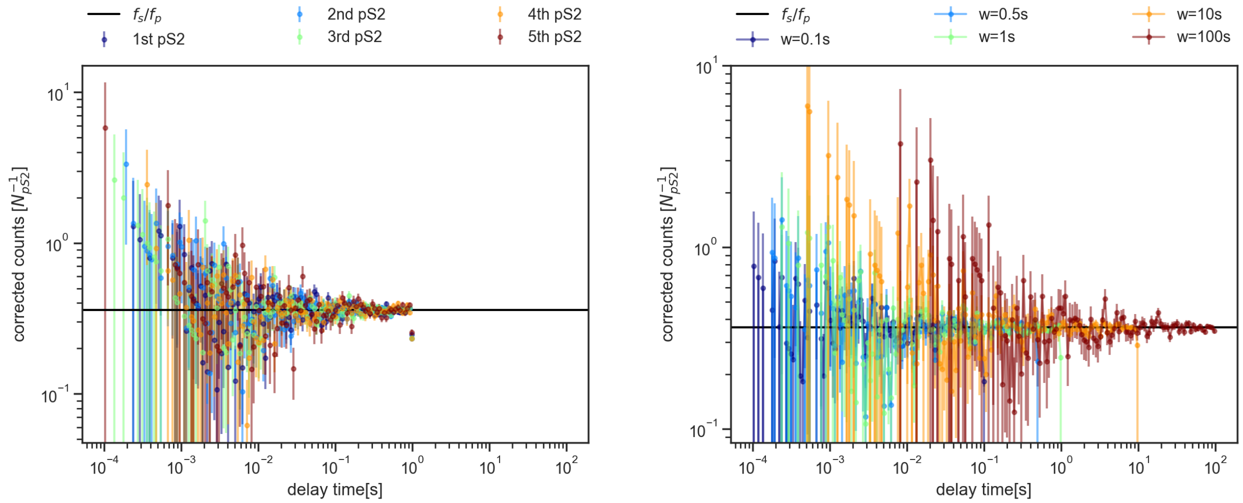

Figure 5.6: Corrected counts of signal per pS2 with correction factor. Left: time gap distribution of 1st to 10th pS2 with a fixed $w = 1$ s; right: time gap distribution of 1st pS2 with different scan windows.

5.3 Pairing Between Delayed Electrons and Primary S2s

DEs are remnants of pS2s and have temporal and spatial correlations with their pS2s. However, in a detector setting, there is no way to know which pS2 caused a certain DE. For each DE, if looking backward by w window, both the correlated pS2 and some other random ones

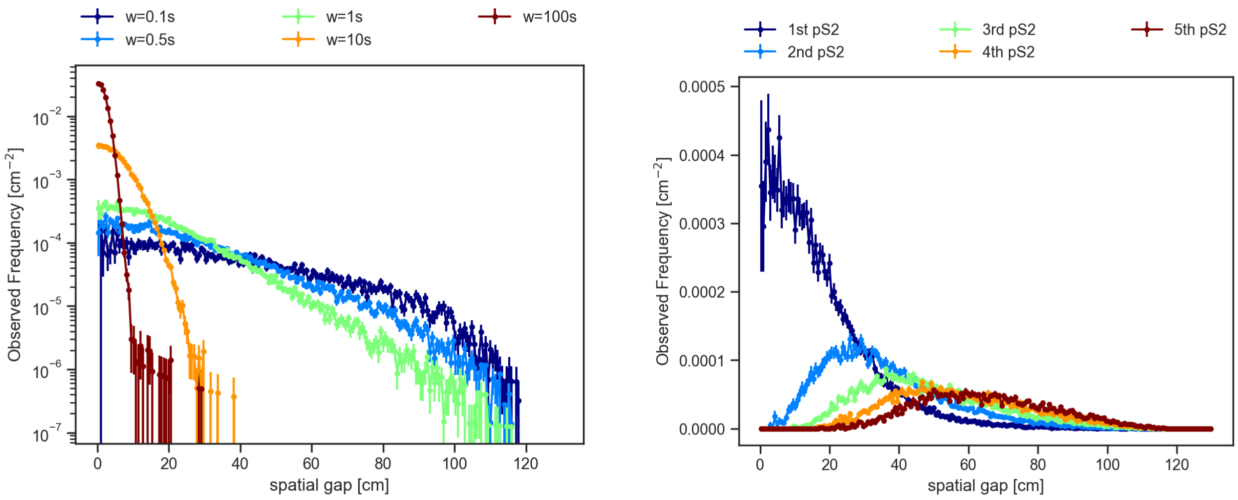

Figure 5.7: Spatial gap distribution from pairings between simulated signals and pS2s. Left: spatial gap distribution of 1st pS2 with different w; right: spatial gap distribution of 1st to 10th pS2 with a fixed $w = 1$ s.

can be seen:

1. expectation of seeing m-pS2 randomly is Poisson$(m; f_p w)$;
2. expectation of seeing the correlated pS2 is $\int\limits_0^w dt' P_t(t')$.

Since the practice of pairing sorts pS2s seen by an sS2 is with their spatial distance, the two cases need to be discussed separately. Still starting from the discussion of the nearest pS2 seen by a DE at (x, y) and discuss the distribution of observing it at a spatial and time gap (r, t):

1. The nearest pS2 is indeed the correlated one. Assume a total m pS2s are observed within the scan window w:
   (a) Observing it at a time gap tdt is simply $P_t(t)dt$;
   (b) All other pS2s in the window fall outside the radius of the correlated one r. Because all the rest are independent events, the probability of this happening is $\left(1 - \frac{A_I(r;x,y)}{\pi R_d^2}\right)^{m-1}$;

   (c) The correlated one lies within $\mathcal{D}r(r;x,y)$: $P_r(r)\mathcal{D}r(r;x,y)$;

   (d) m can be as low as 1;

2. Some random pS2 happens to be closer to the DE:

   (a) If the correlated pS2 is not observed, which has a probability of $1-\int\limits_0^w dt' P_t(t')$, the situation goes back to random pairing as Eqn. 5.7. This allows m to be as low as 1;

   (b) If the correlated pS2 is observed, which happens as $\int\limits_0^w dt' P_t(t')$:

      i. This correlated pS2 needs to lie outside r: $1-\int\limits_0^r \mathcal{R}(r';x,y)r'\, dr' P_r(r')$;

      ii. The rest reduces to the random pair scenario;

      iii. This only allows m to be as low as 2, with 1 correlated pS2 and a nearest random pS2;

   (c) For both scenarios, the key is to have at least one random pS2 to be the nearest one, so the time gap distribution is Eqn. 5.4 with m starting at 1.

For the first scenario where the correlated pS2 is indeed the nearest one, the probability of observing it at (r,t) can be expressed as (after canceling the measure terms)

$$\rho^{(1)}_{\mathrm{DE}}(r,t;x,y;1,w) = P_t(t)P_r(r)\sum_{m\geq 1}\mathrm{Poisson}(m-1;f_p w)\left(1-\frac{A_I(r;x,y)}{\pi R_d^2}\right)^{m-1}. \quad (5.8)$$

For the second scenario where the correlated pS2 is not the nearest one, we need to sum the cases of observation and no observation. The time gap distribution is simply a random pair situation described as Eqn. 5.4. The spatial component is derived as follows:

$$\begin{aligned}
\rho^{(2)}_{\mathrm{DE},r}(r;x,y;1,w) =& \left[\left(1-\int_0^w dt' P_t(t')\right)\sum_{m\geq 1}\mathrm{Poisson}(m;f_p w)\frac{m}{\pi R_d^2}\left(1-\frac{A_I(r;x,y)}{\pi R_d^2}\right)^{m-1}\right.\\
&+\left(1-\int_0^r \mathcal{R}(r';x,y)r'\,dr' P_r(r')\right)\int_0^w dt' P_t(t')\\
&\left.\times\sum_{m\geq 2}\mathrm{Poisson}(m-1;f_p w)\frac{m-1}{\pi R_d^2}\left(1-\frac{A_I(r;x,y)}{\pi R_d^2}\right)^{m-2}\right]\\
=&\left[\left(1-\int_0^r \mathcal{R}(r';x,y)r'\,dr' P_r(r')\int_0^w dt' P_t(t')\right)\right.\\
&\left.\times\sum_{m\geq 1}\mathrm{Poisson}(m;f_p w)m\left(1-\frac{A_I(r;x,y)}{\pi R_d^2}\right)^{m-1}\right].
\end{aligned} \tag{5.9}$$

Summing up the two components gives the final distribution of spatial and time gap of nearest pS2 observed by a DE, expressed as

$$\begin{aligned}
\rho_{\mathrm{DE}}(r,t;x,y;1,w) =& P_t(t)P_r(r)\sum_{m\geq 0}\mathrm{Poisson}(m;f_p w)\left(1-\frac{A_I(r;x,y)}{\pi R_d^2}\right)^{m}\\
&+\frac{1}{w\pi R_d^2}\left[\left(1-\int_0^r \mathcal{R}(r';x,y)r'\,dr' P_r(r')\int_0^w dt' P_t(t')\right)\right.\\
&\left.\times\sum_{m\geq 1}\mathrm{Poisson}(m;f_p w)m\left(1-\frac{A_I(r;x,y)}{\pi R_d^2}\right)^{m-1}\right]\\
\equiv& \rho_{\mathrm{cor}}(r,t;x,y;1,w)+\rho_{\mathrm{AC}}(r,t;x,y;1,w).
\end{aligned} \tag{5.10}$$

It is important to notice that even if we have fully correlated DE (i.e., absolutely no signal), we would see some ACs forming a flat background in t distribution that looks like what the signals would have formed. A few qualitative observations:

- ρ_{AC} has no explicit t dependence. This means similar to signal-pS2 pairing situation, the AC distribution for DE-pS2 pairing is also a flat trend, resembling Fig. 5.5;

- if $f_p w \ll 1$, the distribution is dominated by ρ_{cor};
- at large t we should expect ρ_{AC} to dominate, as $\lim\limits_{t\to\infty} P_t(t) = 0$. Of course, observation of large t is only enabled if w is large enough. In turn, a large w boosts the Poisson terms and allows more random pS2s to be observed, thus boosting the AC population;
- in cases where the correlated pS2 is observed within the window but is overcome by AC, such pS2 would be pushed to higher n-th pS2s. This is an important phenomenon with large w. In this case, the function $P_t(t)$ and $P_r(r)$ can be divided into branches that would show up in $n > 1$ pS2s-DE pairs.

The extension of Eqn. 5.10 to n-th pS2 needs to consider also that the correlated pS2, if observed, is pushed to which rank. The full scenarios are

1. The correlated pS2 is the n-th pS2. This is only allowed if m is larger than or equal to n:
    (a) This scenario will just follow $P_t(t)P_r(r)$ distribution;
    (b) There has to be $(n-1)$ random pS2s within r: $\frac{(m-1)!}{(n-1)!(m-n)!}\left(\frac{A_I(r;x,y)}{\pi R_d^2}\right)^{n-1}$;
    (c) The rest has to be all outside r: $\left(1-\frac{A_I(r;x,y)}{\pi R_d^2}\right)^{m-n}$;
2. The correlated pS2 is not the n-th pS2, the time gap distribution will be then reduced to random pairing case in Eqn. 5.5:
    (a) The correlated pS2 is observed and closer to the DE than n-th pS2. This allows m to be as low as n. Be careful here as if $n = 1$, this scenario is prohibited:
        i. For this to happen: $\int\limits_0^r \mathcal{R}(r';x,y)r'\,dr' P_r(r') \int\limits_0^w dt' P_t(t')$;
        ii. Observe a random pS2 at $\mathcal{D}r(r;x,y)$: $(m-1)\frac{\mathcal{D}r(r;x,y)}{\pi R_d^2}$;

    iii. There has to be $(n-2)$ random pS2s within r: $\frac{(m-2)!}{(n-2)!(m-n)!}\left(\frac{A_I(r;x,y)}{\pi R_d^2}\right)^{n-2}$;

    iv. The rest has to be outside r: $\left(1-\frac{A_I(r;x,y)}{\pi R_d^2}\right)^{m-n}$;

(b) The correlated pS2 is observed and farther to the DE than n-th pS2.This allows m to be as low as $n+1$:

    i. For this to happen: $\left(1-\int\limits_0^r \mathcal{R}(r';x,y)r'\,dr' P_r(r')\right)\int\limits_0^w dt' P_t(t')$;

    ii. Observe a random pS2 at $\mathcal{D}r(r;x,y)$: $(m-1)\frac{\mathcal{D}r(r;x,y)}{\pi R_d^2}$;

    iii. There has to be $(n-1)$ random pS2s within r: $\frac{(m-2)!}{(n-1)!(m-n-1)!}\left(\frac{A_I(r;x,y)}{\pi R_d^2}\right)^{n-1}$;

    iv. The rest has to be outside r: $\left(1-\frac{A_I(r;x,y)}{\pi R_d^2}\right)^{m-n-1}$;

(c) The correlated pS2 is not observed, then this is reduced to a random pairing scenario with a factor $1-\int\limits_0^w dt' P_t(t')$. This allows m to be as low as n.

All these scenarios give rise to the following distributions:

$$
\begin{aligned}
\rho_{\mathrm{AC}}(r,t;x,y;n>1,w) = \frac{1}{w\pi R_d^2}\Bigg\{ &\Bigg[\int_0^r \mathcal{R}(r';x,y)r'\,dr' P_r(r')\int_0^w dt' P_t(t') \\
&\times \sum_{m\geq n}\mathrm{Poisson}(m-1;f_p w)\frac{(m-1)!}{(n-2)!(m-n)!} \\
&\times \left(\frac{A_I(r;x,y)}{w\pi R_d^2}\right)^{n-2}\left(1-\frac{A_I(r;x,y)}{\pi R_d^2}\right)^{m-n}\Bigg] \\
&+\Bigg[\left(1-\int_0^r \mathcal{R}(r';x,y)r'\,dr' P_r(r')\int_0^w dt' P_t(t')\right) \\
&\times \sum_{m\geq n}\mathrm{Poisson}(m;f_p w)\frac{m!}{(n-1)!(m-n)!} \\
&\times \left(\frac{A_I(r;x,y)}{\pi R_d^2}\right)^{n-1}\left(1-\frac{A_I(r;x,y)}{\pi R_d^2}\right)^{m-n}\Bigg]\Bigg\};
\end{aligned}
\tag{5.11}
$$

$$\begin{aligned}\rho_{\text{cor}}(r,t;x,y;n,w) =& P_t(t)P_r(r)\sum_{m\geq n}\text{Poisson}(m-1;f_pw)\frac{(m-1)!}{(n-1)!(m-n)!}\\ &\times\left(\frac{A_I(r;x,y)}{\pi R_d^2}\right)^{n-1}\left(1-\frac{A_I(r;x,y)}{\pi R_d^2}\right)^{m-n};\end{aligned} \tag{5.12}$$

$$\rho_{\text{DE}}(r,t;x,y;n,w) = \rho_{\text{cor}}(r,t;x,y;n,w) + \rho_{\text{AC}}(r,t;x,y;n,w). \tag{5.13}$$

For the $n = 1$ case, the first bracket in Eqn. 5.11 is prohibited and should be set to 0. In this way $\rho_{\text{AC}}(r,t;x,y;n=1,w)$ is consistent with Eqn. 5.10. A close inspection of Eqn. 5.11 shows no t dependence, which is expected as AC is, by definition, random pairing.

It is hard to analyze the r distribution, but we can still try to extract information based on simple observations. Firstly, an integration over t and r should give unity subtracted by cases that are not allowed, i.e., when $m < n$. Since the only explicit t dependence comes from ρ_{cor}, the integration can be separated into three components as

$$\begin{aligned}\int_0^w dt\int_r \mathcal{D}r(r;x,y)\rho_{\text{DE}}(r,t;x,y;n,w) &= 1-\sum_{m=0}^{n-1}\text{Poisson}(m;f_pw)\\ &= c_1(n,w;x,y)\int_0^w dtP_t(t) + c_2(n,w;x,y)\\ &\equiv \mathcal{P},\end{aligned} \tag{5.14}$$

where $c_1(n,w;x,y)$ and $c_2(n,w;x,y)$ are integration results from r dependent parts in Eqn. 5.12 and Eqn. 5.11. They only depend on the actual position of the observed DE, the n index considered, and the w window (besides the detector-specific f_p, but it is not treated as a variable). Notice that $\int_0^w dt\frac{1}{w} = 1$. While the t and r dependencies are decoupled, since what we are interested in is the $P_t(t)$ function, we can integrate over $\mathcal{D}r$ without disturbing c_1 and c_2.

$$\begin{aligned}\int\limits_r \mathcal{D}r(r;x,y)\rho_{\text{DE}}(r,t;x,y;n,w) &= c_1(n,w;x,y)P_t(t)+\frac{c_2(n,w;x,y)}{w} \\ &\equiv \rho_{\text{cor},t}(t;x,y;n,w)+\rho_{\text{AC},t}(t;x,y;n,w). \end{aligned} \tag{5.15}$$

Notice that although $\rho_{\text{AC},t}$ has no explicit t dependence, I added in the argument for consistency. Unless we know the exact $P_r(r)$, it is hard to guess what $c_1(n,w;x,y)$ and $c_2(n,w;x,y)$ are. However, the analysis can still go further if we assume a large w and a reasonably decreasing $P_t(t)$. For a large w where $P_t(w) \sim 0$ and $\int\limits_0^w dtP_t(t) = 1$, Eqn. 5.14 is reduced to

$$c_1(n,w;x,y)+c_2(n,w;x,y)=\mathcal{P} \tag{5.16}$$

Focusing only on the AC term (Eqn. 5.11), we can rearrange Eqn. 5.14 and drop the time integral, which will result in a time correlation function for the ACs as

$$\begin{aligned}\rho_{\text{AC},t}(t;x,y;n,w) &= \int\limits_r \mathcal{D}r\rho_{\text{AC}}(r,t;x,y;n,w) \\ &= \frac{1}{w}\left(\mathcal{P}-\int\limits_0^w dt\int\limits_r \mathcal{D}r\rho_{\text{cor}}(r,t;x,y;n,w)\right) \\ &= \frac{1}{w}\sum_{m\geq n}\text{Poisson}(m;f_pw)\left(1-c_1(n,w;x,y)\int\limits_0^w dtP_t(t)\right). \end{aligned} \tag{5.17}$$

Eqn. 5.17 has the same form as Eqn. 5.5, except for the extra coefficients where the correlated pS2 is paired with DE on its n-th position.

Implementing Eqn. 5.2 to Eqn. 5.13 and use Mathematica [121] to evaluate the functions. The time correlation function $P_t(t)$ is assumed to be exponential, and the spatial correlation

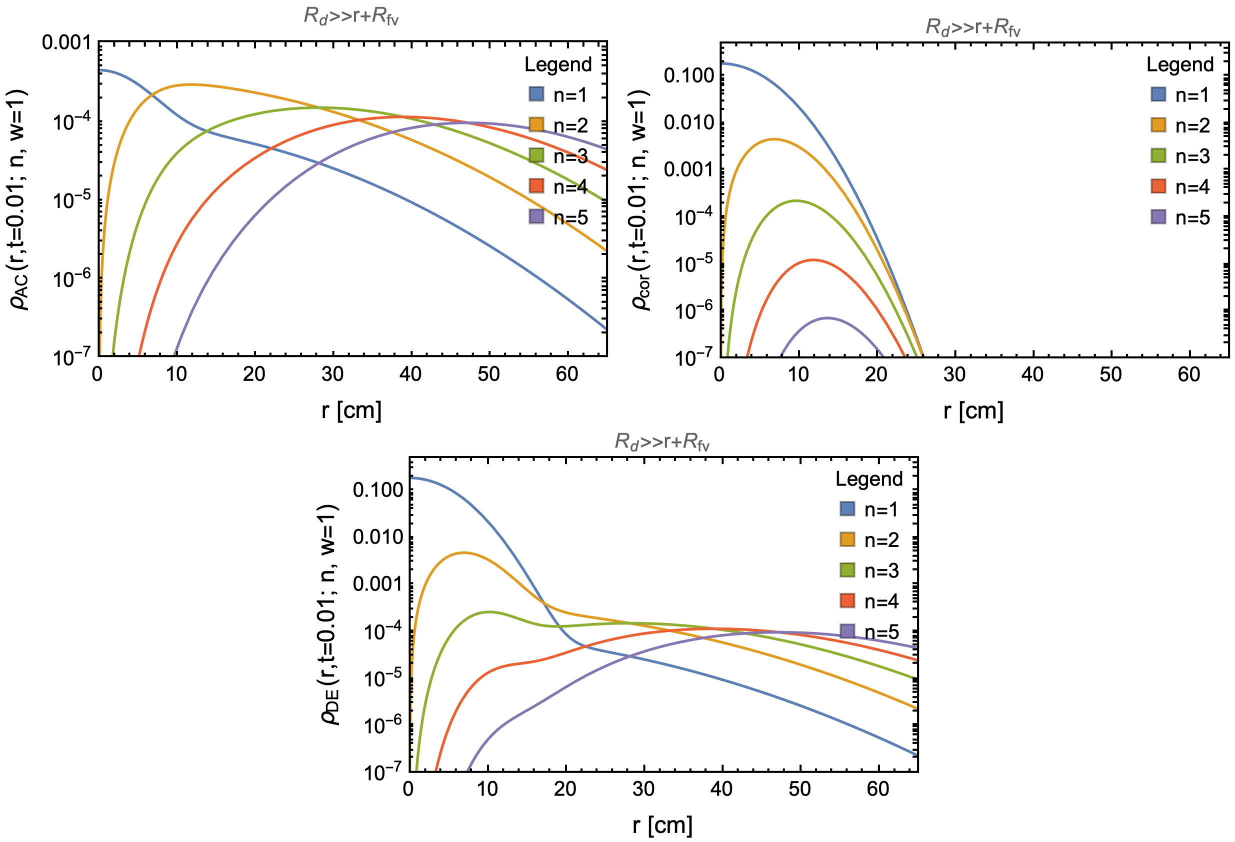

Figure 5.8: ρ_{AC}, ρ_{cor}, and ρ_{DE} with large R_d condition (Eqn. 5.2) implementation, in the sequence from left to right, and from top to bottom. The scan window w is fixed at 1 s, and the functions are evaluated at $t = 0.01$ s.

function is a 2-D Gaussian. They are summarized as

$$\begin{aligned} P_t(t; \tau = 0.01\text{s}) &= \frac{1}{\tau} e^{-\frac{t}{\tau}} \\ P_r(r; \sigma = 5\text{cm}) &= \frac{1}{\sqrt{2\pi^3}\sigma^2} e^{-\frac{r^2}{2\sigma^2}}. \end{aligned} \tag{5.18}$$

With a fixed $w = 1$ s and different n, ρ_{cor}, ρ_{AC}, and their sum ρ_{DE} are evaluated at a fixed $t = 0.01$ s and the results are shown in Fig. 5.8. It is clear that for $n = 1$, i.e. the nearest pS2 distribution, the correlated pS2-DE pair dominates completely. At large n, AC is, in general, more dominant than in the nearest pS2 distribution.

For t distribution, I integrated over r as discussed and plotted $\rho_{\text{cor},t}$, $\rho_{\text{AC},t}$, and $\rho_{\text{DE},t}$ in Fig. 5.9. The shape of $\rho_{\text{DE},t}$ proves that the AC flat background overwhelms the correlated

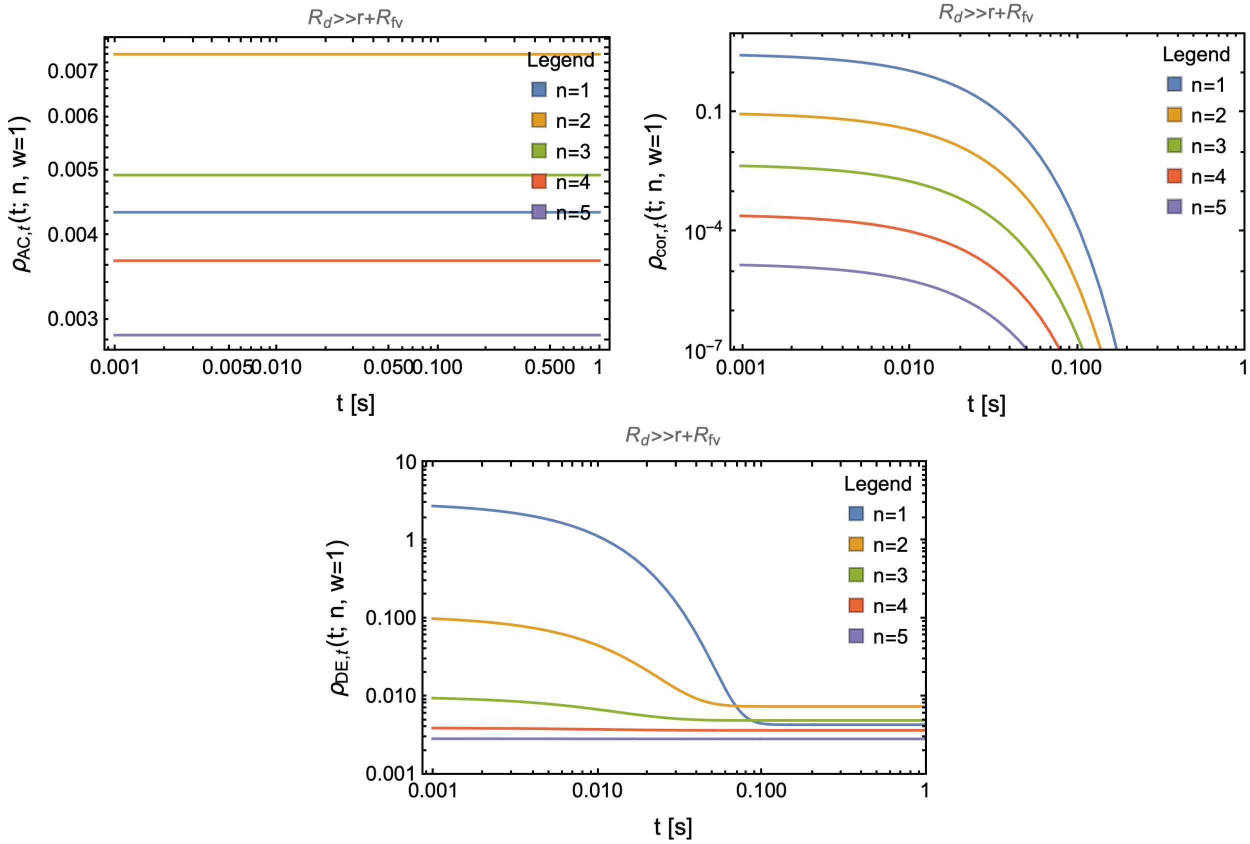

Figure 5.9: $\rho_{\mathrm{AC},t}$, $\rho_{\mathrm{cor},t}$, and $\rho_{\mathrm{DE},t}$ with large R_d condition (Eqn. 5.2) implementation, in the sequence from left to right, and from top to bottom. The scan window w is fixed at 1 s. These plots prove that at small t, ρ_{cor} dominates the DE-pS2 pairing distribution, and at large t, AC dominates. Also trends of $P_t(t)$ show up in larger n's, with decreasing strengths as AC becomes dominant. With large w, more AC can happen and make $P_t(t)$ contribution in $n = 1$ suppressed.

pS2-DE distribution at large t, as ρ_{AC} has no t dependence, and ρ_{cor} drops with $P_t(t)$.

Evaluations of $\rho_{\mathrm{DE},t}$ and ρ_{DE} with fixed $n = 1$ are shown in Fig. 5.10. ρ_{DE} is evaluated with a fixed $t = 0.01$ s. A larger w enables more AC to happen and thus reduces the contribution of $\rho_{\mathrm{cor},t}$ in $\rho_{\mathrm{DE},t}$. This results in both a suppressed time gap distribution and a bounded spatial gap distribution:

- A large w makes it less likely to not observe the correlated pS2, and thus the spatial gap distribution of the nearest pS2 is bounded by $P_r(r)$, and will only be suppressed if a random pS2 gets even closer than the correlated pS2;

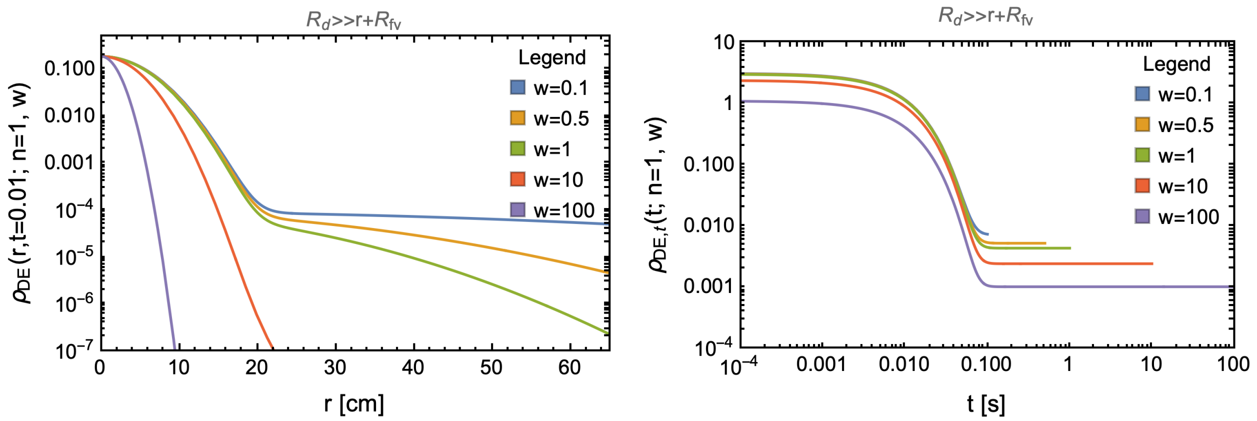

Figure 5.10: Spatial (left) and time (right) gap distributions of the nearest pS2-DE pairings for different scan windows w with large R_d condition (Eqn. 5.2) implementation.

- However, if w is small, there is still a good chance that the correlated pS2 is not observed within the scan window, and the result is the AC tail at large r in the left plot of Fig. 5.10;

- A large w enables more AC, and thus, it is more likely to have a random pS2 being closer to the DE than the correlated one. This boosts the AC flat background. (The overall lower flat parts in $\rho_{\mathrm{DE},t}$ for larger w's in the right plot in Fig. 5.10 are caused by the $\frac{1}{w}$ factor from $\rho_{\mathrm{AC},t}$, which doesn't affect the $\rho_{\mathrm{cor},t}$ component).

Notice that the valid range of t only spans from 0 to w.

It is instructive to compare Fig. 5.10 to the pure AC cases (signal-pS2 pairing) in Fig. 5.4:

- For small w, the Poisson term suppresses the AC rates as the chance of forming a random pairing is small. However, for ρ_{DE} there is a strong peak near $r = 0$ due to the dominant ρ_{cor} that follows $P_t(t)$ time correlation function, which is supposed to be much stronger than Poisson statistics at small t;

- As w goes up and AC increases accordingly, the spatial gap gets dominated by random pairing, and $\rho_{\mathrm{DE}}|_t$ (ρ_{DE} evaluated at a fixed t, as opposing to $\rho_{\mathrm{DE},r}$ where we integrate ρ_{DE} over t) becomes similar to $\rho_{s,r}$. But with a proper choice of w, $\rho_{s,r}$ has a more

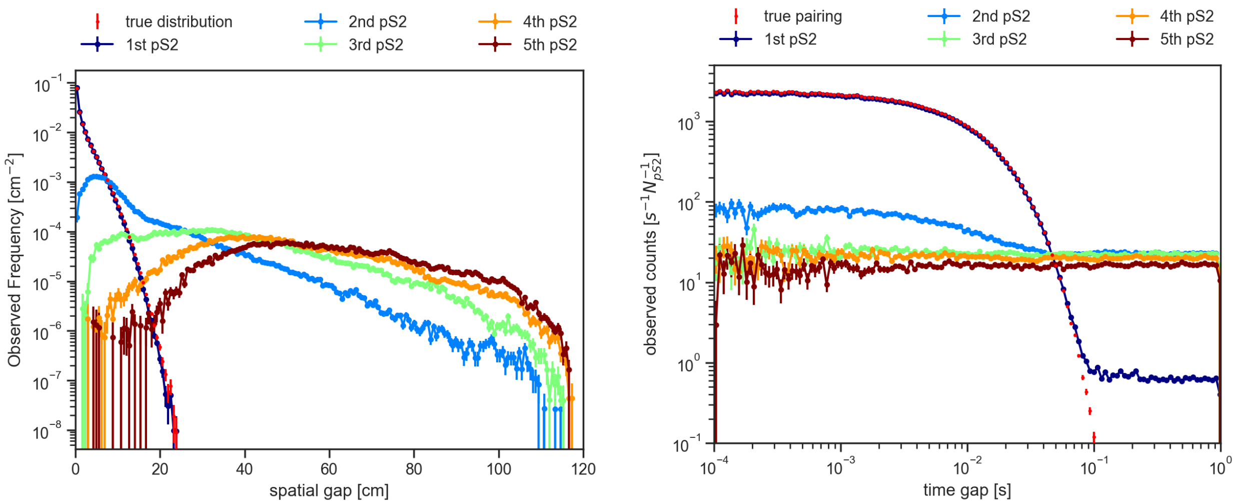

Figure 5.11: Spatial (left) and time (right) gap distribution for $n = 1$ to $n = 5$ from $w = 1$ s MC. For spatial gap distribution, the time gap was limited to between 0 and 0.05 s. The distributions share a similar shape as ρ_{DE} in Fig. 5.8 and $\rho_{\text{DE},t}$ in Fig. 5.9. Since in the simulation, there is no approximation as Eqn. 5.2, and the normalization of the trend is arbitrary, the exact distribution doesn't match the analytical results numerically.

extended distribution than $\rho_{\text{DE}}|_t$ (for example, compare the two $w = 10$ s lines).

A simple MC can be constructed for this DE-only scenario. With $f_p = 4.7$ Hz, $f_{DE} = 35 f_p$ (so for each pS2, a total of 35 DEs is expected), $R_{fa} = 53.5$ cm and $R_d = 65$ cm, the resulted distributions are shown in Fig. 5.11 and Fig. 5.12. Compared to the formulations, this MC is closer to a real-world scenario without the assumption of Eqn. 5.2. While the absolute values don't match with their counterparts in Fig. 5.8, Fig. 5.9, and Fig. 5.10, the main features are consistent:

1. The suppression of time and spatial gap distributions by ACs with the increasing w;
2. The flat AC background in time gap distribution and their relative intensity with different n;
3. The shape of spatial gap distribution with different n.

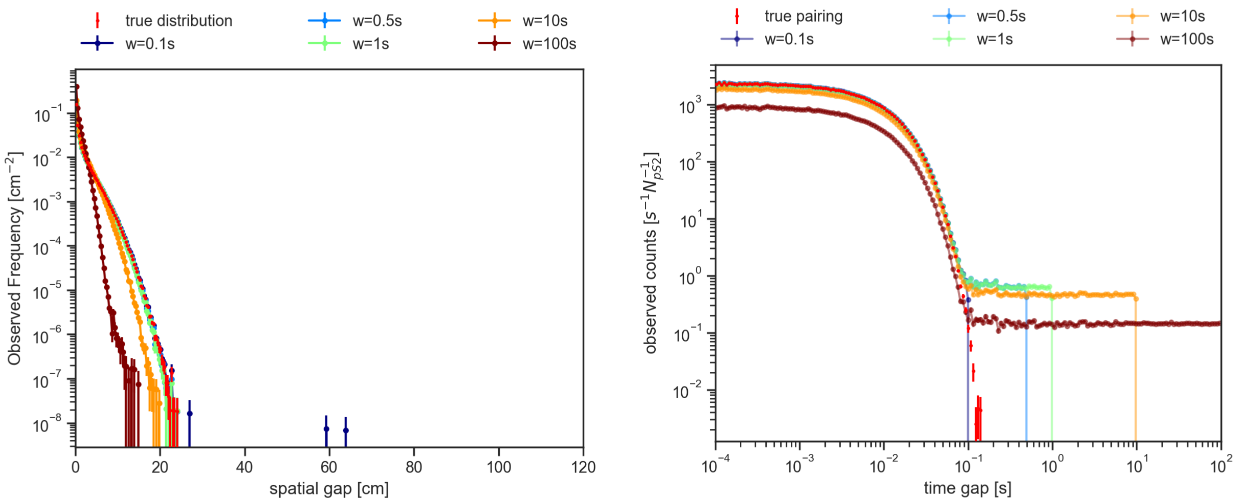

Figure 5.12: Spatial (left) and time (right) gap distribution for the nearest pS2-DE pairings with different w from MC. For spatial gap distribution, the time gap was limited to between 0 and 0.05 s. The distributions share a similar narrowing down with increasing w as ρ_{DE} and $\rho_{\mathrm{DE},t}$ in Fig. 5.10.

5.4 Two Strategies For $P_t(t)$ Reconstruction

All these calculations are for the sole purpose of obtaining an accurate and unbiased time correlation function $P_t(t)$. In this section, I will provide two methods. The first one is related closely to the formulations of Sec. 5.3, and the second one is more empirical and intuitive but lacks rigorous proof. Both strategies were tested on simulated populations as described in Sec. 5.3.

5.4.1 Strategy 1: Obtaining $P_t(t)$ with Individual n

This strategy utilizes a combination of Eqn. 5.5, Eqn. 5.15, Eqn. 5.16 and Eqn. 5.17. $\frac{c_2(n,w;x,y)}{w}$ can be obtained from simulated results or actual data from experiments by evaluating the flat background at large t from time gap distributions. I will drop the (x, y) dependence of c_1 and c_2 because, normally, it is not possible to have enough statistics for any satisfactory position resolution. (This (x, y) dependence drop was implicitly carried out in all previous simulation handling). Since the variables when dealing with data are normally observed counts, for example, as in the right plot in Fig. 5.11, the actual computation is the following:

$$\begin{aligned}
c_{norm} &\equiv \frac{f_{DE}}{f_p} = \lim_{w\to\infty}\int_0^w dt\ \left\{\text{Observed Counts } [s^{-1}N_{pS2}^{-1}]\right\} \\
c_{2,raw}(n,w) &\equiv w \times \{\text{Flat Background } [s^{-1}N_{pS2}^{-1}]\} \\
c_2(n,w) &= \frac{c_{2,raw}(n,w)}{c_{norm}} \\
c_1(n,w) &= \mathcal{P} - c_2(n,w) \\
P_t(t) \equiv P_t(t)|_{n,w} &= \frac{1}{c_1(n,w)}\left(\frac{\left\{\text{Observed Counts } [s^{-1}N_{pS2}^{-1}]\right\}}{c_{norm}} - \frac{c_2(n,w)}{w}\right) \\
&= \frac{\{\text{Observed Counts - Flat Background}\}}{c_{norm}\mathcal{P} - c_{2,raw}}[s^{-1}N_{pS2}^{-1}].
\end{aligned} \tag{5.19}$$

$\left\{\text{Observed Counts } [s^{-1}N_{pS2}^{-1}]\right\}$ is just the raw observed time gap distribution in the unit of absolute rate $[s^{-1}N_{pS2}^{-1}]$. For example, each curve in the right plot in Fig. 5.12 is the $\left\{\text{Observed Counts } [s^{-1}N_{pS2}^{-1}]\right\}$ for $w = 1$ and each corresponding n. It, by definition, equals $\rho_{\mathrm{DE},t}(t; n, w) \cdot f_{DE}/f_p$, while from data, the individual components in this expression cannot be obtained. $\{\text{Flat Background } [s^{-1}N_{pS2}^{-1}]\}$ can be obtained by taking the average of the flat region at large t, for example the average value between 1s and 100s for the $w = 100$ s curve in the right plot of Fig. 5.12. Fig. 5.13 shows some results of practicing Eqn. 5.19 with $w = 100$ s. The effectiveness, as well as the limitations of this method, are shown clearly:

- For large w and small n, the reconstruction is very satisfactory, because the prior of Eqn. 5.16 is true and c_{norm} is closed to unbiased;
- For large n, the calculation of c_{norm} starts to be smaller than the true value, because $\int_0^w dt\ \rho_{\mathrm{DE},t}(t; n, w) < 1$ as there are more DEs with no n-th pS2. The reconstructed $P_t(t)$ is thus different than the true function (being larger or smaller depends on the actual

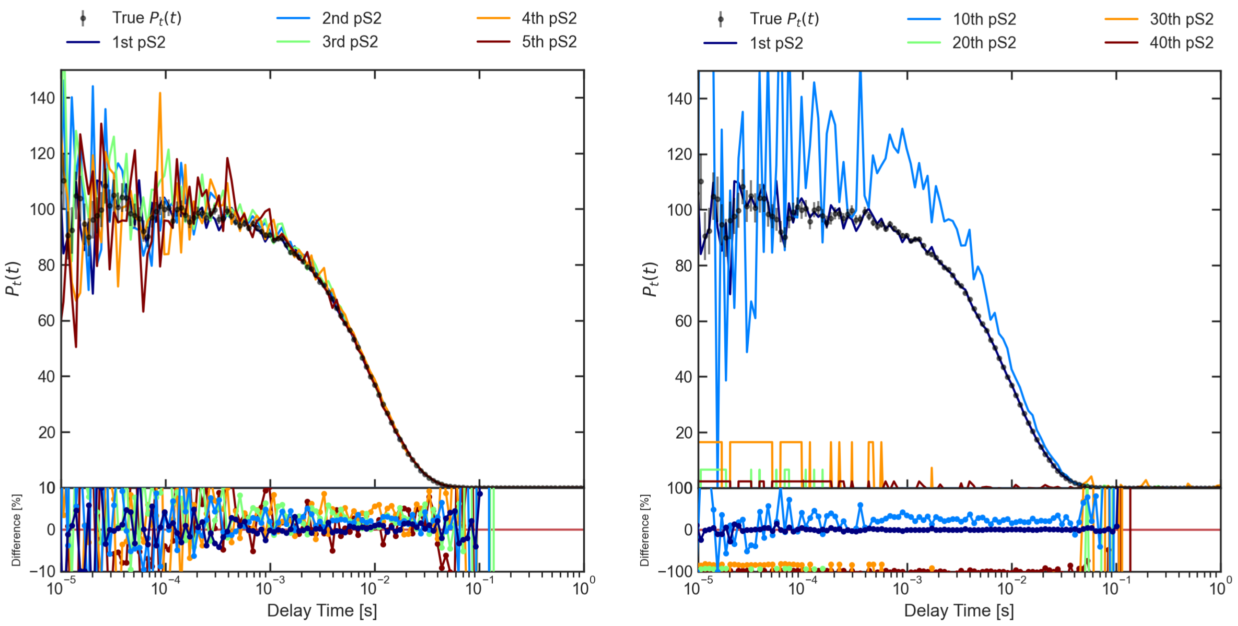

Figure 5.13: Reconstruct $P_t(t)$ from the simulated population, with no knowledge of pre-defined values (f_p, f_{DE}, $P_t(t)$, etc.). The top panels are reconstructed $P_t(t)|_{n,w}$'s (colored) and the true $P_t(t)$ (black), and the bottom panels are difference ratios $\left(P_t(t)|_{n,w} - P_t(t)\right)/P_t(t)$. Left: reconstruction with small n; right: reconstruction with large n.

relation between the flat AC rate and the $P_t(t)$ branch amplitude). This sometimes leads to too large AC flat background estimation and results in unphysical negative values;

- For really large n where there are no longer $P_t(t)$ branches left, the reconstructed quantity doesn't represent any physical correlation but statistical fluctuations.

The reconstructed time correlation function with $n = 1$ is within 0.15% statistical fluctuation from the true $P_t(t)$ (examined that all DEs have paired pS2s, so no systematic bias). The reconstructed $P_t(t)$ and their difference ratio with the true $P_t(t)$ are shown in Fig. 5.13.

However, thus far, only DE-pS2 pairing has been considered, with no addition of signal-pS2 pairing. Adding in a flat signal background will effectively lift the whole distribution and cause a bias, as shown in Fig. 5.14 on the right. Such bias can be probed with an extra term in Eqn. 5.19. Define δ to be the added flat signal background, i.e., according to Eqn. 5.5:

$$\delta \equiv \frac{f_s}{w f_p} \sum_{m \geq n} \text{Poisson}(m; f_p w). \tag{5.20}$$

Then the modified parameters in Eqn. 5.19 will carry this extra component as:

$$\begin{aligned}
c'_{norm} &= \lim_{w \to \infty} \int_0^w dt \ \{\delta + \text{Observed Counts}\} = w\delta + c_{norm} \\
c'_{2,raw}(n, w) &\equiv w \times \{\delta + \text{flat background}\} = w\delta + c_{2,raw}(m, w) \\
c'_2(n, w) &= \frac{c'_{2,raw}(n, w)}{c'_{norm}} = \frac{w\delta + c_{2,raw}(n, w)}{w\delta + c_{norm}} \\
c'_1(n, w) &= \mathcal{P} - c'_2(n, w) = \mathcal{P} - \frac{w\delta + c_{2,raw}(n, w)}{w\delta + c_{norm}} \\
P'_t(t)|_{n,w} &= \frac{1}{c'_1(n, w)} \left(\frac{\{\delta + \text{Observed Counts}\}}{c'_{norm}} - \frac{c'_2(n, w)}{w} \right) \\
&= \frac{\{\text{Observed Counts - Flat Background}\}}{c_{norm}\mathcal{P} - c_{2,raw} - w\delta(1 - \mathcal{P})}.
\end{aligned} \tag{5.21}$$

Compared with Eqn. 5.19, the term $w\delta\,(1 - \mathcal{P})$ in the denominator is the bias term. In the limits of $\mathcal{P} \to 1$ or $w\delta \ll c_{norm}$, this term is negligible. However, if this is not the case, the reconstructed $P'_t(t)|_{n,w}$ would be systematically larger than the true time correlation function. It is, in general, safe to use $n = 1$ and large w trends to reconstruct $P_t(t)$.

5.4.2 Strategy 2: Summing Over All n's

There is another strategy for $P_t(t)$ reconstruction. Intuitively, when scanning backward, as long as w is large enough and all DEs see their correlated pS2, it is only a matter of how far this correlated pS2 is pushed to higher rank by ACs. As shown in Eqn. 5.15, the shape of $P_t(t)$ is maintained with a coefficient $c_1(n, w)$ (ignoring xy dependence as discussed). Ideally, we should be able to obtain the full $P_t(t)$ by summing up branches from all n's.

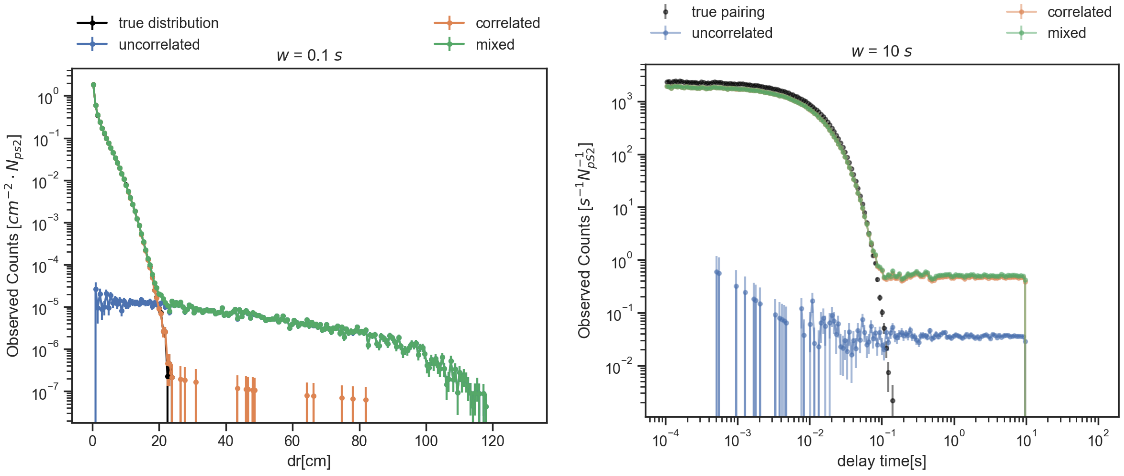

Figure 5.14: Left: Spatial gap distribution (unnormalized) from simulation for the nearest pS2-sS2 pairings with the presence of an independent background (green) with a scan window of 0.1 s, compared with DE-only (orange), background-only (blue), and the true $P_r(r)$ (black). It is clear that without the presence, the spatial gap distribution with small w would be a good estimator for the true $P_r(r)$ as the orange line overlaps with the black line perfectly. However, the existence of the background makes the spatial gap distribution more extended to larger r. Right: observed time gap distribution.

Such a strategy can be formalized into a procedure described as

$$\begin{aligned} &\frac{f_{DE}}{f_p}\rho_{\mathrm{cor},t}(t;n,w) = (\{\text{Observed Counts}\} - \{\text{Flat Background}\})\,[s^{-1}N_{pS2}^{-1}] \\ &\Rightarrow \frac{f_{DE}}{f_p}P_t(t) \equiv \frac{f_{DE}}{f_p}P_t(t)|_w = \frac{f_{DE}}{f_p}\sum_{n\geq 1}\rho_{\mathrm{cor},t}(t;n,w). \end{aligned} \tag{5.22}$$

This equation directly gives the $P_t(t)$ with the absolute rate of DE per pS2, and the calculation procedure is much simpler. However with a general form of $P_r(r)$, the arc length function $\mathcal{R}(r;x,y)$ and the area overlap function $A_I(r;x,y)$, I couldn't find a way to prove that

$$\sum_{n\geq 1} c_1(n,w) = 1 \tag{5.23}$$

Therefore this strategy, although tested against multiple w's with sufficiently large n's with accurate reconstructed $P_t(t)$'s, is regarded empirical and awaits further proof. If Eqn. 5.23

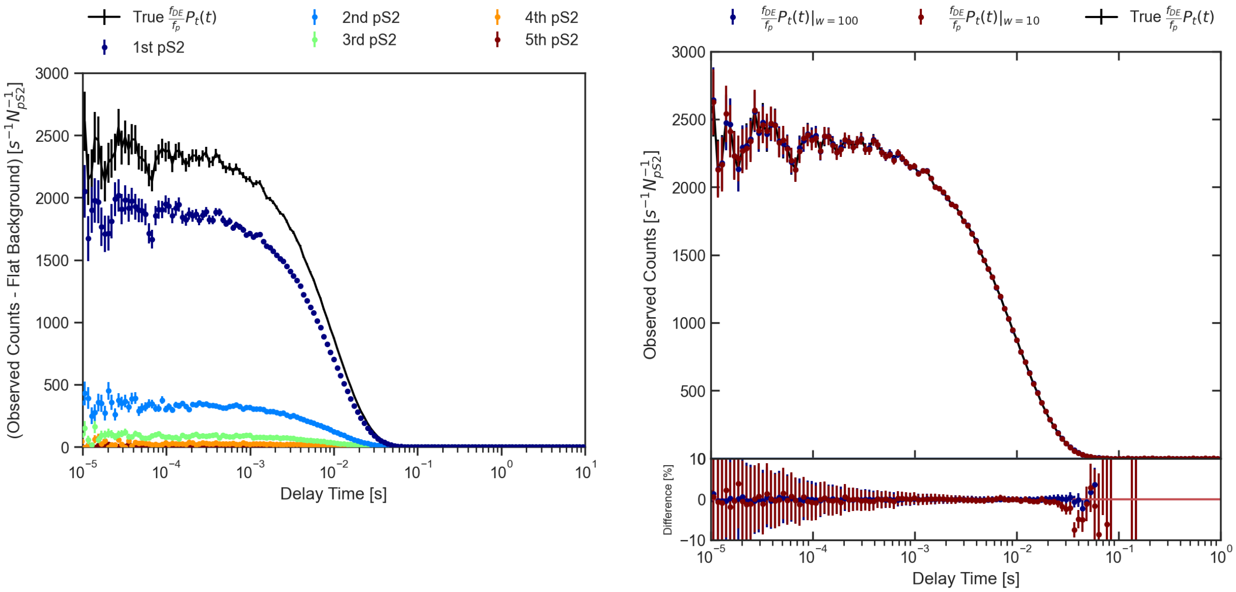

Figure 5.15: Reconstruction of $P_t(t)$ by summing up contributions from all n's. The true $P_t(t)$ is shown in black lines. Left: examples $\rho_{cor,t}(t; n, w = 10)$ obtained by {Observed Counts} minus {Flat Background} for several n's with $w = 10$ s; right: reconstructed $P_t(t)|_w$'s from $w = 10$ s (dark red dots) and $w = 100$ s (dark blue dots) with a bottom panel of difference ratios $\left(P_t(t)|_{n,w} - P_t(t)\right)/P_t(t)$.

is true, this strategy provides an unbiased method of obtaining $P_t(t)$. It is robust if a flat signal background is present: unlike the first strategy, where the flat background component causes a bias, this strategy subtracts all ACs from DEs or signals indistinguishably. The only requirement is to have information up to a sufficiently large n. Two results from $w = 10$ s and $w = 100$ s from the MC population are shown in Fig. 5.15. Both $w = 10$ s and $w = 100$ s trends achieved satisfactory reconstruction results (The observations are all 0 above 1 s because of the choice of $P_t(t)$, so I only plotted up to 1 s in Fig. 5.15).

5.4.3 Conclusion

In conclusion, strategy 1 utilizes some arithmetic relations depicted in Eqn. 5.19 and can reconstruct $P_t(t)$ from each n, with a strong power with small n and large w. Strategy 2 uses trends from all n's and reconstructs $P_t(t)$ by summing up contributions from all n's. Strategy

1, because of the bias introduced by the unknown signal background, has a potential bias of overestimating the true $P_t(t)$, i.e. $P_t(t)|_{n=1,w} \geq P_t(t)$ (only $n = 1$ should be used in actual experiments as shown in Fig. 5.13). Strategy 2, on the contrary, tends to underestimate $P_t(t)$ because of an incomplete inclusion of n's. Due to limited computer power, only a limited amount of n can be saved in real data. It might be beneficial to combine the two methods, taking the nominal time correlation function to be the mean of the two and treating the individual results as uncertainties.

$$\begin{aligned} P_t(t) &= \frac{P_t(t)|_{n=1,w} + P_t(t)|_w}{2} \\ \delta P_t(t) &= \frac{P_t(t)|_{n=1,w} - P_t(t)|_w}{2}. \end{aligned} \tag{5.24}$$

5.5 Estimation of $P_r(r)$

The involvement of $P_r(r)$ in Eqn. 5.11 makes it hard to reconstruct this position correlation function. However, as observed in Sec. 4.4 (in the Position-Correlated Small S2 subsection), the position correlation between DEs and pS2s is independent of the delay time. We can utilize this observed fact and the fact that with a small w, Eqn 5.10 is dominated by ρ_{cor} due to the Poisson term (at small w, $f_p w \sim 0$, thus Poisson$(m > 0, f_p w) \sim 0$) to get a good estimation of $P_r(r)$ by simply looking at the r distribution from small scan windows, as shown on the left in Fig. 5.12.

However, with the existence of an independent background (Eqn. 5.7 and Fig. 5.7), the observed spatial gap distribution will be a mixture of the DE and background distributions, as shown in Fig. 5.14 on the left. (Another good example from real data is Fig. 4.28, although such a plot was not obtained by pairing sS2s with pS2s with a fixed scan window, but looking at the immediate preceding pS2s from each sS2). Because we have no way to know a priori the amplitude of f_{DE} and f_s, we cannot ignore the contribution to the reconstructed $P_r(r)$ from the backgrounds. The best practice is to use the same method discussed in Sec. 4.4

in the Position-Correlated Small S2 subsection: we can construct a background model by randomly pairing up sS2s and pS2s and then subtract it from the reconstructed $P_r(r)$.

CHAPTER 6

SUMMARY AND OUTLOOKS

In this work, I summarized the efforts of understanding and modeling the low-energy S2 signals inside XENONnT detector during SR0. I started with a full description and derivation of a semi-analytical model that describes the pulse shape of the low-energy S2s (and more broadly, all S2 signals) in Ch. 3. Then utilizing the model, I discussed the details of the Few-Electron analysis using XENONnT SR0 data, by which we established competitive constraints on the cross-section of the dark-matter electron scattering, the kinetic mixing angle of dark photon and the Standard Model photon, and the coupling strength between Axion-like Particles and the Standard Model electron in Ch. 4. Eventually, I discussed a mathematical model that aimed to provide a novel way to establish an empirical and model-independent description of the Delayed Electron and their preceding Primary S2s in Ch. 5, which remains the greatest obstacle on the path of searching for light dark matter signals using the two phase TPC detectors.

In the future, I hope to

1. verify experimentally[1] the S2 Pulse Shape model developed in Ch. 3 with dedicated small-scale detector design and operation;
2. develop further the semi-analytical model, discussed in Ch. 5, for a more robust profiling of the DE population;
3. verify the source of the DE population experimentally with innovative small-scale detector design.

---

[1] I designed and operated a small local detector, from which we obtained promising data that can be used to verify this model. We are in the process of analysing the data.

APPENDIX A

RESULTS OF RECONSTRUCTING THE NUMBER OF ELECTRONS

This is a summary of plots showing the results of the reconstruction algorithm that retrieves the number of electrons from S2 waveforms, discussed in Sec. 4.3.

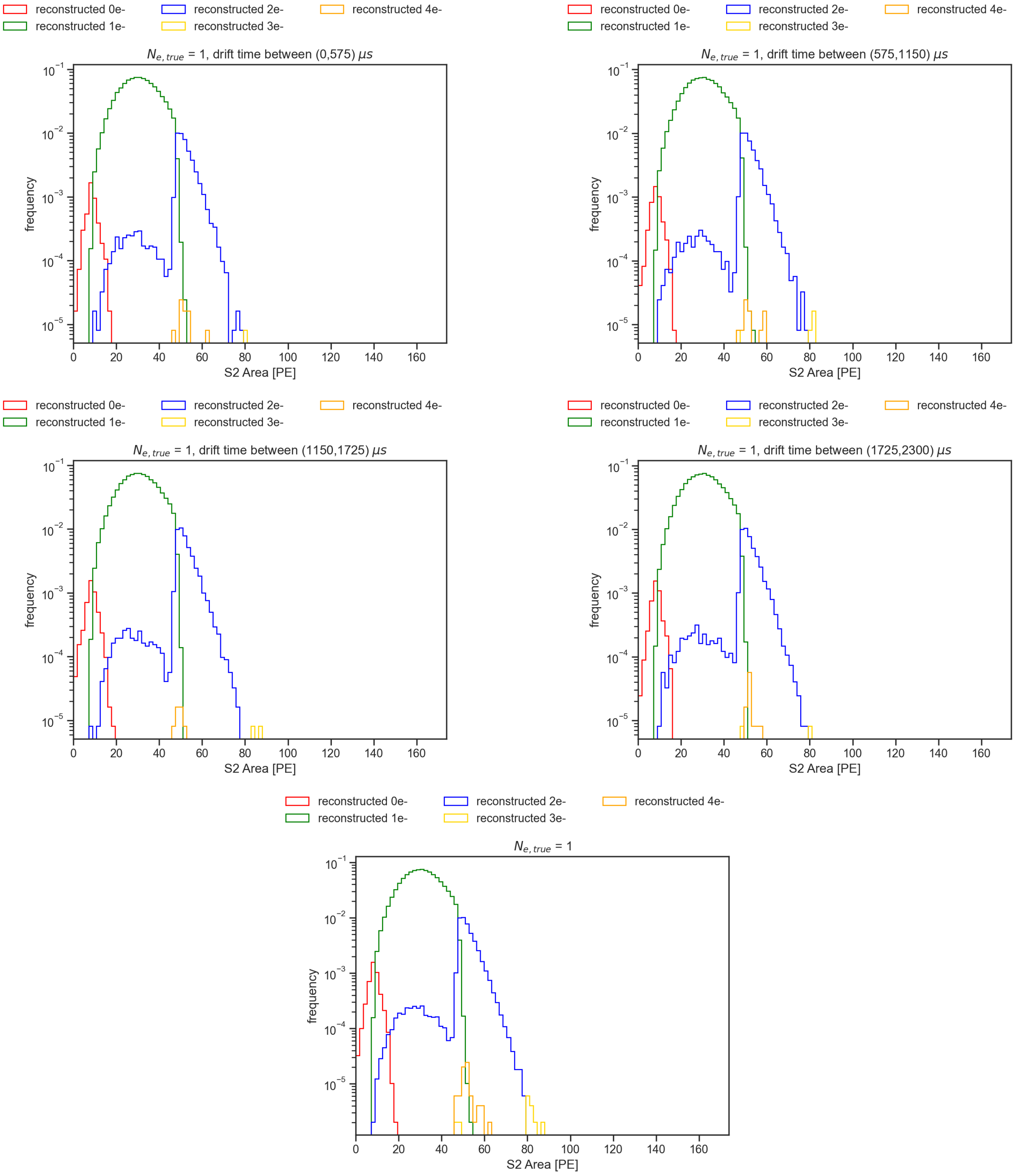

Figure A.1: Map from $N_{e,true} = 1$ to $N_{e,rec}$, with and without drift time dependence.

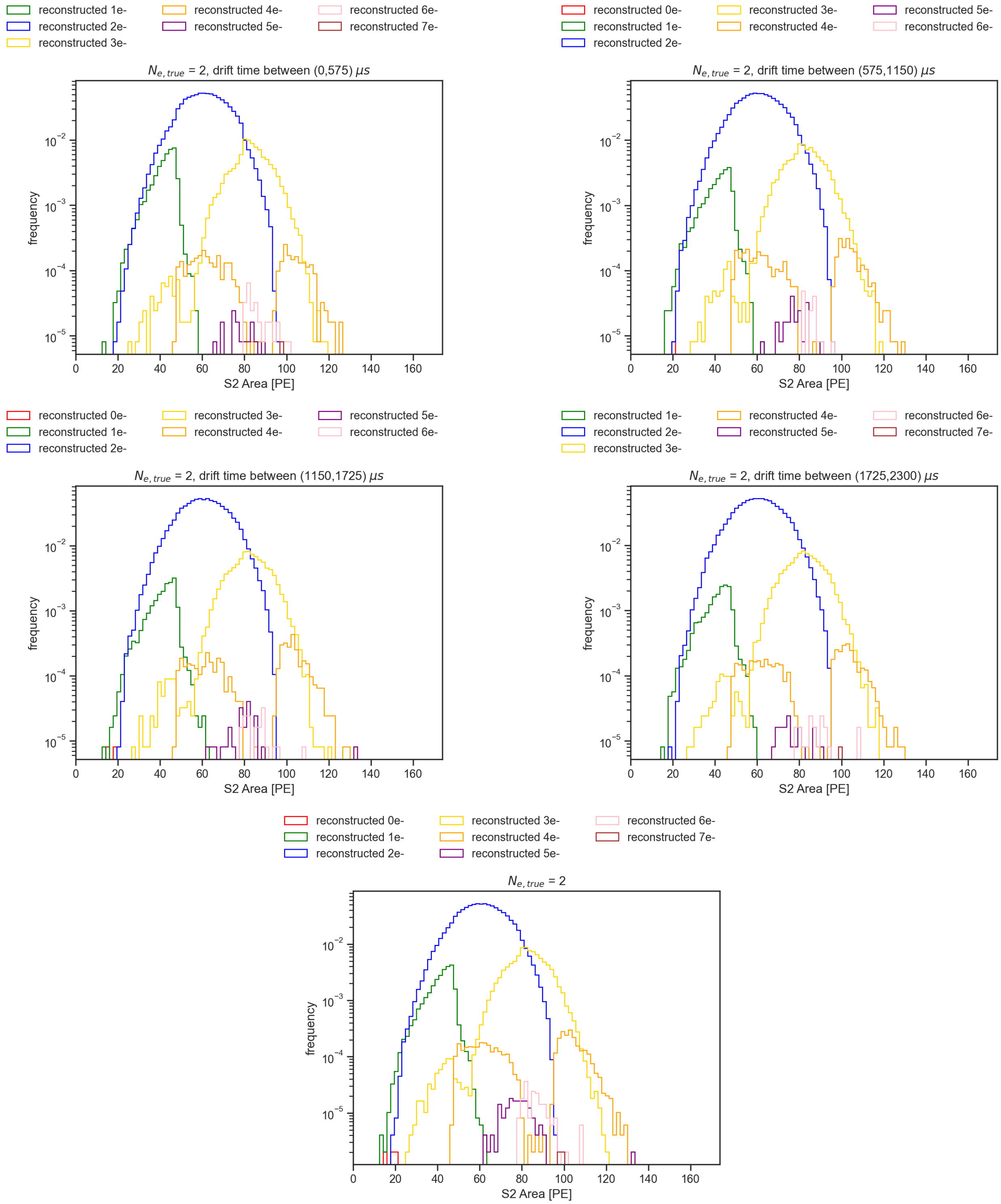

Figure A.2: Map from $N_{e,true} = 2$ to $N_{e,rec}$, with and without drift time dependence.

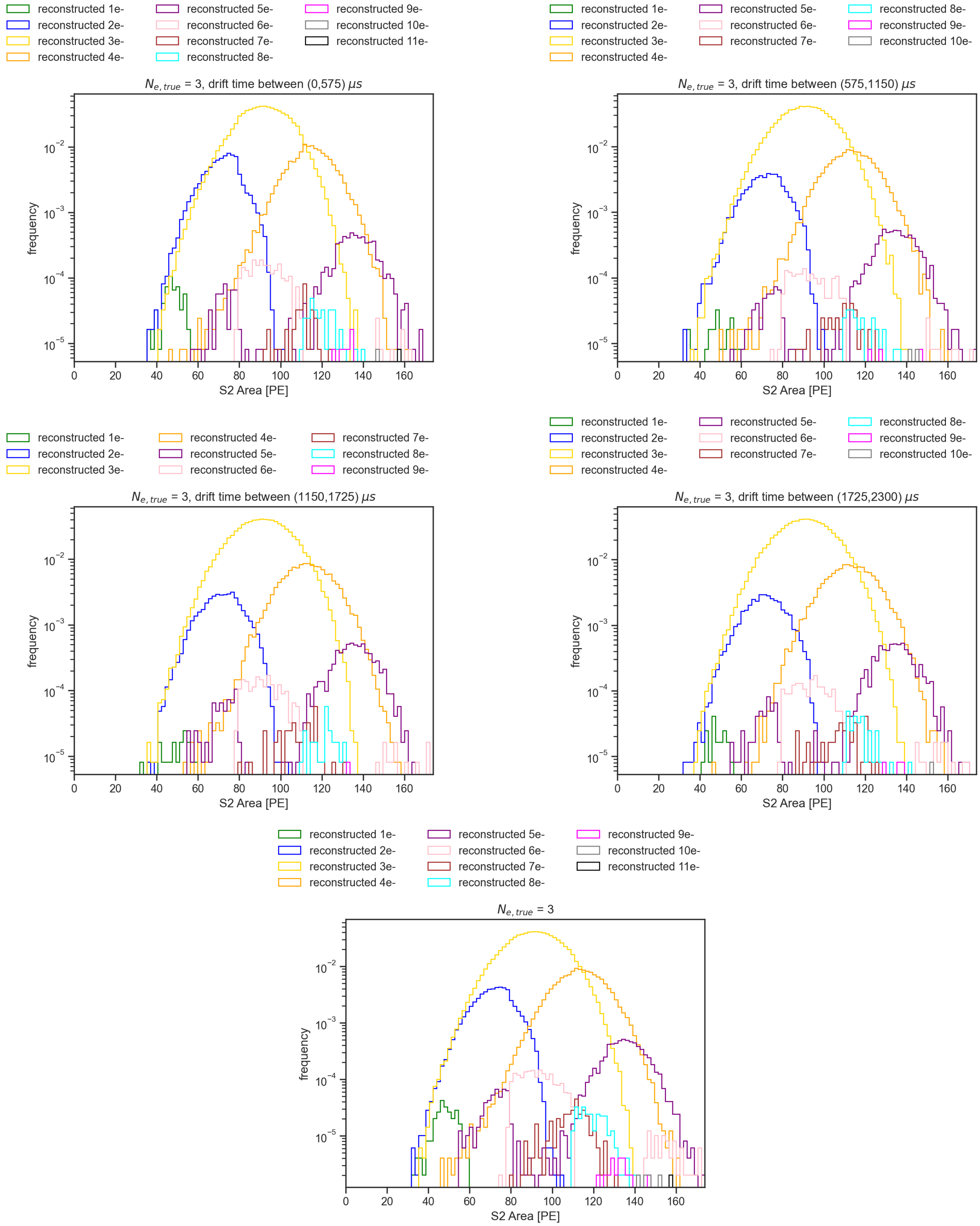

Figure A.3: Map from $N_{e,true} = 3$ to $N_{e,rec}$, with and without drift time dependence.

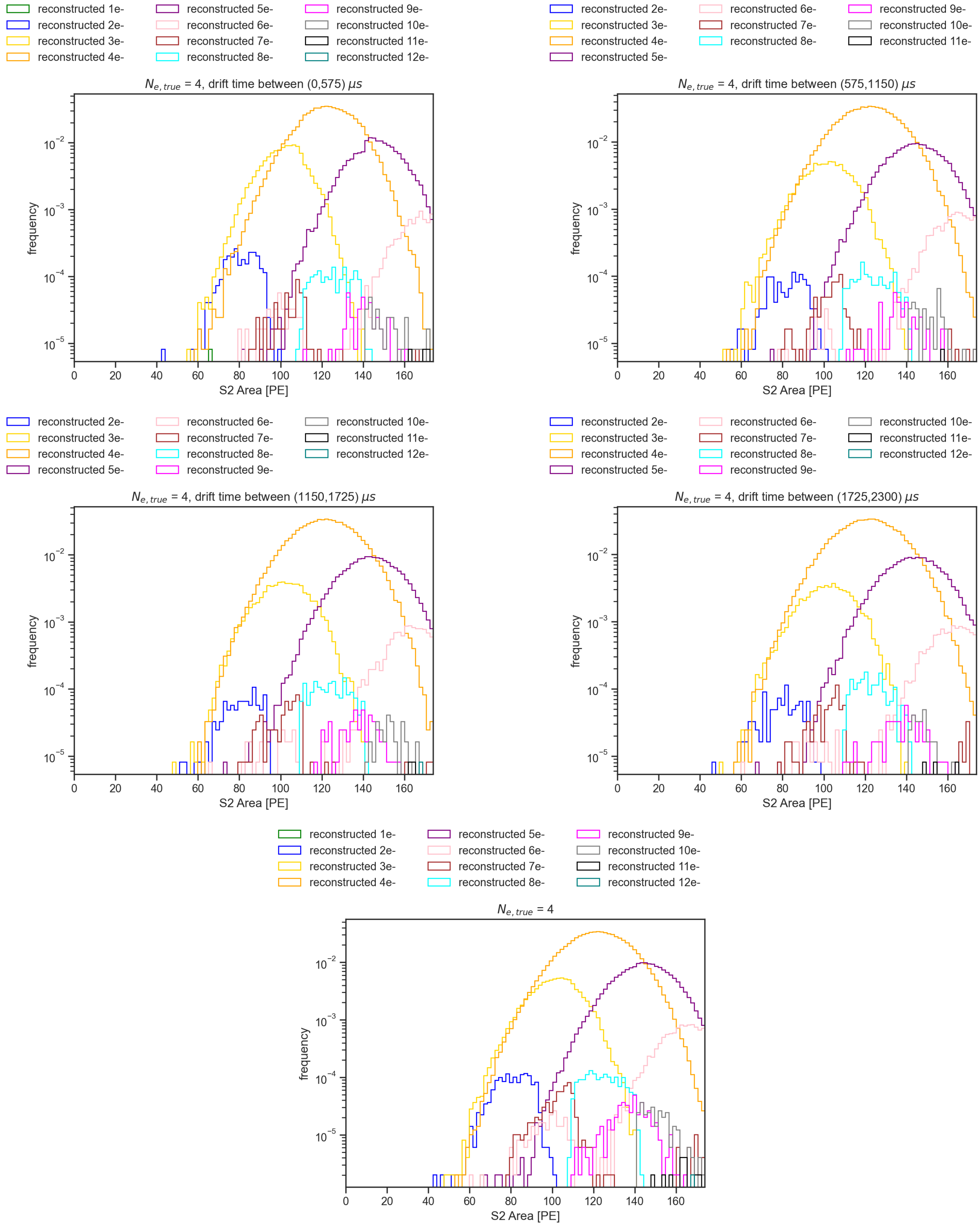

Figure A.4: Map from $N_{e,true} = 4$ to $N_{e,rec}$, with and without drift time dependence.

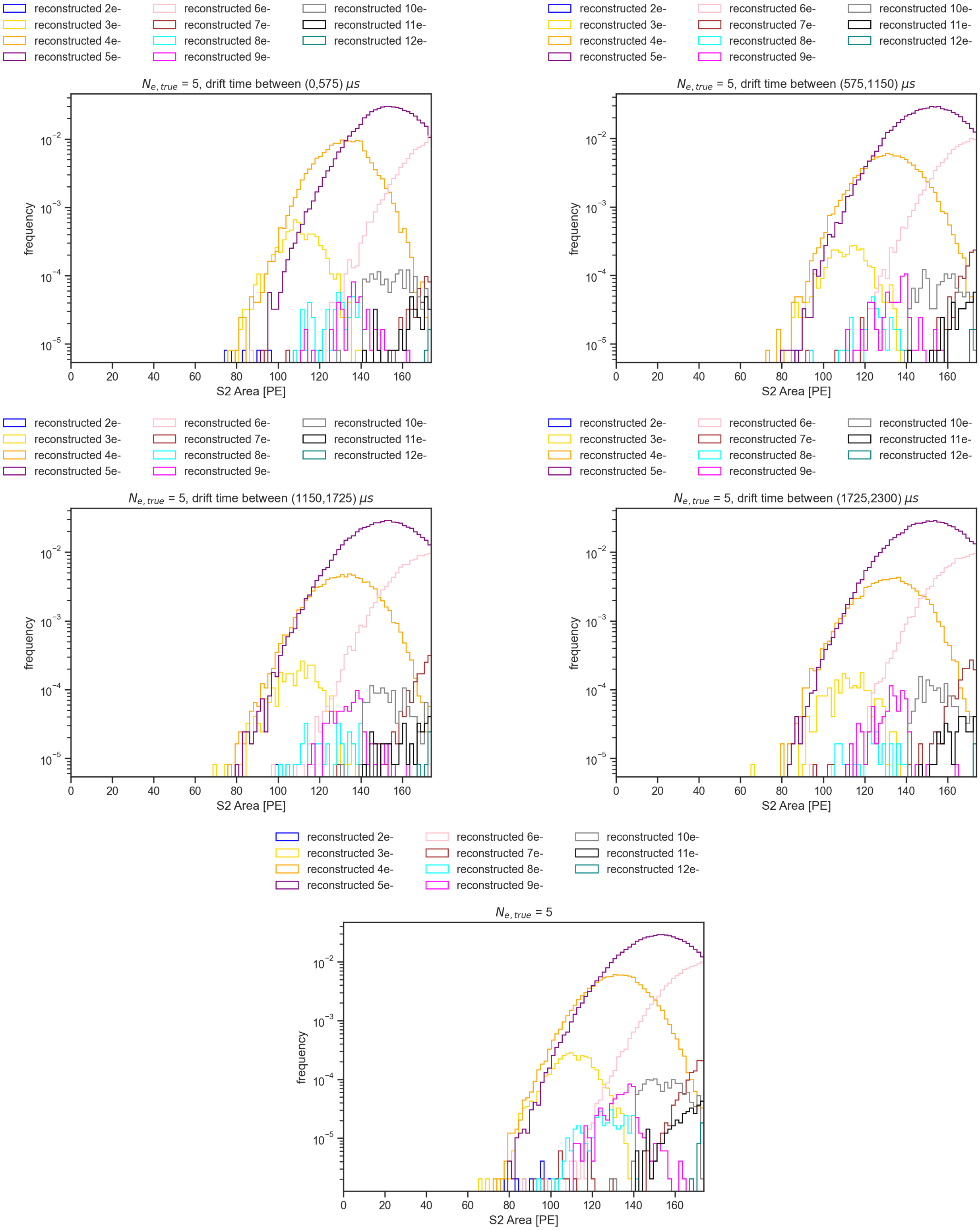

Figure A.5: Map from $N_{e,true} = 5$ to $N_{e,rec}$, with and without drift time dependence.

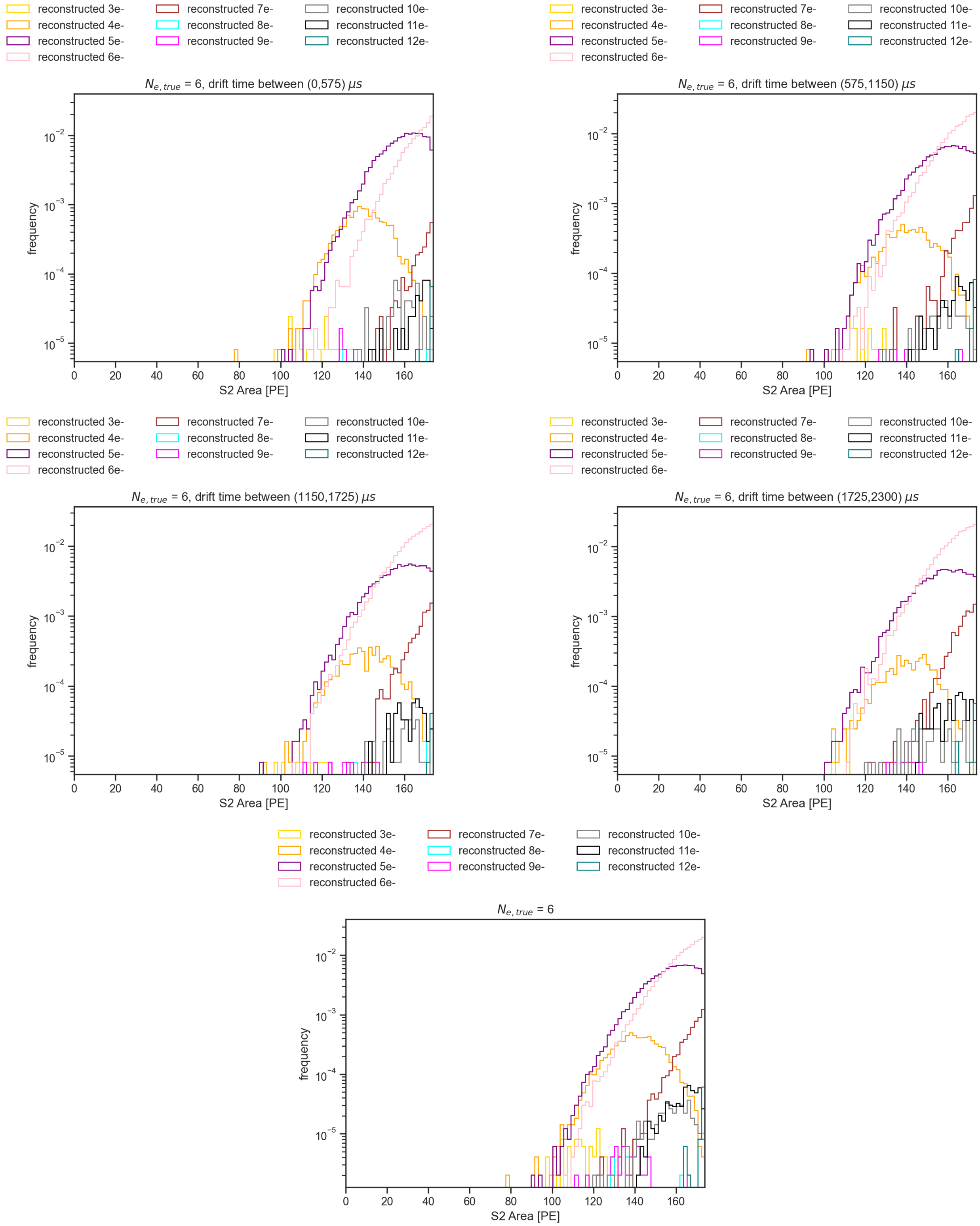

Figure A.6: Map from $N_{e,true} = 6$ to $N_{e,rec}$, with and without drift time dependence.

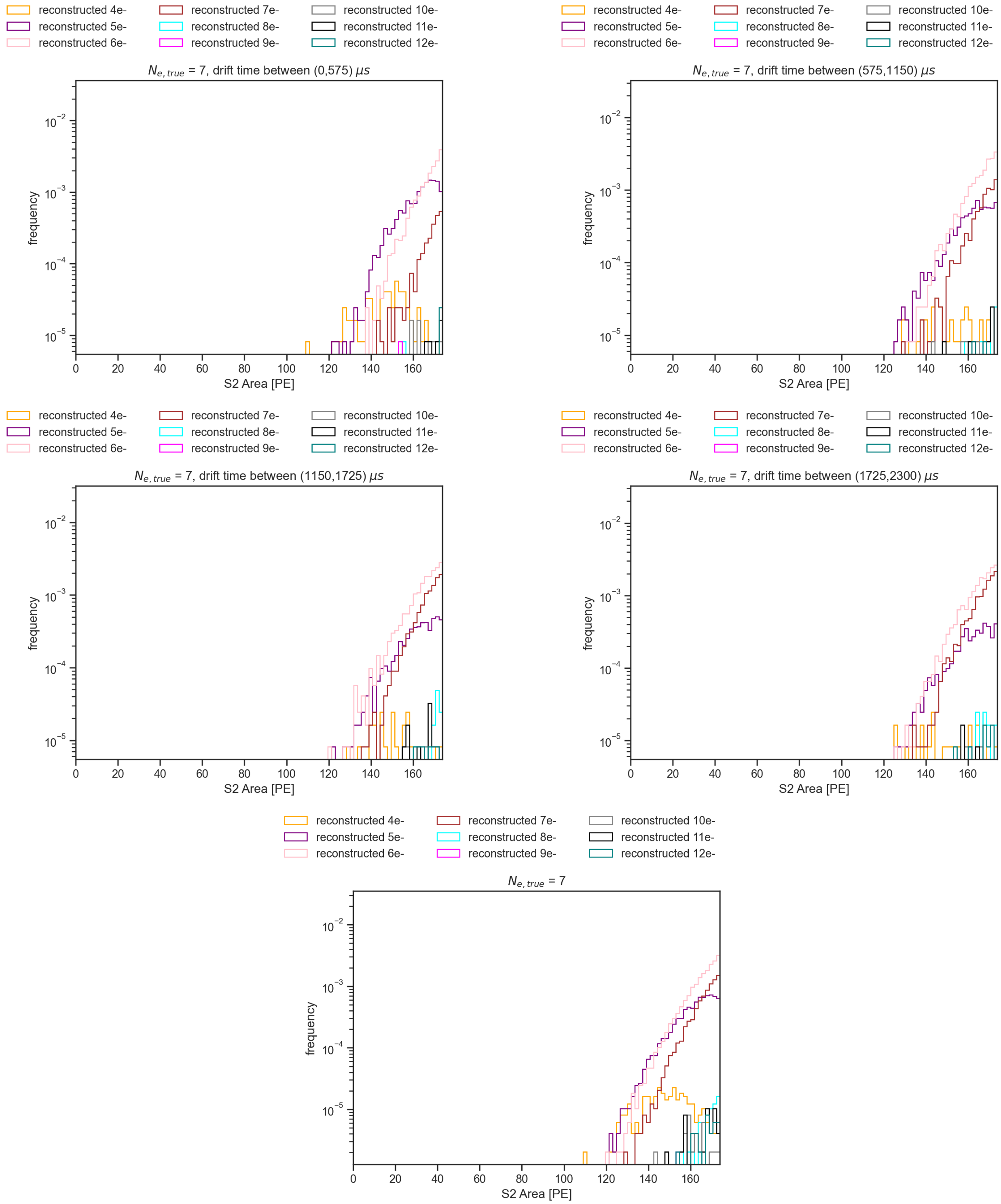

Figure A.7: Map from $N_{e,true} = 7$ to $N_{e,rec}$, with and without drift time dependence.

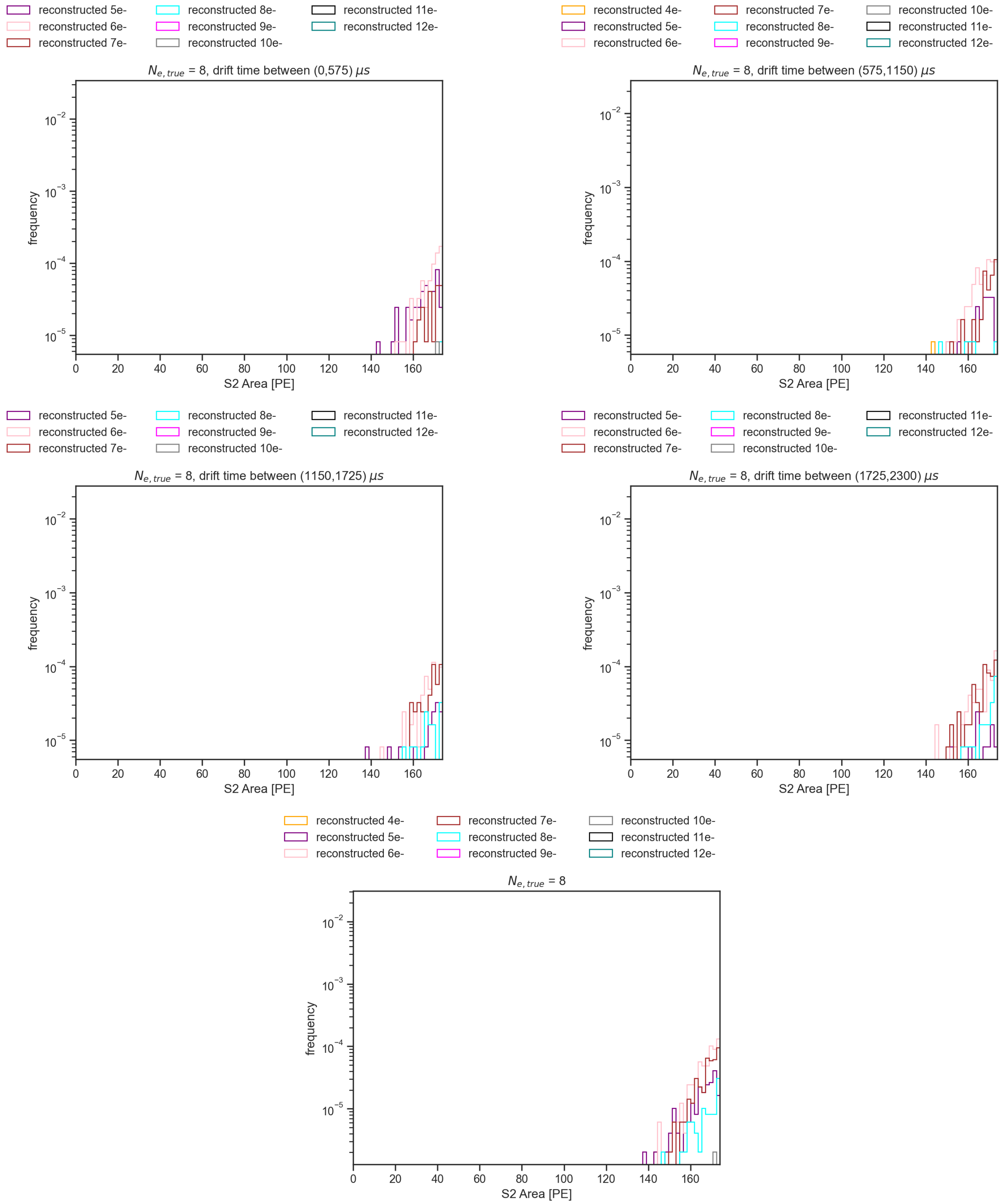

Figure A.8: Map from $N_{e,true} = 8$ to $N_{e,rec}$, with and without drift time dependence.

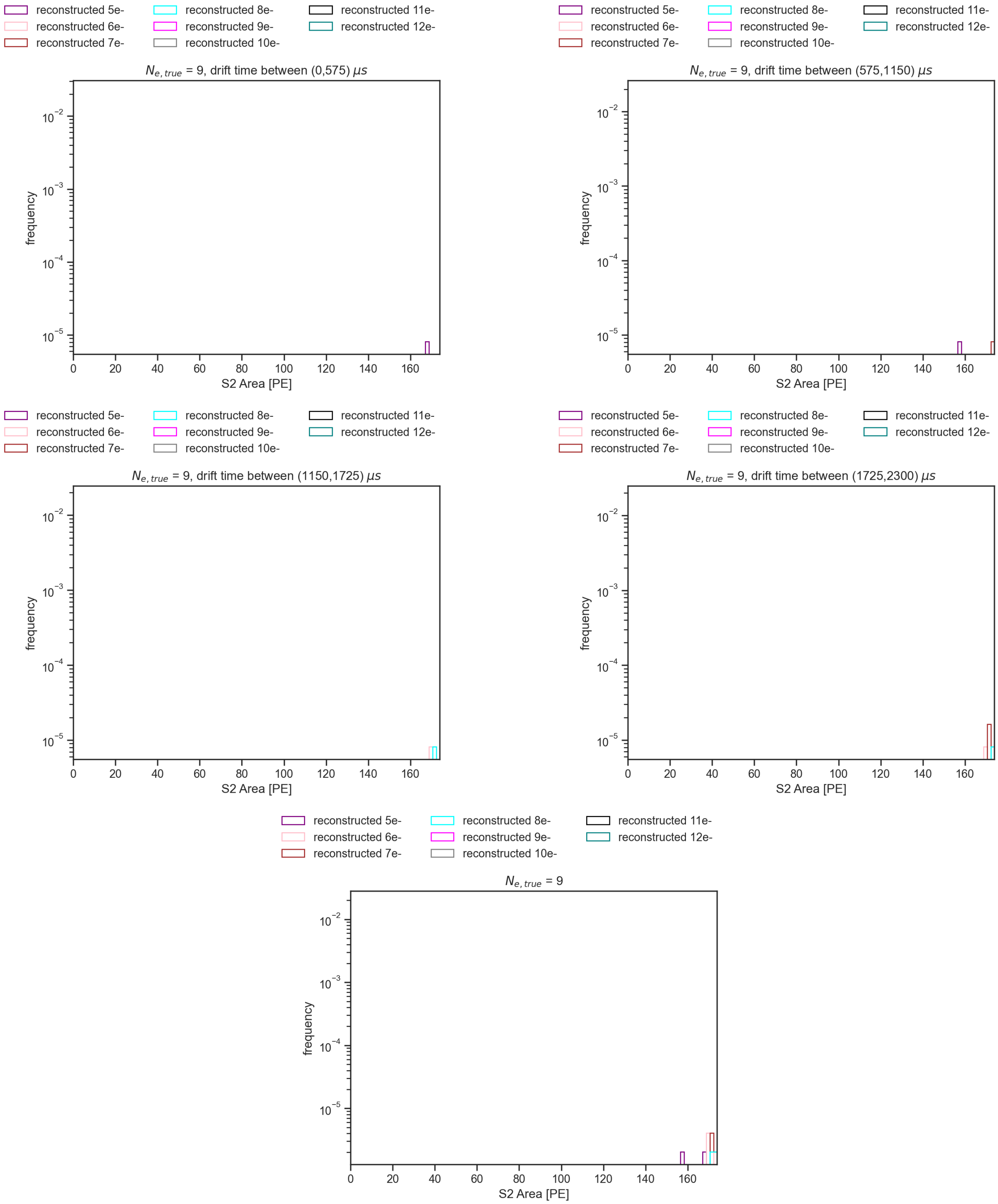

Figure A.9: Map from $N_{e,true} = 9$ to $N_{e,rec}$, with and without drift time dependence.

APPENDIX B

S2 WIDTH DISTRIBUTION AND CUTS

This is a summary of S2 width distributions for different $N_{e,true}$ and their cut boundaries, discussed in Sec. 4.4.

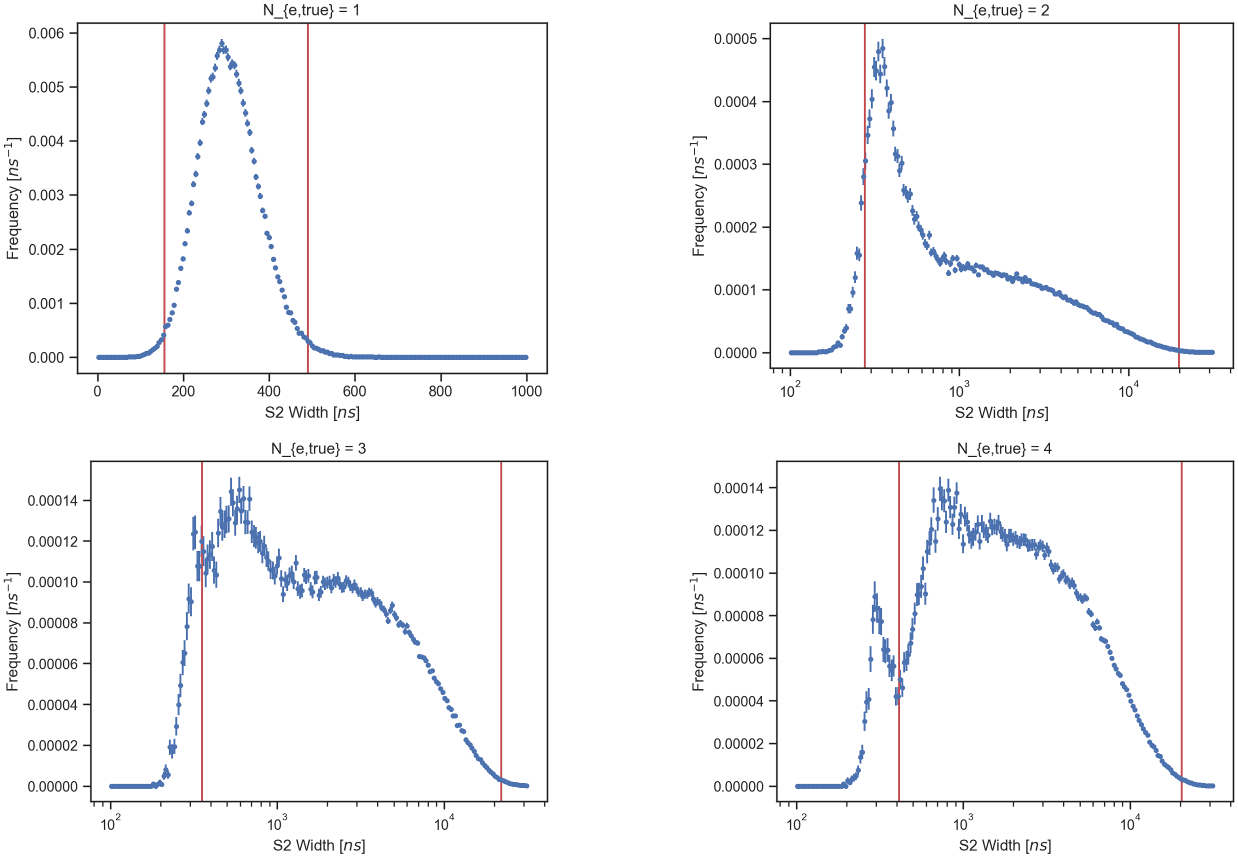

Figure B.1: S2 width distributions ignoring drift time dependence and their cuts (continued).

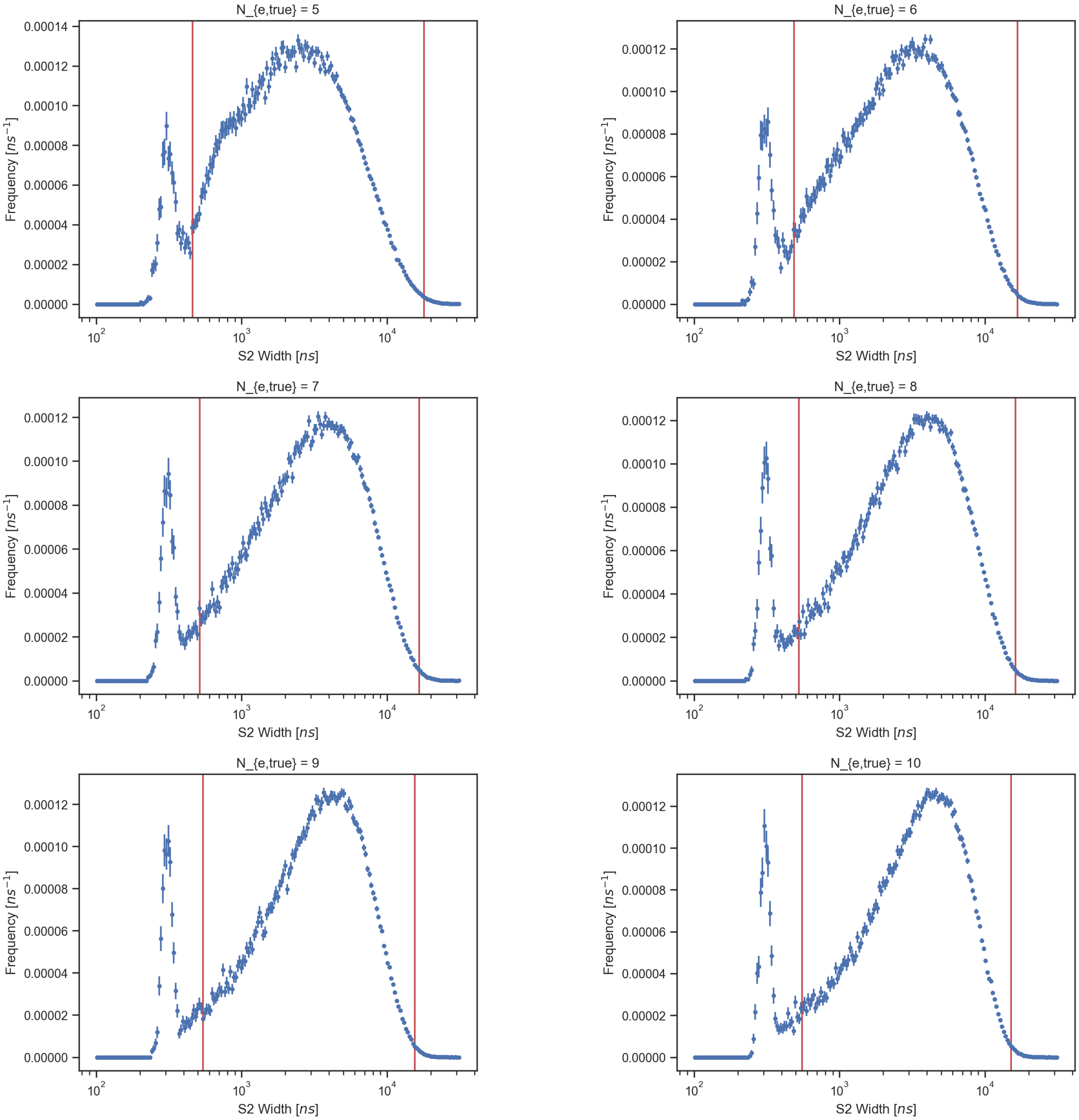

Figure B.2: S2 width distributions ignoring drift time dependence and their cuts.

APPENDIX C

DELAY TIME CUT THRESHOLDS DEVELOPMENT

These thresholds were optimized by Dr. Jacques Pienaar. All the plots were taken from his study note.

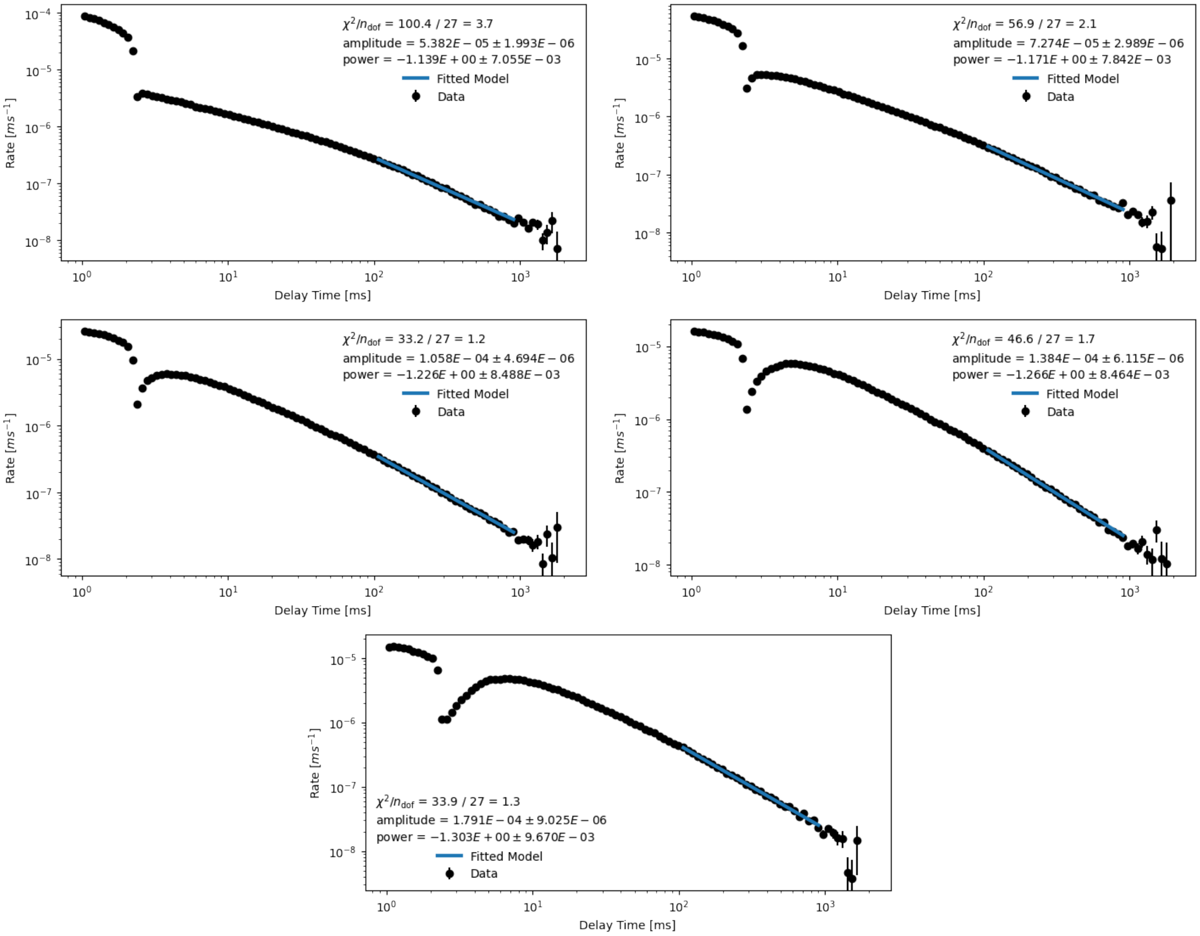

Figure C.1: Fitting the trends of sS2 with $N_{e,rec} = 1$ with power law in the five pS2 bins. All the plots were taken from Dr. Jacques Pienaar's study note

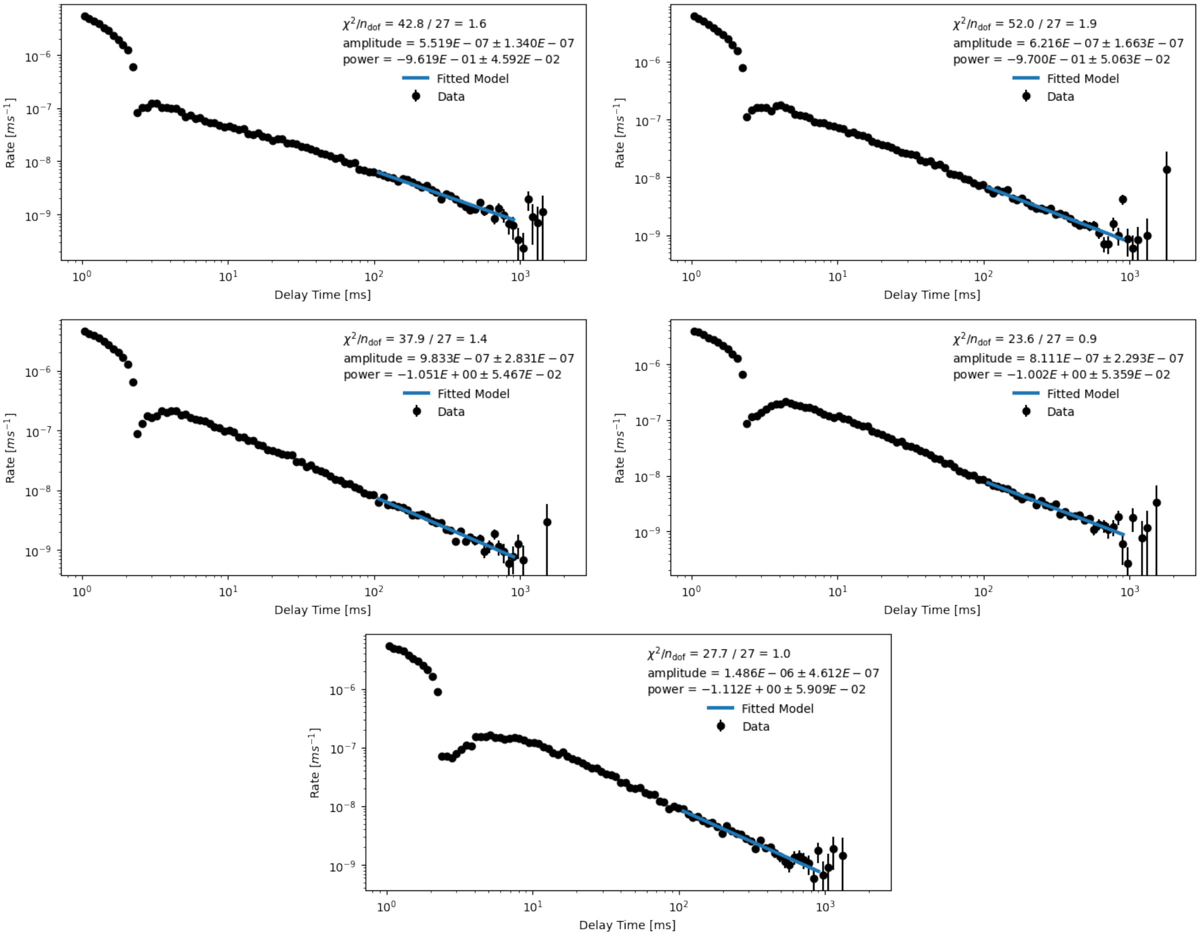

Figure C.2: Fitting the trends of sS2 with $N_{e,rec} = 2$ with power law in the five pS2 bins. All the plots were taken from Dr. Jacques Pienaar's study note

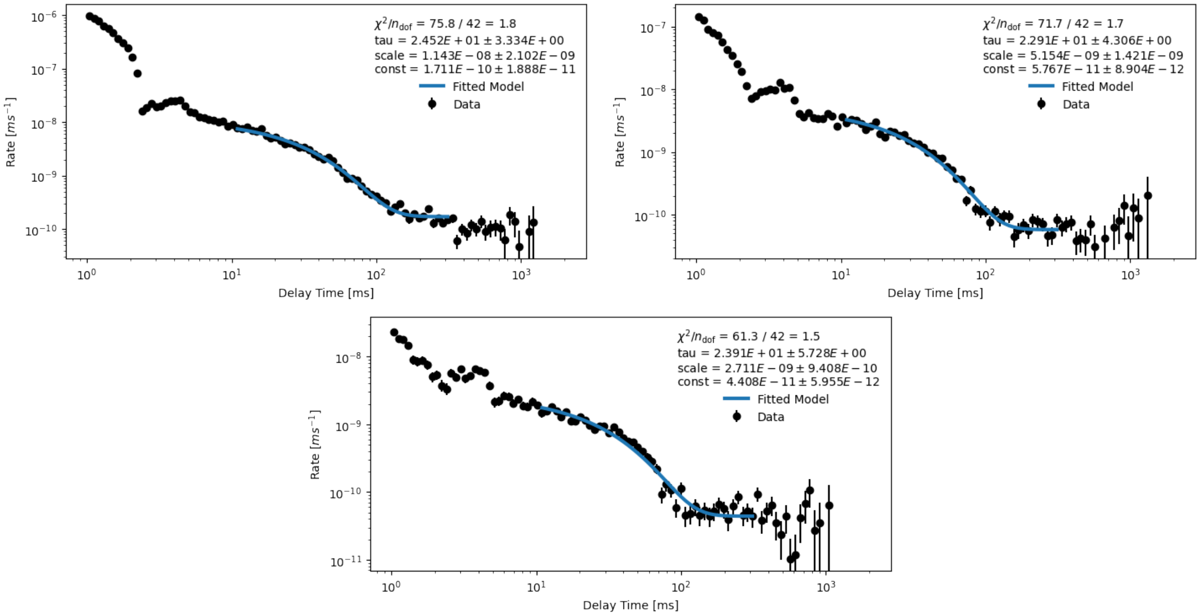

Figure C.3: Fitting the trends of sS2 with $N_{e,rec} = 3$ to 5 with exponential. No binning in pS2s due to a lack of statistics. All the plots were taken from Dr. Jacques Pienaar's study note

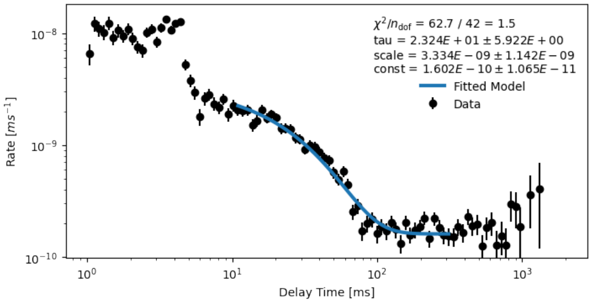

Figure C.4: Fitting the trend of sS2 between $N_{e,rec} = 6$ and 10 with exponential. No binning in pS2s nor in $N_{e,rec}$ due to a lack of statistics. All the plots were taken from Dr. Jacques Pienaar's study note

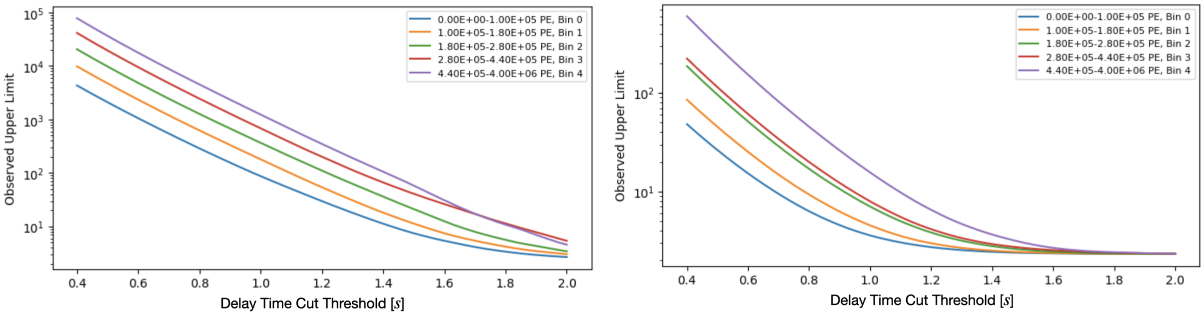

Figure C.5: 90% CL UL from expected sS2 rate fitting for $N_{e,rec} = 1$ and 2. All the plots were taken from Dr. Jacques Pienaar's study note

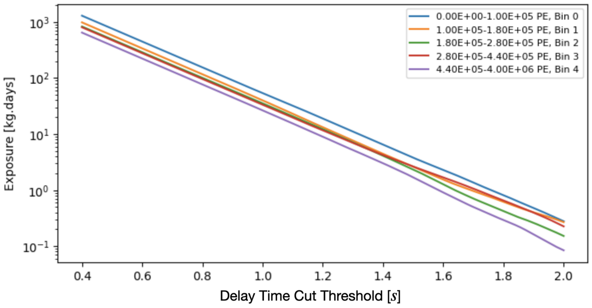

Figure C.6: Expected exposures in the 5 pS2 bins. All the plots were taken from Dr. Jacques Pienaar's study note

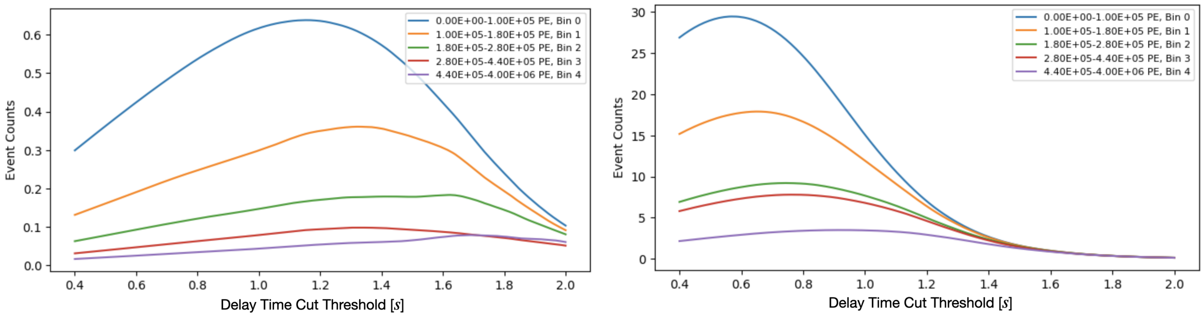

Figure C.7: Ratio of the 90% CL UL and the exposure for $N_{e,rec} = 1$ and 2. All the plots were taken from Dr. Jacques Pienaar's study note

APPENDIX D

CLOSED-FORM FOR POISSON UPPER LIMIT

I acknowledge my lack of in-depth understanding of the statistical concepts. However, I will document some calculations of the Poisson upper limit (UL) with a predetermined confidence level (CL). For more rigorous discussions, please refer to [115, 122].

The whole setup is based on the fact that we don't have a full background model. Suppose, after dedicated developments of cuts, cut acceptances, and signal model calculations, we observed n total events from the experiment, and a total of μ observations are expected from a specific BSM model. Due to a lack of background information, we cannot know how many events, out of the n observed ones, are from the BSM interaction. Assuming the BSM model is true (the hypothesis), the probability of observing n total events, without a quantifiable background, is the p-value of Poisson distribution:

$$p(n;\mu) \equiv \sum_{k=0}^{n} \left(\frac{\mu^k}{k!} e^{-\mu} \right) = 1 - F_{\chi^2}(2\mu; 2(n+1)) \tag{D.1}$$

The function $F_{\chi^2}(x; 2(n+1))$ is the cumulative density function of the χ^2 distribution with $2(n+1)$ degrees of freedom, evaluated at x. Intuitively, the above formula means observing n events can only happen if the number of observed events from BSM is less than or equal to n.

We are able to reject the hypothesis with $(1-\alpha)$ CL if the p-value is less than α. Setting Eqn. D.1 $= 1 - \alpha$, we can establish the relation between the confidence level α and the expected number of events μ:

$$\mu = \frac{1}{2} F_{\chi^2}^{-1}(1-\alpha; 2(n+1)) \tag{D.2}$$

For different usages, Eqn. D.2 can provide either a μ value that satisfies the required rejection

CL α, or the rejection CL α if μ cannot change.

For the concern of this thesis, in which we set constraints on BSM models without the full background model, we adjust the parameters in the BSM model and change the expected numbers to meet the CL. Typically, we set $1 - \alpha$ to be 0.9 (the 90% CL UL).

This summarizes the naive review of the definition of Poisson Upper Limit.

BIBLIOGRAPHY

[1] Dragan Huterer and Daniel L Shafer. "Dark energy two decades after: observables, probes, consistency tests". In: *Reports on Progress in Physics* 81.1 (Dec. 2017), p. 016901. ISSN: 1361-6633. DOI: `10.1088/1361-6633/aa997e`.

[2] N. Aghanim et al. "Planck2018 results: VI. Cosmological parameters". In: *Astronomy & Astrophysics* 641 (Sept. 2020), A6. ISSN: 1432-0746. DOI: `10.1051/0004-6361/201833910`.

[3] E. Öpik. *The question of selective absorption of light in space viewed from the viewpoint of the dynamics of the universe*. 2022. DOI: `10.48550/arxiv.2203.14871`. arXiv: `2203.14871 [astro-ph.GA]`.

[4] F. Zwicky. "On the Masses of Nebulae and of Clusters of Nebulae". In: *apj* 86 (Oct. 1937), p. 217. DOI: `10.1086/143864`.

[5] E. Corbelli and P. Salucci. "The extended rotation curve and the dark matter halo of M33". In: *Monthly Notices of the Royal Astronomical Society* 311.2 (Jan. 2000), pp. 441–447. ISSN: 1365-2966. DOI: `10.1046/j.1365-8711.2000.03075.x`.

[6] D. Burstein and C. Heiles. "H I, galaxy counts, and reddening: variation in the gas-to-dust ratio, the extinction at high galactic latitudes, and a new method for determining galactic reddening." In: *apj* 225 (Oct. 1978), pp. 40–55. DOI: `10.1086/156466`.

[7] S. M. Faber and J. S. Gallagher. "Masses and mass-to-light ratios of galaxies." In: *araa* 17 (Jan. 1979), pp. 135–187. DOI: `10.1146/annurev.aa.17.090179.001031`.

[8] R. H. Hildebrand. "The determination of cloud masses and dust characteristics from submillimetre thermal emission." In: *qjras* 24 (Sept. 1983), pp. 267–282.

[9] Albert Einstein. "Lens-Like Action of a Star by the Deviation of Light in the Gravitational Field". In: *Science* 84.2188 (Dec. 1936), pp. 506–507. DOI: `10.1126/science.84.2188.506`.

[10] Russell J. Smith et al. “Discovery of Strong Lensing by an Elliptical Galaxy at z = 0.0345”. In: *The Astrophysical Journal* 625.2 (May 2005), pp. L103–L106. ISSN: 1538-4357. DOI: `10.1086/431240`.

[11] Matts Roos. “Astrophysical and Cosmological Probes of Dark Matter”. In: *Journal of Modern Physics* 03.09 (2012), pp. 1152–1171. ISSN: 2153-120X. DOI: `10.4236/jmp.2012.329150`.

[12] A. N. Taylor et al. “Gravitational Lens Magnification and the Mass of Abell 1689”. In: *The Astrophysical Journal* 501.2 (July 1998), p. 539. DOI: `10.1086/305827`.

[13] M. Markevitch, A. Vikhlinin, and W. R. Forman. “A High resolution picture of the intracluster gas”. In: *ASP Conf. Ser.* 301 (2003), p. 37. DOI: `10.48550/arxiv.astro-ph/0208208`. arXiv: `astro-ph/0208208`.

[14] Douglas Clowe et al. “A direct empirical proof of the existence of dark matter”. In: *Astrophys. J. Lett.* 648 (2006), pp. L109–L113. DOI: `10.1086/508162`. arXiv: `astro-ph/0608407`.

[15] *The European Space Agency*. URL: `https://www.esa.int/ESA_Multimedia/Images/2007/07/The_Bullet_Cluster2`.

[16] RALPH A. ALPHER and ROBERT HERMAN. “Evolution of the Universe”. In: *Nature* 162.4124 (Nov. 1, 1948), pp. 774–775. ISSN: 1476-4687. DOI: `10.1038/162774b0`.

[17] A. A. Penzias and R. W. Wilson. “A Measurement of Excess Antenna Temperature at 4080 Mc/s.” In: *apj* 142 (July 1965), pp. 419–421. DOI: `10.1086/148307`.

[18] D. J. Fixsen. “THE TEMPERATURE OF THE COSMIC MICROWAVE BACKGROUND”. In: *The Astrophysical Journal* 707.2 (Nov. 2009), p. 916. DOI: `10.1088/0004-637X/707/2/916`. URL: `https://dx.doi.org/10.1088/0004-637X/707/2/916`.

[19] Robert H. Brandenberger. *Formation of Structure in the Universe*. 1995. arXiv: `astro-ph/9508159 [astro-ph]`.

[20] Karsten Jedamzik and Maxim Pospelov. "Big Bang nucleosynthesis and particle dark matter". In: *New Journal of Physics* 11.10 (Oct. 2009), p. 105028. ISSN: 1367-2630. DOI: `10.1088/1367-2630/11/10/105028`. URL: `http://dx.doi.org/10.1088/1367-2630/11/10/105028`.

[21] Planck Collaboration et al. "Planck 2018 results - I. Overview and the cosmological legacy of Planck". In: *A&A* 641 (2020), A1. DOI: `10.1051/0004-6361/201833880`.

[22] Wayne Hu. *Baryons and Inertia*. the University of Chicago. 2001. URL: `http://background.uchicago.edu/~whu/intermediate/baryons.html` (visited on 04/28/2024).

[23] Wayne Hu. *Radiation Driving Force*. the University of Chicago. 2001. URL: `http://background.uchicago.edu/~whu/intermediate/driving.html` (visited on 04/28/2024).

[24] Wayne Hu. *Ringing in the New Cosmology*. the University of Chicago. 2001. URL: `http://background.uchicago.edu/~whu/intermediate/intermediate.html` (visited on 04/28/2024).

[25] *WMAP*. URL: `https://wmap.gsfc.nasa.gov/universe/uni_matter.html`.

[26] Andrew R. Liddle and David H. Lyth. *Cosmological Inflation and Large-Scale Structure*. Cambridge University Press, 2000.

[27] P. J. E. Peebles. *The large-scale structure of the universe*. 1980.

[28] Wayne Hu and Daniel J. Eisenstein. "Structure of structure formation theories". In: *Phys. Rev. D* 59 (8 Mar. 1999), p. 083509. DOI: `10.1103/PhysRevD.59.083509`. URL: `https://link.aps.org/doi/10.1103/PhysRevD.59.083509`.

[29] Volker Springel, Carlos S. Frenk, and Simon D. M. White. "The large-scale structure of the Universe". In: *Nature* 440.7088 (Apr. 2006), pp. 1137–1144. ISSN: 1476-4687. DOI: `10.1038/nature04805`. URL: `http://dx.doi.org/10.1038/nature04805`.

[30] Benoît Famaey and Stacy S. McGaugh. "Modified Newtonian Dynamics (MOND): Observational Phenomenology and Relativistic Extensions". In: *Living Reviews in Relativity* 15.1 (Sept. 7, 2012), p. 10. ISSN: 1433-8351. DOI: `10.12942/lrr-2012-10`.

[31] Jacob D. Bekenstein. "Relativistic gravitation theory for the modified Newtonian dynamics paradigm". In: *Phys. Rev. D* 70 (8 Oct. 2004), p. 083509. DOI: `10.1103/PhysRevD.70.083509`.

[32] Gerard Jungman, Marc Kamionkowski, and Kim Griest. "Supersymmetric dark matter". In: *Physics Reports* 267.5 (1996), pp. 195–373. ISSN: 0370-1573. DOI: `10.1016/0370-1573(95)00058-5`. URL: `https://www.sciencedirect.com/science/article/pii/0370157395000585`.

[33] Tongyan Lin. *TASI lectures on dark matter models and direct detection.* 2019. DOI: `10.48550/arxiv.1904.07915`. arXiv: `1904.07915 [hep-ph]`.

[34] Particle Data Group et al. "Review of Particle Physics". In: *Progress of Theoretical and Experimental Physics* 2022.8 (Aug. 2022), p. 083C01. ISSN: 2050-3911. DOI: `10.1093/ptep/ptac097`. eprint: `https://academic.oup.com/ptep/article-pdf/2022/8/083C01/49175539/ptac097.pdf`.

[35] Gianfranco Bertone, Dan Hooper, and Joseph Silk. "Particle dark matter: evidence, candidates and constraints". In: *Physics Reports* 405.56 (Jan. 2005), pp. 279–390. ISSN: 0370-1573. DOI: `10.1016/j.physrep.2004.08.031`.

[36] Teresa Marrodán Undagoitia and Ludwig Rauch. "Dark matter direct-detection experiments". In: *Journal of Physics G: Nuclear and Particle Physics* 43.1 (Dec. 2015), p. 013001. ISSN: 1361-6471. DOI: `10.1088/0954-3899/43/1/013001`.

[37] Rouven Essig et al. *Direct Detection of sub-GeV Dark Matter with Semiconductor Targets*. 2016. DOI: `10.48550/arxiv.1509.01598`. arXiv: `1509.01598 [hep-ph]`.

[38] Rouven Essig, Tomer Volansky, and Tien-Tien Yu. “New constraints and prospects for sub-GeV dark matter scattering off electrons in xenon”. In: *Phys. Rev. D* 96 (4 Aug. 2017), p. 043017. DOI: `10.1103/PhysRevD.96.043017`.

[39] P. Agnes et al. “Constraints on Sub-GeV Dark-MatterElectron Scattering from the DarkSide-50 Experiment”. In: *Physical Review Letters* 121.11 (Sept. 2018). ISSN: 1079-7114. DOI: `10.1103/physrevlett.121.111303`.

[40] Bob Holdom. “Two U(1)’s and charge shifts”. In: *Physics Letters B* 166.2 (1986), pp. 196–198. ISSN: 0370-2693. DOI: `10.1016/0370-2693(86)91377-8`. URL: `https://www.sciencedirect.com/science/article/pii/0370269386913778`.

[41] Clifford Cheung et al. “Kinetic mixing as the origin of a light dark-gauge-group scale”. In: *Physical Review D* 80.3 (Aug. 2009). ISSN: 1550-2368. DOI: `10.1103/physrevd.80.035008`.

[42] C.F. Bunge, J.A. Barrientos, and A.V. Bunge. “Roothaan-Hartree-Fock Ground-State Atomic Wave Functions: Slater-Type Orbital Expansions and Expectation Values for Z = 2-54”. In: *Atomic Data and Nuclear Data Tables* 53.1 (1993), pp. 113–162. ISSN: 0092-640X. DOI: `10.1006/adnd.1993.1003`. URL: `https://www.sciencedirect.com/science/article/pii/S0092640X8371003X`.

[43] C. C. J. Roothaan. “New Developments in Molecular Orbital Theory”. In: *Rev. Mod. Phys.* 23 (2 Apr. 1951), pp. 69–89. DOI: `10.1103/RevModPhys.23.69`.

[44] J I Read. “The local dark matter density”. In: *Journal of Physics G: Nuclear and Particle Physics* 41.6 (May 2014), p. 063101. ISSN: 1361-6471. DOI: `10.1088/0954-3899/41/6/063101`.

[45] Jelle Aalbers. *wimprates, v0.5.0*. `https://github.com/JelleAalbers/wimprates`.

[46] Peter Galison and Aneesh Manohar. “Two Z’s or not two Z’s?” In: *Physics Letters B* 136.4 (1984), pp. 279–283. ISSN: 0370-2693. DOI: `10.1016/0370-2693(84)91161-4`. URL: `https://www.sciencedirect.com/science/article/pii/0370269384911614`.

[47] Ann E. Nelson and Jakub Scholtz. “Dark light, dark matter, and the misalignment mechanism”. In: *Physical Review D* 84.10 (Nov. 2011). ISSN: 1550-2368. DOI: `10.1103/physrevd.84.103501`.

[48] Itay M. Bloch et al. “Searching for dark absorption with direct detection experiments”. In: *Journal of High Energy Physics* 2017.6 (June 2017). ISSN: 1029-8479. DOI: `10.1007/jhep06(2017)087`.

[49] B.L. Henke, E.M. Gullikson, and J.C. Davis. “X-Ray Interactions: Photoabsorption, Scattering, Transmission, and Reflection at E = 50-30,000 eV, Z = 1-92”. In: *Atomic Data and Nuclear Data Tables* 54.2 (1993), pp. 181–342. ISSN: 0092-640X. DOI: `10.1006/adnd.1993.1013`. URL: `https://www.sciencedirect.com/science/article/pii/S0092640X83710132`.

[50] Haipeng An, Maxim Pospelov, and Josef Pradler. “Dark Matter Detectors as Dark Photon Helioscopes”. In: *Physical Review Letters* 111.4 (July 2013). ISSN: 1079-7114. DOI: `10.1103/physrevlett.111.041302`.

[51] Tianqi Sai et al. “Designing refractive index fluids using the KramersKronig relations”. In: *Faraday Discuss.* 223 (0 2020), pp. 136–144. DOI: `10.1039/D0FD00027B`.

[52] XENON Collaboration, E. Aprile, et al. “Emission of single and few electrons in XENON1T and limits on light dark matter”. In: *Phys. Rev. D* 106 (2 July 2022), p. 022001. DOI: `10.1103/PhysRevD.106.022001`.

[53] R. D. Peccei and Helen R. Quinn. “CP Conservation in the Presence of Pseudoparticles”. In: *Phys. Rev. Lett.* 38 (25 June 1977), pp. 1440–1443. DOI: `10.1103/PhysRevLett.38.1440`.

[54] R. D. Peccei and Helen R. Quinn. “Constraints imposed by CP conservation in the presence of pseudoparticles”. In: *Phys. Rev. D* 16 (6 Sept. 1977), pp. 1791–1797. DOI: `10.1103/PhysRevD.16.1791`.

[55] A. G. Dias et al. “The quest for an intermediate-scale accidental axion and further ALPs”. In: *Journal of High Energy Physics* 2014.6 (June 2014). ISSN: 1029-8479. DOI: `10.1007/jhep06(2014)037`.

[56] F. T. Avignone III et al. “Laboratory limits on solar axions from an ultralow-background germanium spectrometer”. In: *Phys. Rev. D* 35 (9 May 1987), pp. 2752–2757. DOI: `10.1103/PhysRevD.35.2752`.

[57] Maxim Pospelov, Adam Ritz, and Mikhail Voloshin. “Bosonic super-WIMPs as keV-scale dark matter”. In: *Physical Review D* 78.11 (Dec. 2008). ISSN: 1550-2368. DOI: `10.1103/physrevd.78.115012`.

[58] XENON Collaboration, E. Aprile, et al. “Design and performance of the XENON10 dark matter experiment”. In: *Astroparticle Physics* 34.9 (Apr. 2011), pp. 679–698. ISSN: 0927-6505. DOI: `10.1016/j.astropartphys.2011.01.006`.

[59] XENON Collaboration, E. Aprile, et al. “The XENONnT Dark Matter Experiment”. In: *To be published* (). DOI: `00.0000/FancyJournal.InstrumentPaper`.

[60] XENON Collaboration, E. Aprile, et al. “"Material radiopurity control in the XENONnT experiment"”. In: *The European Physical Journal C* 82.7 (July 8, 2022), p. 599. ISSN: 1434-6052. DOI: `10.1140/epjc/s10052-022-10345-6`.

[61] XENON Collaboration, E. Aprile, et al. "Projected WIMP sensitivity of the XENONnT dark matter experiment". In: *Journal of Cosmology and Astroparticle Physics* 2020.11 (Nov. 2020), p. 031. DOI: `10.1088/1475-7516/2020/11/031`.

[62] XENON Collaboration, E. Aprile, et al. *The XENONnT Dark Matter Experiment.* 2024. DOI: `10.48550/arxiv.2402.10446`. arXiv: `2402.10446 [physics.ins-det]`.

[63] XENON Collaboration, E. Aprile, et al. "Application and modeling of an online distillation method to reduce krypton and argon in XENON1T". In: *Progress of Theoretical and Experimental Physics* 2022.5 (Apr. 2022), 053H01. ISSN: 2050-3911. DOI: `10.1093/ptep/ptac074`. eprint: `https://academic.oup.com/ptep/article-pdf/2022/5/053H01/43860921/ptac074.pdf`.

[64] XENON Collaboration, E. Aprile, et al. "^{222}Rn emanation measurements for the XENON1T experiment". In: *Eur. Phys. J. C* 81.4 (2021), p. 337. DOI: `10.1140/epjc/s10052-020-08777-z`. arXiv: `2009.13981 [physics.ins-det]`.

[65] G. Zuzel and H. Simgen. "High sensitivity radon emanation measurements". In: *Applied Radiation and Isotopes* 67.5 (2009). 5th International Conference on Radionuclide Metrology - Low-Level Radioactivity Measurement Techniques ICRM-LLRMT'08, pp. 889–893. ISSN: 0969-8043. DOI: `10.1016/j.apradiso.2009.01.052`. URL: `https://www.sciencedirect.com/science/article/pii/S0969804309000608`.

[66] XENON Collaboration, E. Aprile, et al. "First Dark Matter Search with Nuclear Recoils from the XENONnT Experiment". In: *Phys. Rev. Lett.* 131 (4 July 2023), p. 041003. DOI: `10.1103/PhysRevLett.131.041003`.

[67] XENON Collaboration, E. Aprile, et al. "Search for New Physics in Electronic Recoil Data from XENONnT". In: *Phys. Rev. Lett.* 129 (16 Oct. 2022), p. 161805. DOI: `10.1103/PhysRevLett.129.161805`.

[68] E. Aprile et al. “Simultaneous Measurement of Ionization and Scintillation from Nuclear Recoils in Liquid Xenon for a Dark Matter Experiment”. In: *Phys. Rev. Lett.* 97 (8 Aug. 2006), p. 081302. DOI: `10.1103/PhysRevLett.97.081302`.

[69] J. Thomas and D. A. Imel. “"Recombination of electron-ion pairs in liquid argon and liquid xenon"”. In: *Phys. Rev. A* 36." " (2 July 1987), pp. 614–616. DOI: `10.1103/PhysRevA.36.614`.

[70] XENON Collaboration, E. Aprile, et al. “XENONnT SR0 Analysis: Signal Reconstruction, Calibration and Event Selection”. In: *To be published* (). DOI: `00.0000/FancyJournal.InstrumentPaper`.

[71] XENON Collaboration, E. Aprile, et al. “Design and performance of the field cage for the XENONnT experiment”. In: *The European Physical Journal C* 84.2 (Feb. 8, 2024), p. 138. ISSN: 1434-6052. DOI: `10.1140/epjc/s10052-023-12296-y`.

[72] XENON Collaboration, E. Aprile, et al. “XENONnT dark matter data analysis: Signal and background models and statistical inference”. In: *To be published* (). DOI: `00.0000/FancyJournal.InstrumentPaper`.

[73] Tadayoshi Doke et al. “Absolute Scintillation Yields in Liquid Argon and Xenon for Various Particles”. In: *Japanese Journal of Applied Physics* 41.3R (Mar. 2002), p. 1538. DOI: `10.1143/JJAP.41.1538`.

[74] Laura Baudis, Patricia Sanchez-Lucas, and Kevin Thieme. “A measurement of the mean electronic excitation energy of liquid xenon”. In: *The European Physical Journal C* 81.12 (Dec. 2021). ISSN: 1434-6052. DOI: `10.1140/epjc/s10052-021-09834-x`.

[75] Mona Piotter et al. “First time-resolved measurement of infrared scintillation light in gaseous xenon”. In: *The European Physical Journal C* 83.6 (June 2023). ISSN: 1434-6052. DOI: `10.1140/epjc/s10052-023-11618-4`.

[76] M Szydagis et al. “NEST: a comprehensive model for scintillation yield in liquid xenon”. In: *Journal of Instrumentation* 6.10 (Oct. 2011), P10002–P10002. ISSN: 1748-0221. DOI: `10.1088/1748-0221/6/10/p10002`.

[77] J Lindhard, M Scharff, and H E Schioett. “RANGE CONCEPTS AND HEAVY ION RANGES (NOTES ON ATOMIC COLLISIONS, II)”. In: *Kgl. Danske Videnskab. Selskab. Mat. Fys. Medd.* Vol: 33: No. 14 (Jan. 1963). URL: `https://www.osti.gov/biblio/4153115`.

[78] Peter Sorensen and Carl Eric Dahl. “Nuclear recoil energy scale in liquid xenon with application to the direct detection of dark matter”. English (US). In: *Physical Review D - Particles, Fields, Gravitation and Cosmology* 83.6 (Mar. 1, 2011). ISSN: 1550-7998. DOI: `10.1103/PhysRevD.83.063501`.

[79] D.-M. Mei et al. “A model of nuclear recoil scintillation efficiency in noble liquids”. In: *Astroparticle Physics* 30.1 (2008), pp. 12–17. ISSN: 0927-6505. DOI: `10.1016/j.astropartphys.2008.06.001`. URL: `https://www.sciencedirect.com/science/article/pii/S0927650508000765`.

[80] Giovanni Volta. “Characterization and Monitoring of XENONnT Photosensors and Search for New Physics with the First XENONnT Science Data”. Ph.D. dissertation. Switzerland: University of Zurich, Mar. 2023. URL: `https://xe1t-wiki.lngs.infn.it/lib/exe/fetch.php?media=xenon:phd_thesis_final_giovanni_volta.pdf`.

[81] J. Xu et al. “Electron extraction efficiency study for dual-phase xenon dark matter experiments”. In: *Physical Review D* 99.10 (May 2019). ISSN: 2470-0029. DOI: `10.1103/physrevd.99.103024`.

[82] CAEN. *WEB_UM3248_V1724_rev32*. Version Rev. 32 - 18/04/2017. CAEN. 2017. URL: `https://www.caen.it/products/v1724/`.

[83] G. Volta et al. *Characterization and Monitoring of XENONnT Photosensors and Search for New Physics with the First XENONnT Science Data*. Universität Zürich, 2023. URL: `https://books.google.com/books?id=ALtb0AEACAAJ`.

[84] R. Saldanha et al. "Model Independent Approach to the Single Photoelectron Calibration of Photomultiplier Tubes". In: *Nucl. Instrum. Meth. A* 863 (2017). Ed. by Guoqing Xiao, Hao Shen, and Guanghua Du, pp. 35–46. DOI: `10.1016/j.nima.2017.02.086`. arXiv: `1602.03150 [physics.ins-det]`.

[85] XENON Collaboration, E. Aprile, et al. "XENON1T dark matter data analysis: Signal reconstruction, calibration, and event selection". In: *Phys. Rev. D* 100 (5 Sept. 2019), p. 052014. DOI: `10.1103/PhysRevD.100.052014`.

[86] James H. Parker and John J. Lowke. "Theory of Electron Diffusion Parallel to Electric Fields. I. Theory". In: *Phys. Rev.* 181 (1 May 1969), pp. 290–301. DOI: `10.1103/PhysRev.181.290`.

[87] Peter Sorensen. "Anisotropic diffusion of electrons in liquid xenon with application to improving the sensitivity of direct dark matter searches". In: *Nuclear Instruments and Methods in Physics Research Section A: Accelerators, Spectrometers, Detectors and Associated Equipment* 635.1 (Apr. 2011), pp. 41–43. ISSN: 0168-9002. DOI: `10.1016/j.nima.2011.01.089`.

[88] P. Sorensen and K. Kamdin. "Two distinct components of the delayed single electron noise in liquid xenon emission detectors". In: *Journal of Instrumentation* 13.02 (Feb. 2018), P02032. DOI: `10.1088/1748-0221/13/02/P02032`.

[89] Peter Sorensen. "Electron train backgrounds in liquid xenon dark matter search detectors are indeed due to thermalization and trapping". In: (Feb. 2017). DOI: `10.48550/arxiv.1702.04805`. arXiv: `1702.04805 [physics.ins-det]`.

[90] Ikuko Murayama and Shogo Nakamura. “Time profile of the scintillation from liquid and gaseous xenon”. In: *Nuclear Instruments and Methods in Physics Research Section A: Accelerators, Spectrometers, Detectors and Associated Equipment* 763 (2014), pp. 533–537. ISSN: 0168-9002. DOI: `10.1016/j.nima.2014.07.003`. URL: `https://www.sciencedirect.com/science/article/pii/S0168900214008456`.

[91] J Mock et al. “Modeling pulse characteristics in Xenon with NEST”. In: *Journal of Instrumentation* 9.04 (Apr. 2014), T04002–T04002. ISSN: 1748-0221. DOI: `10.1088/1748-0221/9/04/t04002`.

[92] C M B Monteiro et al. “Secondary scintillation yield in pure xenon”. In: *Journal of Instrumentation* 2.05 (May 2007), P05001–P05001. ISSN: 1748-0221. DOI: `10.1088/1748-0221/2/05/p05001`.

[93] XENON Collaboration, E. Aprile, et al. “Observation and applications of single-electron charge signals in the XENON100 experiment”. In: *J. Phys. G* 41 (2014), p. 035201. DOI: `10.1088/0954-3899/41/3/035201`. arXiv: `1311.1088 [physics.ins-det]`.

[94] V. C. Antochi et al. “Improved quality tests of R11410-21 photomultiplier tubes for the XENONnT experiment”. In: *JINST* 16.08 (2021), P08033. DOI: `10.1088/1748-0221/16/08/P08033`. arXiv: `2104.15051 [physics.ins-det]`.

[95] K. Lung et al. “Characterization of the Hamamatsu R11410-10 3-in. photomultiplier tube for liquid xenon dark matter direct detection experiments”. In: *Nuclear Instruments and Methods in Physics Research Section A: Accelerators, Spectrometers, Detectors and Associated Equipment* 696 (2012), pp. 32–39. ISSN: 0168-9002. DOI: `10.1016/j.nima.2012.08.052`. URL: `https://www.sciencedirect.com/science/article/pii/S0168900212009230`.

[96] Daniel Z. Freedman. “Coherent effects of a weak neutral current”. In: *Phys. Rev. D* 9 (5 Mar. 1974), pp. 1389–1392. DOI: `10.1103/PhysRevD.9.1389`.

[97] D. Akimov et al. “Observation of coherent elastic neutrino-nucleus scattering”. In: *Science* 357.6356 (2017), pp. 1123–1126. DOI: `10.1126/science.aao0990`.

[98] Jingke Xu. *Low-energy ionization background in LUX/LZ and its implications*. Presentation at Nagoya Workshop on Future Noble Gas Detectors. Feb. 2024.

[99] R. H. Fowler and L. Nordheim. “Electron Emission in Intense Electric Fields”. In: *Proceedings of the Royal Society of London Series A* 119.781 (May 1928), pp. 173–181. DOI: `10.1098/rspa.1928.0091`.

[100] L. W. Nordhiem and Ralph Howard Fowler. “The effect of the image force on the emission and reflexion of electrons by metals”. In: *Proceedings of the Royal Society of London. Series A, Containing Papers of a Mathematical and Physical Character* 121.788 (1928), pp. 626–639. DOI: `10.1098/rspa.1928.0222`.

[101] A. Tomás et al. “Study and mitigation of spurious electron emission from cathodic wires in noble liquid time projection chambers”. In: *Astroparticle Physics* 103 (Dec. 2018), pp. 49–61. ISSN: 0927-6505. DOI: `10.1016/j.astropartphys.2018.07.001`.

[102] D. S. Akerib et al. “Investigation of background electron emission in the LUX detector”. In: *Phys. Rev. D* 102.9 (2020), p. 092004. DOI: `10.1103/PhysRevD.102.092004`. arXiv: `2004.07791 [physics.ins-det]`.

[103] Shuaijie Li et al. “Search for Light Dark Matter with Ionization Signals in the PandaX-4T Experiment”. In: *Phys. Rev. Lett.* 130 (26 June 2023), p. 261001. DOI: `10.1103/PhysRevLett.130.261001`.

[104] D.Yu. Akimov et al. “Observation of delayed electron emission in a two-phase liquid xenon detector”. In: *Journal of Instrumentation* 11.03 (Mar. 2016), p. C03007. DOI: `10.1088/1748-0221/11/03/C03007`.

[105] Abigail Kopec et al. “Correlated single- and few-electron backgrounds milliseconds after interactions in dual-phase liquid xenon time projection chambers”. In: *JINST* 16.07 (2021), P07014. DOI: `10.1088/1748-0221/16/07/P07014`. arXiv: `2103.05077 [physics.ins-det]`.

[106] XENON Collaboration, E. Aprile, et al. “Light Dark Matter Search with Ionization Signals in XENON1T”. In: *Phys. Rev. Lett.* 123 (25 Dec. 2019), p. 251801. DOI: `10.1103/PhysRevLett.123.251801`.

[107] XENON Collaboration, E. Aprile, et al. “Full-chain simulation from energy deposits and yielding records with exactly the same strax(en) format as used in XENONnT”. In: *To be published* (). DOI: `00.0000/FancyJournal.InstrumentPaper`.

[108] Jelle Aalbers, Joran Angevaare, et al. *Straxen*. `https://github.com/XENONnT/straxen`. 2018.

[109] Jelle Aalbers, Joran Angevaare, and the others. *Strax*. `https://github.com/AxFoundation/strax/tree/master?tab=License-1-ov-file`. 2019.

[110] *Garfield++*. `https://garfieldpp.web.cern.ch/garfieldpp/`.

[111] *GEANT4*. `https://geant4-userdoc.web.cern.ch/UsersGuides/PhysicsReferenceManual/html/generalities/index.html`.

[112] COMSOL. *COMSOL Multiphysics v. 6.2.* `www.comsol.com`. COMSOL AB, Stockholm, Sweden.

[113] NEST Collaboration. *NEST*. `https://github.com/NESTCollaboration/nest/blob/master/README.md`.

[114] S. Yellin. “Finding an upper limit in the presence of an unknown background”. In: *Physical Review D* 66.3 (Aug. 2002). ISSN: 1089-4918. DOI: `10.1103/physrevd.66.032005`.

[115] Pueh Leng Tan. “Solar Reflected Dark Matter with XENON1T and XENONnT”. Ph.D. dissertation. Stockholm, Sweden: Stockholm University, 2024. URL: `In%20Preparation`.

[116] I. T. Steinberger and U. Asaf. “Band-Structure Parameters of Solid and Liquid Xenon”. In: *Phys. Rev. B* 8 (2 July 1973), pp. 914–918. DOI: `10.1103/PhysRevB.8.914`.

[117] SENSEI Collaboration et al. *SENSEI: First Direct-Detection Results on sub-GeV Dark Matter from SENSEI at SNOLAB*. 2023. DOI: `10.48550/arxiv.2312.13342`. arXiv: `2312.13342 [astro-ph.CO]`.

[118] I. Arnquist et al. “First Constraints from DAMIC-M on Sub-GeV Dark-Matter Particles Interacting with Electrons”. In: *Physical Review Letters* 130.17 (Apr. 2023). ISSN: 1079-7114. DOI: `10.1103/physrevlett.130.171003`.

[119] E. Depaoli et al. *Deployment and performance of a Low-Energy-Threshold Skipper-CCD inside a nuclear reactor*. 2024. DOI: `10.48550/arxiv.2401.07885`. arXiv: `2401.07885 [hep-ex]`.

[120] Shuaijie Li et al. “Search for Light Dark Matter with Ionization Signals in the PandaX-4T Experiment”. In: *Physical Review Letters* 130.26 (June 2023). ISSN: 1079-7114. DOI: `10.1103/physrevlett.130.261001`.

[121] Wolfram Research, Inc. *Mathematica, Version 13.2*. Champaign, IL, 2022.

[122] G. Cowan. *Statistical data analysis*. Oxford University Press, USA, 1998.